Mechanical Resonators for Material Characterization: Sensor Development and Applications

Casci Ceccacci, Andrea

Publication date:
2017

Document Version
Publisher's PDF, also known as Version of record

TECHNICAL UNIVERSITY OF DENMARK
DEPARTMENT OF MICRO AND NANOTECHNOLOGY
KONGENS LYNGBY,DENMARK

Mechanical Resonators For Material Characterization

Sensor Development and Applications

Andrea Casci Ceccacci

PhD Thesis

3/31/2017

Preface

This thesis has been written as a partial fulfilment of the requirements for obtaining the PhD degree at the Technical University of Denmark (DTU), Department of Micro and Nanotechnology during the period from April 1st 2014 to March 31st 2017. The PhD project was carried out within the ERC project HERMES.

Main Supervisor: Professor Anja Boisen

Co-Supervisor: Alberto Cagliani Researcher

Co-Supervisor: Filippo Giacomo Bosco, CEO and Founder of BluSense Diagnostic

Acknowledgments

It is not about of being rhetoric, but I would like to thank you first Anja. You have made this possible and guide me through my achievements. Your guidance and your unconditional optimism even in the toughest moments have been simply fundamental. Thanks for giving me the chance to do my PhD in the Nanoprobes group. Here I feel to have grown personally and scientifically.

A special thanks go to Albi, for simply transmitting the passion for science and giving me the criticism a scientist must have. Thanks for having "adopted" me as your student and for all the suggestions you have been giving me (work-wise and life-wise).

Filo, thanks for all the strategy meetings in the most unusual places of Copenhagen. Thanks for being the "the devil's advocate" and pushing me beyond the comfort zone. Thanks for going straight to the point and quickly trying to put me back on the right track. But actually, thanks for making me seeing things from a different perspective maybe more business-like.

Thanks to Sanjukta and Kinga for all your support especially in this last period, and the precious feedback you gave me for the thesis.Then I would like to acknowledge Edwin for all the technical support you have been providing me with the Blu-Ray system and get me acquainted with the philosophy of "trial and error". Thanks also to Albert for all the efforts you have been put in the designing the software, and the funny moments in the lab. Thanks to Professor Ole Hansen, for his infinite help with rather complex mathematical modelling.

Thanks to all the Italian firm at Nanotech, plus Olly Edo and the good old Marco De Paolis mates of memorable moments.Thanks to my master students Luca and Cristoforo for all their wonderful work. I would like to say thank you to Lidia my officemate, you´ve probably the best officemate I could ever have; maybe sometimes we have been slightly pessimistic regarding the outcomes of our "scientific" results, but all in all, it was more than 1 out of 100. Thanks to Letizia for opening me the world of research -back in time- for having believed in me and for the invaluable help you have been giving me since I have arrived here in Denmark.

I would like to say thank you to my flatmates, Fani and Juan for allowing me to invade the living room with laptops monitors papers and the stuff a PhD student needs during the writing time. Thanks to Vale and Luci, first officemates, then being mates of parties, discussions but moreover gossip. Thank you Paolo, for trying to give me a more chemistry side but for be great friend.

Thanks to my parents my sister, for their endless support and love especially in this last year where I have not been very present.

To all my hometown friends “Quelli del Quindi”, for make me feel like I have never left home, giving me mindless fun and support. Especially, I would like to say thank you to Balo, Uba, Alessandra, and Michele for always be there whenever I need.

Thank you Lalli. I know that you would probably upset that I decided to acknowledge you of something but I will take the risk. Thanks for reminding me that work is not the only thing that matters, for tolerating me and making me aware what I need.

Andre

Abstract

The goals of this PhD project were to provide new approaches and developing new systems for material characterization, based on micro and nanomechanical sensors.

Common issues that have shown to hinder large-scale integration of sensing techniques based on a micromechanical sensor are the readout and sample handling. To address the first point, a semi-automatic characterization platform based on the optics and the mechanics of a commercial Blu-Ray pickup head unit was developed. Microbridges were chosen instead of microcantilevers to provide more robustness to the sensor. By embedding the sensor in a single-use microfluidic cartridge, the experimental condition was improved. The sample handling, as well as the environmental condition of the phenomena under test, are better controlled. As proof of concept to test the capabilities of the system, we studied the biopolymer degradation of Poly Lactic-co-Glycolic Acid (PLGA), which is of high relevance in the biomedical research field. A second version of the system is currently under development, and it aims to increase the throughput of the system allowing to read out multiple microbridge arrays.

For material characterization, spectroscopy analysis is often considered a benchmark technology. Conventional infrared spectroscopy approaches commonly require milligram amount of sample. Considering the frame of reference given by the overall aim of the project, mechanical sensors can be exploited to provide a unique tool for performing spectroscopy on a limited amount of sample. In this project, a nanomechanical photothermal sensor has been designed, developed and exploited to perform thin film Infrared Spectroscopy. Contrary to what has been previously shown, this work has focused on a membrane sensor providing a robust experimental approach which better suit sample quantification and preparation. The purpose of the studies presented here is to show the real potential of photothermal spectroscopy based on a nanomechanical sensor and to provide a method to maximise the signal to noise ratio (SNR) from a single acquisition. The methodology presented showed that it is possible obtaining a high SNR of 300 on a 20nm thick polymer layer showing a substantial improvement compared to the benchmark technique, attenuated total reflectance spectroscopy (ATR-FTIR).This high sensitivity allowed us to observe the chemical modification occurring during the gelification of a submicron thick layer of poly-vinyl-pyrrolidone (PVP) corresponding to picogram quantity of material.

Resume

Målet med dette ph.d.-projekt var at udvikle et nyt system til karakterisering af materialer baseret på mikro og nanosensorer.

Nogle af de største udfordringer når det kommer til integration af mikromekaniske sensor-teknikker er readout'et samt håndteringen af prøver. For at forbedre readout'et udvikledes en semi-automatisk karakteriseringsplatform, baseret på optikken og mekanikken fra et pickuphoved i en Blu-Ray afspiller. For at gøre sensoren mere robust blev der brugt mikro-broer fremfor mikro-cantilevere. Det eksperimentielle setup blev væsentligt forbedret ved at integrere sensoren i et halv-lukket mikrofluid-system. Hermed blev håndtering af prøver gjort nemmere og miljøet omkring eksperimenterne mere kontrolleret. For at teste systemet undersøgte vi nedbrydningen af biopolymeren Poly Lactic-co-Glycolic Acid (PLGA) som en en yderst relevant biopolymer indenfor biomedicinsk forskning. En ny version af systemet med flere mikro-bro-arrays, og dermed et højere gennemløb, er lige nu under udvikling.

Indenfor materiale karakterisering er spektroskopi ofte opfattet som en standartteknik, men for eksempel traditionel infrarød spektroskopi kræver normalt en prøvestørrelse på nogle miligram. Mekaniske sensorer som den udviklet i dette projekt vil kunne bruges som et unikt værktøj til at udføre spektroskopi selv når kun en meget begrænset mængde prøve er tilgængelig. For eksempel kan den nanomekaniske phototermiske sensor designet, udviklet og testet i dette projekt kan udnyttes til tyndfilm infrarød spektroskopi. I modsætning til tidligere studier har dette projekt fokuseret på membransensorer i stedet for strenge hvilket har givet et mere robust setup som passer bedre til forberedelsen og kvantificeringen af prøver. Formålet med dette studie var at vise det store potentiale der er i at bruge nanomekaniske sensorer til fototermisk spektroskopi, samt at udvikle en metode til at maksimere forholdet mellem signal of støj (SNR) i hver enkelt måling. Med denne metode var det muligt at opnå en høj SNR på 300 ved 20 nm. Dette er en signifikant forbedring sammelignet med standart teknikken 'Attenuated totoal relflectance spectroscopy' (ATR-FTIR). Den høje sensitivitet gjorde det muligt at se den kemiske modifikation der sker under geleringen af et mikrometer tyndt lag a poly-vinyl-pyrrolidone (PVP), svarende til en ændring i materiale på nogle få picogram.

Paper Contribution

Paper1. I directed the development of the automated system. I planned and performed the experiments for the optimisation of the automated algorithm. I fabricated the microbridge structures and optimised the spray coating parameters for sensor functionalization. I further performed all the data analysis and gave the major contribution in the manuscript writing.

Paper 2. I fabricated the membrane resonators, planned the experiments, and performed all experiments. I developed the Matlab code for the analysis of the results; analysed the results and give the main contribution in the manuscript writing.

Paper 3. I designed and performed the calibration experiments (Figure 3). I participated in the design of the experiments and supervised the execution of the crosslinking experiments (Figure 4). I analysed the data, and did the main contribution in the manuscript writing.

Table of Contents

List of Figures

Good times bad
times you know I
had my share

1. Introduction

1.1. The Scientific Scenario

The development of new material can be seen as an iterative work consisting of two essential steps: the synthesis of the main compound and its characterization Figure 1.1. The purpose of the characterization is to acquire a certain material's properties and behaviour. In this regard, a high degree of availability and simplicity of the characterization techniques clearly makes the iteration process faster. This enhancement of the information throughput allows realising a more efficient and cost-effective material development process, making it capable of assessing and tailoring the final material application with a smaller number of iterations.

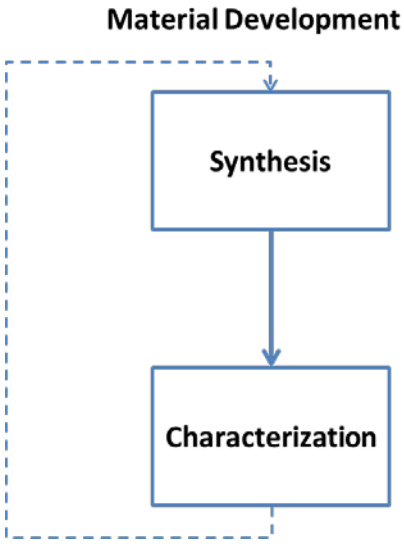

Figure 1.1 The iteration approach involved in the development of new materials. The synthesis and the characterization.

Polymer based materials are nowadays present in many aspects of our everyday life. Among polymers, biopolymers, which include all the polymers synthesised by living organisms [1], have received particular attention due to their extensive use in the biomedical and pharmaceutical industries. Noteworthy biopolymer-based

applications are; drug delivery devices [2–6], scaffolds for tissue engineering [7–9], bioabsorbable surgical sutures [10] ophthalmic system [11] and implantable devices [2,12]. Furthermore, biopolymers have been used to form a coating of functional parts[13,14], enabling the modification of the physio-chemical properties of the surface without interfering with bulk material properties. Such refinement of the surface properties by the simple application of a polymer layer has gained attention in the recent years. The vast library of available polymers and the ample processes enabled the tailoring of the final properties with infinite possibilities [5,7,15–20].

Hence, the development of novel, cost-effective and information-rich characterization methods of both physical and chemical properties of biopolymers throughout their life-cycle, is a challenge of primary importance.

Lactide-based polymers have aroused interest for application the pharmaceutical and biomedical devices compartment as they are biodegradable, meaning that they can be degraded in a natural environment yielding non-toxic degradation products. The ester bonds on the backbone of the chain undergo hydrolytic cleavage, catalysed by the presence of enzymes[21,22] or by an alkaline environment[23]. The knowledge of the biopolymer degradation rate is important as it defines the release profile of an active pharmaceutical ingredient (API) [5,24,25] or the stability of the implantable device[26]. The biopolymer properties can be modified using crosslinking to engineer their 3D structure and the crosslinking of biopolymers such as poly(vinylpyrrolidone) [27–29], hydroxypropyl methylcellulose (HPMC) [25], or chitosan [30] have been exploited to form a novel class of material commonly known as hydrogels. Hydrogels are hydrophilic water insoluble materials, wich have the ability to swollen in water or humid environment. Their properties can be easily tuned to fit a particular application, from drug delivery [31–33] to tissue engineering [34] or becoming the functional part of sensing device [13,35,36].

The current conventional approaches for measuring the biopolymer degradation are cumbersome [24] and extremely time-consuming requiring an experimental timeframe lasting from weeks to months [24,37–39].A possible route to boost the

degradation is studying the polymer behaviour in very harsh condition[40] i.e. very high or very low pH or high temperature. Indeed, this methodology does not represent a validation of the biopolymer properties for many of the biomedical applications. Enzymatic degradation of biopolymer has been studied using quartz crystal microbalance(QCM) and surface plasmon resonance(SPR) [16,41–43]. This method was employed to measure the enzymatic degradation on sub-micron thick layer biopolymer. Although the experimental time frame was drastically reduced, QCM bases studies are limited to submicron film thickness and request a high uniformity of the polymer coating [44,45].

It is known[46] that the behaviour of material may change drastically between the thin film regime(<1μm) and the bulk regime[47–49]. Therefore there is the need to provide a scheme able to bridge between these two regimes.

The advances of micro and nanofabrication techniques allowed the production of the micromechanical sensor, which has been used for biosensing [50,51], environmental sensing [52,53] and material characterization[54–57]. Micromechanical sensors such as cantilever or bridges offer the possibility to study behaviour biopolymer in the thin film regime and in bulk. Del Ray et. al. [54], monitored the swelling and deswelling behaviour of submicron-thick layers of poly(hydroxyl ethyl methacrylate) PHEMA. In this study, they showed an inverse relation of the swelling properties as a function of the molecular weight. Bose et. al., used microcantilevers to characterise the enzymatic degradation behaviour of polymer films [56,58]. The results here presented showed that the degradation parameters obtained from micromechanical-based studies, matches with the conventional ones that achievable with conventional approach.

A powerful analytical tool to characterise the chemical structure of polymers is the infrared spectroscopy. An example of its importance it is the use of such technique to monitor the crosslinking, a fundamental chemical reaction in polymer chemistry, exploited to modify the physical and chemical properties of a polymer. In this case, the infrared spectroscopy is able to track the changes happening in the

polymer structure during the crosslinking, providing useful information on the evolution of different chemical bonds. Among the infrared spectroscopies techniques, Fourier Transform Infrared Spectroscopy (FTIR) and its implementations, have been the most widely used infrared spectroscopic analysis methods [17,59]. The most common implementation for infrared analysis is the attenuated total reflectance Fourier transforms infrared spectroscopy (ATR-FTIR) which exploits a single reflection crystal. Infrared analysis has been performed down to the single-molecule layer using advanced infrared spectroscopy analysis such as infrared reflection absorption spectroscopy (IRRAS), but it is limited to the study of a thin layer on metallic substrates[60,61]. IRRAS and ATR-FTIR suffer from extremely low signal to noise ratio (SNR) for film thickness in the nanometers range. The common and most intuitive route to overcome this issue is to perform several acquisitions[62] or decreasing the spectral resolution, leveraging on the averaging effect. This kind of solution clearly limits the throughput of the analysis and calls for new approaches for thin film infrared spectroscopy.

Photothermal spectroscopy methods are based on the recordings of signals which are generated as a side effect of light absorption. When a photon is absorbed in the sample, there is a consequent photoinduced modification in the thermal state of the sample that results in sample heating. A measurement of such sample heating, by probing the temperature as well as other thermodynamic parameters becomes a measurement of the wavelength-specific light absorption[63]. Photothermal signals are generated only upon light absorption since scattering and refraction losses do not contribute to the formation of the photothermal signal. Moreover, the photothermal response is dependent on the thermal properties of the material, these allow the photothermal signal to be used to derive such properties from an accurate study and modelling of the photothermal signal.

Micromechanical sensors, fabricated by conventional microfabrication technologies have been used as photothermal sensors. The variation of temperature, localised on a small sensor such as a cantilever or a string, induces thermal stress, which can be

probed as bending [35,64–71] or change in the resonance frequency of the structure[72–78]. The majority of the mechanical based photothermal spectroscopy studies are based on single clamped structures (cantilever) and as sensing variable is used the deflection of the cantilever tip. A more robust sensing scheme has been demonstrated by measuring the resonance frequency instead of the displacement of the tip [74].

At the same time, microcantilever-based studies [44,58] represent a breakthrough compared to the currently available methods for biopolymer degradation studies. An added benefit of analysing - biopolymer degradation using mechanical resonators consist in the possibility to integrating them within an automated sensing device. The readout of the cantilever resonance frequency could be directly embedded in the sensor [79,80], but this requires a more complex fabrication scheme. Instead, a more cost effective solution is leveraging on an optical readout, which has shown to allow high throughput measurements [81]. Furthermore, micromechanical sensor can be easily integrated with microfluidic devices [81,82] providing a higher degree of control of the degradation environment.

Given all these technical advantages, there is a great opportunity in developing mechanical sensors, dedicated not only for polymer degradation studies, but also for studying the chemical modifications occurring during the crosslinking process.

In this respect, several general considerations should be addressed regarding the robustness and simplicity of such micromechanical sensors. In particular, string based photothermal analysis has shown to be able to record the infrared spectra on femtogram amount of material [72], but the limited type of samples that can be analysed and a complex experimental setup hinder a large scale integration of the method. Hence there is the need to develop a more robust sensor which would better comply with agile sample preparation and straightforward analysis.

Regarding the polymer degradation studies, the principal point to be addressed is the implementation of an automated readout. Integrating an electrical based

readout, for instance, piezoelectric or magnetomotive, complicates the fabrication process of the sensor. In order to keep the sensor simple, an alternative solution to the readout is represented by optical readout. In particular DVD unit have shown to resolve linear displacement up to 1.3 $pmHz^{-1/2}$ [83,84]. Blu-Ray or DVD optical unit can be easily programmed and controlled[81,85], and they are available on the market at a very low cost.

The goal of this work has been to provide tools based on mechanical sensors for promoting a fast feedback during the material characterization. Pharmaceutical relevant materials are used to test their feasibility and capability.

1.2. Aim of the project

The Ph.D. project is carried out in the framework of the High Exponential Rise in Miniaturised cantilever-like Sensing (HERMES) project funded by the European Research Council (ERC). The primary goal of the project is the creation of cantilever based sensing technology and their integration in automated readout setups. Focus is on the development of tailored sensors capable of fitting to high-throughput sensing scenario.

The activities which have been carried out to address the focal point of the overall project aim were:

i) The development of a high-throughput system for studying the biopolymer behaviour in a natural environment. This task has been carried out in collaboration with Academia Sinica Taiwan (Professor En-Te Hwu).

ii) Improve the knowledge on the nanomechanical photothermal signal, understanding the limit of detection, and providing a mechanical photothermal sensor capable of providing high throughput material characterization.

1.3 Thesis Outline

Chapter 2: Describes the principle of mechanical based sensing applied on the resonators designed and developed in this thesis. The focus is on the sensing properties useful for designing a micromechanical sensor for biopolymer characterization

Chapter 3: Contains the discussion of the analytical model describing the photothermal signal and finite element simulations which have been done to

evaluate the accuracy of the models. The chapter ends with an experimental validation of the analytical method.

Chapter 4: Describes the methodologies developed in this thesis: the two version of the automated system used in this thesis are presented. Furthermore, the nanomechanical infrared spectroscopy (NAM-IR) setup and acquisition methods are described.

Chapter 5: Includes a summary of the published papers and the prepared manuscripts.

Chapter 6: Contains concluding remarks and the future perspective.

Appendix: Analytical models (developed by Professor Ole Hansen) and standard operating procedures for operating the system V2.

2. Theoretical Background for Mechanical Based Sensing

In this chapter, the mathematical background for mechanical based sensing is described. Starting from the equation of motion, the mass sensing properties are derived, showing how the environment surrounding the microresonator affects the mass sensing performance.

2.1. Damped And Forced Vibration[1]

Membranes and microbridges can store potential energy in the form of deformation energy. During oscillations, these structures are moving between equilibrium positions and the mechanical system converts the potential energy into kinetic energy and vice versa. In the absence of dissipative forces, this conversion of energy would infinitely continue. In a real system, energy dissipation occurs and at each cycle part of the potential energy is not converted into kinetic energy, causing the motion to stop. Micro and nanomechanical system have been engineered to provide structures aimed to minimise the loss of energy and finally enhancing the sensing performances [86–88].

[1] This section adapted from[1] except where elsewhere referred.

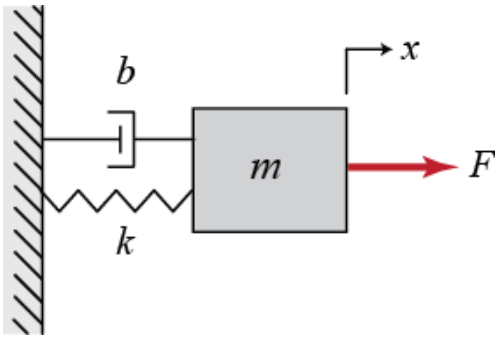

Figure 2.1 A single degree of freedom system. Adapted from [89]

2.2. Lumped Model

Vibration can be represented by a simple harmonic oscillator (Figure 2.1). When a mass connected to a spring is displaced from its equilibrium position, it will experience a force, proportional to the elastic constant of the spring and the magnitude of the displacement x. In the absence of dissipative forces, the mass *m* will oscillate between equilibrium positions undergoing to simple harmonic motion. Natural systems are damped and the amplitude of the oscillation decades over time. In a lumped system, the effect damping mechanisms are summarised by the dashpot *b.*

As a consequence of this damping, the vibration can only be maintained if the mass is subjected to a force. If the amplitude of the forced oscillations is small such that any non-linear behaviour can be neglected the equation of motion for a periodic sinusoidal force is

$$m\ddot{x}+b\dot{x}+kx \quad =f_0\sin(\omega_0 t) \tag{1}$$

where *m* is the concentrated mass, k the spring constant and *b* is the damping factor.

The solution of the homogeneous differential equation led to the definition of the eigenfrequency described by:

$$\omega_n = \frac{1}{2\pi}\sqrt{\frac{k}{m}} \ . \tag{2}$$

The eigenfrequency describes the frequency of the free oscillations, in the absence of any losses. The damping factor can be described as:

$$\xi = \frac{b}{2\sqrt{km}} \tag{3}$$

The homogeneous solution of the differential equation leads to the following equation of motion:

$$x(t) = e^{-\omega_p t}[c_1 \cos(\omega_p t) + c_2 \cos(\omega_p t)] \tag{4}$$

Equation 4 indicates the amplitude is decaying exponentially due to damping, whereas ω_p represents frequency of the damped oscillations, commonly known as resonance frequency, and it is equal to:

$$\omega_p = \omega_n \sqrt{1 - \xi^2} \tag{5}$$

The particular solution of the equation of motion in case of a sinusoidal force of amplitude f_0 leads to:

$$x(t) = Hcos(\omega t + \varphi) \tag{6}$$

$$H = \frac{{}^{f_0}\!/_{k}}{\sqrt{[(\omega^2 - {\omega_n}^2)]^2 + (2\xi\omega\omega_n)^2}} \tag{7}$$

$$\varphi = arctan\left(\frac{2\xi\omega\omega_n}{\omega^2 - {\omega_n}^2}\right) \tag{8}$$

Where the term ${}^{f_0}\!/_{k}$ is called static defelection. H is the amplitude of the oscillations φ is the phase lag between the exicitation force and the sustem response Equation 7 and Equation 8 are represented in Figure 2.2 and Figure 2.3

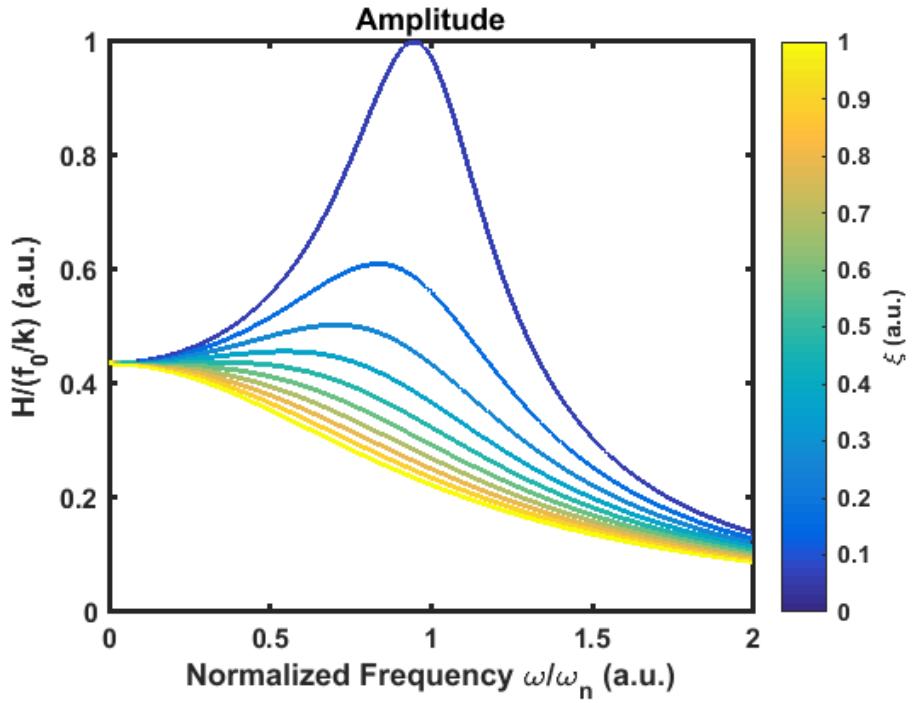

Figure 2.2 Frequency response of the amplitude of the motion in case of a sinusoidal force.

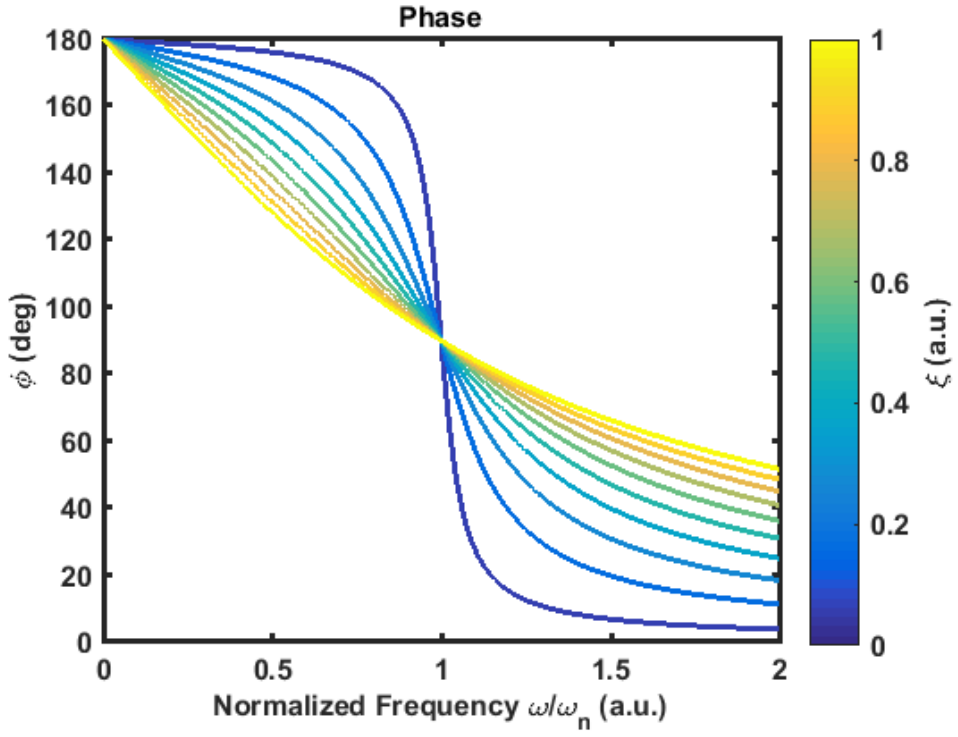

Figure 2.3 Phase diagram in the case of an exciting sinusoidal force.

The sharpness of the resonance peak is commonly defined by the quality factor Q. The quality factor determines the ability f the resonator of store energy in a single cycle. The ratio between the energy loss W and the energy stored ΔW defines the Q factor.

$$Q = 2\pi \frac{W}{\Delta \mathrm{W}} = \frac{\sqrt{1-\xi^2}}{2\xi} \tag{9}$$

From a sensor perspective, a high Q factor resonator intrinsically increases the limit of detection of the nanomechanical based sensor[86,90]. The quality factor, in fact, determines the smallest frequency shift measurable. In other terms, the value of the quality factor can be seen as the summation of the overall dissipation mechanisms of the system being those:

$$\frac{1}{Q} = \frac{1}{Q_{medium}} + \frac{1}{Q_{intrisic}} + \frac{1}{Q_{others}} + \frac{1}{Q_{clamping}} \tag{10}$$

Q_{medium} indicates the losses due to interaction of the mechanical structure with the surrounding fluid, $Q_{intrisic}$ are all the dissipation mechanism taking place in the resonator, Q_{others} indicates all the loss mechanism not considered in the other terms, and finally $Q_{clamping}$ considers energy losses atscribed to clamping.

In Section 2.9 the effect of the damping related to the viscous environment is treated, and a review of the models used to predict the behaviour of beams is provided.

2.3. Resonance Frequency For a Double Clamped Beam[2]

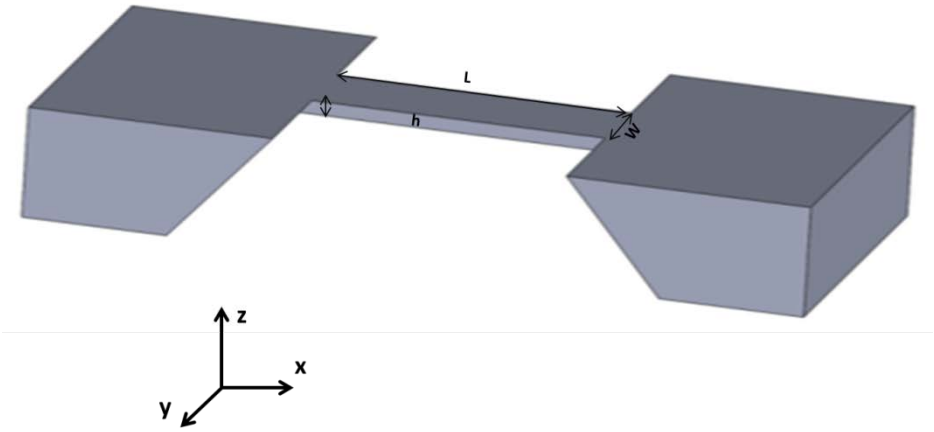

Figure 2.4 Schematic representation of double clamped beam or bridge

In this thesis, microbridges structures (Figure 2.4) are designed, developed, characterised and finally exploited for performing biopolymer degradation experiments. Considering high aspect ratio beams (L/h>10), it is possible to neglect both the rotational inertia and the shear deformation. In this case, the bending behaviour can be derived by the Euler-Bernoulli beam equation, under the assumption of small deflection for linear elastic beams.

$$EI\frac{\partial^4 U(x,t)}{\partial x^4} + \rho A\frac{\partial^2 U(x,t)}{\partial t^2} = 0 \tag{11}$$

$U(x,t)$ describes the displacement of the beam, E is the Young's modulus, I the moment of inertia and ρ is the density and A is the cross sectional area (W x h).

The free vibrations are described by the linear superposition of the eigenmodes multiplied by a time-dependent term.

$$u(x,t) = \sum_{n=1}^{\infty} U_n(x)cos(\omega, t) \tag{12}$$

Where $U_n(x)$is the eigenfunction and the general solution can be written as:

[2] This section is mainly adapted from[114]

$$U_n(x) = a_n \cos(\beta_n x) + b_n \cos(\beta_n x) + c_n \cosh(\beta_n x) + d_n \sinh(\beta_n x) \quad (13)$$

β_n is the wavenumber and it depends on the boundary conditions(i.e., the clamping). By inserting (12) in (11) the differential equation becomes

$$-\rho A \omega^2 u(x,t) + EI \beta_n^4 u(x,t) = 0 \quad (14)$$

$$\Lambda_n = \omega = \beta_n^2 \sqrt{\frac{EI}{\rho A}} \quad (15)$$

Considering a beam with a rectangular cross-section characterised by a moment of inertia $I = {Ah^2}/{12}$ and assuming a flexural rigidity D_E:

$$D_e = \frac{Eh^3}{12} \quad (16)$$

The eigenfrequencies can be expressed as:

$$\Lambda_n = \omega = \beta_n^2 = \sqrt{\frac{D_e}{\rho A}} \quad (17)$$

If the width to height ratio of the beam becomes larger than w/h>5, the flexural rigidity of the beam is described by the rigidity of a plate.

$$D_e = \frac{Eh^3}{12(1-v^2)} \quad (18)$$

The final mode shape Figure 2.5 is determined by the values of the wavenumber, resulting in the coefficient a_n , b_n , c_n , d_n which are specific for each boundary condition. Thus, they will depend on the type of structure.

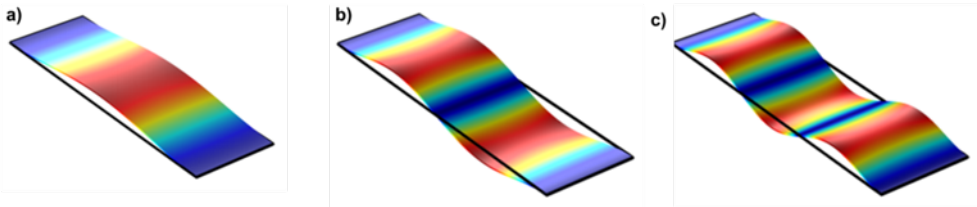

Figure 2.5 Mode shapes of the first three modes for a doubly clamped beam.

2.4. Resonance Frequency of Pre-Stressed Membrane

In this thesis, pre-stressed Silicon Nitride Membranes are fabricated to be used as sensing elements in a nanomechanical photothermal spectrophotometer (NAM-IR). In this section, the mathematical description of the eigenfrequency of a pre-stressed structure is presented.

If the membrane is fabricated with a linear elastic material, the equation of motion of a pre-stressed rectangular membrane can be derived adopting the two-dimensional wave equation:

$$\sigma \nabla^2 u - \rho \frac{d^2 u}{dt^2} = 0 \tag{19}$$

As in the case of a beam resonator the equation of motion can be thought of as a superposition of the mode shape with the time dependent term via separation of variables.

$$u(x, y, t) = U(x, y) e^{i\omega t} \tag{20}$$

The mode shape (Figure 2.6) has to fulfil the boundary conditions, and it can be expressed as:

$$U(x, t) = \sum_{n=0}^{\infty} \sum_{j=0}^{\infty} U_{0,nj} \, sin\left(\frac{n\pi x}{L_x}\right) \sin\left(\frac{j\pi y}{L_y}\right) \tag{21}$$

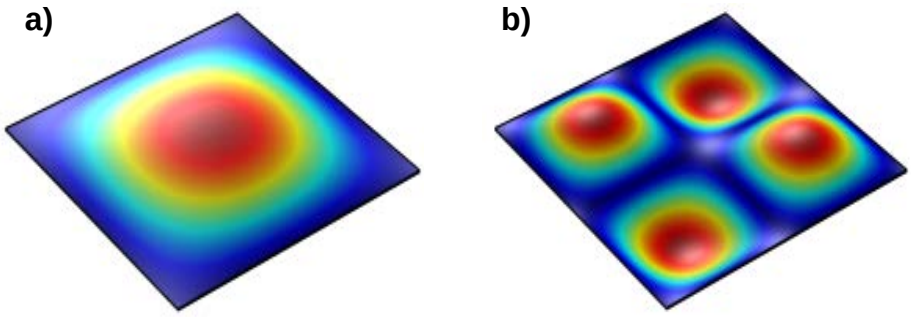

Figure 2.6 Mode shapes of the first two even modes for a membrane resonator.

where ω is the frequency, n and j denote the modal numbers and L_x and L_y the side length in x and y directions. The eigenfrequencies of a rectangular membrane are:

$$\omega_{n,j} = \sqrt{\frac{\sigma}{\rho}}\sqrt{\left(\frac{n\pi}{L_x}\right)^2 + \left(\frac{j\pi}{L_y}\right)^2} \tag{22}$$

2.5. Effective Parameters

The dynamic characteristics of the structure can be represented in terms of effective parameters. Each mode can be studied by a single lumped system which describes the nth eigenfrequency of the system:

$$\Lambda_n{}^2 = \frac{k_{eff}}{m_{eff}} \tag{23}$$

where the effective stiffness and effective mass are mode dependent quantities defined as:

$$m_{eff} = \rho A \int_0^L \phi(x)^2 dx \tag{24}$$

$$m_{eff} = EI_z \int_0^L \ddot{\phi}(x)^2 dx \tag{25}$$

2.6. Mass Sensing

Thanks to their very tiny mass, micromechanical sensors have been widely employed for mass sensing purposes[88,91–93]. Variation in the effective mass of the resonator can be sensed as a resonance frequency shift. In general, the responsivity of the mechanical sensor is defined as the slope of the sensing variables, i.e., the resonance frequency, as a function of the input parameter to be measured.

In this chapter, the mass responsivity is discussed. The responsivity to the local heating induced by light absorption is discussed in Chapter 3.

In general terms, the sensor responsivity R can be defined as

$$\mathrm{R} = \left.\frac{\partial \Lambda}{\partial \psi}\right|_{\psi=\psi_0} \tag{26}$$

Where Λ is the measured parameter(the resonance frequency), and ψ is the parameter that needs to be quantified, in this case, the mass. Assuming a linear

response of the resonance, and a given $\Delta\Lambda_{min}$ as the smallest resolvable frequency shift, the smallest detectable value for the parameter:

$$\Delta_{\psi_{min}} = R^{-1}\Delta\Lambda_{min} \quad (27)$$

The case of a mechanical resonator used as a mass sensor is explained. In this context, $\Delta\psi$ represents the mass variation and$\Delta\Lambda$ is the consequent variation of the resonance frequency. The mass detection thorough mechanical resonator applies in two specific cases; the point mass detection and the distributed mass detection.

2.7. Point Mass Responsivity[3]

Point mass detection is when the added mass is localised. In this case, the location of the added mass is defined by two coordinates $x_{\Delta m}$ and $y_{\Delta m}$. Considering the deposition of a particle of a certain mass Δm the effect of the mass deposition on the resonance frequency can be investigated by the Raylegh-Ritz method[53], which states that, at resonance, the time average kinetic energy equals the time average strain energy. Thereby,

$$E_{kin} = \frac{1}{2} m_{eff} {\beta_n}^2 {\omega_{\Delta m}}^2, \quad (28)$$

where, m_{eff} is the effective mass defined in Equation 24.

Substituting the Equation 24 in Equation 27, the latter becomes:

$$E_{kin,\Delta m} = \frac{1}{2}\Delta m[\beta_n \, U(x_{\Delta m}, y_{\Delta m})]^2 {\omega_{\Delta m}}^2 \quad (29)$$

By assumption, the mode shape and the k_{eff} are not changed.

The resonance frequency due to the addition of the mass:

$$\omega_{\Delta m} = \omega_0 - \Delta\omega \quad (30)$$

Hence, the point mass responsivity (PMR):

[3] This section is mainly adapted from [116]

$$R = \frac{\Delta f}{\Delta m}\Big|_{PMR} = \frac{f_0}{2meff}\, U(x_{\Delta m}, y_{\Delta m})^2 \tag{31}$$

2.7.1. Distributed Mass Responsivity[4]

Contrary to what has been discussed so far, relatively to the point mass detection, the deposited mass displacement is not constant. Therefore, the kinetic energy of the resonator due to the deposition characterised by a density distribution $\rho_{\Delta m}(x, y)$ and thickness distribution $t_{\Delta m}(x, y)$, becomes:

$$\begin{aligned} & E_{kin} + E_{kin,\Delta m} \\ & = \frac{1}{2} m_{eff} {\beta_n}^2 {\omega_{\Delta m}}^2 \\ & + \frac{1}{2} {\beta_n}^2 {\omega_{\Delta m}}^2 \int_A \rho_{\Delta m}(x, y)\ t_{\Delta m}(x, y)\, U(x_{\Delta m}, y_{\Delta m})^2\, dx\, dy \end{aligned} \tag{32}$$

$$\frac{m_{eff}}{\int_A \rho_{\Delta m}(x, y)\ t_{\Delta m}(x, y)\, U(x_{\Delta m}, y_{\Delta m})^2\, dx\, dy} = \frac{{\omega_{\Delta m}}^2}{{\omega_0}^2 - {\omega_{\Delta m}}^2} \tag{33}$$

Equation 32 is found by applying the Rayleigh-Ritz theorem and considering the strain energy $E_{kin} = \frac{1}{2} m_{eff} {\beta_n}^2 {\omega_0}^2$.

If we consider $\omega_{\Delta m} = \omega_0 - \Delta\omega_{\Delta m}$. Let $\omega_0 \gg \Delta\omega_{\Delta m}$ the total frequency shift, Δf_d, is given by (considering the density and the thickness of the added layer constant over the resonator surface)

$$\Delta f_d = (t_a \rho_a) \frac{f_0}{2 m_{eff}} \int_A U_n(x, y)^2\, dx\, by. \tag{34}$$

The distributed mass responsivity (DMR) can be finally defined as:

$$R = \frac{\Delta f}{\Delta m}\Big|_{DMR} = \frac{f_0}{2meff} A_{eff} \tag{35}$$

[4] This paragraph is adapted from [116]

Where the value of the effective area:

$$A_{eff} = \int_A U(x,y)^2 \, dx \, dy \tag{36}$$

In both the cases (point mass detection and distributed mass detection) the minimum detectable mass depends on to the uncertainty affecting the measurement. This the noise measured by means of Allan Deviation or the uncertainty of independent measurements called here δ_f. In both cases, the limit of detection described in equation 26 can be rewritten as:

$$\delta_{M,point\ mass} = \frac{\delta_f}{\frac{f_0}{2meff} U(x_{\Delta m}, y_{\Delta m})^2} \tag{37}$$

$$\delta_{M,Distributed} = \frac{\delta_f}{\frac{f_0}{2meff} A_{eff}} \tag{38}$$

2.8. Resonance Frequency of a Layered Structure

For a multilayer structure, the resonance frequency can be written as [44]

$$f_n \approx \frac{1}{2\pi} \frac{\beta_n^2}{L^2} \sqrt{\frac{\sum_{i=1}^{N} I_i E_i}{w \sum_{i=1}^{N} \rho_i t_i}} \tag{39}$$

Considering non-coated structure Equation 36 reduces to Equation 17 matching the resonance frequency of a beam, according to the Euler-Bernoulli theory.

Considering a beam coated with a uniform layer of polymer, the resonance frequency changes compared to the non-coated beam. The Young's modulus of a polymer is typically orders of magnitude lower than the Young's modulus of the silicon. The increase in the mass of the resonating structure can be detected as a change in the resonance frequency shift. This condition holds only below a certain

value of polymer thickness, where the bending stiffness of the polymer layer is neglectable.

A finite element model can be used to estimate this effect. Considering the structures utilised in paper 1, which are 1000μm long 300 μm wide and 5μm thick and considering the polymer properties showed in [4], this limit is seen to be found equal to the beam thickness of polymer coating where there is an inversion in the trend of the relative frequency shift.

The effect of the addition of a polymer coating[5] is shown in Figure 2.7 where the relative frequency is represented as a function of the added polymer layer. In the graph, three different regimes can be identified. The first regimes for $\frac{t_{POL}}{t_{BRIDGE}} < 1$, here the main effect on the resonance frequency is due to the added mass, $1 < \frac{t_{POL}}{t_{BRIDGE}} < 2.25$, where the effect of the increased thickness due to the polymer layer counteract the effect of the added mass, and finally $\frac{t_{POL}}{t_{BRIDGE}} > 2.25$ where the stiffness due to the polymer layer is predominant. The width of the structure instead is seen not to play a significant role.

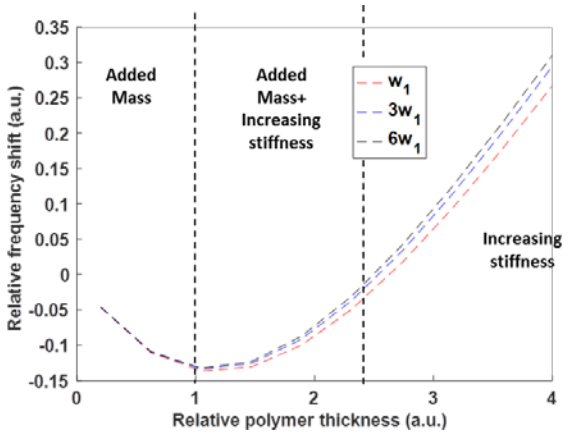

Figure 2.7 Effect of the addition of a polymer layer on a double clamped beam. For thickness smaller than the beam thickness the main effect is the decrease in the resonance frequency, whereas once this threshold is overcome the enhancement of stiffness is also sensed and becoming the leading cause of frequency when the thickness of the polymer layer is higher 2.25times the thickness of the beam.

[5] For these simulations these elastomechanical properties pf the polymer are used: E=2GPa, p=1.3g cm^{-3}.

2.9. Frequency Response in Liquid Environment

In this thesis, the resonating behaviour of microbridges is tested. The Blu-Ray readout system that is designed and employed to characterise the degradation of biopolymer is described in Paper 1. The system allowed a characterization of the frequency response in air and water environment. The theoretical background of the frequency response of microstructure in a liquid environment is illustrated accompanied with by experimental results.

2.9.1. The Hydrodynamic Function

The frequency response of a mechanical structure is highly dependent on the fluid in which it is vibrating. The benchmark theoretical studies describing the behaviour in liquid environment were done by Sader and colleagues [94–96].

The theoretical treatment exposed in the previous paragraphs holds for vacuum and air environment, where the effect of the load due to the liquid and so the viscous damping can be neglected. In the model proposed by Chu[97], the liquid is treated as inviscid, and it gives a reasonable approximation of the value of the resonance frequency of a beam when immersed in liquid environment for high working frequency. On the other hand, the validity of the inviscid model may not be accurate depending on the structure properties. According to this model, the resonance frequency drops due to the hydrodynamic load caused by the surrounding water

$$\frac{\omega_{\text{fluid}}}{\omega_{\text{vac}}} = \left(1 + \frac{\pi \rho_l w}{4 \rho_c t}\right)^{-\frac{1}{2}} \tag{40}$$

where ρ_l and ρ_c are the density of the liquid and the beam respectively, whereas w and t are the width and the thickness. Equation (37) is often considered as benchmark to evaluate the decrease in the resonance frequency due to added apparent mass of the layer of fluid which load the structures. Sader's works[95,98–100] extends the validity of this equation considering the effect of the viscosity.

The formulations of the frequency response in viscous environment are described in terms of Reynolds number $\overline{\mathrm{Re}}$ and T and the hydrodynamic function Γ:

$$\overline{\mathrm{Re}}=\frac{\rho_l 2\pi f_n w}{4\eta} \tag{41}$$

$$T=\frac{\rho_l w}{\rho_c t} \tag{42}$$

ή is the cinematic viscosity of the fluid and f_n the resonance frequency. In the light of this, the extension of the Chu model becomes:

$$\frac{\omega_{\mathrm{fluid}}}{\omega_{\mathrm{vac}}}=\left(1+\frac{\pi\rho w^2}{4\mu}\Gamma_r(\omega_{\mathrm{fluid}})\right)^{-1/2} \tag{43}$$

where $\mu=\rho A$ is the linear density of the beam and Γ_r is the real part of the hydrodynamic function Γ [95]. For the sake of clarity, a representation of the hydrodynamic function is reported Figure 2.8. The real part of this function takes into account the inertial forces which are leading the dynamics for very high Reynolds number where the viscous effects vanish. In this regime, the inviscid model is a good approximation of the dynamic behaviour of the beam.

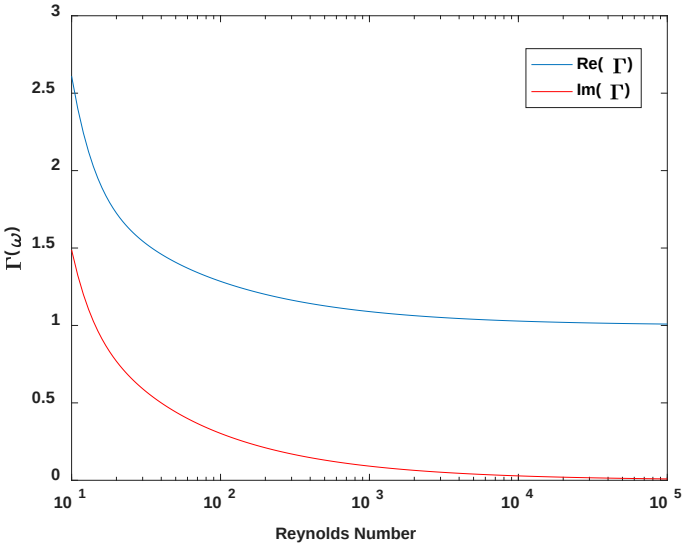

Figure 2.1 Hydrodynamic function[95] **for a rectangular beam immersed in water.**

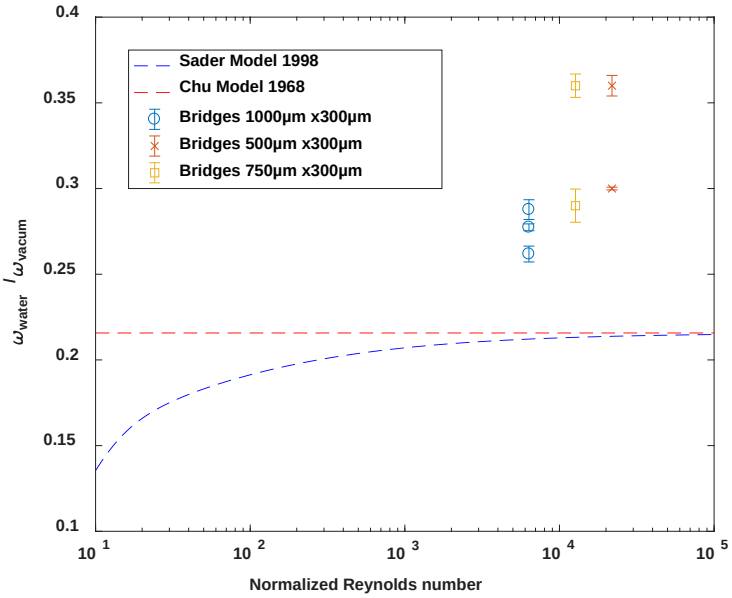

Figure 2.2 Resonance frequency drop due to the hydrodynamic load. Comparison of the Sader and Chu(inviscid model) with the experimental results

The model of Sader and Chu overestimates the resonance frequency drop due to the hydrodynamic load of the fluid layer. The gap between the model and the experimental results reported a deviation in which is in the range of previously reported work[100]. One possible reason is that in the calculation of the experimental frequency drop, as reference value, the measured resonance frequencies in air are considered, which are 2-3% lower compared to the theoretical values(Equation 5) considered in the analytical models.

2.9.2. Q factor for vibrating structures in a liquid environment

To minimise the energy losses and to increase the sensing performance, the resonator has to work within a regime where the viscous forces are negligible. The latter are linked to energy losses, and it is evident how the Q factor can be maximised by achieving high values of Reynolds number (see Figure 2.10). The equation that describes the Q factor in a liquid environment for the n^{th} mode:

$$Q_n = \frac{\frac{4\mu}{\pi\rho_l w^2} + \Gamma_r(\omega_{fluid,n})}{\Gamma_i(\omega_{fluid,n})} \tag{44}$$

where $\omega_{fluid,n}$ is the resonant frequency of the n^{th} mode in liquid.

The Γ function (Figure 2.8) indicates the importance of the viscous forces relatively to the inertial ones. For a given value of T a lower Reynolds number makes the resonance peak broaden at lower frequencies. The same trend is observed for a given value of $\overline{Re}$ and an increase of T[95]. It is clear that the viscosity of the media increases the energy losses, leading to a reduction of the Q factor which is translated into a worse sensing performance.

The combination of wider cross section and a doubly clamped beam leads to higher $\overline{Re}$ limiting the energy losses and therefore higher values of Q factor are reached. In our experiment the value of $\overline{Re}$ and T are around 7000 and 26 respectively, leading to an experimental Q of about 20 for the first three modes, which matches the prediction of the model[95,96].

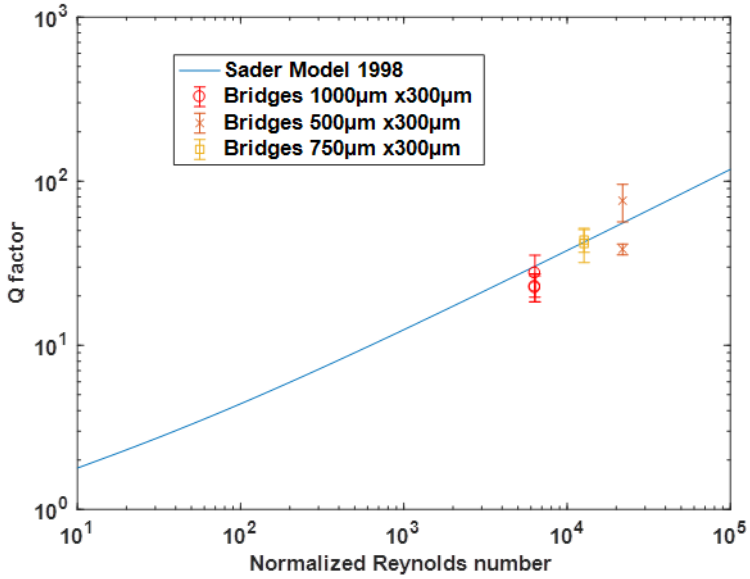

Figure 2.3 Q factor for microbridges in water environment.

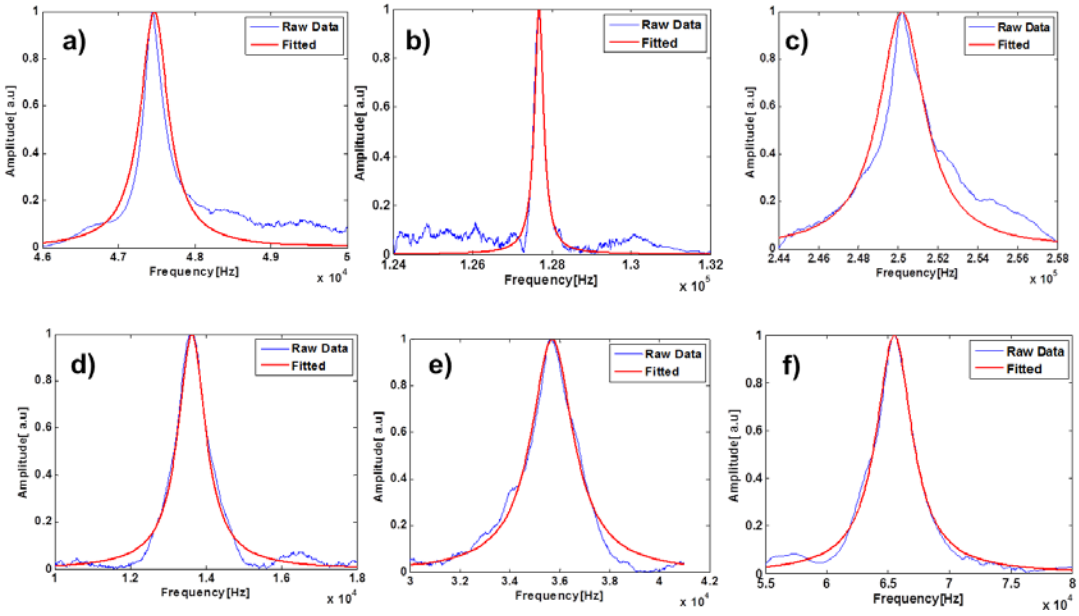

Figure 2.4 Resonance frequency of 1000µm 300µm wide and 5µm thick bridges in air a-c, and in water, d- f. For the sake of clarity, only one spectrum are reported. The standard deviation ranges from 3 to 5% on a sample size of n=20

2.9.3. Increase of the Effective Mass

The mass sensing characteristics are explained in Section 2.6 and it has been shown that the lower the effective mass the higher will be the mass responsivity.

From a mass sensing perspective, working in a viscous environment is translated to an increase of the effective mass of the resonator, yielding to a decrease of the mass responsivity of the sensor. Under the assumption that the effective stiffness of the structure is not influenced by the liquid environment, the ratio between the resonance frequency in air and the resonance frequency in water is

$$\left(\frac{\omega_{\mathrm{Air}}}{\omega_{\mathrm{water}}}\right)^2 = \frac{m_{\mathrm{eff,water}}}{m_{\mathrm{eff,air}}} \tag{45}$$

Considering the 1000µm long 300 µm wide and 5 µm thick bridges, the effective mass is in air is 1.75µg. The decrease of the resonance frequency can be seen as an increase in the effective mass of the resonator. In water environment the effective

mass is seen to increase by a factor of 13, yielding an effective mass of around 20 μg. The experimental uncertainty on the resonance frequency measurements does not allow a proper monitoring of the degradation phenomena. Higher modes can be used to perform mass sensing in liquid environment[98], on the other hand integrating a readout able to monitor this condition can be challenging.

In this thesis, the microbridges are used for characterising the biopolymer degradation of polymer layer with thickness that ranges between 1 to 5 microns.

The values of the mass responsivities for the first three flexural modes are shown in Table 1. The minimum detectable distributed mass for each mode in air environment allows us to correctly follow the degradation phenomena. Instead, in liquid environment, the mass responsivity is on the same order of magnitude as the deposited mass, hence tracking the degradation phenomena would be unfeasible. Therefore, to characterise biopolymer degradation, a wet & dry approach has been used as discussed in Paper 1.

Table 1 Minimum detectable mass sensitivity for 1000μm long 300 μm wide and 5 μm thick microbridges. Analogous trivial calculation leads to similar results for different sized microbridges.

Mode	Mass Responsivity $[Hz\ \mu g^{-1}\ mm^2]$		Uncertainty $\Delta_f[Hz]$		Minimum Detectable Distributed Mass $[\mu g\ mm^{-2}]$	
	Air	Water	Air	Water	Air	Water
I flexural	2304	114.7	103.68	594	0.09	10.34
II flexural	5344	308.82	187.04	1125	0.07	7.92
III flexural	11304	1941	395.64	3250	0.07	3.34

2.10. Conclusion

In this chapter, the theoretical background of a micromechanical resonator is provided. The variables that play a major role in determining the performances for mass sensing application are discussed. Micromechanical bridges have shown a sufficient minimum detectable mass in air environment to perform mass sensing. Despite a good Q factor even in aqueous environment, the increase of the effective mass does not allow the use of the structure as mass sensor. The deposited mass is in the same order of magnitude as the minimum detectable mass. This, combined with the uncertainty on the measurement does not allow to properly monitor the degradation mechanism. Instead, working in air environment, yields an increase of the mass responsivity two orders of magnitude less than the deposited mass, allowing a proper tracking of the degradation process. The employment of the microbridge structure as a biopolymer degradation sensor is discussed in Paper 1.

3. Finite Element Simulations for Nanomechanical Infrared spectroscopy

This chapter provides the in-silico validation of the analytical model used to describe the steady state and the transient response of the mechanical photothermal signal.

3.1. Steady state model for photothermal induced frequency shift

The phenomena involved in generation of the photothermal signal have been modelled to provide a better understanding of the experimental variables' roles in the production of the signal. The analytical model describing the resonance frequency shift for a membrane-like structure was developed by Professor Ole Hansen, DTU Nanotech[6]. Considering the high aspect ratio of the membrane structures considered in this thesis, the problem can be solved as a 2D thin membrane. To obtain an analytical representation of the photothermal response, there are three problems to be solved. First, the heat transport equation throughout the membrane when heated in response to the local absorbed power P; then the thermal stress field induced by the heating load; iii) the eigenproblem solved for the thermal stress field caused by the power absorption. Addressing this problem for a square geometry is ill-posed, and deriving a closed analytical solution is not possible. Instead, this is possible only for a circular geometry. In this section, the accuracy of the analytical model is compared with the finite element model.

The analytical solution for the photothermal a circular membrane is:

$$\frac{\Delta f}{f} \approx -\frac{\alpha E P}{8\pi k h \sigma_0}\left(\frac{2-v}{1-v} - 0.642\right) \tag{46}$$

[6] The analytical solution of the model is reported in Appendix 1

Where α is the thermal expansion coefficient of the material, E is the elastic modulus, P is the absorbed power, k is the thermal conductivity, h the thickness of the structures, σ_0 is the native tensile stress and v is the Poisson ratio. It is noteworthy remind that the model was solved for a point-like power source.

In the experimental phase, the heat source is represented by the IR laser source, having a defined diameter of 100μm. Intuitively, the magnitude of the frequency shift is directly linked with the average temperature established upon heat absorption. Thus, the location of the laser spot and its size clearly plays a fundamental role in defining the magnitude of the frequency shift. The analytical model represents the optimal case of a perfect collimated light. This approximation may lead to an overestimation of the absorbed power calculated for a given frequency shift. Therefore the role of the spot size is discussed.

3.2. Model Definition

To simulate these phenomena the Heat Transfer in thin shell and the Membrane Comsol tool packages are used. The FEM model replicates the membrane geometry employed in the experimental case; 1000μm wide, 100nm thick and fabricated in low-stress silicon nitride. The used parameters are presented in Table 2.

Table 2 Summary of the properties used in the FEM modelling, with Comsol Multiphysics v 5.2 ®. The results were obtained setting a 2D geometry and the thermal stress physics interface.

Properties	Value
Thermal Conductivity	20 W m^{-1} K^{-1}
Density	3100 kg m^{-3}
Young Modulus	250 GPa
Poisson Ratio	0.23
Initial stress	250 MPa
Heat Capacity at Constant Pressure	700 J kg^{-1} K^{-1}
Thickness	100nm
Width	1000μm

3.2.1. Boundary Condition

A consideration regarding the boundary condition (BC) assumed in the derivation of the analytical model must be done. Both analytical formulations (the steady state and the transient problem) bear the temperature of the membrane rim to be fixed at a certain value T_0(considered equal to 293.15K). Such approximation corresponds to the assumption that the body chip acts as a perfect heat sink. In the experimental condition, the boundary of the membrane will exchange heat with the rest of the body chip and with the surrounding gas. The model that better fits the experimental condition corresponds to a membrane of silicon nitride, surrounded by a silicon body chip isolated from the surroundings. The temperature field will vary according to the boundary condition, and the effects of the approximation are represented in Figure 3.1

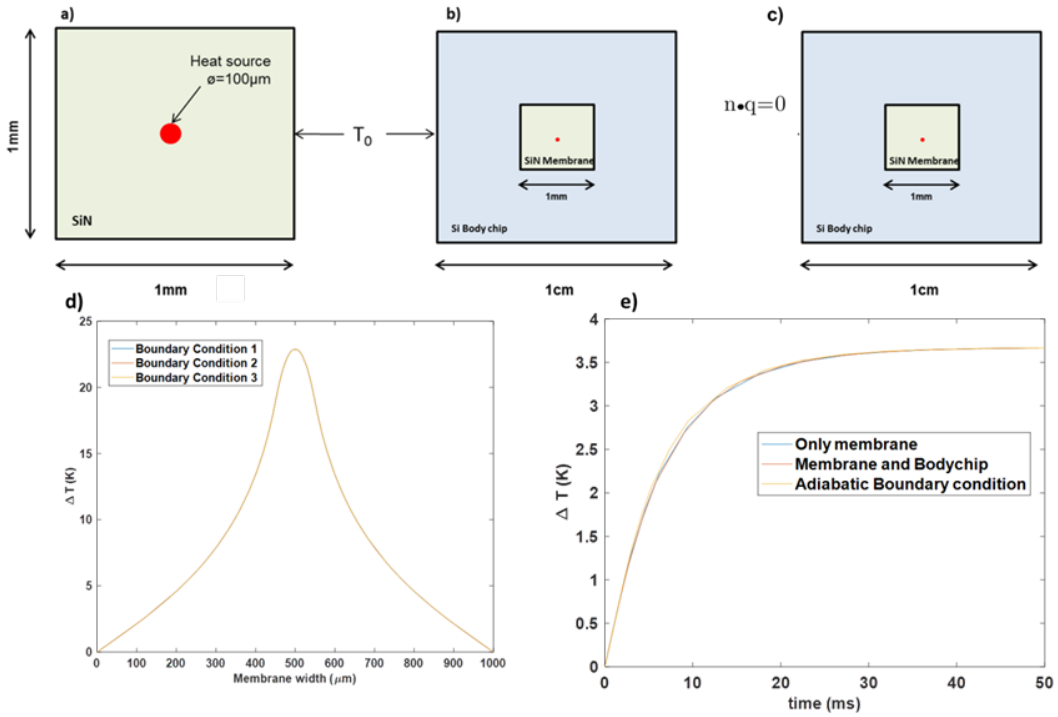

Figure 3.1Schematic representation of the geometry and BC used in this work: a) only the membrane T_0 =293.15 K; b) the membrane chip is allowed to exchange heat with the body chip, acting as heat sink. The rim temperature is set at T_0 =293.15 K c) adiabatic boundary condition the thermal energy provided by the heat source is dissipated only within the domain; d) difference in the temperature evaluated in the centre of the membrane considering the BC a and b and c, the three temperature profile perfectly overlap; e) average temperature profile for the three boundary condition

The three boundary conditions simulated consist of: i) a fixed temperature on the rim of 293.15K Figure 3.1a; ii) a fixed temperature of 293.15K on the bodychip, rim Figure 3.1b iii) and adiabatic condition on the rim of the bodychip Figure 3.1c. The average steady temperature profile is showed in Figure 3.1d calculated for each of the BCs showed in Figure 3.1a-c. The three profiles are completely overlapping, and the differences between models are less than 1%. The average temperature of the membrane is also evaluated in the time domain where, also in this case, no remarkable differences are noticed. All the simulations consider an incident power of 100μW over a circular area of 100μm in diameter. The Silicon bodychip has a higher thermal conductivity than the membrane chip. Therefore, the heat will be dissipated towards the bodychip and rapidly the temperature of the membrane's rim will reach the boundary condition temperature.

These simulations reveal that average temperature within the membrane domain does not depend on the BC used. Since the temperature field within the membrane upon heat absorption determines the magnitude of the frequency shift, we can say that for the sake of simplicity all the simulations in this thesis are performed using the BC illustrated in Figure 3.1a, as they do not give rise to any further error.

3.3. Linearity of the photothermal induced frequency shift

The first simulation aims to test the linearity of the photothermal induced frequency shift upon heat absorption. The analytical model is solved for the mode (1,1) and the match with the finite element method is shown in Figure 3.2. The relative frequency shift yielded by the models matches with the analytical one, the difference is in the order of 1-2 ppm for 100 μW of absorbed power. This value, in the experimental case scenario, is within the limit of detection, meaning that the error introduced by the approximation will not induce to a significant quantitative errors in terms of absorbed power. The limit of detection, concerning the structure used in this thesis ranges from 3 to 20nW depending on the thickness of the

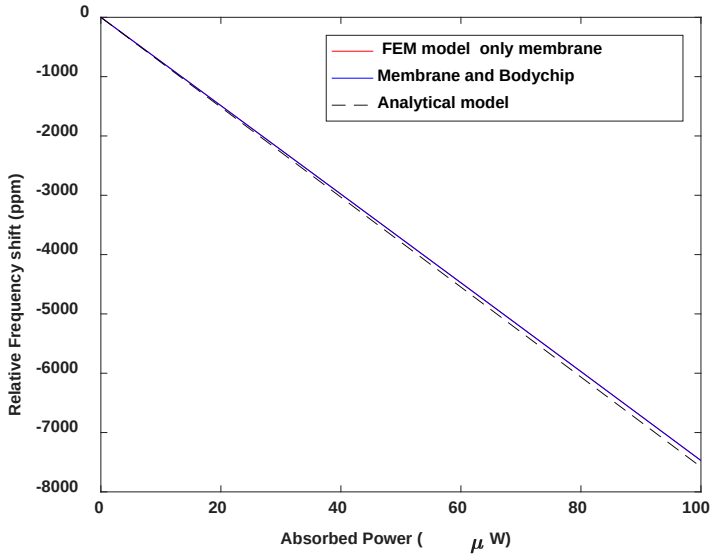

Figure 3.2 Simulated relative frequency shift vs Analytical model. The relative frequency yielded by the model also simulating the body chip yield to a relative frequency shift which is almost 2 times smaller. This is due to the lower temperature established in the membrane when it is not treated as isolated system.

coating layer which yields a different noise background. These arguments are described in paper 2 and paper 3.

Compared to the analytical model, the finite element model slightly underestimates the relative frequency shift. Such gap might be because the analytical solution is drawn from a Delta function heat source, instead, in the FEM model, the heat source is meant to simulate the laser source of 100 μm diameter.

The effect of the spot size dimension (Irradiance) on the relative frequency shift was simulated. An incident power of 100μW is used and the diameter of the laser spot size is varied from 1μm up to 1mm. The magnitude of the relative frequency shift decreases for higher laser spot size. The relative frequency shift is normalised relatively to the value of the analytical frequency shift (43). The normalised frequency shift then drops down to the 50% for a laser spot size that matches with the dimension of the membrane. Instead, it remains above the 90% for a heat source size smaller than half of the membrane width. The reason for this decrease is because the photothermal induced frequency shift is also sensitive to the location where the heat is generated, being maximum in the centre and minimum in the proximity of the border as shown in Figure 3.3a.

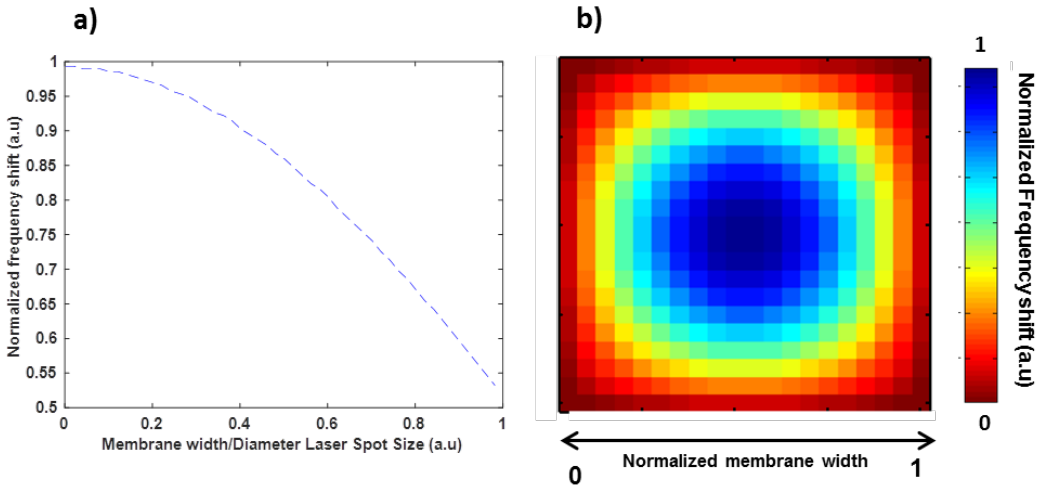

Figure 3.3 Steady-state simulations.a) Effect of the heat source dimension; b) and of heat source location.

In the experimental setup, the laser spot has to be aligned with the membrane resonator. The site of the laser plays a major role in determining the magnitude of the relative frequency shift. In the light of this, the spatial sensitivity is modelled. A heat source is swept across the membrane domain. The relative frequency shift is maximum when the membrane is heated in the centre and decades towards the boundary of the membrane, being zero for a heat source placed at the border. Intuitively, the closer the heat source is located in the proximity of the heatsink the lower the average temperature will be within the membrane domain and ultimately the relative frequency shift.

3.4. Time Dependent Simulations

The membrane resonator upon heat absorption reaches a stable value of temperature and therefore a stable stress field which finally yields a particular frequency shift. The transient problem is exclusively related to the thermal transport phenomena, and therefore only the thermal property (and the geometry of the structure) regulates such dynamics. Professor Ole Hansen developed the analytical model and the calculations are reported in Appendix.

The knowledge of the thermal transient is fundamental for two main reasons:

i. The time the sensor needs to reach a stable temperature and therefore a stable resonance frequency determines the rapidity of the system to follow transition between subsequent heat absorption. Therefore this parameter determines how fast a spectral sweep can be run and intrinsically determines the acquisition parameters of the lock-in scheme used to track the resonance frequency shift, hence the noise. These arguments are discussed in the paper II.

ii. The transient dynamics depends on the thermal properties of the domain; it may allow the identification of the thermal properties of the analytes and the chip material.

The analytical model that characterise the transient behaviour for a squared layered structure is

$$\tau_0 = \left(\frac{2\pi^2}{L^2} \frac{\sum_{i=1}^{N} h_i k_i}{\sum_{I=1}^{n} h_i c_i} + \frac{H}{\sum_{I=1}^{n} h_i c_i} \right)^{-1} \tag{47}$$

$$H_{1mbar} = 92.21 \, {}^{W}\!/_{m^2 K} \tag{48}$$

$$H_{10^{-5}mbar} = 9.221 \; 10^{-4} \, {}^{W}\!/_{m^2 K} \tag{49}$$

Where the $h_i k_i\ c_i$ are respectively the thickness and thermal conductivity and the heat capacity for the ith layer L is the width of the membrane. The parameter H instead takes into account the dissipation of the heat due to the convective heat transport phenomena taking place at different pressure. For a silicon nitride membrane of width 1000 μm in high vacuum condition the time constant is 5.5 ms.

3.4.1. Accuracy of the Analytical Model

The analytical time constant is drawn from the resolution of the heat transport equation in 2 dimensions. The time constant results from the solution of the homogeneous part of the partial differential equation problem (PDE). The resolution of this mathematical problem can be solved by means of eigenfunction.In the expression we consider only the first mode(henceforth called fundamental) being the one that decays slower.

3.4.2. Initial Temperature Distribution

In order to assess the accuracy of the analytical model, the transient led by a different initial condition is tested.

The boundary condition illustrated in Figure 3.1a are used. The decay showed Figure 3.4b is evaluated by considering the average temperature of the membrane when the temperature is let to relax to the temperature boundary considering an initial temperature distribution of $T_0(x,y) = T_{boundary} + \Delta_T \cos(\frac{\pi\, x}{L})\cos(\frac{\pi\, y}{L})$, being $\Delta_T = 10K$.

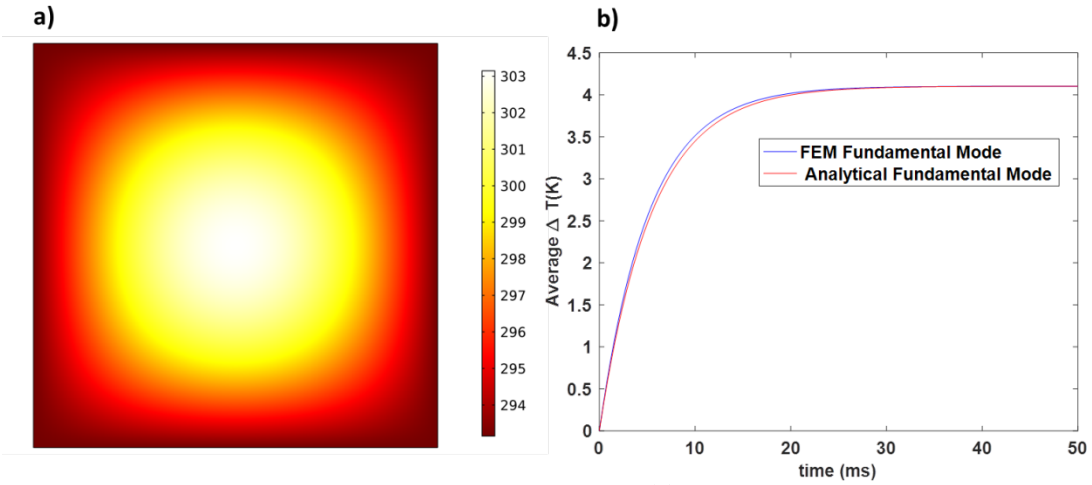

Figure 3.4. a)Cosine-like initial temperature distribution colorbar Temperature in K ; b) Relative temperature shift evaluated by the FEM model and the analytical one.

The finite element model prediction of the transient, considering the initial temperature distribution, matches the transient behaviour predicted by the analytical model. In this particular case of study, the initial temperature distribution is one of the possible solutions that satisfy the PDE, hence the match with the analytical transient is trivial. The full thermal response is described by a superposition of eigenfunctions [101]. Hence the complete description of the thermal transient will depend on particular initial condition as well as the kind of heat source used. In this perspective, we investigate how the thermal transient varies for different types of heat sources aiming to mimic the experimental case scenario.

3.5. Transient for an external power source

In the experimental case, the membrane is heated with an external power source with a spatial distribution P(x,y). Here we simulate i) constant heat source confined within a circular area of radius r ii) Gaussian power distribution. The aim is to investigate how the power distribution influences the thermal time constant.

3.5.1. Constant Heat Source Confined In a Circular Area of Radius r

The case studied in Section 3.4.2, represents the ideal case of temperature distribution led by a Delta function as a heat source, which is unlikely to be available in the experimental phase. Here we studied the influence of the heat spot size on the transient when the power is kept constant. The larger the effective heated area, the faster the membrane will reach the steady average temperature. Similarly, on what we have discussed relatively to the effect of the heat source size on the magnitude of the relative frequency shift, the reached temperature is inversely related to the size of the heat source. Concerning the transient, if the heat source is placed close to the boundary, hence closer to the heat sink, the transient will be shorter, and the reached temperature smaller.

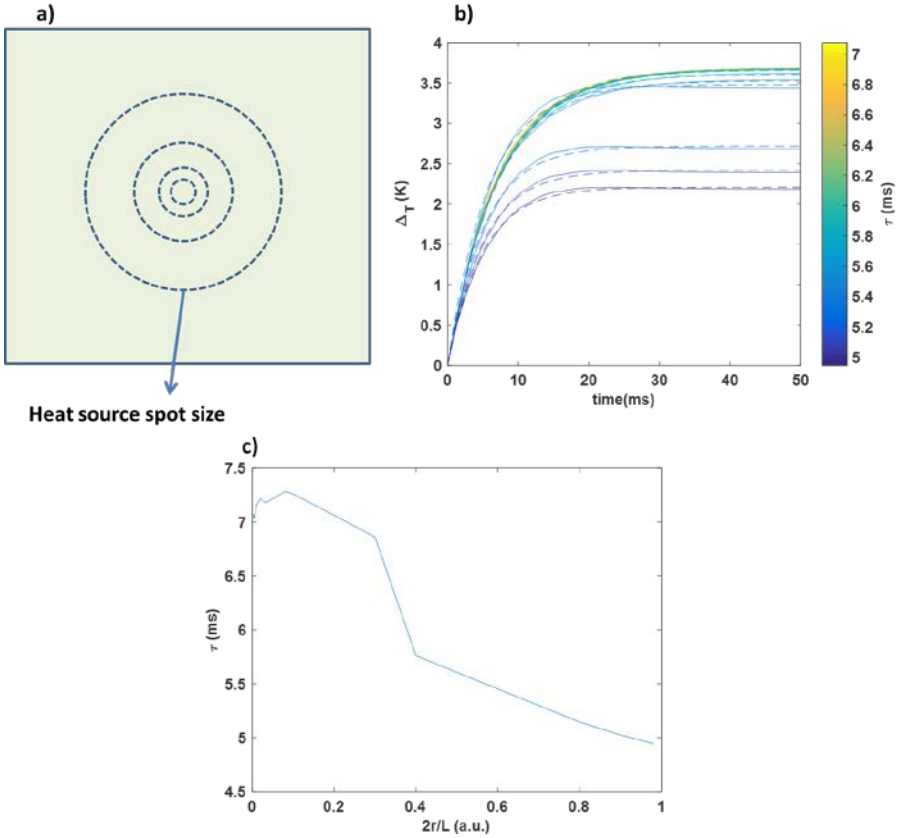

Figure 3.5 Effect of the spot size and time constant. a)The heat source is spread over a different area; b) average temperature transient, dashed represents the single exponential fit; c) value of the time constant as function of the relative radius of the heat source normalised by the dimension of the membrane

3.5.2. Alternative approaches for evaluating τ

To investigate the effect of the heat source size, the value of the time constant can be derived by the temperature distribution led on circular geometry by a Gaussian Power distribution. Equation 49 relates the time constant obtained from a delta power distribution, to the time constant obtained for an arbitrary Gaussian power distribution, Equation 6.

$$\tau = \tau_0 \frac{\left(1 + \frac{2\sigma^2}{a^2} exp\left(-\frac{a^2}{2\sigma^2}\right) - \frac{2\sigma^2}{a^2}\right)}{1 - exp\left(-\frac{a^2}{2\sigma^2}\right)} \tag{50}$$

$$P(x,y) = \frac{P_0}{\sqrt{2\pi}\sigma^2} \exp\left(\frac{1}{2}\left(\frac{x - x_0}{\sigma}\right)^2 + \left(\frac{y - y_0}{\sigma}\right)^2\right) \tag{51}$$

Equation 47 asserts that the wider the distribution, the faster the transient will be, being agreeing with the results of the simulation shown in Figure 3.6

Considering a circular geometry, the transient problem can also be solved by using the Bessel modes as well as Laplace transform for a Delta function power distribution and constant power distribution. The different expressions of the time constant τ are summarised in Table 3.

Table 3 Summary of the different analytical model used for evaluating the transient

Geometry	Method	τ
Circular	Fundamental Mode(Bessel)	$\frac{a^2}{2.4048^2 D}$
Circular	Average Temperature[7]	$\frac{a^2}{4D}$
Circular	Laplace, Delta Function	$\frac{3}{16}\frac{a^2}{D}$
Square	Fundamental Mode, (Equation 2)	$\frac{W^2}{2\pi^2 D}$

[7] This model has a dependency of the spot size, as described in equation 5.

3.5.3. Gaussian Power Distribution

The transient for a Gaussian power distribution (Equation 47) is studied for a circular and a square geometry. Here σ is the width of the distribution x_0 and y_0 represent the localization of the peak.

Regardless of the geometry, the wider the distribution, the faster will be the response, according to what is stated in Equation 47.

For a circular geometry, the Bessel mode does not consider the influence of the power distribution in a calculation of the time constant. The Laplace solution calculated for Delta and uniform power distribution matches with the value yielded for simulations evaluated for a power distribution which is sufficiently narrow or spread.

Considering a square geometry, a narrow distribution led to a value of the time constant which is higher compared to the fundamental one.

To understand this behaviour, it is necessary to recall that the solution of the heat transport equations is described by a superposition of eigenfunctions, that singularly represent an eigenmode which will decay with a particular time constant. The first mode is the one that decays slower, hence is leading the dynamic. However, depending on the characteristics of the heat source the weight of each one of the eigenmodes will change leading to a different value of measured time constant. The value of τ given by the analytical solution is seen to match the value yielded by a Gaussian power distribution characterised with a $\frac{\frac{2\sigma}{L}}{2}$ equal to 0.5.

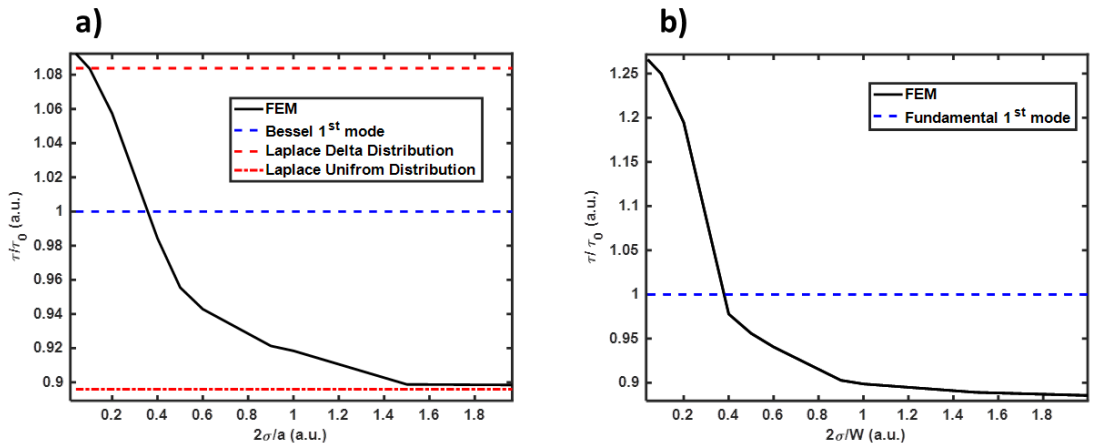

Figure 3.6 Dependence of the thermal time constant from the width of the distribution. Either the circular a) or the square geometry follows the same trend. The dashed lines represent the value given by the analytical solutions. For the sake of clarity, the values are extended all over the horizontal axis.

The dimension of the heat source plays a major role in determining the measured value of the thermal time constant in the experimental phase, hence in the extrapolated values of the thermal properties of the material. The trend in the time constant for the circular and the square geometry are shown in Figure 3.6. Despite a different relative trend, for both the circular and square geometry, the wider the laser spot, the faster the response will be. These findings are correlated with the value of the average temperature established in the membrane upon heat absorption. A narrower distribution leads to a higher average temperature in the membrane that is translated to a higher time constant.

3.6. Experimental Validation

The model described in Equation 44 was validated by studying the transient signal of the mechanical resonance, when the membrane is undergoing periodic IR radiation as described elsewhere[66,69]. The IR light is mechanically chopped at an arbitrary frequency, and the frequency shifts are recorded in the same way as described in Paper II and III. For these experiments, 500μm wide membranes are used. The reason for this choice is that spot size the IR laser which has a diameter of 100μm which places the expected experimental value reasonably close to the τ yielded by the fundamental mode. The value of the thermal diffusivity of the silicon nitride is drawn from Equation 2. For a composite structure, such as a coated membrane, the value of the thermal diffusivity D is:

$$D = \frac{\sum_{i=1}^{N} h_i k_i}{\sum_{I=1}^{n} h_i c_i} \tag{52}$$

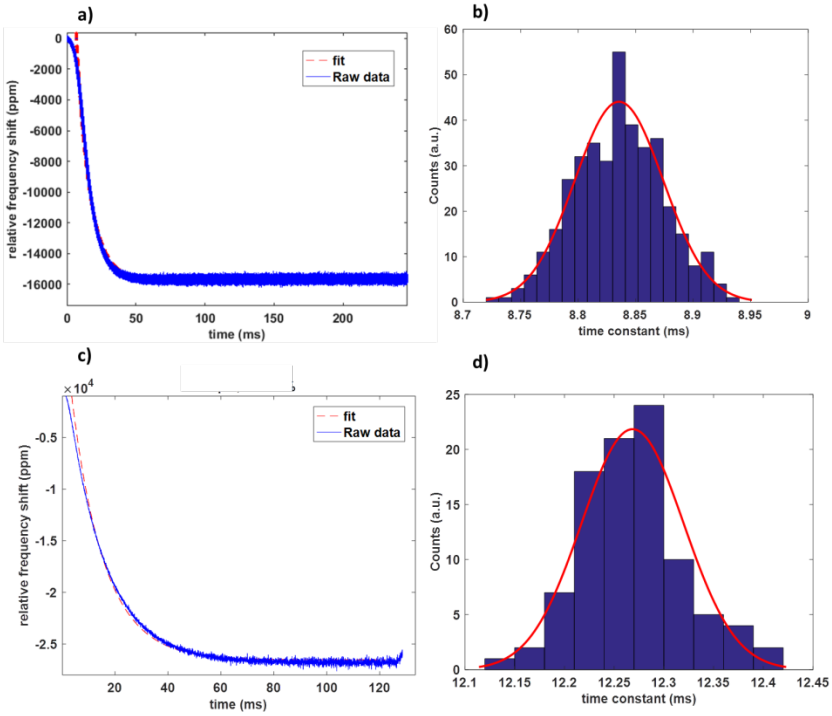

Figure 3.7 Transient curves and distribution of the thermal time constant for a 500μm wide membrane. a-b) Bare Silicon Nitride, c-d) PVP coated Silicon Nitride Membrane.

For a single layer structure, i.e. the bare Silicon Nitride membrane, it is possible to extract directly the thermal diffusivity of the material, which is seen to reasonably match the previously reported results[102] as shown in Table 3.

The thermal diffusivity of a composite structure was evaluated for silicon nitride coated with poly(vinylpyrrolidone) (PVP) layer by applying the same experimental procedure with a thickness layer of 106nm and 110nm respectively. Due to the addition of a polymer layer, the thermal diffusivity of the structure. As reference value is used the value given by Equation 7 and adopting previously published results of thermal conductivity and heat capacity [103]. The error between the experimental thermal diffusivity and the reference thermal diffusivity equal to the 10.5%.

In order to decouple the two thermal diffusivities(of the polymer and the silicon nitride membrane), a calibration procedure has to be performed. The thermal time constant has to be evaluated for increasing thickness of polymer. A fitting of the estimated value thermal time constant as a function of the polymers thickness would be able to disclose the value of the polymer thermal diffusivity and further highlight possible thickness dependent effects, as previously reported for other material properties such as elastic modulus [48] and glass transition temperature [47].

Table 4 Experimental and theoretical values of thermal diffusivities.

Material	Membrane Width	Tau	Experimental Diffusivity	Reference Value
	μm	ms	m^2/s	m^2/s
SiN	500	8.85±0.05	1.40 e-6	1.3-1.7e-6
SiN and PVP(100nm &110nm)	500	12±0.05	1.05e-6	8.88e-7

3.7. Conclusions

This chapter illustrates the accuracy of the analytical models describing the steady state and the transient description of the nanomechanical photothermal signal. The assumptions made in the analytical description of the model resulted in being reasonably correct considering the geometry of the membrane resonator studied in this thesis.

The steady state model allows determining the resonance frequency shift upon heat absorption, this model was used in paper 2 and paper 3 to estimate the power absorption for a given relative frequency shift, and then the temperature of the membrane. Since photothermal spectroscopy is based on the recording of exothermal events, the knowledge of the magnitude of the temperature shift driven by the heat absorption is fundamental. In particular working at low pressure the temperature shift could be high, and in principle cause a phase transition in the material.

The thermal transient is in principle described by a linear superposition of eigenmodes. The first mode is the one that decay slower hence it is dominating the description of the transient. Different initial conditions lead to a diverse superposition of the eigenmodes hence a different transient behaviour. The dependence of the laser spot size and beam width was investigated. Both the circular and the squared geometry reveal an inverse relationship with the beam width, reaching a plateau value for a width larger than the membrane size.

4. Materials and Methods

This chapter provides the description of the process and the experimental approaches employed in this thesis. In particular, the fabrication processes related to the mechanical resonator used for performing biopolymer degradation studies and Nanomechanical infrared spectroscopy (NAM-IR). The working principles of the custom made Blu-Ray based device and of the NAM-IR setup are described.

4.1. Cleanroom Fabrication

All the mechanical structures developed in this thesis were fabricated with standard cleanroom fabrication method. The fabrication phase took place in the cleanroom of DTU Danchip.

4.1.1. Silicon Microbridges

For performing biopolymer degradation studies(Paper 1) double clamped beams are developed. The starting substrate is Silicon on insulator wafer (SOI) with a device layer of 5μm. Conventional fabrication processes are used, and the fabrication parameters are optimised by a trial and error approach. Here we report the design, the process flow and the fabrication process scheme.

4.1.1.1. Mask Design

The fabrication of the microbridge structure is a two masks process (Figure 4.1). The first mask is needed to define the microbridge geometry and it is used to pattern the device layer of the wafer. The bulk removal of the Silicon is performed by anisotropic etching (KOH) upon patterning of the Silicon Nitride masking layer.

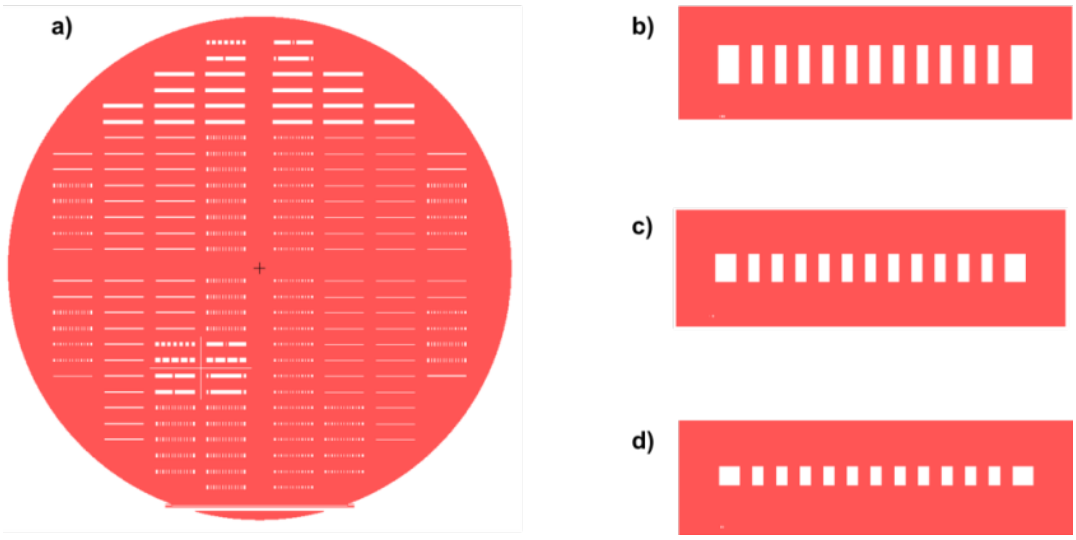

Figure 4.1 Microbridges front mask. a) wafer layout; b) 1000µm long and c) 750 µm long; d) 500µm long. All the structure employed in this thesis were 300 µm wide.

4.1.1.2. Process Flow

The microbridges process flow is reported in Figure 4.2, and the steps are summarised in Table 5. The process is split into three main steps:

i) The patterning of the device layer Figure 4.2(a-e);

ii) The creation of the sacrificial layer and patterning. Two layers of silicon oxide and silicon nitride are grown and deposited respectively. The goal of this step is to form a protective layer for the device layer during the bulk removing of the KOH and act as a mask for the KOH etching from the bottom side of the wafer (Figure 4.2f-h)

iii) The removal of the sacrificial layer and the release of the free standing structures Figure 4.2 i-l

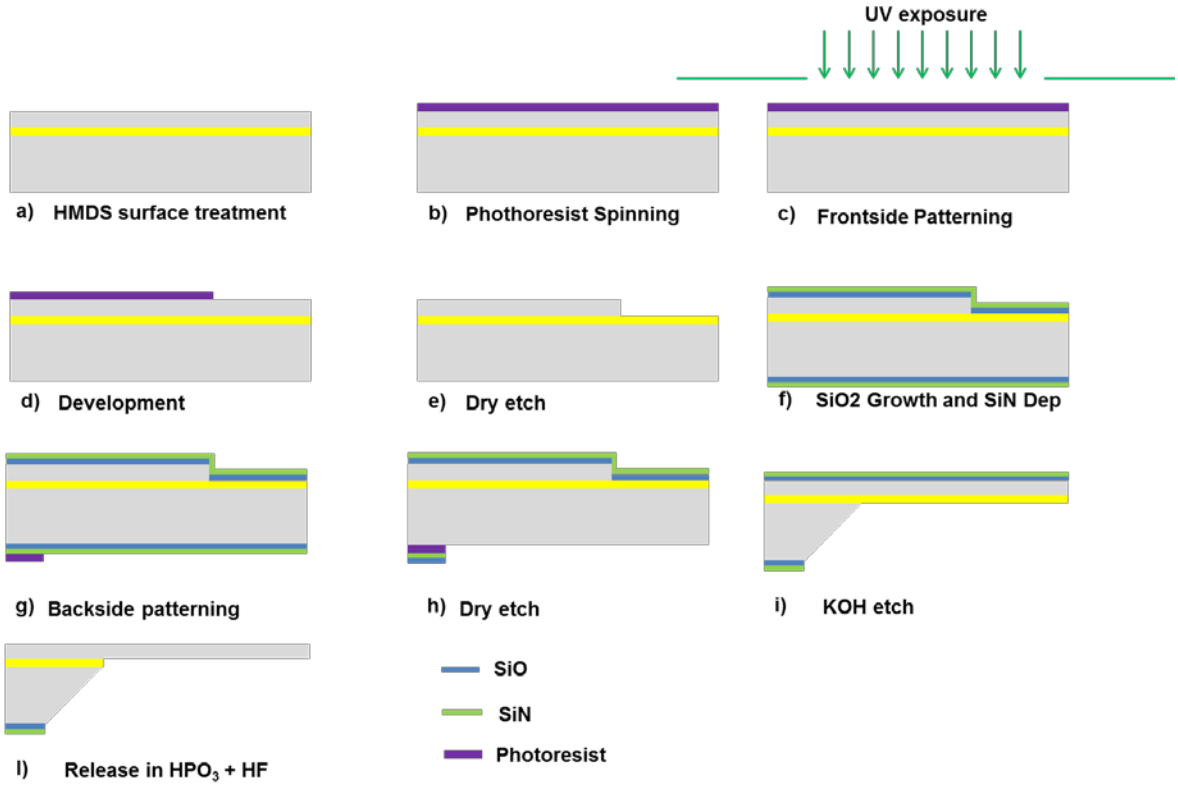

Figure 4.2 Process scheme of microbridge fabrication. For the sake of clarity in the scheme, it is represented the fabrication of a cantilever beam (single clamped) instead of a double clamped cantilever. The resist strip steps are omitted, and the same positive lithography is applied in step c and g.

Table 5 Microbridges fabrication process flow.

Microbridge process flow: Author Andrea Casci Ceccacci				
Mask Label	Bridge front& Bridge Back			
	Step	**Equipment**	**Notes**	**Goal**
Lithography front side	Surface Pre-treatment	HMDS oven	30 min	Improve resist adhesion
	Phothoresist spinning	SSE spinner	AZ-5412E	1.5µm
	UV exposure	6" Aligner	3.5 sec	Positive lithography
	Developer	TMAH Developer	1 min	remove the exposed pattern
	Dryer	Spin drier	1 min	
	Device layer dry etch	Pegasus DRIE	55 sec	Defining the resonator geometry
Sacrifical layer	Phthoresist Strip	Plasma Asher	30min	
	RCA cleaning	RCA bath		
	Silicon Oxide Growth	Furnace B1	Calbrate the dep time accoridng to the last dep rate	200nm
	Silicon Nitride deposition	Furnace E3		300nm
Lithography back side	Surface Pre-treatment	HMDS oven	30 min	Improve resist adhesion
	Phothoresist spinning	SSE spinner	AZ-5412E	1.5µm
	UV exposure	6" Aligner	3.5 sec	Positive lithography
	Developer	TMAH Developer	1 min	remove the exposed pattern
	Dryer	Spin drier	1 min	
	Device layer dry etch	ICP Etcher	4min	Etch rate 70nm/min measured
	Phthoresist Strip	Plasma Asher	30min	
Device Release	KOH wet etching	KOH bath(1 or 3)	3.5h @80C	Remove silicon
	Silicon Nitride etch	HPO3 etch	165C	Remove the Sacrificial Silcon Nitride layer
	Silicon Oxide etch	HF bath		
	Dryer	Ethanol fume dry		

Figure 4.3 Optical microscope images of the microbridge fabricated during this thesis. Scalebar 300μm

4.1.2. Membranes

Low-stress Silicon Nitride membranes are fabricated for NAM-IR spectroscopy application.

4.1.2.1. Mask design

The fabrication of silicon nitride membrane is rather straightforward. It is a single mask process. On a single chip 1cmx1cm, there have been located two pairs of square membrane resonators sized 1mm and 500μm respectively.

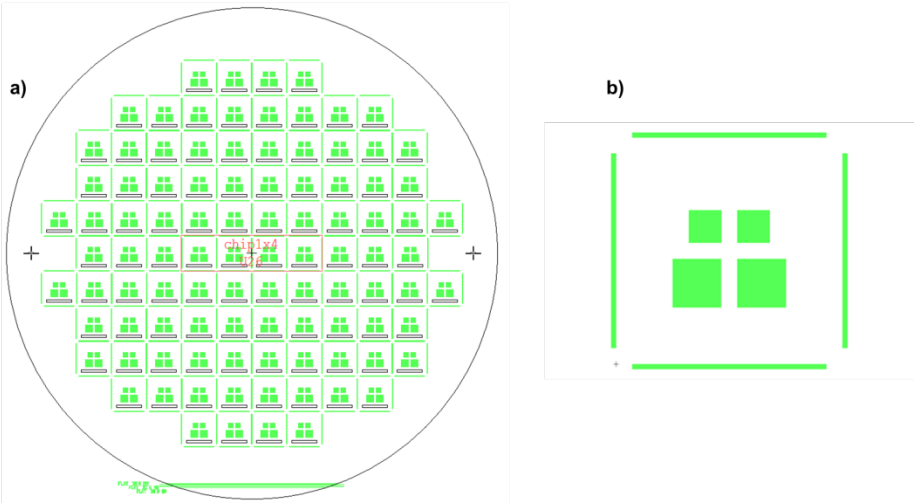

Figure 4.4 Mask design of the membrane chip used in this thesis. a) Wafer layout and b) single chip.1000μm² membrane and 500μm² membrane were fabricated.

4.1.2.2. Process Flow

The process scheme is similar what has been shown in Section 4.1.1.2 for microbridges resonators. Here, the starting substrate is a double polished silicon wafer, and only one lithography step is necessary to define the membrane geometry. The process flow is reported in Table 6 and the process scheme is indicated in Figure 4.5. The final results of a Silicon wafer for obtaining the membrane resonator is showed in Figure 4.6

Table 6 Membrane Fabrication process.

Process flow Author: Andrea Casci Ceccacci				
Mask: Membrane front, BF KOH,DF				
	Step	Equipment	Notes	Goal
Wafer Selection	No wafer pretreatement needed			
Device layer	Low stress silicon Nitride	LPCVD furnace B1	20 min dep time	100nm
Sacrifical layer Deposition	Plasma enanched chemical deposition	PECVD 2	8 min, Front side	500nm
Lithography Backside	Surface Pre-treatment	HMDS oven	30 min	Improve resist adhesion
	Phothoresist spinning	SSE spinner	AZ-5412E, 1 min bake 90 C	1.5µm
	UV exposure	6" Aligner	3.5 sec	Positive lithography
	Developer	TMAH Developer	1 min	remove the exposed pattern
	Dryer	Spin drier	1 min	
	Backside SiN Etch	ICP	2 min	open areas for KOH etching
Release of the device	Phthoresist Strip	Plasma Asher	30min	
	Silicon wet etch	KOH bath	3.5h	Define membrane clamping points
	Silicon Nitride wet etch	HF bath	10 min	Removal of the sacrifical layer
	Dryer	Ethanol fume dry		Drying of the wafers at low vapour pressure

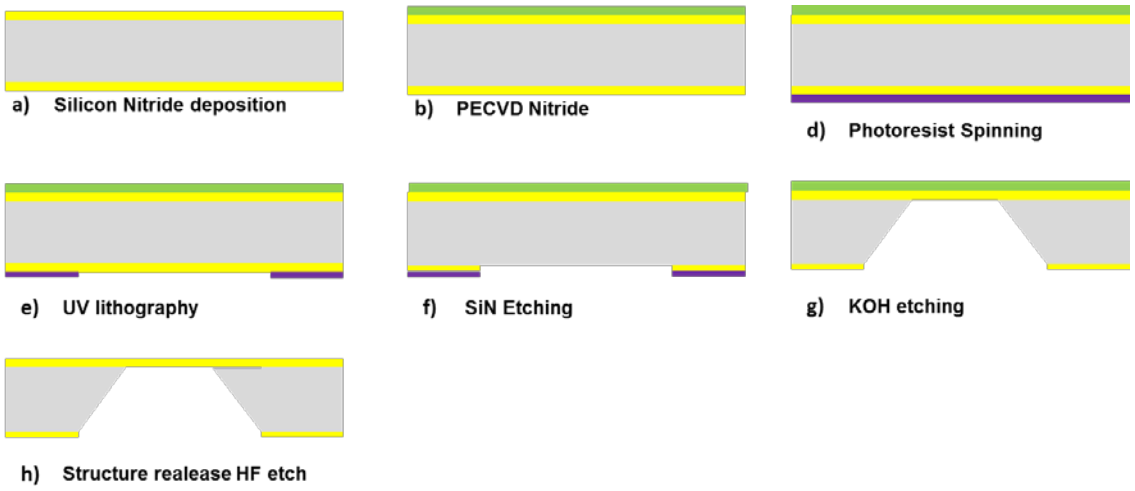

Figure 4.5 Process Scheme of Membrane resonator fabrication. HMDS surface treatment prior to c is omitted and resist strip before step g is omitted

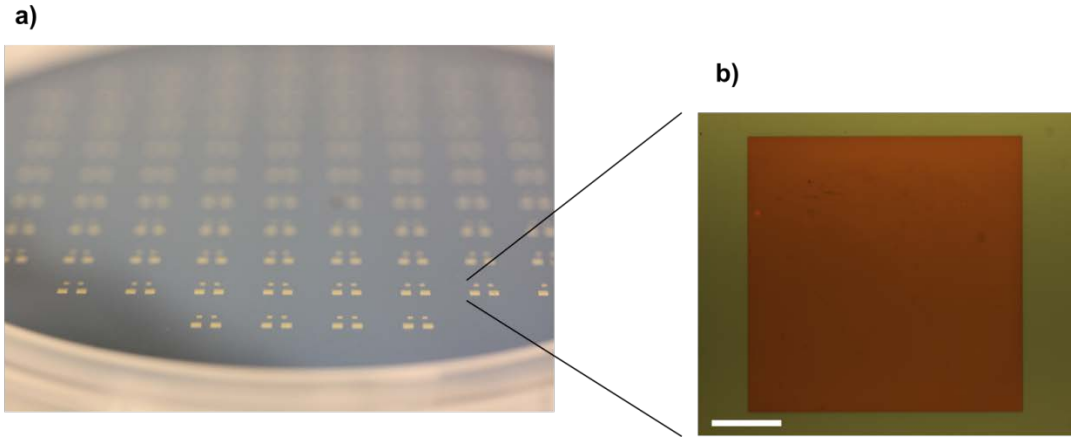

Figure 4.6 Outcome of the fabrication process for Silicon Nitride Membrane. Complete wafer, yield close to 100% and single 1000µm squared membrane. Scalebar 200µm.

4.2. Structure functionalization

4.2.1. Spray coating

Microbridges are functionalized using spray coating Figure 4.7. An extensive description of the role of the experimental parameters involved is intensely studied in [55]. From a general point of view, a spray coating process includes: i) the atomization of the coating solution in the nozzle, where minute droplets are formed, ii) the deposition of the atomised droplets on the substrate, iii) and finally the coalescence of the droplets upon solvent evaporation. The nozzle is actuated ultrasonically, and it causes the atomization of small droplets in the micrometer size. A Nitrogen flow is used to focus the atomised solution on the target sprayed surface.

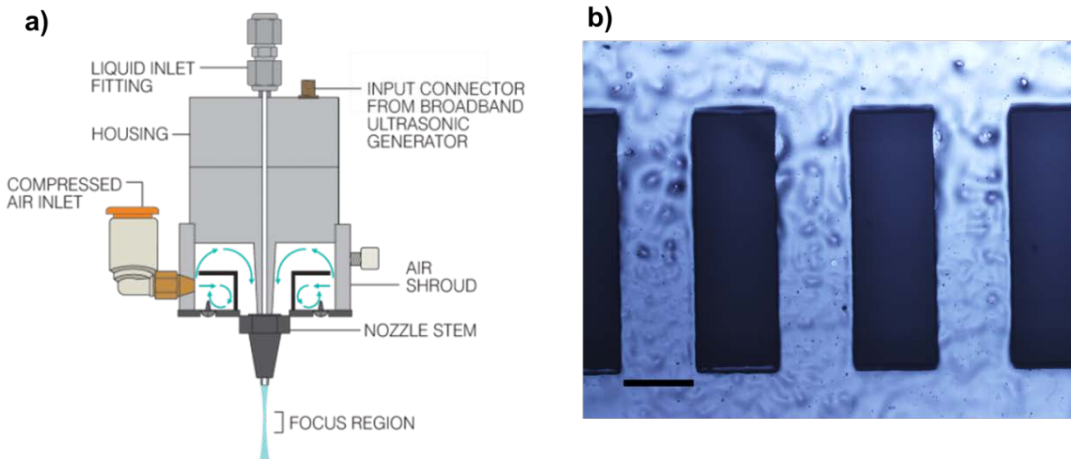

Figure 4.7: a: Scheme of a spray coater nozzle. Adapted from [104]; b) 1000μm long 300 μm wide microbridge coated with PLGA dissolved in DCM 0.5%. Scalebar 300 μm.

4.2.2. Spin Coating

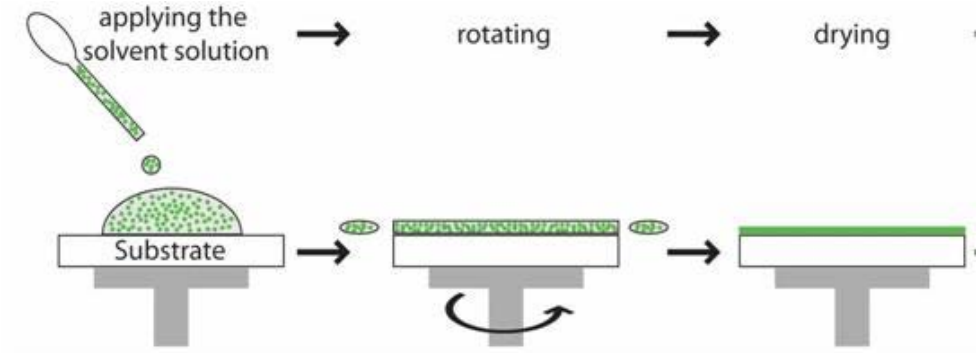

Figure 4.8 Standard operating procedure for spin coating. The solution is applied on the substrate which makes rotate. Adapted from [105]

Another sample preparation method used for deposit a polymer layer onto the sensor is spin coating. A standard operating procedure for spin coating is shown in Figure 4.8. Spin coating is widely applied in the semiconductor fabrication process to form a photoresist layer. In this thesis, spin coating is used to form a poly(vinylpyrrolidone) (PVP) film on membrane resonator device. Spin coating particularly fit the purposes of this study as it allows forming a thin uniform polymer film. On the contrary, besides being a high throughput method for creating thin polymer layer, it does not fit the functionalization of microbridge chips. The working principle of spin coating is rather simple. The solution that has to be deposited on the substrate is cast on the target surface. The substrates are put into rotation at a certain speed, and the centrifugal force spreads the polymer on the substrate. The thinning of the film takes pace in two different stages. The first one is caused by the only radial outflow of the excess solution. In this stage, the evaporation of the solvent is neglected. Subsequently [106], the evaporation rate reaches a stable value, and the film can be considered as immobile, the thinning of the film is due primarily to the solvent evaporation.

4.3. Thickness Measurement

Regardless of the method used for depositing the biopolymer layer on the sensor the knowledge of the thickness is a fundamental parameter for calibrating the sensing performances of the nanomechanical sensor. In this thesis, two methods are used to characterise the thickness of the deposited polymer layer: profilometry and ellipsometry.

4.3.1. Profilometry

A diamond stylus (Figure 4.9a) approach first the analysed surface once the surface is reached the tip is moved laterally across the sample the output variable is the surface height as a function of the stylus position, i.e., the scan length. The range of the measurable thicknesses ranges from 10nm up to 1mm.The vertical tip displacement represents the height of the surface. A profilometer curve is showed in Figure 4.9b

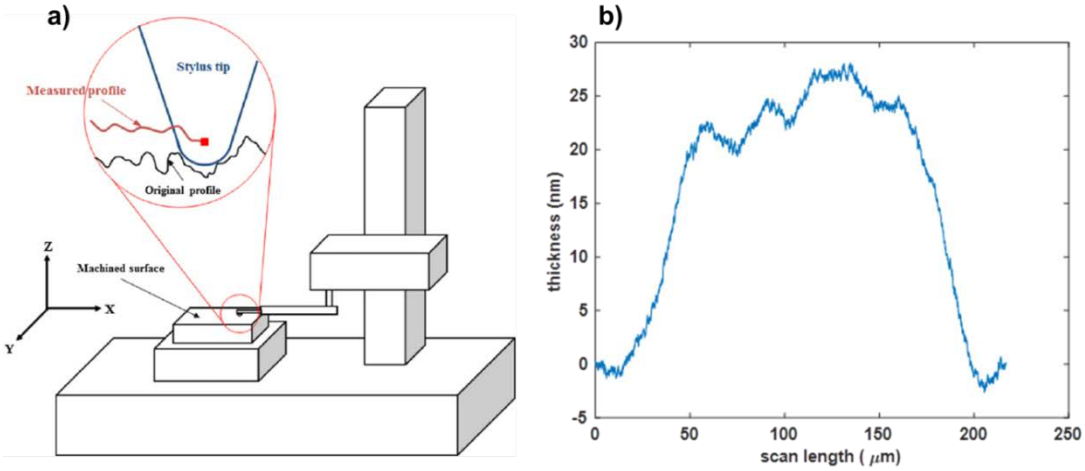

Figure 4.9. Profilometer Scheme and a typical curve. a) Scheme of a stylus profiler adapted from [107]. b) An example of profilometer raw data. Here, the thickness of a membrane chip coated with a thin layer of PVP.

4.3.2. Ellipsometry

Ellipsometry is a non-destructive measurement method where the information about the thickness and the refractive index of the layer can be obtained. Ellipsometry detection scheme is represented in Figure 4.10. Ellipsometry assesses the thickness of the layer indirectly by measuring the changes in the polarisation of an incident light upon reflection of the target surface. The principle of measurement, in fact, stands on the difference in the polarisation of the light once it has been reflected on the target surface. This method particularly fits for very thin layer, being the minimum measurable thickness in the order of tens of angstrom. Differently from the profilometer, an apriori knowledge of the optical property of the substrate layer is needed. The obtained thickness will be in fact the results of a fitting.

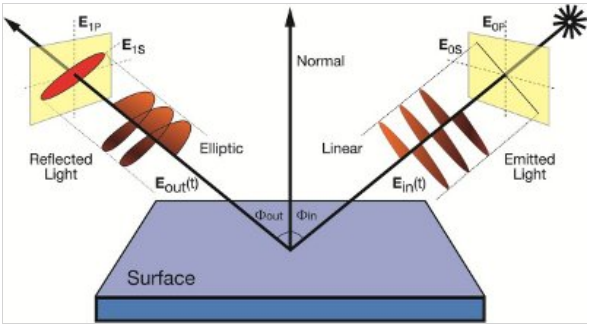

Figure 4.10 Schematic representation of the spectroscopic Ellipsometry. Adapted from [108]

4.4. Readout Integration

In this section, the principles and the building blocks of the optical detection based on a commercial Blu-Ray pickup head unit are presented. The section further includes the description of the integration of an astigmatic detection scheme onto automated systems aimed to characterise the frequency response of the micromechanical resonators.

4.4.1. The Blu-Ray pickup head unit (PUH)

The readout of the frequency response is performed optically, by integrating a readout based on a Blu-Ray ® technology.

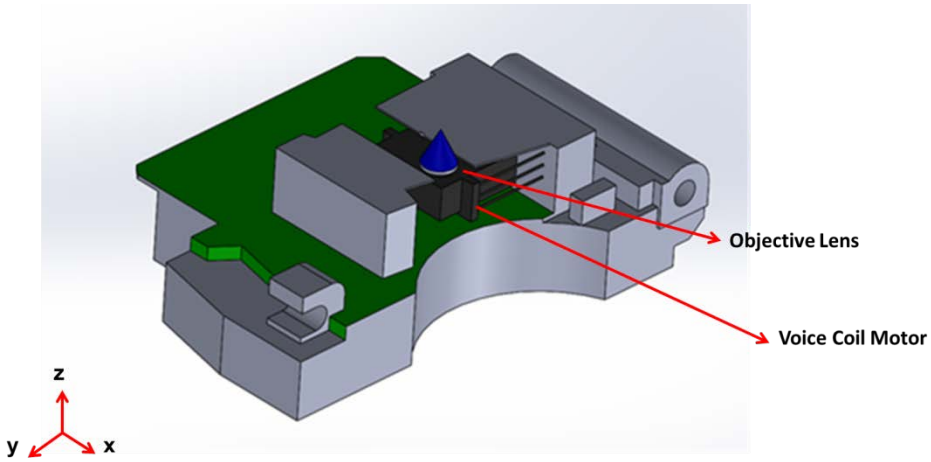

Figure 4.11 Blu-ray Pickup head unit.

The Blu-Ray pickup head unit (PUH) is illustrated in Figure 4.11. It consists of a semiconductor laser emitting diode at three wavelengths, 405nm, 605nm and 780nm[8]; a lens system needed for driving the laser beam, grating, polarisation beam splitter, $\frac{\lambda}{4}$ plate and a voice coil motor. The optical and electrical component embedded inside the OPU are designed to work at very high frequency as they have to be capable to handle data stream in the order of GHz. This makes the OPU the

[8] Blu-Ray OPU integrate also the lasers related to the previous generation of OPU, being those the one available in DVD/CD-ROM based technologies

ideal candidate for the integration of an automated readout for micromechanical sensor. The integration of the PUH in the readout system is presented in Figure 4.13.

4.4.1.1. The Voice Coil Motor (VCM)

The distance between the reflective surface and the objective lens can be finely calibrated by the VCM embedded in the PUH. The VCM Figure 4.12 uses a permanent magnetic field and a coil producing a force proportional to the current applied to the coil. The electromechanical conversion is generated by the Lorentz force principle, according to which, if a conductor material which is carrying a current is located in a magnetic field force will act on it. During the conventional operation (i.e. a readout of the Blu-Ray or DVD) the PUH detects changes in the distance between the refractive surface and OPU. The generated focus error signal (FE) signal is used to evaluate the current necessary to drive the VCM such that the focal point will be on the reflective surface, the disc.

The VCM can move along the x and z-direction, within 1mm range and a resolution of tens of nm. The capability of moving in the z-direction has been used for performing the autofocusing function as described in Section 4.5.1.

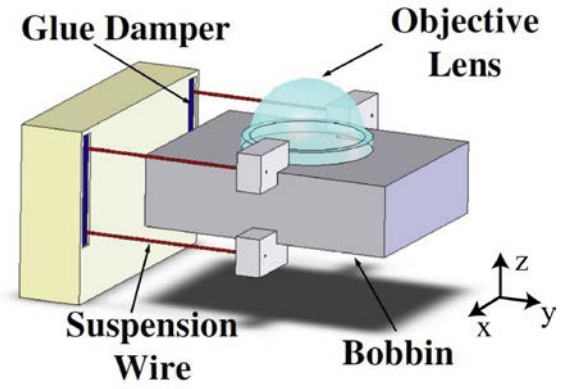

Figure 4.12 Voice coil motor, adapted from[109]

4.4.2. Astigmatic Detection

An optical system which is not symmetric relatively to the optical axis is defined astigmatic. In cylindrical lenses, the optical system is designed to be not symmetric as in the case of DVD or Blu-Ray PUH. An astigmatic optical detection scheme is presented in Figure 4.13, which matches with the detection scheme embedded in the Blu-Ray PUH. The laser light is focused onto a reflecting surface, i.e., the silicon microbridges. The reflected laser light passes through a polarising beam splitter, and an astigmatic lens, finally the reflected light impinges the four quadrants photodetector (PIDC). The four element of the PIDC is equipped with a current preamplifier. The PDIC output signal is named as Focus Error Signal (FES) is defined as:

$$FES=(S_A+S_c)-(S_B+S_D) \tag{53}$$

When the laser spot is perfectly focused on the object surface the FES =0 (Figure 4.14). If the incident light is not focused on the surface the shape of the laser spot on the PIDC is distorted, and the FES signal differs from 0.The shape change of the laser spot in the PIDC sensor corresponds to a specific value of FES.

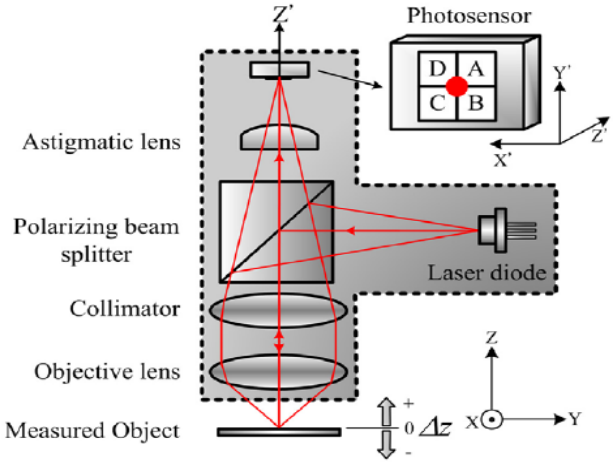

Figure 4.13 Astigmatic detection scheme. Adapted from[83]

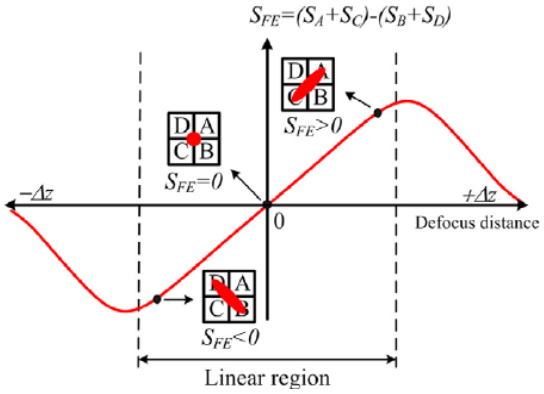

Figure 4.14 Focus Error Signal. Adapted from [83]

It is evident how a specific position of the measured object is univocally transduced in terms of FES value. The linear working range depends on the characteristics of the optical lens as well as by the wavelength of the laser beam. The objective lens used in this thesis for both the system has a numerical aperture NA= 0.6. Under these conditions, the linear range corresponds to about 6μm; the working distance is 1.2-1.4mm.

4.4.3. Integration of the Blu-Ray based readout

The Blu-Ray pickup head unit is integrated into custom made systems[9] aimed to provide a (semi)-automatic characterization of the frequency response of the microbridge structures. The final goal of these systems is to provide a device that can improve the experimental condition as well as the throughput of micromechanical-based biopolymer degradation experiments as previously described by Bose and co-workers [44]. A biopolymer degradation study based on system v1 is described in Paper 1.

Regardless of the system version, the measurement routine relies on the following steps:

i) installation of the microfluidic cartridge in the chip holder;
ii) alignment of the OPU with the microbridges array;
iii) actuation of the piezoelectric crystal and measurement of the frequency response.

4.4.3.1. System V1

The purpose of this system is to provide a device able to:

i) recognise the position of microbridges resonator,
ii) performing autofocus of the probing light on the microresonator surface;
iii) automatically records the frequency response of micromechanical resonators.

[9]The systems (V1 and V2) design and manufacturing was done by En-Te Hwu, Academia Sinica Taiwan. The control software were developed by Ching Hsu-Chen Acadamia Sinica, Taiwan. The microfluidic cartridge used in system V1 was designed and developed by Lidia Morelli, PhD student DTU Nanotech

The height of the chip holder is regulated by adjusting the position of 4 screws that provide the chip holder with 6 degrees of freedom (translation and rotation along the main axes) Figure 4.15a. The chip height is manually regulated by the user, and the PUH microbridge distance is adjusted in such a way that all microbridges will be roughly in the linear range allowing the detection of the position. The fine adjustment of the focus is then handled by the measurement routine where the central position of the S-curve is found, and the measurement is performed.

In the first version of the system a single microbridge array chip is embedded in a microfluidic cartridge (Figure 4.16) which is installed in the chip holder that is kept tight by four screws avoiding any slippery motion of the cartridge.

The microfluidic chip is composed of three PMMA plate(Figure 4.16), bonded together with the microfluidic double sided tape which has also been used to bond the microresonator on the bottom plate.

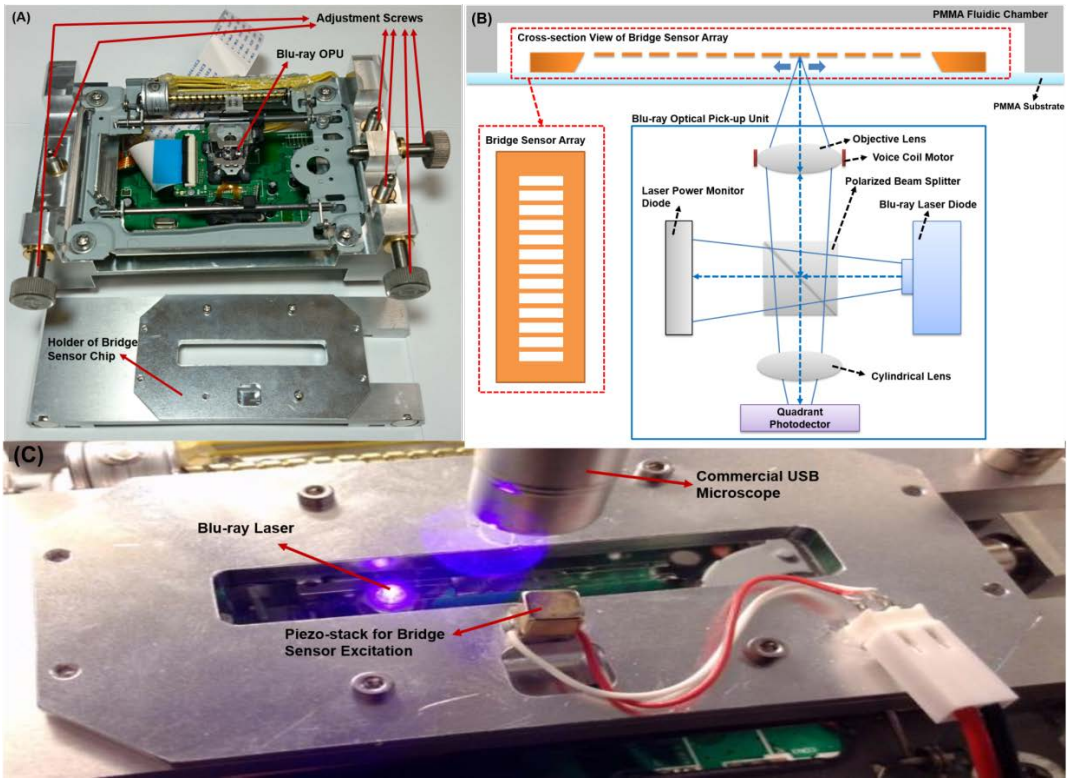

Figure 4.15 First generation of the system measurement: a) system and chip holder, b) detection scheme based on the Blu-ray pickup head unit; c) system in action. The position of the PUH can be monitored in real time by an external USB microscope.

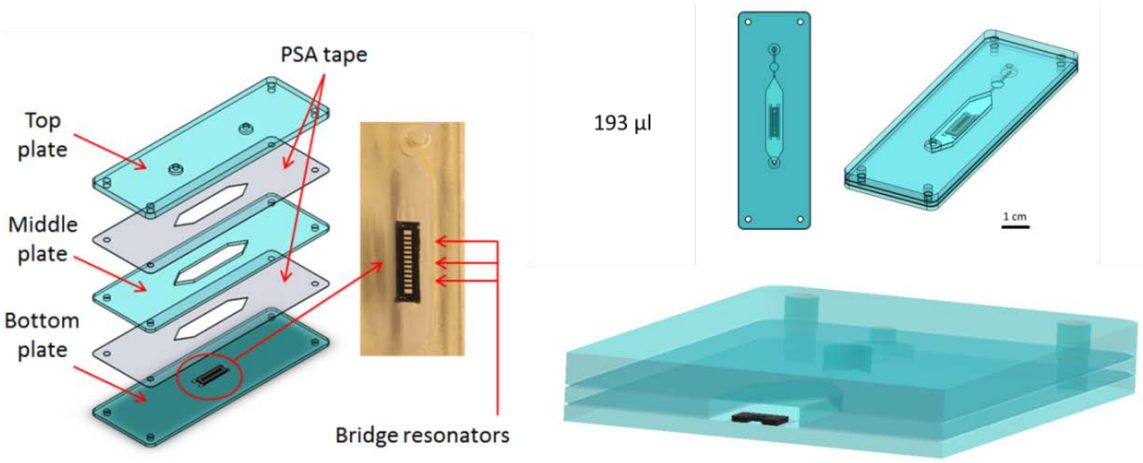

Figure 4.16 Microfluidic device used in Paper 1. the three layer of PMMA are cut by CO_2 laser cutting.The microfluidic channels are embedded in the PSA tape bonding the middle and the top plate. The microfluidic access is provided on the top plate, and tubings are sealed with cured PDMS.

4.4.3.2. System V2

The System V2 aimed to improve the throughput of the measurement. To pursue this goal, the chip holder (Figure 4.17a) is equipped with a stepper motor providing motion in the y direction. In this way measurements are possible in the x-y plane, allowing to locate and measure multiple arrays of bridges. In the light of this, in the microfluidic cartridge was modified up to three microbridges array can be installed. The width of the microfluidic chamber was modified to match the width of the microbridge array Figure 4.17b-c reducing possible tilting of the microbridge sensor in in the x-y plane.

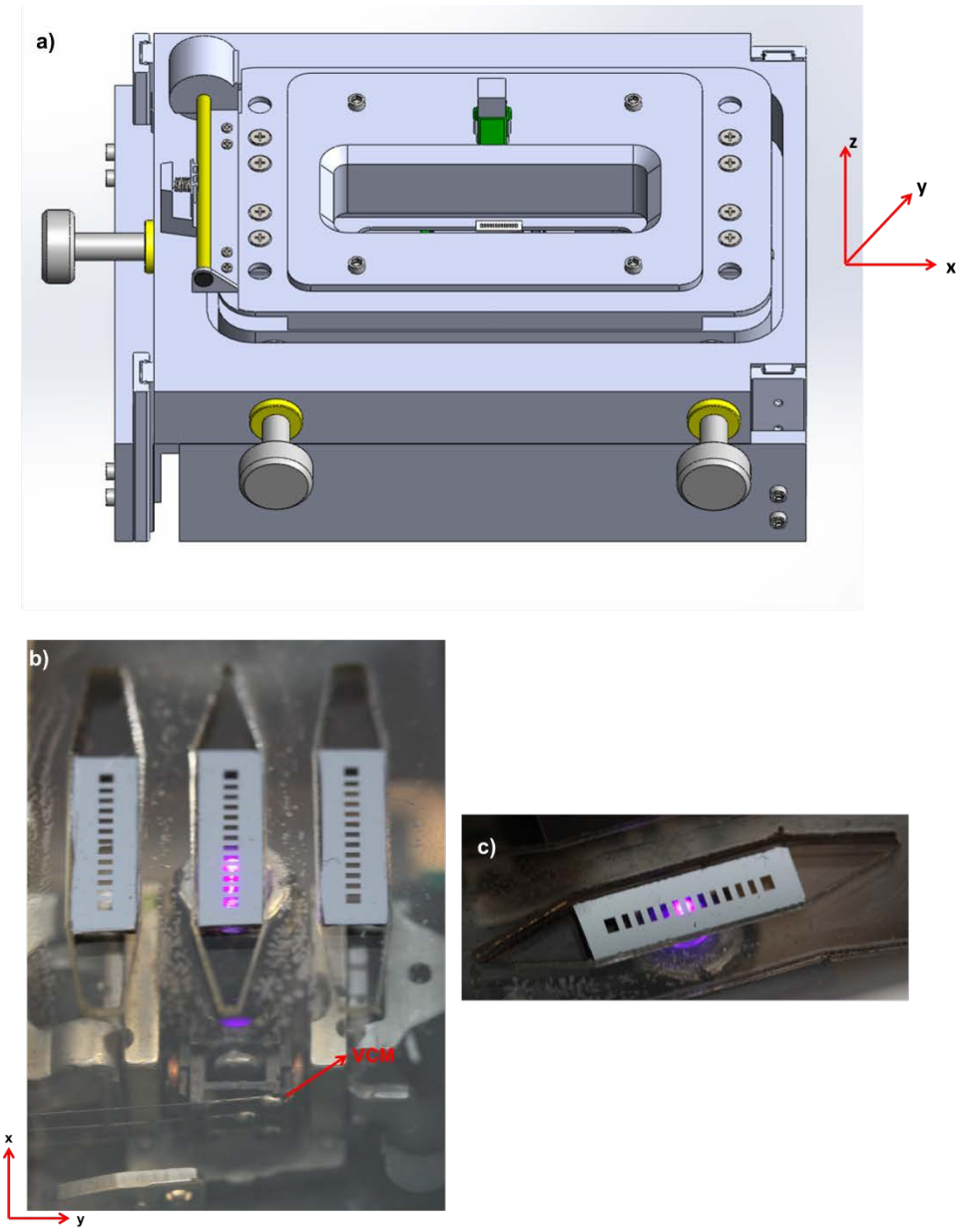

Figure 4.17. System v2 a) Design of the system V2; b) implementation of multiple microbridges chips in the same microfluidic device; c) close up. For the sake of clarity, the top plate of the microfluidic device has not been installed.

4.5. Algorithms for tracking microbridges position

During the tracking phase, the PUH moves along the x direction as shown in Figure 4.17b-c a predefined amount of time and the FES is recorded.

The BR-PHU scans the microbridge arrays and records the FES (Figure 4.18). When the light is reflected a step change in the FES is recorded. The absolute value of the signal is evaluated, and an edge detection is performed on the recorded signal. Once the value overcomes an internal threshold, the central point of the bridge is found, and the bridge position is saved. The procedure iterate until all the bridges have been found.

In its first implementation (Figure 4.18a) the distance between the PUH is kept fixed throughout the whole phase, and it is determined by the manual adjustment performed through the screws. It is essential that all the bridges be well aligned in the x-z plane to have a working distance such that the profile of the bridge can be univocally identified. For instance, as reported in Figure 4.18b the first bridges are well identified instead the last ones are slightly above the SNR level.

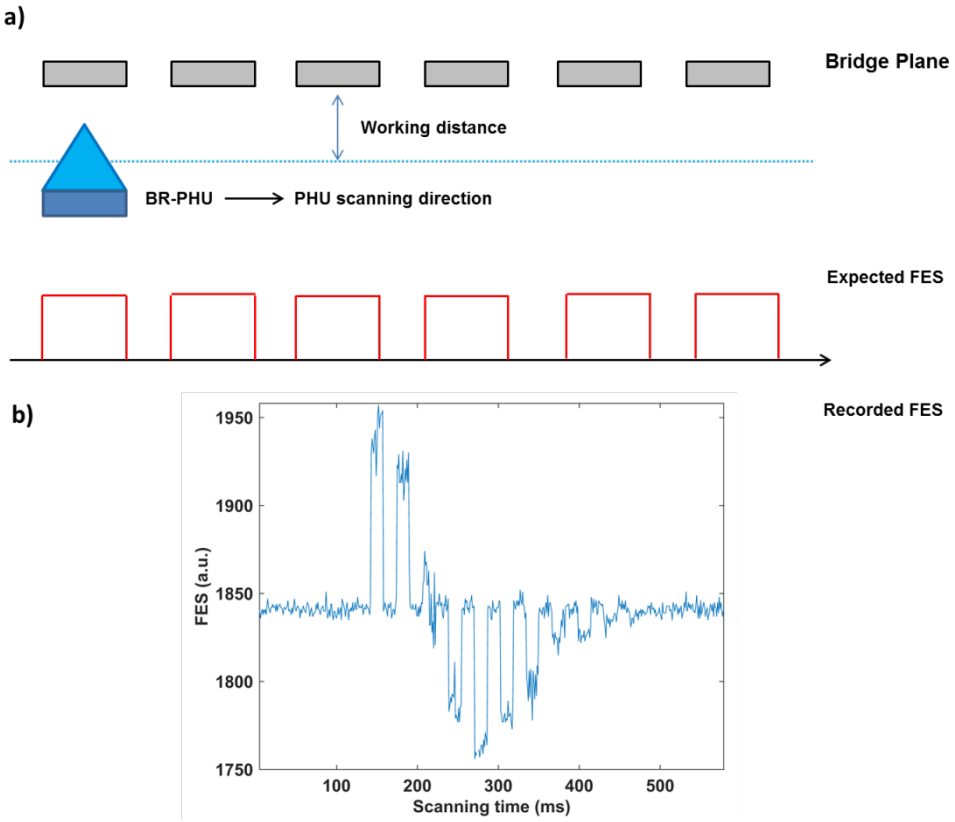

Figure 4.18 First implementation of the bridge localisation algorithm. The FE signal is acquired for a singular working distance, defined during the manual alignment phase.

To improve the experimental conditions and to reduce the number of operation requested by the user, a new tracking algorithm is developed. The FES is acquired for subsequent VCM position allowing the FES signal to be recorded at a different working distance (Figure 4.19). Moreover, at each iteration, the recorded FE signal is evaluated and summed with the already recorded one. Once the cumulative sum overcomes a threshold value, defined by the user the bridges are localised and identified. This implementation drastically reduces the number of operation needed by the user to operate and provide a more stable and robust device.

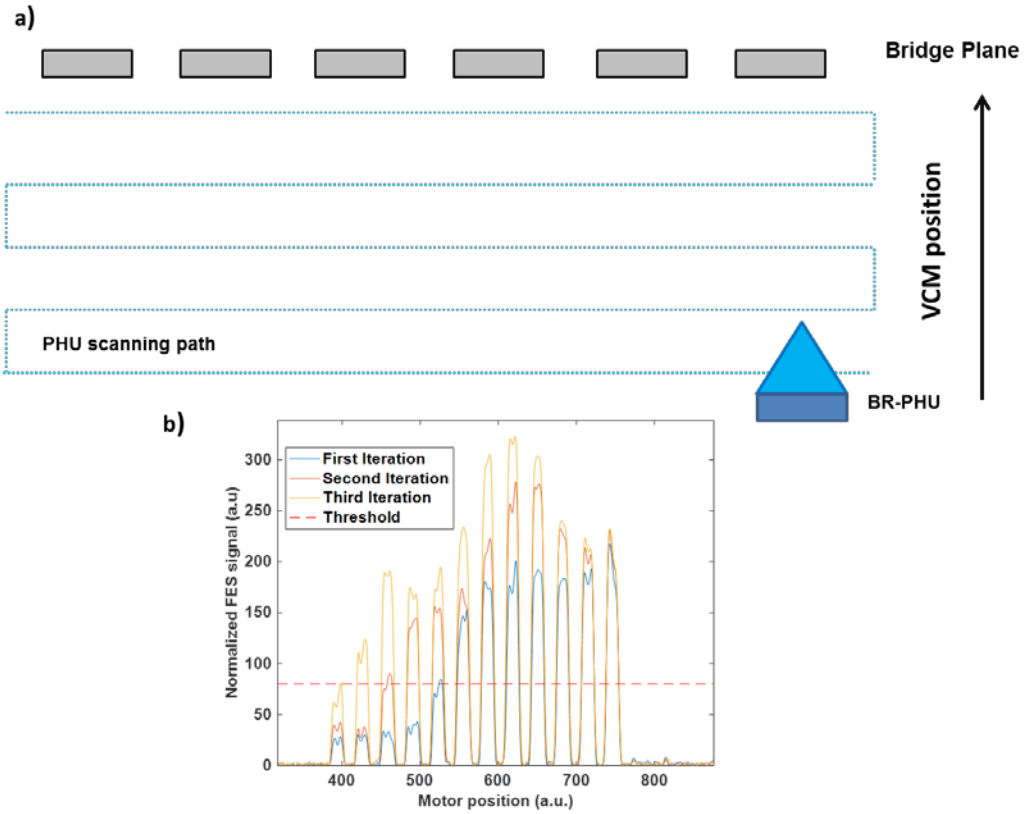

Figure 4.19 Bridge localisation algorithm V2. The PUH is moved within a predefined number of VCM position, and the FE signals are recorded accordingly. Once the cumulative sum of the FE signal overcome a certain threshold, the bridge is identified, and its position saved.

4.5.1. Auto Focusing

After the localisation of the bridges in the array, the system steps into the measurement phase. Before actuating the piezoelectric crystal, the software needs to identify the best working distance in such a way that the measurement will take place with a perfectly focused spot. To do so, the VCM is actuated, and the S-curve recorded. The central part of the S-curve is identified(Figure 4.20), saved and used for the next measurement. Finally, after the localisation of the focal point, the piezo crystal is actuated, and the mechanical spectra are recorded.

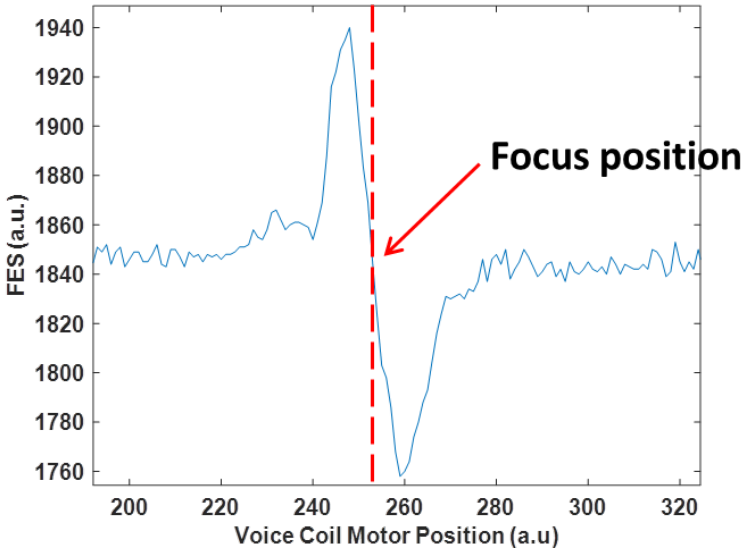

Figure 4.20 Focus error signal recorded on one bridge before the frequency response acquisition. The VCM coil motor is actuated, and the FES acquired. The central spot of the FES is used as a focal point to perform the measurement.

4.6. Nanomechanical Infrared Spectroscopy Setup

The goal of this section is to describe the setup and the acquisition parameters used for photothermal spectroscopy through nanomechanical sensor henceforth called (NAM-IR). The components of the acquisition chain are described. All the main component of the Nam-IR setup are shown in Figure 4.21.

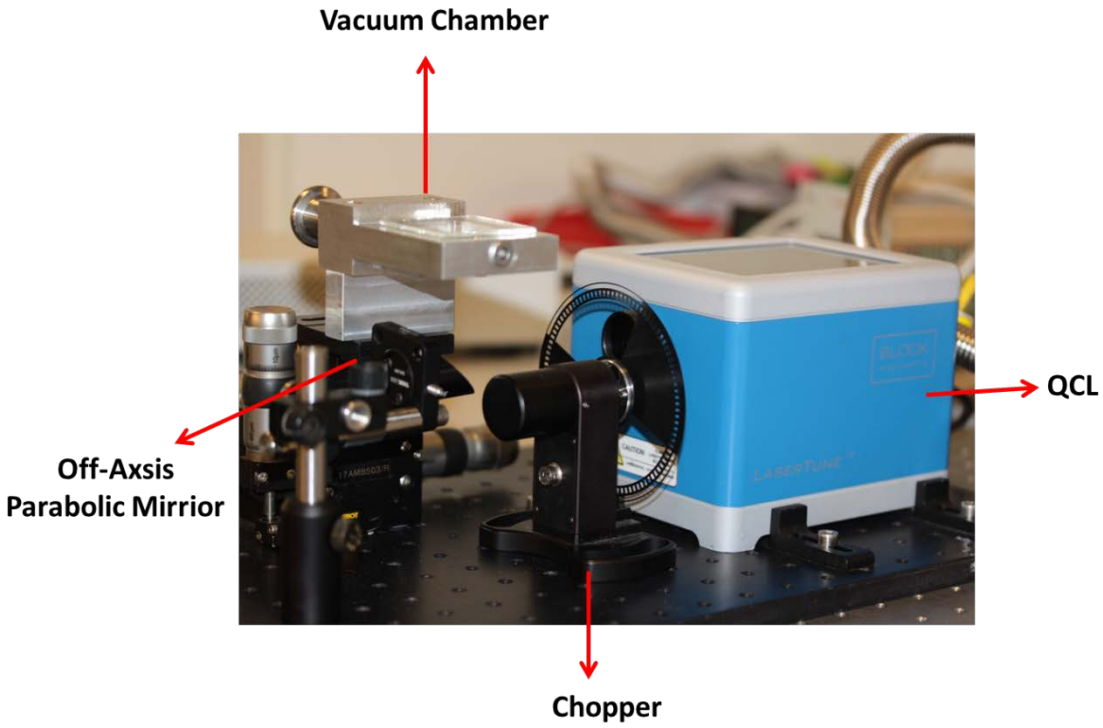

Figure 4.21.The NAM –IR setup. The IR laser is produced by a Quantum Cascade Laser, QCL block engineering. The light can be mechanically chopped, providing a periodic thermal excitation. The path light is deviated on the membrane resonator by an off-axis parabolic mirror that collimates the laser light on a spot of diameter 100 μm. The membrane chip is placed into a customs mated vacuum chamber holder providing electrical access for the actuation of the piezoelectric crystal.

The membrane resonator is placed in a custom made vacuum chamber, which provides optical access from the top, where the readout laser for the laser Doppler Vibrometer can probe the membrane motion and from the bottom, where the IR light is shined through a KBr window. The chamber provides an electrical connection for the actuation of a piezoelectric crystal. The low vacuum (LV) regime is provided by a conventional pump that can reach 1 mbar. Instead, the high vacuum (HV) regime is provided by a turbo pump that allows reaching the 10^{-}

^{5}mbar. The possibility to run experiments at two different pressures allow investigating the phenomena involved in the generation of the mechanical photothermal signal.

4.6.1. Characterization Of The Quantum Cascade Infrared Laser Source

Quantum cascade lasers (QCLs) were developed at the Bell Laboratories in 1994[110]. They are semiconductor based apparatus able of emitting a photon from the mid-infrared to the far-infrared portion of the spectrum. A QCL substantially differs from diode lasers. The latter can emit photons in the process of electron-hole recombination where a single photon is involved resulting in a wavelength that exclusively depends on the band gap about the combination of the material used. Quantum Cascade Lasers consist of sandwich structures of semiconductor materials. These sandwich structures are organised to form regions of local minima of potential energy commonly known as quantum energy well that limit the electrons in a precise energy state. When the electrons, driven by an externally applied voltage moves through subsequent energy barriers (Figure 4.23), which are characterised by a specific energy, the electron transition from one valence band to the lower one yield in a photon emission. The sandwich structure above described, is designed such that they can emit a particular wavelength. The emitted wavelength depends on mostly on the structure rather than the constituting material, allowing fabricating devices that emit up to 25 μm.

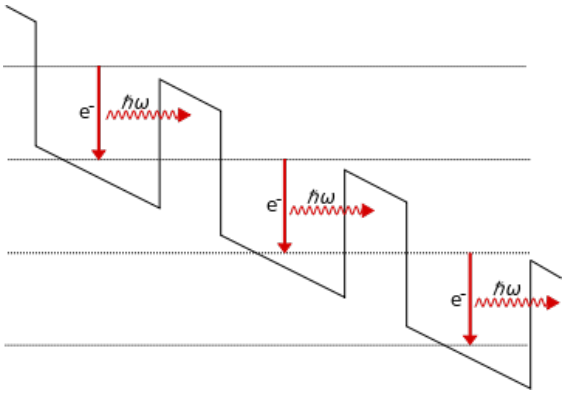

Figure 4.22. Schematic working principle of the QCL.Adapted from[110].

A quantum cascade laser source (QCLs) block was used for all the experiment done during this thesis. The wavelength interval that such device can provide ranges from 768cm^{-1} to 1953cm^{-1}, providing a non-constant power spectrum (see Figure 4.23). The laser is operated in a pulsed mode, and therefore the output power can be modulated throughout the modification of the duty cycle. The output power of the QCL (Block-Engineering) laser source is quantified using a thermal power sensor for different duty-cycle settings.

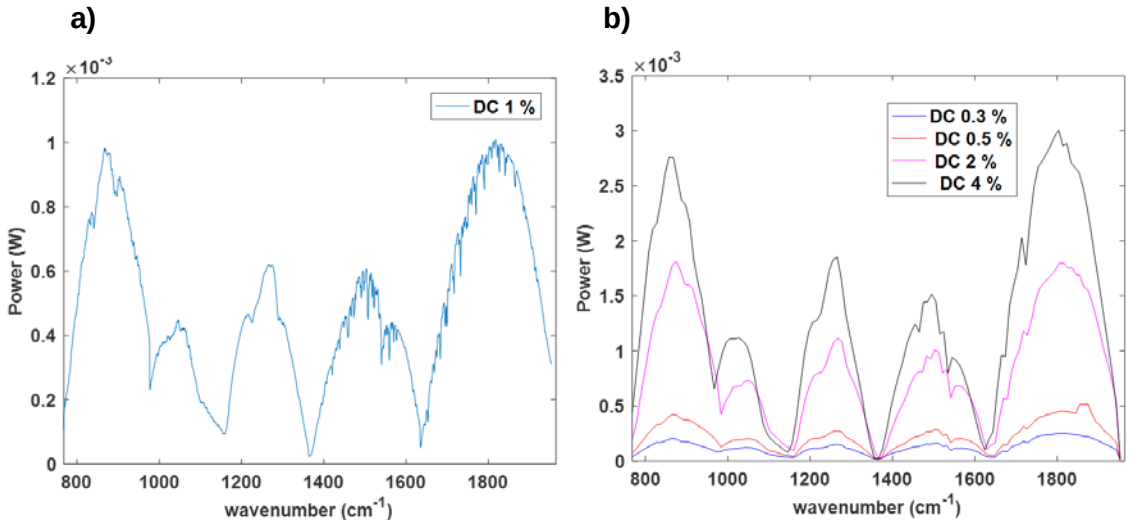

Figure 4.23 Power spectrum of the QCL. a) the DC was set at 1% (to= 100ns T= 1μs) step size 1cm^{-1} constant throughout all the power range used; b) DC set at 0.3-4% step size 10cm^{-1}.

The output power is non-linear throughout the portion of the electromagnetic spectrum. In the region 1400-1800cm^{-1}, several local minima characterise output

which are inevitably reflected in the recorded signal during the spectroscopy application. This may cause that some of the spectral features of a particular analyte will not be sensed.

In the perspective to obtain a quantitative analysis through Nanomechanical infrared spectroscopy an accurate characterization of the laser source is done. A relation that describes the duty cycle and the output power of the IR source are needed therefore a general procedure for obtaining such relation is described.

The output power seems to reach a saturation level after a DC of 4%. The use of higher duty cycle causes an overheating of the device and the control software automatically switch off the emission.

The same trend is noticed either with the membrane photothermal sensor or with the thermal power meter. The normalised curves are shown in Figure 4.24c for the frequency of 1850 cm^{-1}. The fitted curves are described by parameters having reasonable same values Table 7. Consider such similarity the law describing the relation between the duty cycle and the output power is assumed to be the same throughout the entire possible wavelength ranged by the QCL.

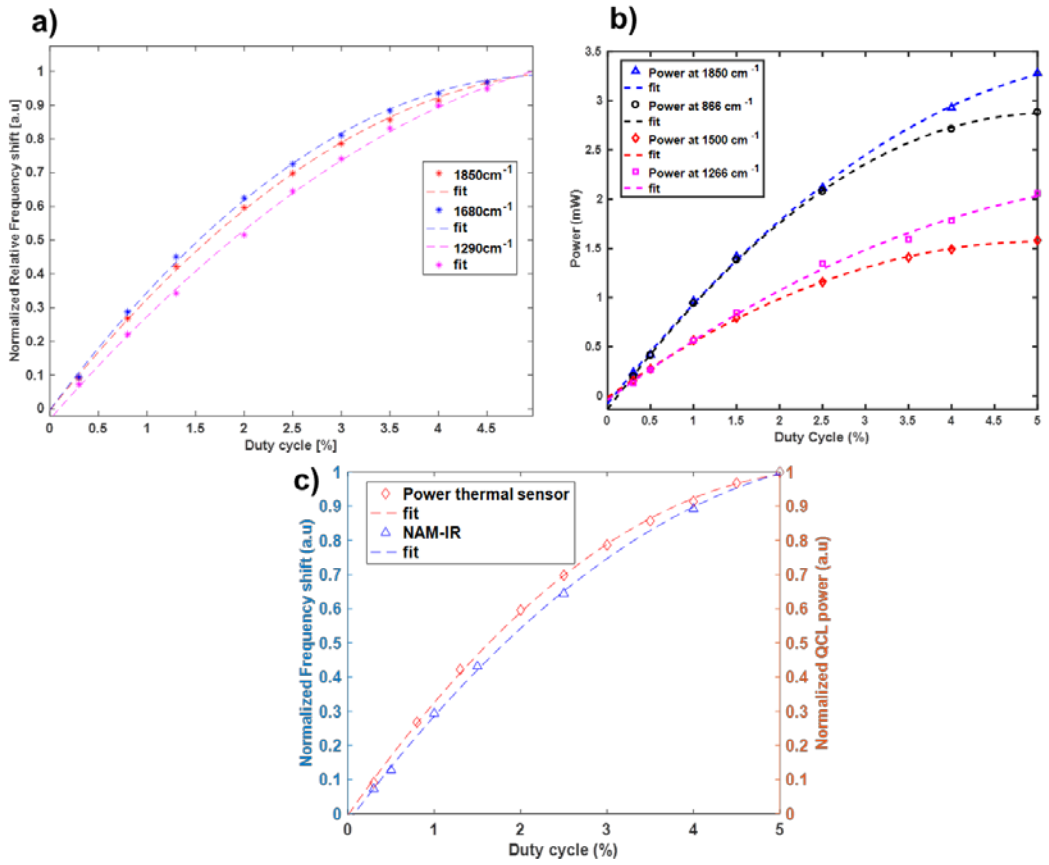

Figure 4.24 QCL power as function of duty cycle. Different output wavelength are different duty cycle values: a) measured through membrane photothermal sensor; b) measured through the optical based power meter; c) comparison of the normalised signal obtained from the thermal power source and the membrane photothermal sensor.

Table 7 Values of the fitted parameter describing the second order polynomial expression that the relationship between the normalised output power and the duty-cycle

Frequency (cm^{-1})	Fitted parameter p_1	Fitted parameter p_2	Fitted parameter p_3
866	-0.0398	0.4078	0.0468
1850	-0.0238	0.3158	0.0194
1500	-0.0386	0.3934	0.0079
1266	-0.0265	0.3366	0.0240

4.6.2. The measurement acquisition chain

The acquisition of the spectra by NAM-IR is a time-varying process; the resonance frequency shift can be written as:

$$\delta_f(t) = f(\omega_{IR}(t)) \tag{54}$$

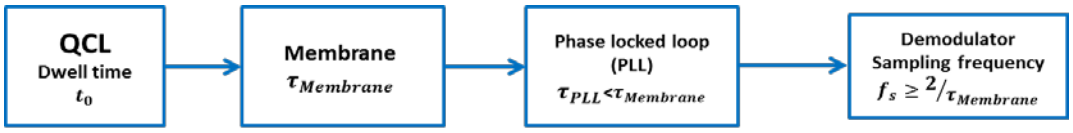

Figure 4.25 Block Diagram of the acquisition chain of the NAM-IR setup.

The QCL sweeps a certain interval of wavelengths by quantizing the wavelength range in a discrete manner. A certain wavelength ω_i is kept as output for a certain dwell time t_0, therefore the time needed for sweep across a wavelength range Δ_ω is $T = t_0 * \Delta_\omega$.The measurement of the photothermal signal matches with the measurement of a thermal process, commonly described by a time constant. As described in chapter 4 and Paper 1, the membrane time constant regulates the minimum amount of time (dwell time, t_0) that a single IR frequency has to be activated for being properly recorded by the membrane resonator. Furthermore, the integration time of the PLL has to be set according to the response of time of the membrane.

4.6.2.1. The Phase locked loop (PLL)

All the frequency shifts are recorded through a phase locked loop detection scheme(Figure 4.26). Although it is not the goal of this project investigating on the capabilities of such device, it is noteworthy to introduce its working principle and the settings parameters as they have a fundamental role in determining the outcome of recorded signal in terms of time responsivity and noise.

The phase locked loop was introduced in the field of telecommunication as key component of frequency (de) modulation transmission based technology. In its broad definition, a phase locked loop is a closed control system that provides a signal that is proportional to the phase difference between the phase of the reference signal and the phase of the system under study (SOS).

A reference signal, generally a sine wave is internally produced and multiplied to the signal of the SOS hence the phases of these two signal are compared and used as input of a PID block which controls a voltage controlled oscillator (VCO) such that its output will have the same frequency of the entry signal. During a measurement, the reference signal is set at the resonance of the (SOS) hence, in the absence any source that can deviate the resonance frequency for the set value; the VCO will oscillate at the same frequency of the SOS. As the signal input is varying the PID will regulate the output of the VCO such that to minimise the error.

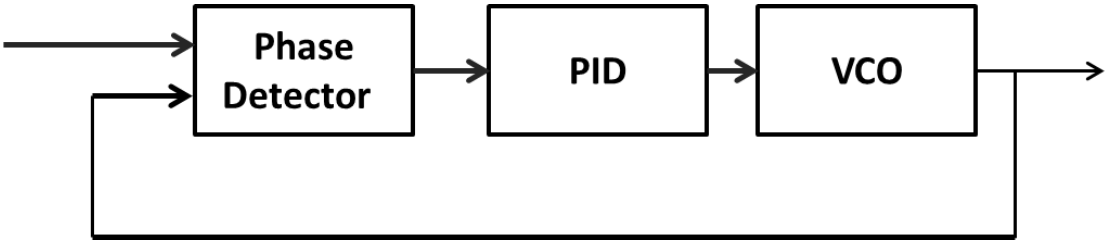

Figure 4.26 Block diagram of the PLL. The phase for the reference signal is compared to one of the input signals. The PID controls the open loop gain, providing a signal that will pilot the Voltage-controlled Oscillator that will finally pilot the piezoelectric crystal with the same frequency and phase of the input signal.

4.6.2.1.1. Influence of the PLL Bandwidth on NAM-IR spectra

The PLL bandwidth is by far the most important parameter that determines the time responsivity of the detection scheme and the gain of the PID control. A smaller bandwidth cut out value determines a higher Signal to noise ratio (SNR) which come at the cost of a slower system (higher value of integration time), on the contrary, a higher bandwidth allows following faster changes of the input signal decreasing the quality of the signal in terms of SNR [111].

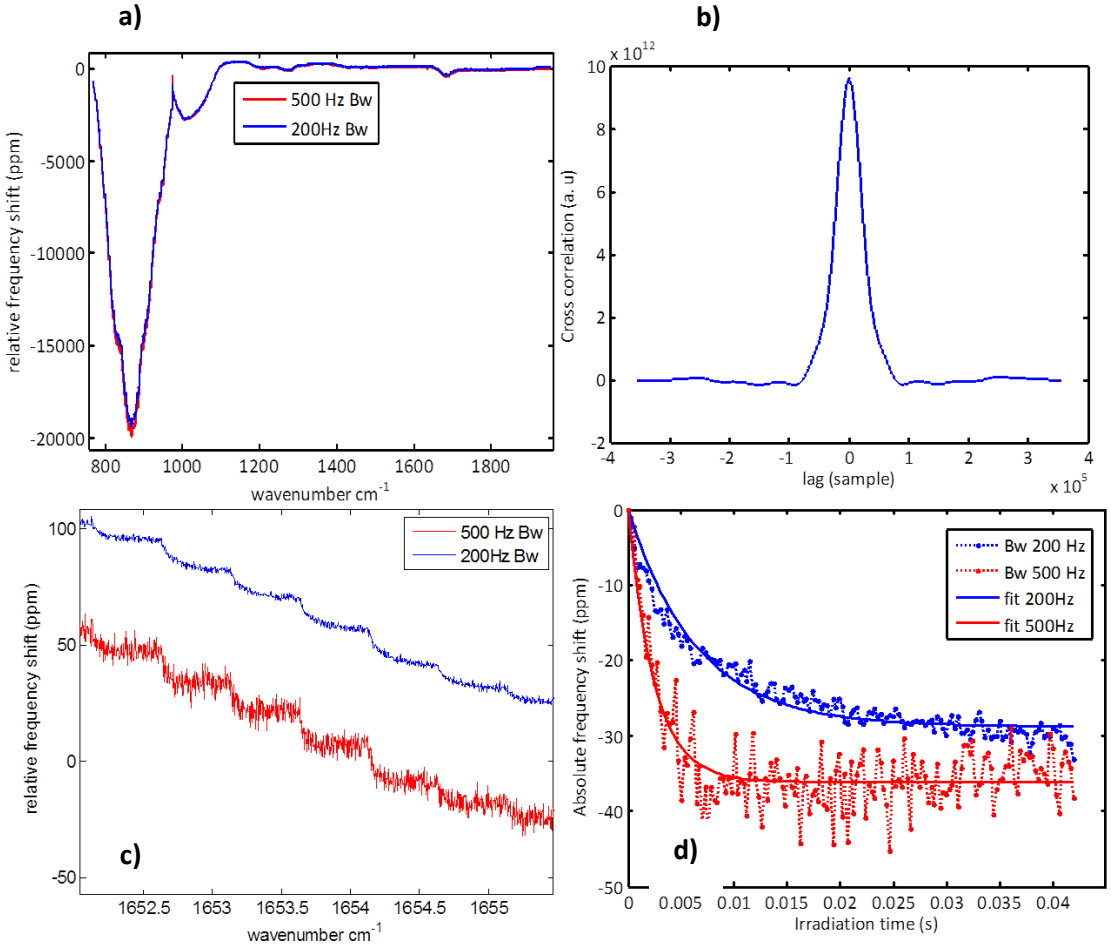

Figure 4.27 Effect of the Phase detector bandwidth on the recording. The cross-correlation function b) has been used to see if between two different PLL settings would influence the phase of the signal. The main effect depending on the settings is due to the low-pass filter effect that a lower bandwidth has on the recordings.

In the present work, the choice of the right bandwidth value revealed to be fundamental to maximise the SNR.

In Figure 4.27 is represented the difference of the NAM-IR spectra recorded at 200 Hz and 500 Hz PLL bandwidth for a 20nm PVP coated membrane. 200 Hz provides a higher integration time which does not comply with the speed of frequency shift transitions taking place upon heat absorption. The two recordings are perfectly aligned, and the cross-correlation function has the maximum at 0 meaning that the NAM-IR shifts are recorded without significant lags. The effect of the lower value of bandwidth can be seen in Figure 3c-d where the spectra recorded with 200Hz bandwidth resulted in being low pass filtered. If the time constant of the PLL is not set at least smaller than the time constant of the analysed phenomenon, this will not be recorded properly.

For photothermal resonance spectroscopy application, the PLL bandwidth has to be chosen to match the thermal time constant of the membrane sensor. In this work for all the spectra recorded the bandwidth was set at least to 500Hz which provides an integration time smaller than the thermal time constant of the membrane resonator. Finally, the sampling frequency of the A/D converter has to fulfil the Nyquist-Shannon theorem and therefore has to be set at least two times the highest frequency component and in the experiment was performed at 3600 sample/sec.

4.7. Polymer Solution Preparation

The polymer used in the paper were: poly(lactic-*co*-glycolic acid) PLGA and poly(vinylpyrrolidone) PVP, both obtained and used as received from Sigma-Aldrich.

For polymer degradation studies PLGA(Mw=16kDa) was used, and it was dissolved in dichloromethane (DCM, 99% HPLC grade Sigma-Aldrich) dissolved in 0.5% wt. and stirred overnight before being sprayed.

For NAM-IR, experiments were focused on the study of PVP. Membranes were coated with poly(vinylpyrrolidone). In this case, the polymer was dissolved in a mixture of water and hydrogen peroxide (H_2O_2:H_2O 30% wv.) in different concentrations: 1%wt. and 5% wt. For performing the experiments reported in paper 2 and paper 3. However, for performing the crosslinking experiments the of paper 3 the polymer concentration was lowered to 0.1%wt to deposit few nanograms of material on the membrane resonator by direct drop casting.

5. Summary of Papers

Paper 1

The working principle of the first version of the Blu-Ray based system for characterising the enzymatic degradation of PLGA is presented. In this paper, an improved methodology of biopolymer degradation studies by micromechanical resonator is shown. The following elements were combined: i)double clamped microbeams as mass sensor, ii) a microfluidic setup where the degradation environment can be easily simulated, and iii) a readout based on a Blu-Ray device which can be easily programmed to perform measurement in an automatic fashion.

Paper 2

This paper shows the working principle of a micromechanical membrane as photothermal sensor. The sensing capabilities of the sensor were characterised studying the photothermal response of membranes coated by thin layer of PVP prepared by spin coating. The behaviour of the nanomechanical photothermal signal is studied in high vacuum and low vacuum showing what effect that the atmosphere has on the overall acquisition of the NAM-IR spectra. NAM-IR spectra were recorded on different polymer thicknesses. The achieved Signal to Noise Ratio is compared to the one obtained by conventional ATR-FTIR spectroscopy on similar samples. Membrane-based NAM-IR spectroscopy provides on a single acquisition an SNR 43 time higher than the conventional ATR. The extracted limit of detection for membrane resonator is in the attomolar range indicating that the analysis of single molecule layer is possible.

Paper 3

In this paper, we want to highlight how an analysis based on membrane photothermal resonators facilitates the study of the modification of chemical properties of thin polymer layer. The linearity of the photothermal response across

two orders of magnitude of polymer coating is showed. The evaluation of the responsivity curve as function of the deposited polymer thickness obtained by spin coating, serves as calibration tool for estimate the deposited thickness by other methods such as drop casting. Films of PVP obtained by drop casting are crosslinked by UV. In the paper is also analysed the phenomena of photooxidation that occurs simultaneously to the gelification. Membrane photothermal sensor allowed featuring the gelification process on picogram quantity of PVP.

6. Conclusions

In this thesis, the goal was to develop technologies to facilitate biopolymer characterization. This was accomplished by working on two different tasks.

i) The development of a Blu-Ray based device to perform biopolymer degradation studies using micromechanical resonators.
ii) The design, modelling and optimisation of a mechanical based photothermal sensor.

Two generation of a semi-automatic system for measuring the biopolymer degradation were developed. In this framework, silicon microbridges were designed and fabricated. Microbridges have shown a reasonably good mass sensing performance, and have been used to monitor the biopolymer degradation. The measured limit of detection was $\Delta m = 0.09$ µ$g\ mm^{-2}$, which enables to describes the biopolymer degradation phenomena, considering the biopolymer density of 1-5 $\mu g mm^{-2}$. In water environment the limit of detection was $\Delta m = 3.34$ µ$g\ mm^{-2}$ of bridges hindering their use for a real-time monitoring of the biopolymer degradation phenomena. In order to overcome this limitation a wet and dry approach has been used. The first generation of the system (system V1) has been used to characterize the enzymatic degradation of poly-lactide-co-glicolyde (PLGA). The enzymatic degradation rate obtained in this work was 25µgcm^{-2}h^{-1} comparable to the one obtained under similar environmental conditions with a conventional approach. Looking at these results from a statistical point of view, the ratio of analysed samples vs total experimental time is 3 orders of magnitude higher compared to the conventional studies. These results were summarized in paper 1.

The second version of the system (systemV2) aims to improve the throughput of the measurements. Compared to the first version, system V2 can perform measurements on two axes, allowing to increase the throughput of degradation analysis. Moreover, system V2 aims to reduce the interaction of the user. The robustness of the controlling algorithms is improved. In particular, the initialization

routines of the measurement sequence: autofocus and tracking of the position of the microresonator have been improved.

Relatively to the second task of this project, micromechanical sensors have also been designed and developed to perform nanomechanical based photothermal spectroscopy (NAM-IR).

The use of a 2D resonator as photothermal sensor is new. Membrane resonators have shown to have several experimental advantages compared to strings. First of all is the simplicity and robustness of the sample preparation on the membrane. Membrane resonators can be easily functionalized by spin coating or drop casting, instead of bulky spray coating or aerosol system which would have been used for string based photothermal analyses.

The nanomechanical photothermal signal has been modelled both analytically and using finite element simulations. The goal was to understand the effects that the experimental variables have on the generation of the photothermal signal. In particular, an accurate knowledge of the transient allowed us to correctly couple the dynamics of the IR source with the acquisition parameters. Thanks to the modelling, the absorbed incident power, but more importantly, the temperature field reached in the membrane for any single power absorption was calculated. The incredibly high SNR (307) obtained on a 20nm thick layer of poly(vinylpyrrolidone) indicates that obtaining the IR fingerprint of single molecule layer is within reach.

The high sensitivity was exploited to characterise the crosslinking mechanism of the picomolar quantity of poly(vinylpyrrolidone), biopolymer for pharmaceutical applications.

Finally, a proof of concept of the potential of the photothermal response was used to evaluate the thermal diffusivity of the silicon nitride and of the bilayer polymer-silicon nitride. These results are seen to reasonably match the values of the thermal diffusivity reported previously reported in literature.

6.1. Outlook

The semi-automated system that was used to characterise the biopolymer degradation can be easily used for measuring other pharmaceutical relevant physical phenomena. For instance, the concept of degradation study can be expanded by exploring the dissolution of drug-polymer mixtures and further characterise the effect of drug on the degradation of a polymer matrix.

Microbridges structures can be optimised to work in liquid environment aiming to perform real-time degradation studies. To accomplish this goal, the design has to take into account that the structure should have a high resonance frequency and a wide cross section to minimise the energy losses.

The development of the photothermal studies performed in this work concerns the possibility of integrating the readout[79], eliminating the need for expensive and bulky readout technology such as the Laser-Doppler Vibrometer used in this thesis. One of the hidden advantages of the NAM-IR technique is that the signal can be obtained by impinging the sensor at any angle and with any polarisation. Applying these concepts and considering the limit of detection demonstrated in Paper 2 a potential application of photothermal spectroscopy is the analysis of the chemical structure of self-assembly monolayers.

The studies presented in Paper 3 can be implemented on hollow structures, which would enable the real-time monitoring of crosslinking of polymer. Indeed, the gelification induces changes in the polymer solution whose rheological properties transit from a purely viscous to a viscoelastic solid. Such modification in a polymer-filled hollow structure would be reflected as changes in the Q.

Mechanical resonators have shown to be able to work as a thermal characterising tool for polymers [56,57,112]. The creation of a setup able to perform a temperature dependent photothermal spectroscopy would enable the disclosure of properties of materials in the form of thin films, while they undergo a multitude of relevant thermal events, such as glass and phase transitions. This technique is going

to contribute more and more to the lively debate in the scientific community around this important topic [47,113].

References

[1] Biopolymers - Latest research and news | Nature, (n.d.). http://www.nature.com/subjects/biopolymers (accessed April 5, 2017).

[2] a. C. Vieira, J.C. Vieira, J.M. Ferra, F.D. Magalhães, R.M. Guedes, a. T. Marques, Mechanical study of PLA-PCL fibers during in vitro degradation, J. Mech. Behav. Biomed. Mater. 4 (2011) 451–460. doi:10.1016/j.jmbbm.2010.12.006.

[3] R.S. Petersen, S.S. Keller, A. Boisen, Hot punching of high-aspect-ratio 3D polymeric microstructures for drug delivery, Lab Chip. 15 (2015) 2576–2579. doi:10.1039/C5LC00372E.

[4] P. Gentile, V. Chiono, I. Carmagnola, P. V Hatton, An overview of poly(lactic-co-glycolic) acid (PLGA)-based biomaterials for bone tissue engineering., Int. J. Mol. Sci. 15 (2014) 3640–59. doi:10.3390/ijms15033640.

[5] C.L. Huang, T.W. Steele, E. Widjaja, F.Y. Boey, S.S. Venkatraman, J.S. Loo, The influence of additives in modulating drug delivery and degradation of PLGA thin films, NPG Asia Mater. 5 (2013) e54. doi:10.1038/am.2013.26.

[6] H.K. Makadia, S.J. Siegel, Poly Lactic-co-Glycolic Acid (PLGA) as biodegradable controlled drug delivery carrier, Polymers (Basel). 3 (2011) 1377–1397. doi:10.3390/polym3031377.

[7] R.H. Harrison, J.A.M. Steele, R. Chapman, A.J. Gormley, L.W. Chow, M.M. Mahat, L. Podhorska, R.G. Palgrave, D.J. Payne, S.P. Hettiaratchy, I.E. Dunlop, M.M. Stevens, Modular and Versatile Spatial Functionalization of Tissue Engineering Scaffolds through Fiber-Initiated Controlled Radical Polymerization, Adv. Funct. Mater. 25 (2015) 5748–5757. doi:10.1002/adfm.201501277.

[8] R. Izquierdo, N. Garcia-Giralt, M.T. Rodriguez, E. Cáceres, S.J. García, J.L. Gómez Ribelles, M. Monleón, J.C. Monllau, J. Suay, Biodegradable PCL scaffolds with an interconnected spherical pore network for tissue engineering, J. Biomed. Mater. Res. Part A. 85A (2008) 25–35. doi:10.1002/jbm.a.31396.

[9] T. Patrício, M. Domingos, A. Gloria, P. Bártolo, Characterisation of PCL and PCL/PLA Scaffolds for Tissue Engineering, Procedia CIRP. 5 (2013) 110–114. doi:10.1016/j.procir.2013.01.022.

[10] C.K.S. Pillai, C.P. Sharma, Review Paper: Absorbable Polymeric Surgical Sutures: Chemistry, Production, Properties, Biodegradability, and Performance, J. Biomater. Appl. 25 (2010) 291–366. doi:10.1177/0885328210384890.

[11] L. Xinming, C. Yingde, A.W. Lloyd, S. V. Mikhalovsky, S.R. Sandeman, C.A. Howel, L. Liewen, Polymeric hydrogels for novel contact lens-based ophthalmic drug delivery systems: A review, Contact Lens Anterior Eye. 31 (2008) 57–64. doi:10.1016/j.clae.2007.09.002.

[12] K.S. Walline, Drug Delivery Coatings for Cardiovascular Stents: Silicone Elastomer and Thrombin Responsive Hydrogel Coatings, (2004). http://citeseerx.ist.psu.edu/viewdoc/download?doi=10.1.1.484.1937&rep=rep1&type=pdf (accessed April 2, 2017).

[13] B. Yu, C. Wang, Y.M. Ju, L. West, J. Harmon, Y. Moussy, F. Moussy, Use of hydrogel coating to improve the performance of implanted glucose sensors, Biosens. Bioelectron. 23 (2008) 1278–1284. doi:10.1016/j.bios.2007.11.010.

[14] B. Butruk, M. Trzaskowski, T. Ciach, Fabrication of biocompatible hydrogel coatings for implantable medical devices using Fenton-type reaction, Mater. Sci. Eng. C. 32 (2012) 1601–1609. doi:10.1016/j.msec.2012.04.050.

[15] Poly(N-vinyl-2-pyrrolidone) hydrogel production by ultraviolet radiation: new methodologies to accelerate crosslinking, Polymer (Guildf). 45 (2004) 4705–4709.

[16] K. Yamashita, T. Funato, Y. Suzuki, S. Teramachi, Y. Doi, Characteristic Interactions between Poly(hydroxybutyrate) Depolymerase and Poly[(R)-3-hydroxybutyrate] Film Studied by a Quartz Crystal Microbalance, Macromol. Biosci. 3 (2003) 694–702. doi:10.1002/mabi.200300004.

[17] Y. Wang, S. Ge, M. Rafailovich, J. Sokolov, Y. Zou, H. Ade, J. Lu, A. Lustiger, G. Maron, Crystallization in the Thin and Ultrathin Films of Poly(ethylene-vinyl acetate) and Linear Low-Density Polyethylene, (2003). doi:10.1021/ma030456b.

[18] G. Bakan, S. Ayas, E. Ozgur, K. Celebi, A. Dana, Thermally Tunable Ultrasensitive Infrared Absorption Spectroscopy Platforms Based on Thin Phase-Change Films, ACS Sensors. (2016) acssensors.6b00591. doi:10.1021/acssensors.6b00591.

[19] G.S. Y Yeh, R. Hosemann, J. Loboda-C, Annealing effects of polymers and their underlying molecular mechanisms*, (n.d.). https://deepblue.lib.umich.edu/bitstream/handle/2027.42/21799/0000198.pdf?sequence=1 (accessed April 2, 2017).

[20] S.M. Louie, J.M. Gorham, E.A. McGivney, J. Liu, K.B. Gregory, V.A. Hackley, Photochemical transformations of thiolated polyethylene glycol coatings on gold nanoparticles, Environ. Sci. Nano. 3 (2016) 1090–1102. doi:10.1039/C6EN00141F.

[21] R. Auras, Poly(lactic acid) : synthesis, structures, properties, processing, and applications, Wiley, 2010.

[22] K.S. Soppimath, T.M. Aminabhavi, A.R. Kulkarni, Biodegradable polymeric nanoparticles as drug delivery devices, 70 (2001) 1–20.

[23] H. Tsuji, Y. Ikada, Properties and morphology of poly(L-lactide). II. hydrolysis in alkaline solution, J. Polym. Sci. Part A Polym. Chem. 36 (1998) 59–66. doi:10.1002/(SICI)1099-0518(19980115)36:1<59::AID-POLA9>3.0.CO;2-X.

[24] Q. Cai, G. Shi, J. Bei, S. Wang, Enzymatic degradation behavior and mechanism of poly(lactide-co-glycolide) foams by trypsin., Biomaterials. 24 (2003) 629–38. doi:10.1016/S0142-9612(02)00377-0.

[25] M. Rahmouni, F. Chouinard, F. Nekka, V. Lenaerts, J.C. Leroux, Enzymatic degradation of cross-linked high amylose starch tablets and its effect on in vitro release of sodium diclofenac, Eur. J. Pharm. Biopharm. 51 (2001) 191–198. doi:10.1016/S0939-6411(01)00127-8.

[26] S. Lyu, D. Untereker, Degradability of Polymers for Implantable Biomedical Devices, Int. J. Mol. Sci. Int. J. Mol. Sci. 10 (2009) 4033–4065. doi:10.3390/ijms10094033.

[27] L.C. Lopérgolo, A.B. Lugão, L.H. Catalani, Direct UV photocrosslinking of poly(N-vinyl-2-pyrrolidone) (PVP) to produce hydrogels, (n.d.). doi:10.1016/S0032-3861(03)00686-4.

[28] G.J.M. Fechine, J.A.G. Barros, L.H. Catalani, Poly(N-vinyl-2-pyrrolidone) hydrogel production by ultraviolet radiation: new methodologies to accelerate crosslinking, (n.d.). doi:10.1016/j.polymer.2004.05.006.

[29] P. Marizza, M. Abrami, S.S. Keller, P. Posocco, E. Laurini, K. Goswami, A.L. Skov, A. Boisen, D. Larobina, G. Grassi, M. Grassi, Synthesis and characterization of UV photocrosslinkable hydrogels with poly(N-vinyl-2-pyrrolidone): Determination of the network mesh size distribution, Int. J. Polym. Mater. Polym. Biomater. 65 (2016) 516–525. doi:10.1080/00914037.2015.1129964.

[30] N. Bhattarai, J. Gunn, M. Zhang, Chitosan-based hydrogels for controlled, localized drug delivery, Adv. Drug Deliv. Rev. 62 (2010) 83–99. doi:10.1016/j.addr.2009.07.019.

[31] P. Marizza, M. Abrami, S.S. Keller, P. Posocco, E. Laurini, K. Goswami, A.L. Skov, A. Boisen, D. Larobina, G. Grassi, M. Grassi, Synthesis and characterization of UV photocrosslinkable hydrogels with poly(N-vinyl-2-pyrrolidone): Determination of the network mesh size distribution, Int. J. Polym. Mater. Polym. Biomater. 65 (2016) 516–525. doi:10.1080/00914037.2015.1129964.

[32] R.K. Mishra, M. Datt, A.K. Banthia, Synthesis and characterization of pectin/PVP hydrogel membranes for drug delivery system., AAPS PharmSciTech. 9 (2008) 395–403. doi:10.1208/s12249-008-9048-6.

[33] N.A. Peppas, P. Bures, W. Leobandung, H. Ichikawa, Hydrogels in pharmaceutical formulations, Eur. J. Pharm. Biopharm. 50 (2000) 27–46. doi:10.1016/S0939-6411(00)00090-4.

[34] O. Chaudhuri, L. Gu, D. Klumpers, M. Darnell, S.A. Bencherif, J.C. Weaver, N. Huebsch, H. Lee, E. Lippens, G.N. Duda, D.J. Mooney, Hydrogels with tunable stress relaxation regulate stem cell fate and activity, Nat. Mater. 15 (2015) 326–334. doi:10.1038/nmat4489.

[35] I. Chae, M.F. Khan, J. Song, T. Kang, J. Lee, T. Thundat, Standoff Mechanical Resonance Spectroscopy Based on Infrared- Sensitive Hydrogel Microcantilevers, (n.d.). doi:10.1021/acs.analchem.6b02540.

[36] A. Mateescu, Y. Wang, J. Dostalek, U. Jonas, Thin hydrogel films for optical biosensor applications, Membranes (Basel). 2 (2012) 49–69. doi:10.3390/membranes2010040.

[37] H. Tsuji, A. Mizuno, Y. Ikada, Properties and morphology of poly(L-lactide). III. Effects of initial crystallinity on long-termin vitro hydrolysis of high molecular weight poly(L-lactide) film in phosphate-buffered solution, J. Appl. Polym. Sci. 77 (2000) 1452–1464. doi:10.1002/1097-4628(20000815)77:7<1452::AID-APP7>3.0.CO;2-S.

[38] A. Södergård, J.-F. Selin, J.H. Näsman, Hydrolytic degradation of peroxide modified poly(L-lactide), Polym. Degrad. Stab. 51 (1996) 351–359. doi:10.1016/0141-3910(95)00271-5.

[39] D. Cam, S.H. Hyon, Y. Ikada, Degradation of high molecular weight poly(L-lactide) in alkaline medium., Biomaterials. 16 (1995) 833–43. http://www.ncbi.nlm.nih.gov/pubmed/8527598 (accessed April 2, 2017).

[40] L. Xu, K. Crawford, C.B. Gorman, Effects of Temperature and pH on the Degradation of Poly (lactic acid) Brushes, Macromolecules. 44 (2011) 4777–4782.

[41] K. Yamashita, Y. Kikkawa, K. Kurokawa, Y. Doi, Enzymatic Degradation of Poly (L -lactide) Film by Proteinase K : Quartz Crystal Microbalance and Atomic Force Microscopy

Study, (2005) 850–857.

[42] L.T. Kearney, J.A. Howarter, QCM-Based Measurement of Chlorine-Induced Polymer Degradation Kinetics, (n.d.). doi:10.1021/la501922u.

[43] C. Sumner, S. Krause, A. Sabot, K. Turner, C.J. McNeil, Biosensor based on enzyme-catalysed degradation of thin polymer films, Biosens. Bioelectron. 16 (2001) 709–714. doi:10.1016/S0956-5663(01)00210-X.

[44] S. Bose, S.S. Keller, A. Boisen, K. Almdal, Microcantilever sensors for fast analysis of enzymatic degradation of poly (d, l-lactide), Polym. Degrad. Stab. 119 (2015) 1–8. doi:10.1016/j.polymdegradstab.2015.04.021.

[45] S. Bose, Micromechanical resonators as a tool for polymer characterization, (2014).

[46] G. Reiter, S. Napolitano, Possible origin of thickness-dependent deviations from bulk properties of thin polymer films, J. Polym. Sci. Part B Polym. Phys. 48 (2010) 2544–2547. doi:10.1002/polb.22134.

[47] † Jae Hyun Kim, *,† and Jyongsik Jang, ‡ Wang-Cheol Zin*, Thickness Dependence of the Glass Transition Temperature in Thin Polymer Films, (2001). doi:10.1021/LA001125K.

[48] A.I. Fedorchenko, A.-B. Wang, H.H. Cheng, Thickness dependence of nanofilm elastic modulus, Appl. Phys. Lett. 94 (2009) 152111. doi:10.1063/1.3120763.

[49] R.M. Michell, I. Blaszczyk-Lezak, C. Mijangos, A.J. Müller, Confinement effects on polymer crystallization: From droplets to alumina nanopores, (2013). doi:10.1016/j.polymer.2013.05.029.

[50] J.W. Ndieyira, N. Kappeler, S. Logan, M.A. Cooper, C. Abell, R.A. McKendry, G. Aeppli, Surface-stress sensors for rapid and ultrasensitive detection of active free drugs in human serum, Nat. Nanotechnol. 9 (2014) 225–232. doi:10.1038/nnano.2014.33.

[51] S.B. Patil, M. Vögtli, B. Webb, G. Mazza, M. Pinzani, Y.-A. Soh, R.A. McKendry, J.W. Ndieyira, Decoupling competing surface binding kinetics and reconfiguration of receptor footprint for ultrasensitive stress assays, Nat. Nanotechnol. 10 (2015) 899–907. doi:10.1038/nnano.2015.174.

[52] A.O.N. T. Larsen,a S. Schmid, L. Grönberg, Ultrasensitive string-based temperature sensors, Appl. Phys. Lett. 98 (2011).

[53] S. Schmid, S. Dohn, A. Boisen, Real-Time Particle Mass Spectrometry Based on Resonant Micro Strings, Sensors. 10 (2010) 8092–8100. doi:10.3390/s100908092.

[54] M. del Rey, R. a. da Silva, D. Meneses, D.F.S. Petri, J. Tamayo, M. Calleja, P.M. Kosaka, Monitoring swelling and deswelling of thin polymer films by microcantilever sensors, Sensors Actuators B Chem. 204 (2014) 602–610. doi:10.1016/j.snb.2014.08.021.

[55] S. Bose, S.S. Keller, T.S. Alstrøm, A. Boisen, K. Almdal, Process optimization of ultrasonic spray coating of polymer films., Langmuir. 29 (2013) 6911–9. doi:10.1021/la4010246.

[56] S. Bose, S. Schmid, T. Larsen, S. Sylvest Keller, A. Boisen, K. Almdal, Micromechanical fast quasi-static detection of α and β relaxations with nanograms of polymer, J. Polym. Sci. Part B Polym. Phys. 53 (2015) 1035–1039. doi:10.1002/polb.23745.

[57] S. Bose, S. Schmid, T. Larsen, S.S. Keller, P. Sommer-Larsen, A. Boisen, K. Almdal, Micromechanical string resonators: Analytical tool for thermal characterization of polymers,

ACS Macro Lett. 3 (2014) 55–58. doi:10.1021/mz400470n.

[58] S.S. Keller, L. Gammelgaard, M.P. Jensen, S. Schmid, Z.J. Davis, a. Boisen, Micromechanical sensors for the measurement of biopolymer degradation, Proc. IEEE Int. Conf. Micro Electro Mech. Syst. (2011) 457–460. doi:10.1109/MEMSYS.2011.5734460.

[59] P.C. Blainey, P.J. Reid, FTIR studies of intermolecular hydrogen bonding in halogenated ethanols, Spectrochim. Acta Part A. 57 (2001) 2763–2774. www.elsevier.com/locate/saa (accessed June 30, 2016).

[60] M.A. Ramin, G. Le Bourdon, N. Daugey, B. Bennetau, L. Vellutini, T. Buffeteau, PM-IRRAS Investigation of Self-Assembled Monolayers Grafted onto SiO_2 /Au Substrates, Langmuir. 27 (2011) 6076–6084. doi:10.1021/la2006293.

[61] R. Mendelsohn, G. Mao, C.R. Flach, Infrared reflection-absorption spectroscopy: principles and applications to lipid-protein interaction in Langmuir films., Biochim. Biophys. Acta. 1798 (2010) 788–800. doi:10.1016/j.bbamem.2009.11.024.

[62] Q. Liu, S. Xiao, Effects of spectral resolution and signal-to- noise ratio of hyperspectral sensors on retrieving atmospheric parameters, (2013). doi:10.1364/OL.39.000060.

[63] S. Bialkowski, Photothermal spectroscopy methods for chemical analysis, Wiley, 1996.

[64] M. Yun, S. Kim, D. Lee, N. Jung, I. Chae, S. Jeon, T. Thundat, Photothermal cantilever deflection spectroscopy of a photosensitive polymer, Appl. Phys. Lett. 100 (2012) 204103. doi:10.1063/1.4719521.

[65] E. Finot, V. Rouger, L. Markey, R. Seigneuric, M.-H. Nadal, T. Thundat, Visible photothermal deflection spectroscopy using microcantilevers, Sensors Actuators B Chem. 169 (2012) 222–228. doi:10.1016/j.snb.2012.04.072.

[66] M.F. Khan, N. Miriyala, J. Lee, M. Hassanpourfard, A. Kumar, T. Thundat, Heat capacity measurements of sub-nanoliter volumes of liquids using bimaterial microchannel cantilevers, 108 (2016). http://dx.doi.org/10.1063/1.4952614 (accessed September 26, 2016).

[67] A. Wig, E.T. Arakawa, A. Passian, T.L. Ferrell, T. Thundat, Photothermal spectroscopy of Bacillus anthracis and Bacillus cereus with microcantilevers, Sensors Actuators B Chem. 114 (2006) 206–211. doi:10.1016/j.snb.2005.04.029.

[68] M.S. Ghoraishi, J.E. Hawk, A. Phani, M.F. Khan, T. Thundat, Clustering mechanism of ethanol- water mixtures investigated with photothermal microfluidic cantilever deflection spectroscopy, Nat. Publ. Gr. (2016). doi:10.1038/srep23966.

[69] N. Miriyala, M.F. Khan, T. Thundat, Thermomechanical behavior of a bimaterial microchannel cantilever subjected to periodic IR radiation, Sensors Actuators B Chem. 235 (2016) 273–279. doi:10.1016/j.snb.2016.05.043.

[70] J.R. Barnes, R.J. Stephenson, M.E. Welland, C. Gerber, J.K. Gimzewski, Photothermal spectroscopy with femtojoule sensitivity using a micromechanical device, Nature. 372 (1994) 79–81. doi:10.1038/372079a0.

[71] J.R. Barnes, R.J. Stephenson, C.N. Woodburn, S.J. O'Shea, M.E. Welland, T. Rayment, J.K. Gimzewski, C. Gerber, A femtojoule calorimeter using micromechanical sensors, Rev. Sci. Instrum. 65 (1994) 3793. doi:10.1063/1.1144509.

[72] T.S. Biswas, N. Miriyala, C. Doolin, X. Liu, T. Thundat, J.P. Davis, Femtogram-scale photothermal spectroscopy of explosive molecules on nanostrings., Anal. Chem. 86 (2014)

11368–72. doi:10.1021/ac503318e.

[73] A. Andersen, Alina Joukainen; Yamada, Shoko; Ek, Pramod Kumar; Andresen, Thomas Lars; Boisen, S. Schmid, Nanomechanical IR spectroscopy for fast analysis of liquid-dispersed engineered nanomaterials, Sens. Actuators B. 233 (2016) 667–673.

[74] T. Larsen, S. Schmid, L.G. Villanueva, A. Boisen, Photothermal analysis of individual nanoparticulate samples using micromechanical resonators., ACS Nano. 7 (2013) 6188–93. doi:10.1021/nn402057f.

[75] M. Kurek, M. Carnoy, P.E. Larsen, L.H. Nielsen, O. Hansen, T. Rades, S. Schmid, A. Boisen, Nanomechanical Infrared Spectroscopy with Vibrating Filters for Pharmaceutical Analysis, Angew. Chemie Int. Ed. 56 (2017) 3901–3905. doi:10.1002/anie.201700052.

[76] S. Yamada, S. Schmid, T. Larsen, O. Hansen, A. Boisen, Photothermal Infrared Spectroscopy of Airborne Samples with Mechanical String Resonators, Anal. Chem. 85 (2013) 10531–10535. doi:10.1021/ac402585e.

[77] X.C. Zhang, E.B. Myers, J.E. Sader, M.L. Roukes, Nanomechanical Torsional Resonators for Frequency-Shift Infrared Thermal Sensing, Nano Lett. 13 (2013) 1528–1534. doi:10.1021/nl304687p.

[78] S. Schmid, K. Wu, P.E. Larsen, T. Rindzevicius, A. Boisen, Low-Power Photothermal Probing of Single Plasmonic Nanostructures with Nanomechanical String Resonators, Nano Lett. 14 (2014) 2318–2321. doi:10.1021/nl4046679.

[79] A. Talukdar, M. Faheem Khan, D. Lee, S. Kim, T. Thundat, G. Koley, Piezotransistive transduction of femtoscale displacement for photoacoustic spectroscopy, Nat. Commun. 6 (2015) 7885. doi:10.1038/ncomms8885.

[80] S. Shin, J.-K. Paik, N.-E. Lee, J.-S. Park, H.-D. Park, J. Lee, Gas Sensor Application of Piezoelectric Cantilever Nanobalance; Electrical Signal Read-Out, Ferroelectrics. 328 (2005) 59–65. doi:10.1080/00150190500311060.

[81] F.G. Bosco, E.-T. Hwu, C.-H. Chen, S. Keller, M. Bache, M.H. Jakobsen, I.-S. Hwang, A. Boisen, High throughput label-free platform for statistical bio-molecular sensing., Lab Chip. 11 (2011) 2411–6. doi:10.1039/c1lc20116f.

[82] A. Mostafazadeh, G.G. Yaralioglu, H. Urey, Optical fiber array based simultaneous parallel monitoring of resonant cantilever sensors in liquid, Sensors Actuators, A Phys. 242 (2016) 132–139. doi:10.1016/j.sna.2016.03.004.

[83] E.-T. Hwu, S.-K. Hung, C.-W. Yang, K.-Y. Huang, I.-S. Hwang, Real-time detection of linear and angular displacements with a modified DVD optical head, Nanotechnology. 19 (2008) 115501. doi:10.1088/0957-4484/19/11/115501.

[84] E.T. Hwu, S.K. Hung, C.W. Yang, I.S. Hwang, K.Y. Huang, Simultaneous detection of translational and angular displacements of micromachined elements, Appl. Phys. Lett. 91 (2007). doi:10.1063/1.2817750.

[85] M. Donolato, P. Antunes, T. Zardán, G. De, E. Hwu, C. Chen, R. Burger, G. Rizzi, F.G. Bosco, M. Strømme, A. Boisen, M.F. Hansen, Quantification of rolling circle amplified DNA using magnetic nanobeads and a Blu-ray optical pick-up unit, 67 (2015) 1–24. doi:10.1016/j.bios.2014.09.097.

[86] S. Schmid, L.G. Villanueva, M.L. Roukes, Quality Factor, in: Fundam. Nanomechanical Reson., Springer International Publishing, Cham, 2016: pp. 57–90. doi:10.1007/978-3-319-

28691-4_2.

[87] S. Schmid, K.D. Jensen, K.H. Nielsen, A. Boisen, Damping mechanisms in high- Q micro and nanomechanical string resonators, Phys. Rev. B. 84 (2011) 165307. doi:10.1103/PhysRevB.84.165307.

[88] S. Schmid, S. Dohn, A. Boisen, Real-Time Particle Mass Spectrometry Based on Resonant Micro Strings, Sensors. 10 (2010) 8092–8100. doi:10.3390/s100908092.

[89] Control Tutorials for MATLAB and Simulink - Introduction: System Modeling, (n.d.). http://ctms.engin.umich.edu/CTMS/index.php?example=Introduction&section=SystemModeling#2 (accessed March 16, 2017).

[90] † Y. T. Yang, ‡ C. Callegari, X. L. Feng, § and K. L. Ekinci, M.L. Roukes*, Zeptogram-Scale Nanomechanical Mass Sensing, (2006). doi:10.1021/NL052134M.

[91] S. Schmid, L.G. Villanueva, M.L. Roukes, Responsivity, in: Fundam. Nanomechanical Reson., Springer International Publishing, Cham, 2016: pp. 91–114. doi:10.1007/978-3-319-28691-4_3.

[92] a K. Naik, M.S. Hanay, W.K. Hiebert, X.L. Feng, M.L. Roukes, Towards single-molecule nanomechanical mass spectrometry., Nat. Nanotechnol. 4 (2009) 445–450. doi:10.1038/nnano.2009.152.

[93] M.S. Hanay, S. Kelber, a K. Naik, D. Chi, S. Hentz, E.C. Bullard, E. Colinet, L. Duraffourg, M.L. Roukes, Single-protein nanomechanical mass spectrometry in real time., Nat. Nanotechnol. 7 (2012) 602–8. doi:10.1038/nnano.2012.119.

[94] J.W.M. Chon, P. Mulvaney, J.E. Sader, Experimental validation of theoretical models for the frequency response of atomic force microscope cantilever beams immersed in fluids, J. Appl. Phys. 87 (2000) 3978. doi:10.1063/1.372455.

[95] J.E. Sader, Frequency response of cantilever beams immersed in viscous fluids with applications to the atomic force microscope, J. Appl. Phys. 84 (1998) 64. doi:10.1063/1.368002.

[96] C.P. Green, J.E. Sader, Frequency response of cantilever beams immersed in viscous fluids near a solid surface with applications to the atomic force microscope, J. Appl. Phys. 98 (2005) 114913. doi:10.1063/1.2136418.

[97] W.-H. Chu, Tech. Rep. No. 2, DTMB, Contract NObs-86396(X), Southwest Research Institute, San Antonio, Texas (1963)., (1963).

[98] M.K. Ghatkesar, V. Barwich, T. Braun, A.H. Bredekamp, U. Drechsler, M. Despont, H.P. Lang, M. Hegner, C. Gerber, Real-time mass sensing by nanomechanical resonators in fluid, Proc. IEEE Sensors, 2004. 3 (2004) 1060–1063. doi:10.1109/ICSENS.2004.1426357.

[99] F. Elmer, M. Dreier, Eigenfrequencies of a rectangular atomic force microscope cantilever in a medium Eigenfrequencies of a rectangular atomic force microscope cantilever in a medium, 7709 (1997). doi:10.1063/1.365379.

[100] M.K. Ghatkesar, T. Braun, V. Barwich, J.P. Ramseyer, C. Gerber, M. Hegner, H.P. Lang, Resonating modes of vibrating microcantilevers in liquid, Appl. Phys. Lett. 92 (2008) 3–5. doi:10.1063/1.2838295.

[101] M.J. Hancock, Solutions to Problems for 2D & 3D Heat and Wave Equations 18.303 Linear Partial Differential Equations, (n.d.). https://ocw.mit.edu/courses/mathematics/18-

303-linear-partial-differential-equations-fall-2006/assignments/probpde3dsolns.pdf (accessed March 29, 2017).

[102] X. Zhang, C.P. Grigoropoulos, Thermal conductivity and diffusivity of free-standing silicon nitride thin films, Rev. Sci. Instrum. 66 (1995) 1115–1120. doi:10.1063/1.1145989.

[103] X. Xie, D. Li, T.-H. Tsai, J. Liu, P. V Braun, D.G. Cahill, Thermal Conductivity, Heat Capacity, and Elastic Constants of Water- Soluble Polymers and Polymer Blends, (n.d.). doi:10.1021/acs.macromol.5b02477.

[104] AccuMist Precision Ultrasonic Nozzle Spray Shaping Technology, (n.d.). http://www.sono-tek.com/accumist/ (accessed March 20, 2017).

[105] S.A. Kandjani, S. Mirershadi, A. Nikniaz, Inorganic–Organic Perovskite Solar Cells, in: Sol. Cells - New Approaches Rev., InTech, 2015. doi:10.5772/58970.

[106] D.B. Hall, P. Underhill, &john M. Torkelson~, Spin Coating of Thin and Ultrathin Polymer Films, (n.d.). http://homepages.rpi.edu/home/40/underp3/public_html/Pubs/Underhill_PolyEngSci_1998.pdf (accessed March 20, 2017).

[107] D.-H. Lee, N.-G. Cho, Assessment of surface profile data acquired by a stylus profilometer, Meas. Sci. Technol. 23 (2012) 105601. doi:10.1088/0957-0233/23/10/105601.

[108] Spectroscopic Ellipsometry Characterization of Thin Films Used in the Food Packaging Industry | American Laboratory, (n.d.). http://www.americanlaboratory.com/914-Application-Notes/138874-Spectroscopic-Ellipsometry-Characterization-of-Thin-Films-Used-in-the-Food-Packaging-Industry/ (accessed March 23, 2017).

[109] Y.-C. Liu, K.-C. Fan, C.-L. Chu, C.A. Werner, G. Jäger, Development of an optical accelerometer for low-frequency vibration using the voice coil on a DVD pickup head, Meas. Sci. Technol. 19 (2008) 84012. doi:10.1088/0957-0233/19/8/084012.

[110] J. Faist, F. Capasso, D.L. Sivco, C. Sirtori, A.L. Hutchinson, A.Y. Cho, Quantum Cascade Laser, Science (80-.). 264 (1994) 553–556. doi:10.1126/science.264.5158.553.

[111] Z. Instruments, Principles of lock-in detection and the state of the art, (n.d.). http://www.zhinst.com/sites/default/files/li_primer/zi_whitepaper_principles_of_lock-in_detection.pdf (accessed March 8, 2017).

[112] N. Jung, H. Seo, D. Lee, C.Y. Ryu, S. Jeon, Nanomechanical Thermal Analysis of the Glass Transition of Polystyrene Using Silicon Cantilevers, Macromolecules. 41 (2008) 6873–6875. doi:10.1021/ma801539m.

[113] M.K. Mundra, C.J. Ellison, R.E. Behling, J.M. Torkelson, Confinement, composition, and spin-coating effects on the glass transition and stress relaxation of thin films of polystyrene and styrene-containing random copolymers: Sensing by intrinsic fluorescence, Polymer (Guildf). 47 (2006) 7747–7759. doi:10.1016/j.polymer.2006.08.064.

[114] S. Schmid, L.G. Villanueva, M.L. Roukes, Fundamentals of Nanomechanical Resonators, Springer International Publishing, Cham, 2016. doi:10.1007/978-3-319-28691-4.

[115] C. Buzea, I.I. Pacheco, K. Robbie, Nanomaterials and nanoparticles: Sources and toxicity, Biointerphases. 2 (2007) MR17. doi:10.1116/1.2815690.

[116] A. Cagliani, High frequency bulk resonators for bio/chemical diagnostics and monitoring applications, 2012. http://orbit.dtu.dk/ws/files/51130208/AlbertoCaglianiPHDthesis..PDF

(accessed April 7, 2017).

Paper 1

Blu-Ray-based micromechanical characterization platform for biopolymer degradation assessment

Sensors and Actuators B 241 (2017) 1303–1309

Contents lists available at ScienceDirect

Sensors and Actuators B: Chemical

journal homepage: www.elsevier.com/locate/snb

Blu-Ray-based micromechanical characterization platform for biopolymer degradation assessment

Andrea Casci Ceccacci[a,*], Ching-Hsiu Chen[b], En-Te Hwu[b], Lidia Morelli[a], Sanjukta Bose[a], Filippo Giacomo Bosco[a], Silvan Schmid[c], Anja Boisen[a]

[a] Department of Micro- and Nanotechnology, Technical University of Denmark, DTU Nanotech, Building 345 East, DK-2800 Kgs. Lyngby, Denmark
[b] Institute of Physics, Academia Sinica, Nangang, Taipei 11529, Taiwan
[c] Institute of Sensor and Actuator Systems, TU Wien, Gusshausstraße 27-29, A-1040 Vienna, Austria

ARTICLE INFO

Article history:
Received 21 June 2016
Received in revised form
27 September 2016
Accepted 30 September 2016
Available online 1 October 2016

Keywords:
Biopolymer degradation
Sensing system
Micromechanical resonator
Blu-Ray
Instrumentation
High throughput sensing system

ABSTRACT

Degradable biopolymers are used as carrier materials in drug delivery devices. A complete understanding of their degradation behaviour is thus crucial in the design of new delivery systems. Here we combine a reliable method, based on spray coated micromechanical resonators and a disposable microfluidic chip, to characterize biopolymer degradation under the action of enzymes in controlled flow condition. The sensing platform is based on the mechanics and optics from a Blu-Ray player, which automatically localize individual sensors within the array, and sequentially measure and record the resonance frequency of up to twelve resonators within 4 min. Such fast and automated measuring technology, combined with the use of thin polymers layers in the degradation experiments, allows to reduce the experimental time needed for degradation studies from 6 weeks to 8 h. We first present a full characterization of sensor properties and then perform degradation studies of poly(lactic-co-glycolic acid) (PLGA) in steady flow for three different enzyme concentrations. The degradation has been performed in liquid environment. Before each resonator measurement, the measuring chamber has been automatically dried, since the resonator characteristics are much approved when measuring in air compared to liquid. The obtained degradation profiles are comparable to profiles obtained by conventional approaches, which have shown to require up to 6 weeks of experimental time frame.

1. Introduction

The biopolymer PLGA, poly(lactic-co-glycolic acid) plays a crucial role in biomedical research. PLGA has been FDA approved and is being used in a wide range of biomedical applications such as: grafts, sutures, micro and nanoparticles, and scaffold material for tissue engineering applications [1]. PLGA has also been used in commercially available drug delivery devices for treating prostate cancer (Lupron Depot®) and type-2 diabetes (Byclureon®) [1]. Monitoring mechanical and degradation properties of the biopolymer matrix is crucial in the development of drug delivery devices. PLGA undergoes degradation by a hydrolysis where water attacks the ester bonds present in the PLGA backbone, a reaction which is catalysed in the presence of acid, alkali, salt and specific enzymes [2]. Conventional degradation studies [3] have required large amount of material, which results in expensive and time consuming degradation experiments (days to weeks [3]) limiting experimental throughput and thereby also the statistical significance of the obtained results. These studies are often performed at high temperature or high/low value of pH [4], in order to accelerate the experimental time frame. Such methods do not comply with demand of high throughput and with the often limited availability of material in the formulation phase. Polymer degradation studies on sub-micrometer thick polymer layers have been performed using QCM [5] and SPR [6]. Although the QCM approach has allowed a time effective analysis, it has shown some limitations: *i)* measurements are limited to the thin film regime [5,7,8], *ii*) thin film properties often differs from the bulk properties [9] and *iii)* measurements are to be performed onto high homogeneous layer [10]. Micromechanical resonators have already shown their potential as sensors for temperature [11], biomarker detection [12] and material characterization [13–16]. Recently, studies on the behaviour of micrometer-sized thin film biopolymers have been performed [17–19] through the monitoring of the resonance frequency of spray-coated micromechanical cantilevers. The studies demonstrate that micromechanical resonators can characterize polymer

* Corresponding author.
E-mail address: ancace@nanotech.dtu.dk (A.C. Ceccacci).

http://dx.doi.org/10.1016/j.snb.2016.09.190
0925-4005/

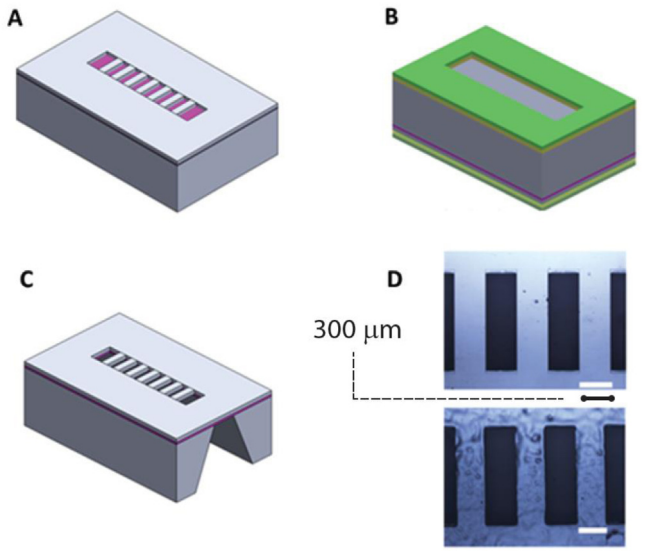

Fig. 1. Schematic view of the fabrication process flow. A deep reactive ion etching has been used for patterning of the device layer; B SiO_2 and SiN are grown and deposited, respectively, to form a protective layer for the anisotropic etch. They also act as mask on the backside of the wafer, which has been defined by photolithography and subsequent reactive ion etching; C Anisotropic etching has been done with KOH, which defines the clamping point of the structures. Then, the silicon nitride and the silicon dioxide were removed with phosphoric acid wet etching; D Optical microscope images of the structures before and after the PLGA coating.

films with thicknesses of even several microns and with different surface morphologies. However, so far the reported measurements have been performed in a tedious manner, where polymer coated cantilevers have been taken out of a degradation media (no flow possible), dried and then characterized at given time intervals in a bulky and expensive laser Doppler vibrometer set-up. With such system, measurements and related degradation studies could not be run under flow conditions. Also, the polymer coating introduces experimental challenges since this often causes the cantilevers to bend out of plane, which complicates/impedes read-out.

In this study, we wish to improve and optimize micromechanical resonator measurements for polymer degradation. This includes the development of an automated liquid handling/read-out system and the use of double clamped microcantilevers, henceforth called microbridges (Fig. 1), since these will not bend out of plane when coated with polymers. For degradation studies, the microbridges will be embedded inside a microfluidic chip, where physiological conditions can be replicated and where degradation in flow can be studied. However, tailoring an integrated readout for resonance frequency measurements is complex and expensive. Optical readout systems like interferometers are usually bulky and expensive, and they require complex and tedious optical alignment processes. Optical units (OPU) from DVD or Blu-Ray(BR) player represents a low-cost, very flexible, and highly- sensitive [20] alternative, which can be easily embedded in portable and automated system for multiple optical readout purposes [21].

Hence, in order to match the need of a method which can overcome the limitation of the conventional biopolymer degradation studies, and the technological challenges of an integrated readout, we have designed and fabricated a system based on a Blu-Ray pickup head which uses an astigmatic detection technique [20]. The system can automatically scan the position of individual microbridges, arranged in a linear array, and control their actuation through a piezoelectric crystal. The recording of vibrational spectra is also performed automatically by the controlling system software.

Arrays of microbridges have been spray coated [17,22] with a thin (1–2 μm) layer of PLGA by an ultrasonic spray coater system. The deposited biopolymer thin film, with a total mass in the sub microgram range, resulted in a drop of the mechanical resonance frequency. Next, the coated microbridges were placed in a microfluidic chip where a steady flow of degradation media was controlled via a syringe pump.

Experiments have been performed using a so-called 'wet and dry' approach (W & D). In this technique, the degradation has been performed under steady flow condition of degradation media. Prior to resonance frequency measurements, the chamber has been emptied and dried and as a result the measurements were obtained in air (Fig. 2D–E). In air environment, a higher value of the quality factor (Q) and a higher signal to noise ratio (SNR) ensure a reliable monitoring of resonance frequency shifts. The method facilitates degradation in flow and measurements can be obtained at desired time intervals.

2. Materials and methods

2.1. Fabrication of microbridges

Microbridges have been fabricated with a standard photolithography technique using a two mask process, on 4" silicon-on-insulator (SOI) substrate. The device layer had a thickness of 5 μm, which defined the thickness of the microbridges. A positive photolithography (1.5 μm AZ-Mir701) step was performed to pattern the device layer and then deep reactive ion etching (DRIE) was used to transfer the photoresist design on the front side to the silicon device layer (Fig. 1A). The buried layer of SiO_2 acts as a stop layer during etching. A subsequent layer of SiO_2 (200 nm) and SiN (200 nm) was grown (Wet Oxidation) and deposited (LPCVD) respectively.

A second lithography step has been performed on the backside of the wafer to release and define the clamping points of the microbridges. Windows were opened in the SiN/SiO_2 mask layer using reactive ion etching (Fig. 1B). Subsequently, the wafers were etched in KOH (80 °C 4 h: 30 min), and the etch stopped on the buried silicon oxide layer (Fig. 1C). Finally, SiN has been etched away by H_3P0_4 at 180 °C and the SiO_2 was removed by BHF. An example of realized microbridges (blank and polymer coated) is showed in Fig. 1D.

2.2. Microfluidic platform fabrication

The microfluidic platform has been composed of 3 plates of PMMA bonded together with pressure adhesive tape (Fig. 2A). The channel is 500−μm wide, 10.5 mm long and 150 μm deep, the chamber in the middle plate defined through laser cutting had total volume of 193 μl. The microbridges have been fixed in the channel using fluidic connectors that are glued to the platform using PDMS and a Luer-Lock connector has been used to connect to the outlet of a syringe pump. The outlet has been connected to a waste chamber. A vacuum pump has been used to create a negative pressure in order to empty the chamber.

2.3. Polymer coating and degradation studies

Exacta Spray Coater (Sonotek, USA) has been used to coat the microbridges [16,17,22]. The parameters for spray coating microbridges have been optimized using the methodology [22] and the parameters found in our previous works [17].

The ultrasonic spray nozzle was actuated at a frequency of 120 kHz with a generator power of 1.3 W. Compressed nitrogen flow was maintained at 0.06 bar for focusing the flow of the sprayed solution to the substrate. The infusion rate of PLGA solution (0.5% wt. in dichloromethane) was set at 0.05 ml/min. The microbridges to spray nozzle distance was kept constant at 15 mm. The microbridge arrays are composed of 12 bridges, of which 4

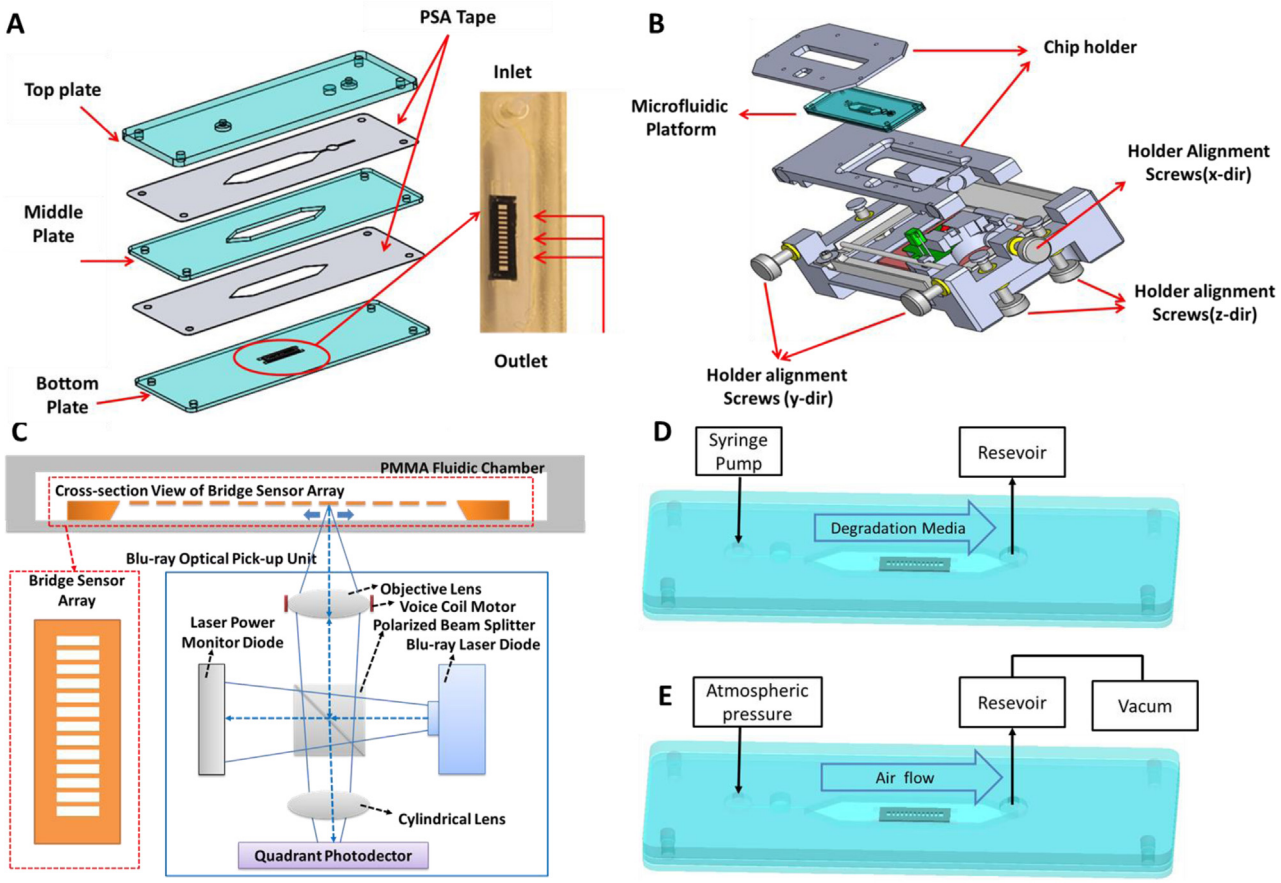

Fig. 2. A: Exploded view of the single-use microfluidc chip and the encapsulation of the resonator. B: Design of the system. The microfluidic plaform is placed inside a chip holder, which can be moved along the three planes thanks to three alignment screws. C: Blu-Ray OPU building blocks. The OPU can move along the microbridges array according to the algorithm explained in the SI.D-E Wet and Dry Approach. D: A syringe pump is connected to the inlet of the chamber and then the degradation media flows inside the camber and ends in the waste reservoir. E: The degradation media flow is stopped and the inlet is unplugged from the syringe pump and left at atmospheric pressure. A negative pressure is generated in the waste reservoir using a vacuum pump, and the measuring chamber is first emptied and then dried with air.

are left uncoated and used as references, see Fig. 1D. Hundreds of nanograms of polymer have been sprayed as it was shown in the results section. PLGA undergoes hydrolytic degradation catalysed by the presence of an enzyme [2]. Here we test the effect of the enzymatic reaction of Proteinase-K in three different concentrations (20–50–100 μg/ml in Tris-HCl buffer solution pH 8.6 at 23 °C) in steady flow. We have further compared these results with the degradation inducted by only water under same flow conditions. The microfluidic chamber was first filled with the degradation media at a flow rate of 200 μl/min. When the system has been completely filled, the flow was reduced to 20 μl/min. The microfluidic platform has been mounted inside a chip holder (Fig. 2A), and it has been kept tight and clamped by four screws. The chip holder has been placed into a custom-built PMMA box where the temperature has been maintained at 37 °C using a heat control system (AirTherm ATX, with 0.1 °C precision) to simulate at best the human physiological condition. The degradation media was degassed for one hour in a vacuum chamber prior to the beginning of the experiment, in order to avoid bubble formation inside the microfluidic chamber.

2.4. Detection method and system layout

Astigmatic detection system (ADS) has previously been used to monitor deflection and resonance frequency changes of microcantilevers [20,21]. A Blu-Ray (BR) laser diode emits light with a wavelength of 405 nm, focused onto the surface of the microbridges using an internal mirror, collimator and a modified objective lens with high numerical aperture (NA = 0.6), which guarantees a focalized beam and a ~350 nm size laser spot (Fig. 2C).

The reflected laser light from the sample surface (i.e. the microbridges) passes through a polarized beam splitter, a set of cylindrical lenses, and impinges on a quadrant photodetector integrated chip (PDIC). The PDIC consists of four single sensors with individual current preamplifiers, which converts photon signal to voltage signal with a bandwidth of 160 MHz. Here, a laser power monitor diode is used to monitor laser power. A voice coil motor (VCM) has been used to control the position of the objective lens in order to focus the light at a desired location.

Fig. 2B illustrates the system. It is composed of two blocks: the chip holder and a frame where a BR-OPU can move along one direction thanks to a sled motor. Blu-Ray optical pick-up head unit (BR-OPU) is equipped with a VCM that gives a 1 μm vertical motion allowing fine adjustment of the focal distance to get the highest possible sensitivity from the ADS. The chip holder is placed on three alignment screws used to do coarse adjustment of the focal distance. The position of the holder can be adjusted in three planes (x–y, x–z and y–z). The working algorithm is shown in the Supplementary information (SI).

Resonance frequencies were measured in air. Microbridges were actuated by means of a piezoelectric crystal, which was set to linearly sweep a range of frequencies in the vicinity of the theoretically predicted resonance frequency. The values of the resonance frequencies and Q factors were obtained from a Lorentzian fitting performed on the recorded spectra.

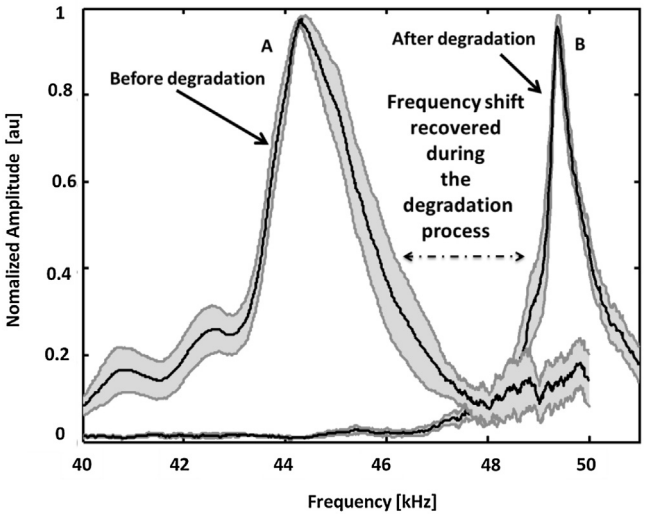

Fig. 3. Frequency shift experienced during biopolymer degradation. A: Resonance peak of a loaded bridge before the degradation process. B: resonance peak of a blank bridge after the degradation process. The shades represent the standard error of the mean n = 5.

3. Results and discussion

3.1. Sensor characterization

The sensing properties of micromechanical resonators have been characterized in air environment. Mass responsivity of microbridges have been evaluated according to Eq. (1). The minimum detectable mass value (Eq. (2)) was calculated considering the deviation of the resonance frequency of multiple measurements on the same microbridge, which has been no greater than 40 Hz. Bridges from the same fabrication batch can differ in the value of the resonance frequency up to 2 KHz. However such uncertainty has not affected our scope, since measurements of polymer degradation have been referenced to the same bridge. The formulae used to evaluate the relative frequency shift have been reported in Supplementary information.

$$R = f_0 / 2m_0 \quad (1)$$

The minimum detectable mass has been then evaluated considering the product of the mass responsivity and two times the standard deviation.

$$\Delta m \approx (2\Delta f) R^{-1} \approx 10ng \quad (2)$$

Where Δf is the standard deviation of 20 consecutive measurements on the same bridge (data not shown). Considering the rectangular area on the microbridges where the biopolymer has been deposited, the thickness of the layer can also be calculated. The measured mass of material ranges between 0.45 μg and 0.75 μg, and the corresponding thickness ranges between 1.2 μm and 2 μm. The deposition of PLGA leads primarily to a drop in the resonance frequency, as a change in stiffness can be neglected. In fact, Young's modulus of PLGA is 2 GPa [23] and Young's modulus of silicon is 170 GPa. Thus, the flexural rigidity (EI) of the silicon microbridges ($0.5\ nNm^2$) is four orders of magnitude times bigger than the flexural rigidity of the polymer film ($50\ fNm^2$). Furthermore, it is known that Young's modulus of biopolymers decreases during degradation. In light of this, the observed changes in resonance frequency can be attributed to mass changing phenomena. A typical frequency drop induced by the added polymer layer is shown in Fig. 3.

3.2. Polymer degradation studies

This work is, to the best of our knowledge, the first investigation of degradation of PLGA under the catalytic action of Proteinase-K (recombinant, PCR grade obtained from Roche Diagnosis GmbH). Coated microbridges have been employed to study the behaviour of PLGA during degradation inducted by the enzyme Proteinase-K in 3 different concentrations. Furthermore, we have studied the degradation induced by only water under the same flow condition, as the polymer can undergo hydrolysis and, at the same time, the shear stress due to the flow might induce some mass removal from the biopolymer layer.

The deposition of a layer of PLGA has led to a drop in the resonance frequency that ranges between 8% and 12%, depending on the microbridge characterized. This large observed deviation is likely due to the non-uniformity of the coating from chip to chip, and, to a minor extends, to geometrical variations of the bridges after the cleanroom microfabrication.

Fig. 4 shows the results of a degradation experiment performed with the W & D approach. The temperature fluctuation has been monitored through the evaluation of the relative frequency shift of uncoated bridges. Temperature was seen to be constant within the experimental time frame.

To monitor degradation, the resonance frequency has been measured at regular intervals of time according to the degradation rate expected for a certain enzyme concentration. Three different concentrations have been tested, with a steady flow of 20 μl/min.

Enzyme concentrations of 50 and 100 μg/ml have not led to any remarkable differences in the degradation profile. However, a lower enzyme concentration of 20 μg/ml has led to longer degradation time. The hydrophilicity of PLGA, due to the presence of the glycolic unit, triggers the degradation process in the early phase (already in the first hour of experiment), which has been not observed for Poly (D,L- lactide) (PDLLA) [17].

We have previously shown that Tris-HCl does not trigger any kind of degradation of PDLLA[17]. Here we have studied the effect of Tris-HCl on PLGA (Fig. 4D) within 36 h and saw that degradation started after 18 h. The complete degradation profile of the polymer is shown in the Supplementary information. Furthermore, we have monitored the frequency shift of coated microbridges which have been exposed to a water flow of 20 μl/min. There is almost no change in the resonance frequency of the coated chips within the 12 h (Fig. 4D) of experimental time frame apart from some fluctuations which are well inside the uncertainty of the measurement. We can thus assert that during the experimental time frame the flow has not influenced the removal of PLGA from the bridge surface. This results has also been confirmed through optical microscope imaging, Fig. 5C.

The relative frequency shift profiles have shown similarities to the weight loss profile previously shown on bulky amount of PLGA under the action of trypsin [3]. Fig. 5A shows how the polymer has been removed during the degradation process. Mass sensivity of micromechanical resonator has a spatial dependence, thus real time estimation of the actual amount of material which is loading the microbridges at a certain time step requires complex techniques [24]. Although both trypsin [3] and Proteinase-K are serine protease, a direct comparison of their degradation rate might lead to an inappropriate conclusion. However, we can see that we are able to perform similar type of experiments to explore degradation mechanisms in just a few hours (see Fig. 6B). Furthermore, we want to emphasize that due to the ability of our system to perform simultaneous measurements we are able to investigate a large number of samples, improving the statistics and facilitating simultaneous studies on different materials.

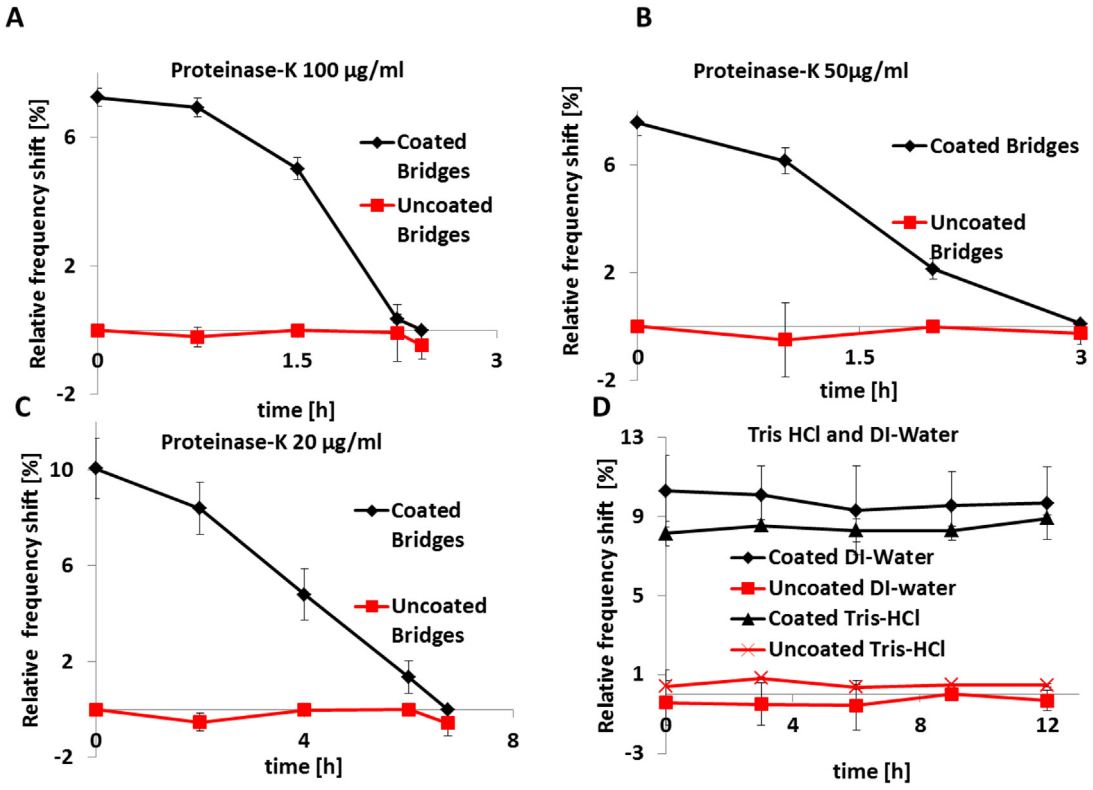

Fig. 4. Degradation profile obtained from different proteinase concentration of A: 100 µg/ml; B: 50 µg/ml; C: 20 µg/ml. D: Relative frequency shift measured when the degradation media is substituted by water and Tris-HCl. Red curves shown the relative frequency shift on the uncoated bridges used as reference. (For interpretation of the references to colour in this figure legend, the reader is referred to the web version of this article.)

3.3. Degradation rate

The mean degradation rate for each enzyme concentration has been derived considering the initial mass deposited on the microbridges and the time needed to reach the 0% in the relative frequency shift curves. Proteinase-K does not possess a specific site to recognize the polyester [5]. The concentration of enzyme reaches the saturation level between 50 µg/ml and 100 µg/ml [5]. When the saturation level is reached, higher concentrations do not lead to any faster degradation as the substrate is completely covered by the enzyme.

The degradation rates per unit area are in the same order of magnitude of the 25 µg/cm^{2}h reported in literature [3], where the degradation of thick films (200 µm) of PLGA has been studied under the action of trypsin (degradation rate of 67 µg/cm^{2}h). This conclusion is obtained by evaluating the amount of material they have analysed and considering the time needed for reaching the 0% in our weight loss curve. In Fig. 6 we have compared the degradation rate observed in our work with the degradation rate obtained by [5] who studied the degradation rate of PDLLA under the action of Proteinase-K. Besides a difference of two orders of magnitude due to the faster degradation of PLGA because of its hydrophilicity, we may notice that the degradation rate it has seemed to reach a plateau around 100 µg/ml.

4. Conclusion

We have developed and tested an automatic platform aimed to characterize the dynamic characteristics of microbridges and their employment as sensors for monitoring biopolymer degradation. The integration of a microfluidic platform allowed characterizing PLGA degradation under steady flow conditions in a Proteinase-K degradation buffer. The simple experimental setup, combined with high level of automation, reduces the time needed to statistically characterize biopolymer degradation. By increasing the parallelization of the microfluidic device, it could be possible to study different degradation conditions simultaneously. The fabricated microbridges have allowed us to study degradation in the sub microgram regime. Although, real time monitoring is not actually possible, as in viscous environments the mass responsivity drops beyond the intrinsic noise level of the readout system, the degradation can be easily studied by employing the W & D method that allows a good time resolution of the investigated phenomena. The combination of the microfluidic setup with the automatic readout platform facilitates an effective evaluation of biopolymer degradation of micrometer-thick biopolymer film by employing micromechanical resonators. Furthermore, the implementation of the microfluidic device has allowed us to simulate a more physiologically realistic condition for polymer degradation. The degradation parameters as well as the degradation profile derived from our approach matches previous study performed over 6 weeks on bulk amount of material. The degradation profile, as well as the degradation rate show similarities with similar works previously done by other groups using bulk amount of material and conventional methods. A full comparison is difficult since the other studies differ in either enzyme or polymer.

Acknowledgments

The authors would like to acknowledge machine shop in Institute of Physics, Academia Sinica, Taiwan for precision machining. The research leading to these results has received funding from the European Research Council under the European Union's Seventh Framework Programme (FP7/2007–2013)/ERC grant agreement no [320535]. This research is further supported by the Villum Foundation Young Investigator Program (Project No. VKR023125). The

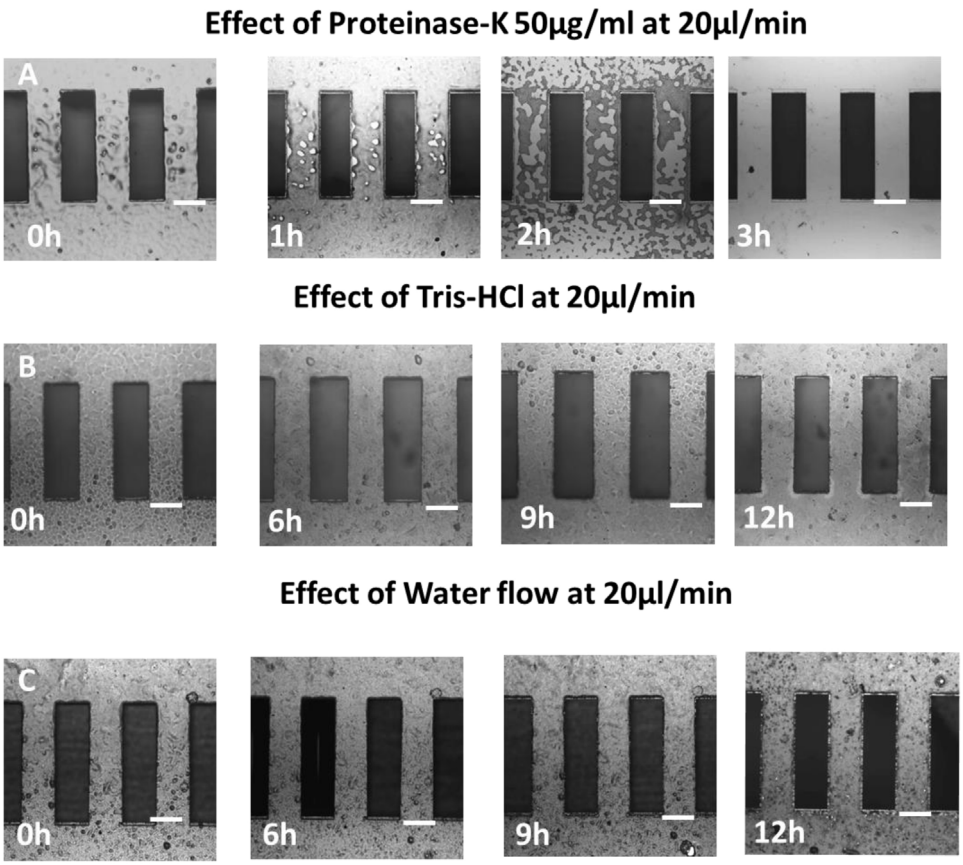

Fig. 5. Optical microscope images of coated microbridges which have undergone to degradation experiments. A Bridges exposed to 50 µg/ml. After 3 h the polymer was completely removed from the surface of the resonator, the few spot are clearly far beyond the detection limit of the resonator. B Bridges exposed at a flow of Tris-HCl at 37 °C at 2 µl/min.C Bridges exposed at a flow of DI water at 20 µl/min. White scale bar 300 µm.

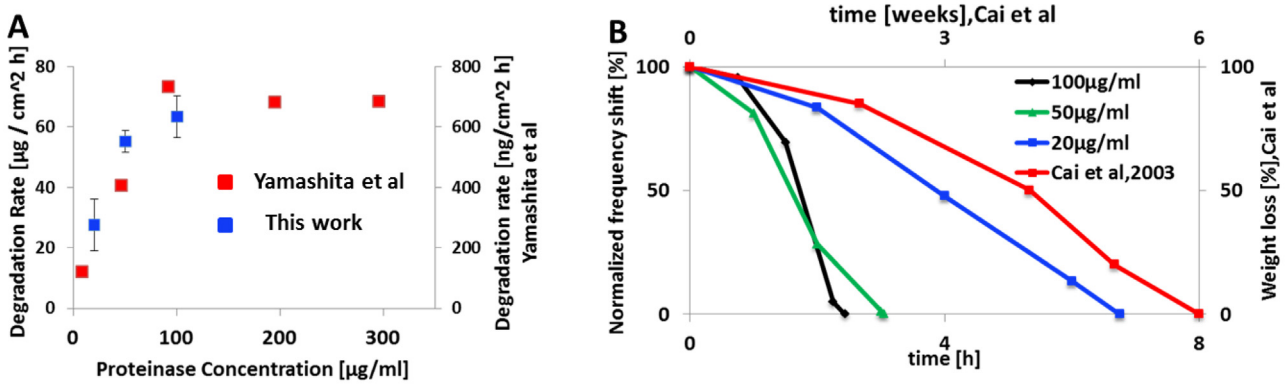

Fig. 6. A Degradation rate dependence from the proteinase concentration. The profile seems to resemble the profile shown from Yamashita et al. B Normalized frequency shift (error bar omitted) and comparison with weight loss curve from Cai et al.

research is funded by the Danish National Research Foundation (DNRF122) and Villum Fonden (Grant No. 9301)

Appendix A. Supplementary data

Supplementary data associated with this article can be found, in the online version, at http://dx.doi.org/10.1016/j.snb.2016.09.190.

References

[1] J.-M. Lu, X. Wang, C. Marin-Muller, H. Wang, P.H. Lin, Q. Yao, C. Chen, Current advances in researcn and clinical applications of PLGA-based nanotechnology, Expert Rev. Mol. Daign. 9 (2009) 325–341, http://dx.doi.org/10.1586/erm.09.15, Current.

[2] H.K. Makadia, S.J. Siegel, Poly Lactic-co-Glycolic Acid (PLGA) as biodegradable controlled drug delivery carrier, Polymers (Basel) 3 (2011) 1377–1397, http://dx.doi.org/10.3390/polym3031377.

[3] Q. Cai, G. Shi, J. Bei, S. Wang, Enzymatic degradation behavior and mechanism of poly(lactide-co-glycolide) foams by trypsin, Biomaterials 24 (2003) 629–638, http://dx.doi.org/10.1016/S0142-9612(02)00377-0.

[4] L. Xu, K. Crawford, C.B. Gorman, Effects of temperature and pH on the degradation of Poly (lactic acid) brushes, Macromolecules 44 (2011) 4777–4782, http://dx.doi.org/10.1021/ma2000948.

[5] K. Yamashita, Y. Kikkawa, K. Kurokawa, Y. Doi, Enzymatic Degradation of Poly (L – Lactide) Film by Proteinase K: Quartz Crystal Microbalance and Atomic Force Microscopy Study, Biomacromolecules (2005) 850–857, http://dx.doi.org/10.1021/bm049395v.

[6] L.G. Sun, Z.Y. Xie, Y.J. Zhao, H.M. Wei, Z.Z. Gu, Optical monitoring the degradation of PLGA inverse opal film, Chin. Chem. Lett. 24 (2013) 9–12, http://dx.doi.org/10.1016/j.cclet.2013.01.012.
[7] K. Yamashita, T. Funato, Y. Suzuki, S. Teramachi, Y. Doi, Characteristic interactions between poly(hydroxybutyrate) depolymerase and poly[(R)-3-hydroxybutyrate] film studied by a quartz crystal microbalance, Macromol. Biosci. 3 (2003) 694–702, http://dx.doi.org/10.1002/mabi.200300004.
[8] O. Wolþ, D. Johannsmann, Viscoelastic properties of thin fims studied with quartz crystal resonators, Faraday Discus. 107 (1997) 91–94, http://dx.doi.org/10.1039/A703017G.
[9] G. Reiter, S. Napolitano, Possible origin of thickness-dependent deviations from bulk properties of thin polymer films, J. Polym. Sci. Part B Polym. Phys. 48 (2010) 2544–2547, http://dx.doi.org/10.1002/polb.22134.
[10] B.D. Vogt, C.L. Soles, H.J. Lee, E.K. Lin, W.L. Wu, Moisture absorption into ultrathin hydrophilic polymer films on different substrate surfaces, Polymer (Guildf) 46 (2005) 1635–1642, http://dx.doi.org/10.1016/j.polymer.2004.11.114.
[11] T. Larsen, S. Schmid, L. Grönberg, a. O. Niskanen, J. Hassel, S. Dohn, A. Boisen, Ultrasensitive string-based temperature sensors, Appl. Phys. Lett. 98 (2011) 121901, http://dx.doi.org/10.1063/1.3567012.
[12] G. Wu, R.H. Datar, K.M. Hansen, T. Thundat, R.J. Cote, A. Majumdar, Bioassay of prostate-specific antigen (PSA) using microcantilevers, Nat. Biotechnol. 19 (2001) 856–860, http://dx.doi.org/10.1038/nbt0901-856.
[13] C. Yim, M. Yun, S. Kim, N. Jung, S. Lim, M. Lee, Nanomechanical thermal analysis of indium films using silicon microcantilevers nanomechanical thermal analysis of indium films using silicon microcantilevers, Jpn. J. Appl. Phys. 07 (2012) 0–4.
[14] S. Bose, S. Schmid, T. Larsen, S. Sylvest Keller, A. Boisen, K. Almdal, Micromechanical fast quasi-static detection of α and β relaxations with nanograms of polymer, J. Polym. Sci. Part B Polym. Phys. 53 (2015) 1035–1039, http://dx.doi.org/10.1002/polb.23745.
[15] S. Bose, S. Schmid, T. Larsen, S.S. Keller, P. Sommer-Larsen, A. Boisen, K. Almdal, Micromechanical string resonators: analytical tool for thermal characterization of polymers, ACS Macro Lett. 3 (2014) 55–58, http://dx.doi.org/10.1021/mz400470n.
[16] S.S. Keller, L. Gammelgaard, M.P. Jensen, S. Schmid, Z.J. Davis, A. Boisen, Micromechanical sensors for the measurement of biopolymer degradation, Proc. IEEE Int. Conf. Micro Electro Mech. Syst. (2011) 457–460, http://dx.doi.org/10.1109/MEMSYS.2011.5734460.
[17] S. Bose, S.S. Keller, A. Boisen, K. Almdal, Microcantilever sensors for fast analysis of enzymatic degradation of poly (d, l-lactide), Polym. Degrad. Stab. 119 (2015) 1–8, http://dx.doi.org/10.1016/j.polymdegradstab.2015.04.021.
[18] N. Jung, H. Seo, D. Lee, C.Y. Ryu, S. Jeon, Nanomechanical thermal analysis of the glass transition of polystyrene using silicon cantilevers, Macromolecules 41 (2008) 6873–6875, http://dx.doi.org/10.1021/ma801539m.
[19] M. del Rey, R. a. da Silva, D. Meneses, D.F.S. Petri, J. Tamayo, M. Calleja, P.M. Kosaka, Monitoring swelling and deswelling of thin polymer films by microcantilever sensors, Sensors Actuators B Chem. 204 (2014) 602–610, http://dx.doi.org/10.1016/j.snb.2014.08.021.
[20] E.T. Hwu, S.K. Hung, C.W. Yang, I.S. Hwang, K.Y. Huang, Simultaneous detection of translational and angular displacements of micromachined elements, Appl. Phys. Lett. 91 (2007), http://dx.doi.org/10.1063/1.2817750.
[21] F.G. Bosco, E.-T. Hwu, C.-H. Chen, S. Keller, M. Bache, M.H. Jakobsen, I.-S. Hwang, A. Boisen, High throughput label-free platform for statistical bio-molecular sensing, Lab Chip 11 (2011) 2411–2416, http://dx.doi.org/10.1039/c1lc20116f.
[22] S. Bose, S.S. Keller, T.S. Alstrøm, A. Boisen, K. Almdal, Process optimization of ultrasonic spray coating of polymer films, Langmuir 29 (2013) 6911–6919, http://dx.doi.org/10.1021/la4010246.
[23] P. Gentile, V. Chiono, I. Carmagnola, P.V. Hatton, An overview of poly(lactic-co-glycolic) acid (PLGA)-based biomaterials for bone tissue engineering, Int. J. Mol. Sci. 15 (2014) 3640–3659, http://dx.doi.org/10.3390/ijms15033640.
[24] A.K. Naik, M.S. Hanay, W.K. Hiebert, X.L. Feng, M.L. Roukes, Towards single-molecule nanomechanical mass spectrometry, Nat. Nanotechnol. 4 (2009) 445–450, http://dx.doi.org/10.1038/nnano.2009.152.

Biographies

Andrea Casci Ceccacci received his B.Sc. in Biomedical engineering from Universitá Politecnica delle Marche, in 2011 and his M.Sc in Biomedical Engineering from Politecnico di Torino in 2014. Since 2014 he is a PhD student at the Department of Micro and Nanotechnology at Technical University of Denmark. His research interests concern the design and the use of micromechanical resonator for the characterization of biopolymer and drugs.

Ching-Hsiu Chen received the B.S. degree in Automatic Control Engineering from Feng Chia University, Taiwan, in 2002 and the M.S. degrees in Mechanical and Electro-Mechanical Engineering from National Sun Yat-Sen University, Taiwan, in 2004. He now works in Institute of Physics, Academia Sinica, Taiwan. His major researches are in scanning probe microscopy, biochemical detection techniques, MEMS/NEMS applications, precision measurement system, signal processing and quantum science.

En-Te Hwu is associate research scientist of institute of physics, Academia Sinica, Taiwan. He received his Ph.D. from National Taiwan University in 2006. He got first prize award of Taiwan National Innovation & Startups project in 2014. In 2015, he received national discover innovation award. He is currently focused on nanoscale sensing/positioning based instrumentation and applications.

Lidia Morelli received her B.Sc. and M.Sc. in biomedical engineering from the University of Pisa in 2011 and 2014, respectively. Since 2014 she is a PhD student at the Department of Micro and Nanotechnology, Technical University of Denmark. Her research interests include centrifugal microfluidics, Surface Enhanced Raman Scattering technologies for sensing, and the integration of these fields for automated and high-throughput sensing of biological samples

Sanjukta Bose Goswami received her M.Tech in Polymer Science and Technology from the Indian Institute of Technology, Delhi in 2011. Then she moved to Technical University of Denmark and started her Ph.D. studies in the Department of Micro and Nanotechnology. She obtained her Ph.D. degree in 2014 on the use of micromechanical sensors as tools for polymer characterizations. She is currently working as a Postdoc in the same department and her current research interest is in using micromechanical sensors for measuring polymer degradation for drug delivery applications.

Filippo Giacomo Bosco is CEO of BluSense Diagnostics, a spin-off from the Technical University of Denmark. He completed his education with MS.c. in Physics Engineering at Politecnico of Milano in 2008. He obtained his PhD in micro- and Nano-engineering at DTU Nanotech in 2011. He was awarded by DTU central committee as "Best DTU young researcher" for his thesis with high innovation degree. In 2012 he received the Strategic Award Prize from the Danish Ministry of Research and Innovation for his strategic research focus during his PhD. From 2011 to 2014 he has been working as Postdoc at DTU Nanotech at the Nanoprobes group, working on developing diagnostics biosensors based on low-cost optical readout. Since 2015 he is full-time employed at BluSense Diagnostics.

Silvan Schmid is associate professor of micro and nanotechnology at the Technical University of Denmark. He completed his education with the degree of Dipl. Ing. ETH from the Swiss Federal Institute of Technology Zurich in 2003. He performed his doctorate in the Micro and Nanosystems Group at ETH Zurich and received his doctoral degree in 2009. He got awarded with the ETH medal 2009 for an outstanding doctoral thesis. In 2013 he received the Villum Foundation's Young Investigator Programme grant which supports especially talented young Danish researchers in science and technology. His research focus is in micro- and nanomechanical resonators for sensor applications and fundamental research.

Anja Boisen is professor at DTU Nanotech and has many years experience in nanomechanical sensors. She is heading a DNRF and Villum Center of excellence focusing on nanomechanical sensors and new microfabricated solutions for oral drug delivery.

Supplementary information:

1. Astigmatic Detection:

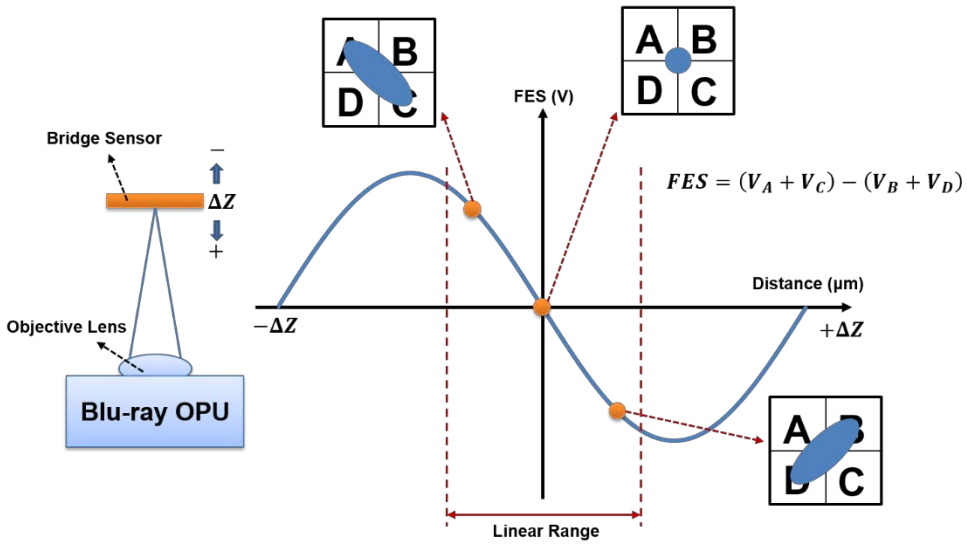

FIG S 1 Focus error signal for a Blu ray-OPU.

Figure S1 shows the signal calculation of the astigmatic detection method. The quadrant photodetector is defined as four independent sensing areas A, B, C and D. The converted output voltage can be defined as V_A, V_B, V_C and V_D. The signal focus error $S_{FE,}$ is defined as $(V_A+V_C)-(V_B+V_D)$. If the beam is perfectly focused in the center the output voltage is zero.

The output signal, also known as the S-curve, depends on the working distance Δz(fig 2) . In a certain range the behavior of the sensor is linear, and we will use such range to make our measurement.

2. Measurement Routine

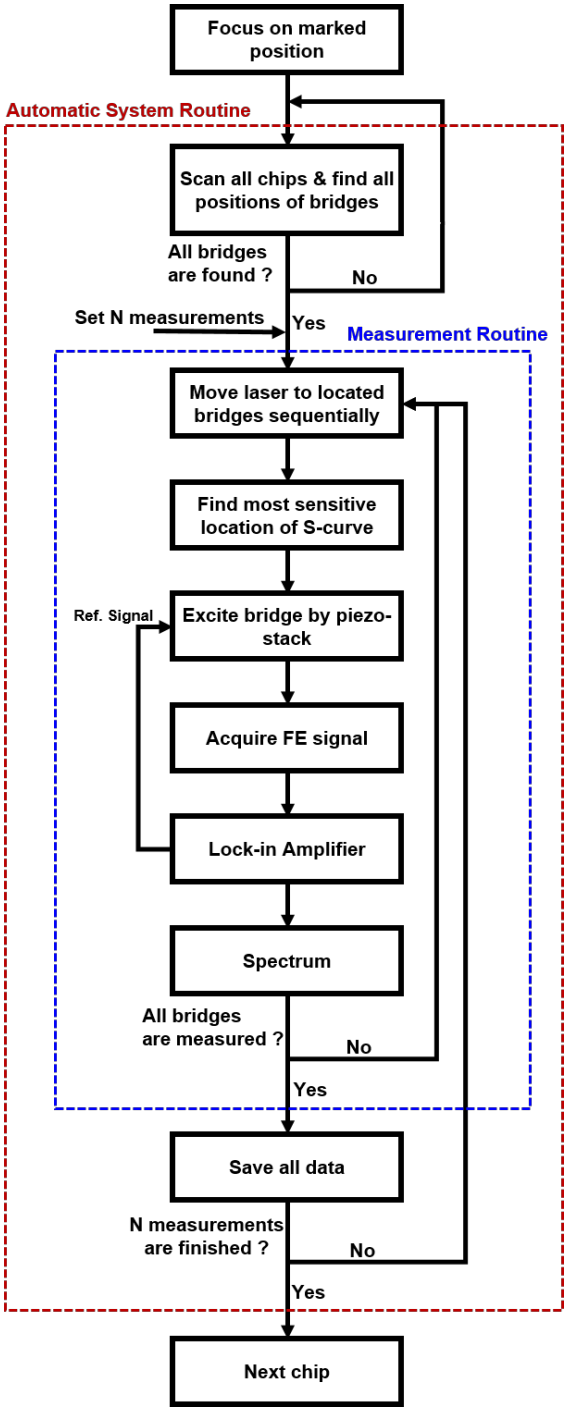

FIG S 2 Measurement routine for automatic positon detection actuation and readout:

As the first step the user has to focus on one bridge, making the distance between the bridges and the lens within a reasonable range such that by the motion of the VCM all the bridges are in the linear range. In the automatic system routine (reds) the sled motor is moving along the chip and the position of the bridges are found and saved. In the measurement routine(blue) the blu-ray pickup head moves on the position of the bridges, the VCM coil motor is actuated and the best position within the linear range in found. Then the piezo element is actuated and recorded. At the end of i^{th} measurment the spectra are recorded into one file.

3. Theoretical background

The resonance frequencies of the bridges have been recorded both in air and water environment. For multilayer structures the resonance frequency can be approximated as (Bose et al., 2015a; Keller et al., 2011)

$$f_n \approx \frac{1}{2\pi}\frac{\beta_n^2}{L^2}\sqrt{\sum_{i=1}^{N} I_i E_i \Big/ w\sum_{i=1}^{N}\rho_i t_i} \quad (1)$$

where β_n represents the mode number which for a doubly clamped beam is 4.73, 7.85, 10.99, for n =1,2,3, *L* is the length of the beam,I_i and E_i are the beam's moment of inertia and the Young's modulus respectively, $\rho_i t_i$ are the density and the thickness of the i^{th} layer. The degradation process is evaluated in terms of relative frequency shift of the coated microbridges. The mass responsivity can be written as:

$$R = {}^{\partial f}\,/_{\partial m} \approx {}^{f_n}/_{2m_0}\,[Hz/g] \quad (2)$$

f_n is the value of the resonance frequency and m_0 is the mass of the resonator.

In order to obtain the frequency values that are comparable to the degradation experiments, we can consider as a reference value, for the *i* th microbridge its resonance frequency at the end of the degradation when the polymer has been completely removed from the surface. The degradation on the i^{th} coated microbridge at the j^{th} time step is evaluated in terms of relative frequency shift $\Delta_{fi,tj}$:

$$\Delta_{fi,tj}\% = {f_{i,tf} - f_{i,tj}}\Big/{f_{i,tf}}\, 100. \, (3)$$

This shift is measured *n* times on the same bridges and then averaged:

$$\overline{\Delta_{fi,tj}} = \frac{1}{n}\sum_{k=1}^{n}(\Delta_{fi,tj})_k \ (4)$$

The N frequency shifts measured on the array are then averaged on N microbridges employed to perform the degradation analysis.

$$\overline{\Delta_{f,tj}} = \frac{1}{N}\sum_{k=1}^{N}(\overline{\Delta_{fi,tj}})_k \ (5)$$

The mean degradation rate is evaluated considering the time taken for the degradation process to remove the initial mass deposited.

$$DR = m/(A\Delta_t)\ [\mu g/h] \ (6)$$

Where *m* is the initially mass deposited on the microbridges, *A* is the area of the microbridges (*lw*) and Δ_t is the time needed to reach 0% in the relative frequency shift (the resonance frequency returns to the value for an uncoated microbridge).

The stability of the readout has been monitored thorough a lock-in amplifier. The shift in the resonance frequency has been monitored through a lock-in amplifier for 4 minutes.

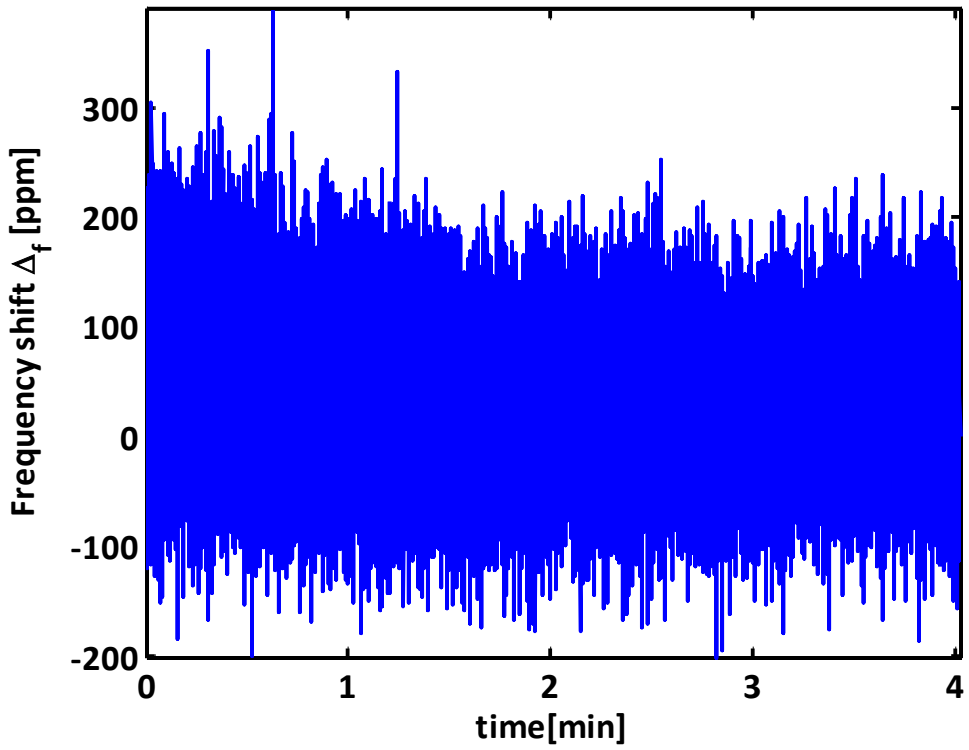

Figure S 3. Fluctuation on the resonance frequency measured through the lock-in amplifier

The root mean square of the noise is of 143 ppm and the max value +/- 200 ppm which is translated with a minimum detectable mass of 2.6 ng.

This value is greater in the actual configuration used during the degradation experiments. The shift in the resonance frequency was not followed during the degradation experiments through the lock-in amplifier but by repeating the measurement at different time step; the minimum detectable mass is thus higher, since independent measurement they are seen to have a larger variation than the fluctuation of the resonance frequency recorded with the lock-in amplifier.

4. Degradation experiments

We report here the complete degradation profile under the action of the only Tris-Hcl at 20 µl/min.

PLGA showed to be degraded in 33 hours of experiment..

Nevertheless, in the experimental time frame that was used for all the enzymatic degradation studies of PLGA, Tris-HCl did not show any degradation effect. The degradation starts around 18h and ended after 33 hours.

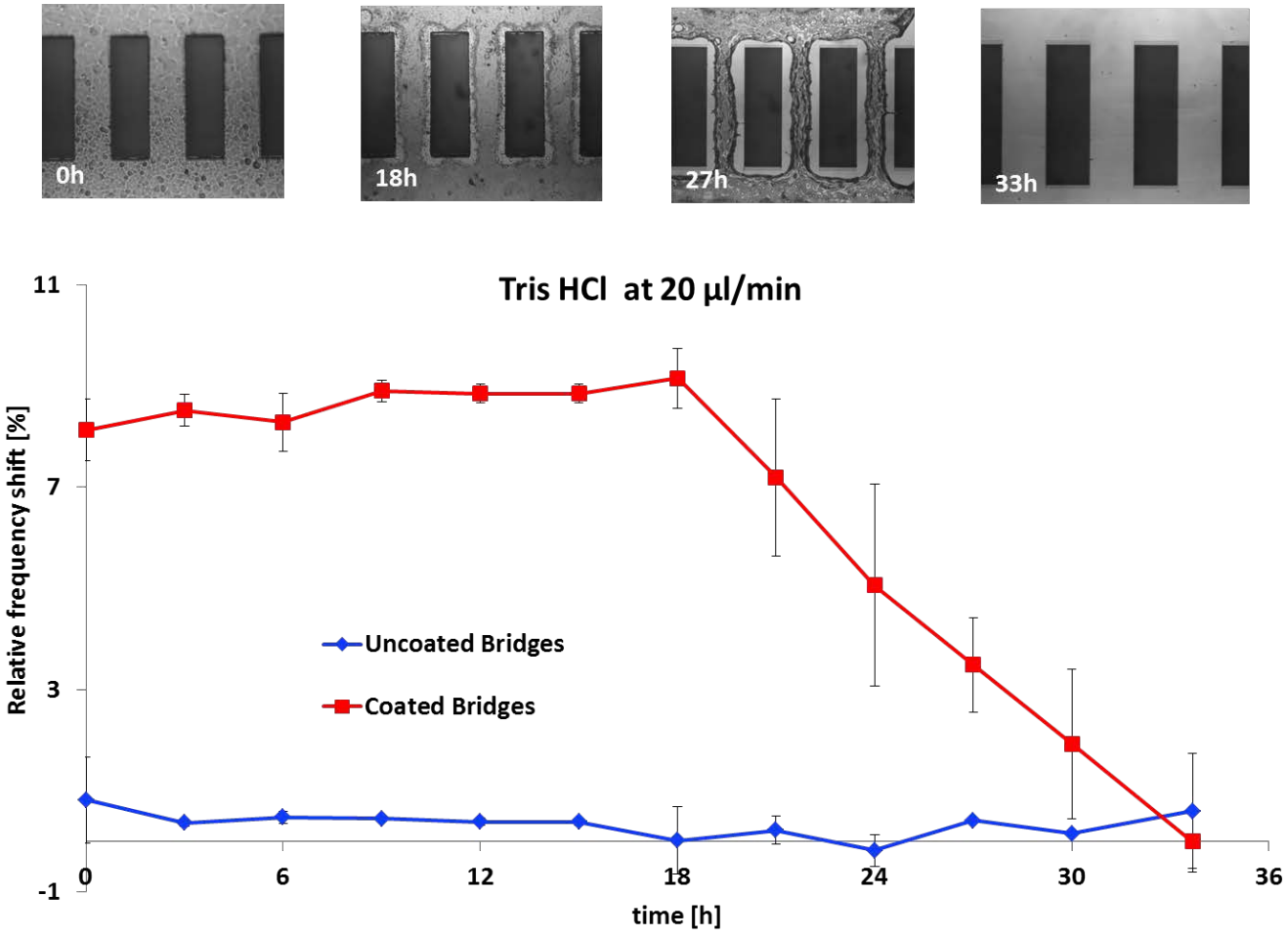

Figure S4 Degradation profile of PLGA under the action of Tris-HCl at 20 µl/min

PAPER 2

Thin Film Analysis by Nanomechanical Infrared Spectroscopy

Thin Film Analysis by Nanomechanical Infrared Spectroscopy

Andrea Casci Ceccacci[1], Alberto Cagliani[1], Paolo Marizza[1], Silvan Schmid[2] and Anja Boisen[1]

[1] Department of Micro and Nanotechnology, Technical University of Denmark, 2800 Kgs. Lyngby, Denmark.

[2] Institute of Sensor and Actuator Systems, TU Wien, 1040 Vienna, Austria.

Abstract

There is a fundamental need for techniques to characterise materials in the thin film regime.The current options for obtaining infrared spectra suffer from low signal to noise ratio (SNR) for sample thickness confined on few nanometers. We demonstrate how, through a detailed study of the fundamental parameters of nanomechanical infrared spectroscopy, it is now possible to obtain a complete fingerprint of a polymer layer of down to 20 nm in thickness with an SNR of 307. A frequency stability of 2ppm upon IR absorption indicates an effective minimum detectable film thickness of only 160 pm corresponding to 3 attomol. We show that nanomechanical infrared spectroscopy can improve the SNR by a factor of 43 compared to a conventional ATR-FTIR system on a single acquisition.These results are paving the way for potent sensing tools applicable on minute sample sizes where confinement effects can reveal unexpected behaviour.

Introduction

The ability to engineer chemical and physical properties of surfaces using dedicated functionalization methods is of fundamental importance for the advancement in many technological fields, e.g. bio- and chemical sensing[1], drug delivery[2], tissue engineering[3], solar cells[4], thin films batteries[5] and fabrication of semiconductor devices[6]. In recent years, the possibility of engineering the chemical and physical properties of a surface by applying a thin polymer film has attracted considerable attention due to its

simplicity, robustness and flexibility, thanks to the vast selection of polymer films[2,3,7–9]. Thin polymer films can exhibit, confinement induced peculiar physico-chemical properties, such as changes in glass transition temperature[10], elastic moduli[11], and crystallization[12]. Characterising the properties of such thin films is therefore of high relevance both technologically and scientifically.

The chemical behaviour and structure of thin films[13–16] is often characterised by infrared (IR) absorption spectroscopy. One of the most commonly used implementations for thin films IR spectroscopy is the attenuated total reflectance Fourier transform infrared spectroscopy (ATR-FTIR), with the typical configuration with only one reflection within the crystal[16–18]. An issue connected with the use of ATR-FTIR is that the signal-to-noise-ratio (SNR) degrades quickly when the sample thickness is much smaller than the sampling depth [13], thereby effectively limiting the thickness range that can be studied. One possibility to overcome such problem is using very long acquisition times[16], but this restricts the throughput of the analytical system. A multi-reflection ATR accessory could also be used to boost the signal, but such approach is suitable only when the crystal is in contact with a liquid or the thin functionalization layer to be studied is irreversibly attached to the very expensive crystal. These drawbacks make ATR-FTIR unsuitable for testing a large variety of very thin functionalization layers with a high throughput, high spectroscopically precision and at a reasonable low cost. There is thus a need for a fast, reliable, non-destructive and preferably less expensive method to characterise very thin layers.

Photothermal spectroscopy methods are based on the transduction of the light absorbed by the sample, and its subsequent change in temperature, into a signal that can be recorded. There are different types of transduction depending on which physico-chemical property of the sample is monitored. Typically, density, pressure or temperature changes induced by wavelength specific light absorption, have been exploited to obtain an IR absorption fingerprint of the sample[19–21].

A main advantage of the photothermal spectroscopy is that it does not suffer from the typical artefacts of ATR-FTIR or absorbance-reflection techniques in the recorded spectra. Moreover, it allows the user to hit the sample at any angle or light polarization, giving much more freedom in terms of optical design and analysis possibilities.

Nanomechanical based IR absorption sensing (NAM-IR) has been widely exploited in the last fifteen years for biosensing purposes[23–26] and material characterization[27]. Nanomechanical sensors have also been employed to perform photothermal based analysis, implementing both the deflection and resonance frequency detection schemes[20,21,28–34]. However, the samples examined so far have been limited to airborne deposited materials or liquids. This limitation is due to the lack of mechanical robustness of previous nanomechanical transducers, such as nanostrings and microcantilevers. Moreover, such nanomechanical structures suffer from the AFM-like readout laser alignment issues that can drastically limit the final analysis throughput A filter-like structure[35] has been developed to improve the efficiency of the inertial sampling for airborne particles. However, the perforated geometry of the structure hinders their employment for thin film analysis. Membranes better support sampling techniques typical of surface functionalization such as drop casting spin coating, immersion in liquid solutions, thanks to their much higher mechanical robustness.

Our IR spectroscopy system is based on 1 mm $\times$ 1 mm large and 100 nm thick pre-stressed SiN membranes.These structures not only show even better performance that previously discussed IR photothermal schemes but also offers the mechanical robustness to withstand treatments in liquid, including spray coating or spin coating, which is often essential in the field of surface functionalization. As a demonstrator of the capabilities of our IR spectroscopic system, we present infrared photothermal spectroscopy characterization of polyvinylpyrrolidone (PVP) thin films with thicknesses down to 20 nm. PVP polymer thin films have recently attracted much attention thanks to their high versatility in drug delivery devices[36], and hydrogels[37], where its thin film physical and chemical

properties are crucial. The low thermal mass of our resonating membranes allows running analysis over a range of 1100cm^{-1} wavenumbers in 30 seconds with an SNR of 200, even for a polymer film as thin as 20 nm.

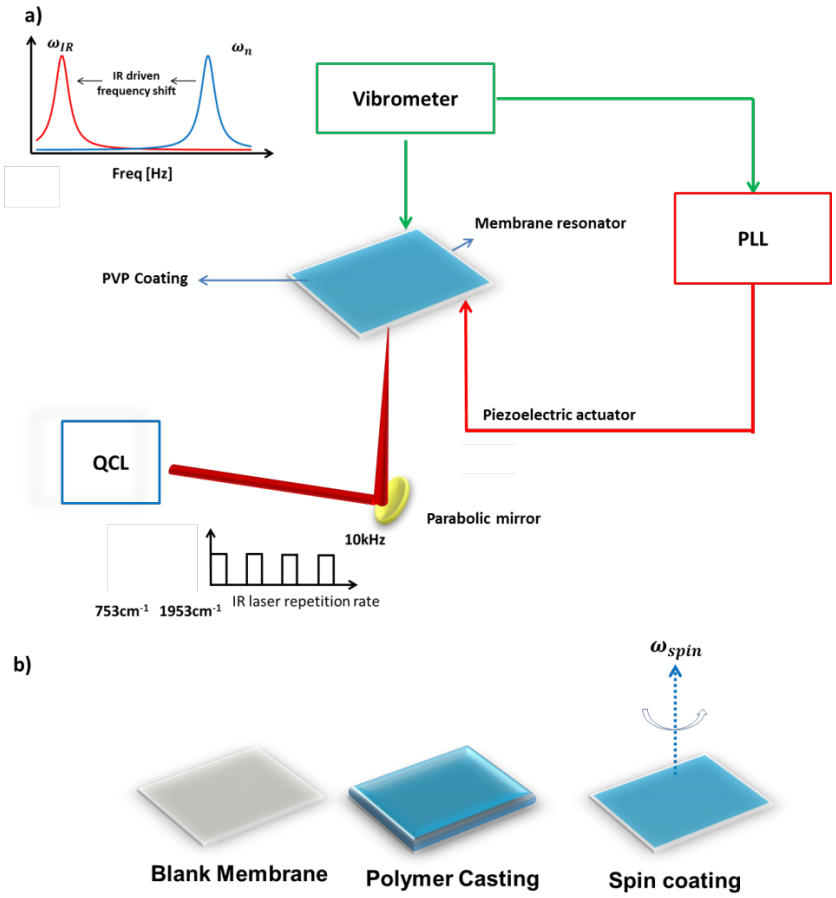

Figure 1 NAM-IR setup. a) The NAM-IR spectrometer comprises: i) a pressure controlled chamber providing optical access from both sides of the sensor, ii) a quantum cascade laser (QCL Block engineering) that generates monochromatic IR light in the range from 768cm^{-1}-1953cm^{-1}, and an optical readout system based on a laser-Doppler vibrometer (Polytech MSA-500), a phase lock-in amplifier and a piezo driver [31,38,39];b) Polymer deposition method.

Results and Discussion

The three most important bands of PVP recorded by NAM-IR matches well the spectra recorded by reference methods (ATR-FTIR and transmission FTIR) as well as previously published results[40]

(Figure 2). NAM-IR spectra did not reveal further spectral features. However, some of the bands are not visible due to the local minima of the IR laser source (e.g. small peak at 1390cm^{-1}) (SI). The shift in the ATR-FTIR bands is due to the modification of the refractive index of the sample upon IR light absorption[22].This phenomenon is clearly visible in the carbonyl band visible around 1680cm^{-1} which appears shifted towards lower frequency in the ATR-FTIR spectra.

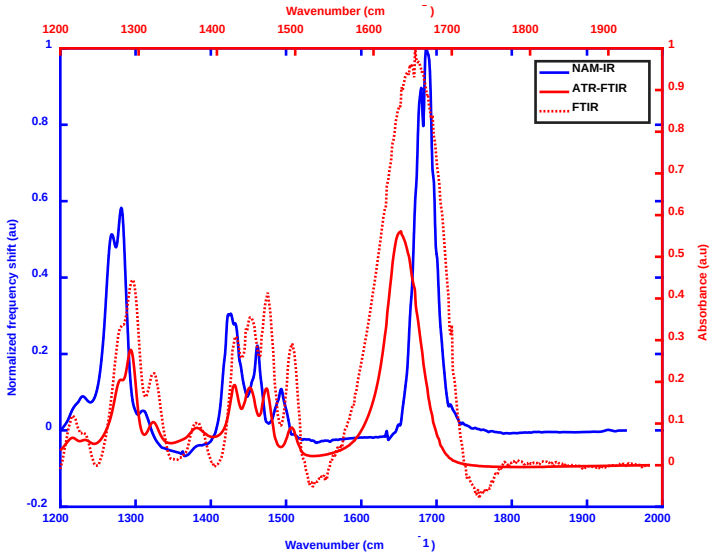

Figure 2 Comparison of the NAM-IR spectrum of a PVP film with respect to ATR and FTIR ones. Three main bands characterize the polymer fingerprint: the signal at 1300 cm^{-1} is referred to the C-N bond stretching and the CH_2ring wag mode. The band with three peaks between 1400 and 1500 cm^{-1} corresponds to the ring-CH_2 wag and the C-N stretching. The peak at 1680 cm^{-1} corresponds to the C=O stretching mode.

Upon IR absorption the mechanical resonance frequency of the membranes decreases following a first order exponential decay (Figure 3a).The knowledge of the thermal time constant of the membrane allows to determine the minimum settling time for each wavelength of the IR source and the optimal signal integration time, for maximising the SNR. The time transient of the resonance frequency shift of the membrane sensor upon periodic IR irradiation[41] at a fixed IR wavelength was characterized in order to extract the thermal relaxation time constant (see Figure 3a). Each cycle was fitted with an exponential decay function $\delta_f(t)=\Delta_f(1-e^{-t/\tau_M})$ and extracting the correspondent τ_M. The transient

was evaluated for 2 different vacuum pressures, which yielded (for a 20nm PVP coated membrane) $\tau_M = 4.1 \pm 0.08$ ms at a low vacuum of 1 mbar and $\tau_M = 17 \pm 0.9\ ms$ at a high vacuum of 10^{-5}mbar. These two regimes result in two different behaviours. In high vacuum and at room temperature the mean free path of the gas molecules becomes roughly 10 m, which is significantly larger than the critical dimension of the nanomechanical resonator. Hence, the heat transport due to natural convection can be neglected and all, heat generated in the membrane is dissipated by conduction through the body chip alone. Contrary, at 1 mbar, the mean free path corresponds to roughly 100 µm, which is comparable to the dimensions of the device, hence, allowing part of the heat to be dissipated by conduction through the surrounding gas. The two regimes threfore have very different time transient responses. The response time is also influenced by the sample and the corresponding values are reported in the supplementary information. Precise knowledge of the thermal time constant τ_M is required in order to choose an optimal settling time for each wavelength emitted by the QCL. The settling time was set such that the membrane would be exposed for no less than 3 x τ_M for each discrete IR wavelength, in order to ensure that the membrane reaches the maximum frequency shift at each wavelenght step. Considering that the QCL sweeps 1185cm^{-1} with steps of 0.5 cm^{-1}, the total acquisition time for a 20 nm thin polymer layer becomes 28.4 seconds, given a τ_M of ~4 ms in low vacuum.

The membranes transient thermal constant further influences the choice of the integration time of the PLL detection scheme. To correctly follow the resonance frequency shift upon light absorptions, the lock-in amplifier bandwidth has to be set sufficiently high to follow the full dynamics of the resonance frequency signal variations for each IR wavelength step. At the same time, a low bandwidth is desirable to reduce the frequency acquisition noise. In particular, such noise is typically quantified as the Allan deviation of the frequency signal as function of the PLL bandwidth[42] (see supplementary information).

Finally, as shown Figure 3c, these settings permit to clearly resolve each distinct IR wavelength step of 0.5 cm^{-1}, since the exponential thermal response of the membrane frequency is clearly visible and the signal arrives at the maximum amplitude within each step.

In the present work, the integration time was set to 1.5 ms for low vacuum experiments and 7 ms for high vacuum experiments leading to a resolvable frequency shift of 2 ppm calculated for a 20 nm coated membrane.

An analytical model can be used to estimate the power absorbed by the membranes[35]and in our case, considering a frequency noise floor of 2ppm, the minimum power that can be detected is 5 nW for an integration time of 7ms and an SNR of one, which corresponds to a local temperature increase in the membrane center of 3 mK (see supporting information). In the case of a 20nm coated membrane, the maximum absorbed power is 3.5 µW (at 1680 cm^{-1}), which is about 1% of the incident QCL laser power at that wavelength. Such power gives rise to a temperature increase of 0.9 K in the centre of the membrane (see supporting information), indicating that an SNR on the temperature estimation as high as 300. Finally, a calibrated power absorption spectrum is shown in Figure 3d (see SI), where the temperature reached through the all spectrum is shown.

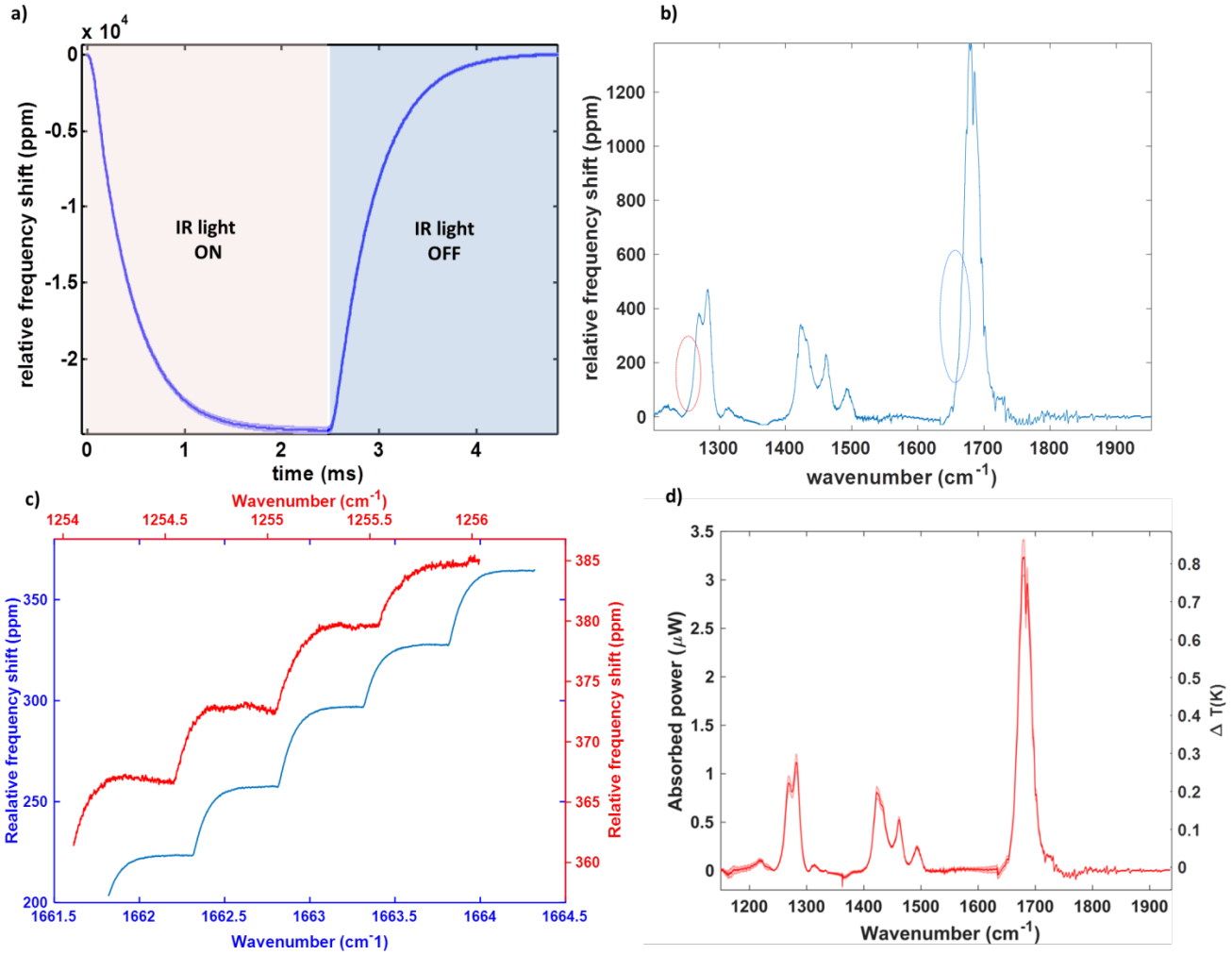

Figure 3. a) Relative frequency shift upon periodic light absorption. Values recorded on a 200 nm coated membrane at 1 mbar; shades represent the standard deviation of 485 overlapped cycles; b) Raw NAM IR spectra, highlighted region are represented in subfigure (c) ;c) zoom in of two regions of the spectra. Membrane NAM-IR spectrophotometer can recognise the QCL steps of 0.5cm^{-1} d) Absorbed power throughout the wavelength range, and relative temperature reached during a sweep on a 20 nm PVP coated membrane in HV. On the right-hand vertical axis, the relative temperature shift established in the membrane upon absorption. As reference value the baseline temperature was considered as 293.15K.

Figure 4 shows spectra of various PVP thicknesses ranging from 20 nm to 500 nm recorded by ATR-FTIR with (Perkin Elmer Spectrum 100) and our membrane-based NAM-IR system. Signal acquisition parameters and post-processing techniques are shown in the supplementary information. ATR-FTIR spectra were acquired at 4 cm^{-1} and 2 cm^{-1} resolution, finer resolution did not provide any reliable results due to a too low SNR. When ATR-FTIR was used, the three bands of PVP were clearly visible

for sample thicknesses higher than 100 nm, but only a very broad peak corresponding to the carbonyl frequency at 1680 cm^{-1} was observable for thinner samples (Figure 4a). Instead, our NAM-IR spectroscopy reveals all the expected features in the spectra, resolving clearly the three PVP spectroscopic bands down to 20 nm sample thickness, both in low and high vacuum (Figure 4b-c).

To compare the performance of the ATR-FTIR and our NAM-IR systems, SNRs were calculated on baseline corrected spectra. The noise was calculated as the standard deviation of the spectra between 1800 cm^{-1} and 1953 cm^{-1} since, in this range, no light absorption occurs. As signal, we analysed the amplitude of the carbonyl peak around 1680 cm^{-1}. For all the examined thicknesses the SNRs of NAM-IR (Figure 5a-b) were always at least one order of magnitude higher than ATR-FTIR values. For NAM-IR the SNR is further increased for spectra recorded at 10^{-5} mbar. It is worth to note that the high vacuum measurements, due to the higher values of the thermal time constant, need a longer settling time of the QLC source for each wavelength to match the transient characteristics of the sensor. SNR of NAM-IR spectroscopy reveals to be nearly independent of the total acquisition time (Figure 5b), as long as the settling time at each IR wavelength is larger than the thermal response time of the nanomechanical resonator.

The SNR of ATR-FTIR spectra depends on the resolution of the acquisitions[44], which is typically 4cm^{-1} or 2cm^{-1}, and the comparison of the SNR between spectra are made considering such spectral resolutions. Although FTIR based spectrophotometers increase the SNR of spectra by coarsening the resolution, spectra acquired at 4cm^{-1} on 20 and 40nm sample thick, did not lead to a remarkable difference regarding SNR.

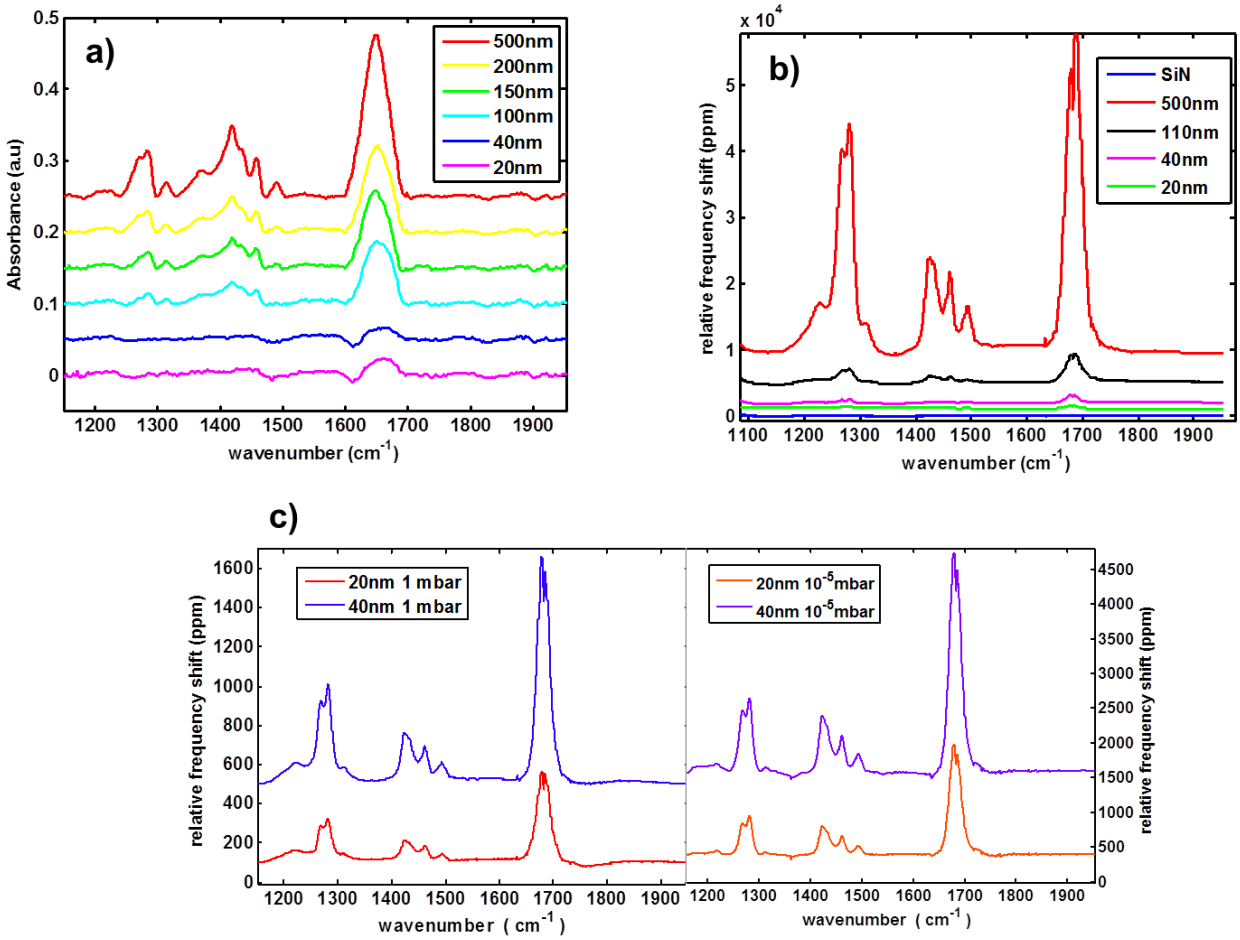

Figure 4 a) ATR spectra b)NAM-IR spectra at 1 mbar c) close up of 20 nm and 40 nm spectra at 1 mbar and 10^{-5}5 mbar. For the sake of comparison, all the spectra were offset, and the NAM-IR spectra were mirrored on the horizontal axis.

Considering that the NAM-IR spectra recorded on 20nm thick layer showed an impressive SNR of 307 in high vacuum, we are confident that this technique is now capable of recording the IR spectrum of a single molecule PVP layer. In fact, extrapolating the SNR versus thickness relation towards smaller thicknesses(SI) and considering an SNR of 2 as the lowest value needed to clearly recognise a spectral feature of PVP, the limit of detection regarding mass per unit area for NAM-IR is 0.13 fg/um^2. This mass per unit area limit corresponds to an equivalent thickness of PVP of 112 pm, approximately corresponding to 3 attomoles of PVP. This data strongly indicate that single-molecule layers can be probed with NAM-IR, with very high performance regarding SNR and short acquisition time.

The NAM-IR spectroscopy not only outperforms the ATR-FTIR in terms of SNR, but potentially also in terms of simplicity in the interpretation of the spectrum. In fact, another important feature to bear in mind when comparing our photothermal NAM-IR with an ATR-FTIR spectrometer regards which vibrational modes can be excited by the IR light in case the sample is a thin film that presents good molecular ordering[13,16,22]. ATR-FTIR probes the surface sample with the IR beam obliquely oriented to the normal of the sample surface with a nearly fixed angle. Therefore, the IR radiation is probing the perpendicular as well as the horizontal (with respect to the surface) molecular vibrational modes. In this case the resulting spectra contain both the information about the horizontal as well as the perpendicular modes, calling for precautions in the interpretation of spectra from thin layers ordered at molecular level. Moreover, ATR-FTIR spectra further depend on the reflection occurring at the substrate and sample interface[13]. In fact, when the sampling depth is higher than the sample thickness, the evanescent wave is partially reflected by the substrate leading to an extinctions of the transversal mode and enhancement of the longitudinal ones[13,46].

Instead, the NAM-IR approach is much more flexible, and the IR light can probe the sample with any angle and any polarisation. This flexibility simplifies the interpretation of spectra for samples where molecules follow a specific orientation on the surface, like self-assembled monolayers, Langmuir block monolayers or partially crystallised polymer layers. A spectrum acquired with the IR light impinging the sample surface perpendicularly would contain information only on the vibrational modes that have a component of the dipole moment parallel to the sample surface. Changing the impinging angle of the IR light, the vibrational modes with a dipole moment component orthogonally oriented to the sample surface will be probed. These advantages and the much higher SNR for sub-50 nm layers make membrane based NAM-IR a very strong candidate for a new generation of single molecule layer IR spectroscopy tools.

Finally, we would like to discuss the benefits of using a resonant membrane structure on nanostring resonators[30,31,34]. The use of a membrane allows to efficiently focus the light within the membrane area employing all the given power by the IR source and close up to 1% of the incident light a considerably higher fraction compared to string based photothermal spectroscopy[34]. The use of strings[31,34,38,39] would require using a highly collimated light source which can be difficult to handle.

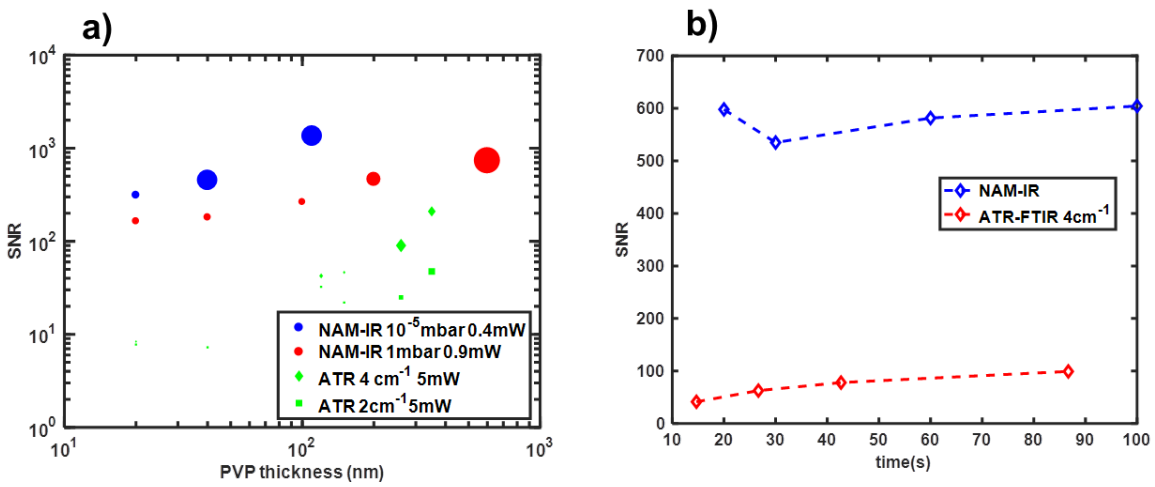

Figure 5: Comparison of SNR between NAM-IR spectroscopy and ATR-FTIR for different thickness the size of the marker represents the standard deviation on the SNR calculation. SNR of 200nm PVP coated membrane for different acquisition times. The SNR is not sensitive to a prolonged acquisition time, instead ATR-FTIR spectrophotometer increment the SNR for increased number of scans.

Conclusions

Membrane resonator based NAM-IR spectroscopy enabled new possibilities for performing IR spectroscopy on sub-50 nm organic films. The SNR of 307 obtained on a 20nm PVP polymer layer, combined with a detection limit in the attomol range, position membrane based NAM-IR as a possible technique for single molecule layer analysis. NAM-IR spectroscopy measurements were performed in less than 30 seconds on a 20 nm PVP layer, whereas using commercial ATR-FTIR technique the same SNR would be achieved with an acquisition time 43 times longer.

Moreover, the vibrational modes in ordered organic thin layers can be potentially selectively probed since the IR light can hit the surface with virtually any angle. and the interaction of the electric field in the case of reflection of the incident beam at the substrate sample interface[13].

In term of the mechanical robustness, the membranes comply better with the experimental conditions typical of surface functionalization experiments compared to microstrings, allowing the user to prepare the samples in an ample kind of methods. The high capability to dissipate heat makes the response one order of magnitude faster compared to microstrings.

Finally, the read-out of the membrane motion can be integrated using a more advanced design, creating a compact yet extremely sensitive, versatile and fast IR spectroscopy tool for ultra-thin organic layers.

METHODS

MEMBRANE FABRICATION. Details of the membrane fabrication process are described in the supplementary information.

SAMPLE PREPARATION Polymer solution was prepared by dissolving polyvinylpyrrolidone powder (PVP, Sigma-Aldrich Mw 360000) in an aqueous solution hydrogen peroxide)($H_2O_2$30% w/v) in 2 different concentration 1 % wt. and 5% wt. The deposition on the membrane was performed by spin-coating: the solution (4 mL) was poured on a silicon wafer containing the membrane chip and then spun at various rotational speeds. The sample was let dry at room temperature and atmospheric pressure. Ellipsometry was used to measures the thickness of the polymer layers.

NAM-IR SPECTRA RECORDING NAM-IR signal was recorded through a lock-in scheme. The membrane resonator is placed in a vacuum chamber which guarantees optical access from the top and from the bottom side of the sensor of the membrane. The resonance frequency of the membrane resonator is probed optically (Polytech MSA-500), the infrared light is provided by a tunable quantum cascade laser (QCL, Block Engineering 768 cm^{-1} -1953 cm^{-1}) and collimated by a parabolic mirror on the membrane resonator providing a laser spot size of 100 µm. A lock-in amplifier records the frequency shift. The phase detector bandwidth was 500 Hz for LV measurement, and 200 Hz for HV measurement and the sampling rate was set at 3600 Hz. The thermal time constant was determined by irradiating the membrane resonator periodically at a certain wavelength as described elsewhere[41]. The IR radiation was mechanically chopped providing an irradiation time of 50 ms for LV measurement. In HV mode the irradiation time was increased to 250 ms to allow the membrane to reach the steady value of resonant frequency shift at each cycle.

ATR SPECTRA ACQUISITION The ATR spectra were recorded with (Perkin Elmer Spectrum 100) providing a constant power throughout the spectral range of 5 mW. The spectra were acquired sample composed by a silicon nitride substrate and a PVP layer, prepared in the same way as membrane resonator. The PVP layer is placed in tight contact with a single reflection ZnSe crystal. The gauge force of the crystal was set to its optimal value achieving the highest signal intensity. For all spectra at least 3 signals were recorded for each sample thickness. A single acquisition spectrum is acquired at the spectral resolution of 2cm^{-1} and 4cm^{-1}. The amplitude of the acquired spectra is then corrected to compensate the different absorption amplitude throughout the spectral range using the built-in function of the software.

1. Sun, F. *et al.* Hierarchical zwitterionic modification of a SERS substrate enables real-time drug monitoring in blood plasma. *Nat. Commun.* **7,** 13437 (2016).

2. Huang, C. L. *et al.* The influence of additives in modulating drug delivery and degradation of PLGA thin films. *NPG Asia Mater.* **5,** e54 (2013).

3. Harrison, R. H. *et al.* Modular and Versatile Spatial Functionalization of Tissue Engineering Scaffolds through Fiber-Initiated Controlled Radical Polymerization. *Adv. Funct. Mater.* **25,**

5748–5757 (2015).

4. Green, M. A. Thin-film solar cells: review of materials, technologies and commercial status. *J. Mater. Sci. Mater. Electron.* **18,** 15–19 (2007).

5. Jie Lin, Jianlai Guo, Chang Liu, and H. G. Ultrahigh-Performance Cu2ZnSnS4 Thin Film and Its Application in Microscale Thin-Film Lithium-Ion Battery: Comparison with SnO2.

6. Ross, C. A., Berggren, K. K., Cheng, J. Y., Jung, Y. S. & Chang, J.-B. Three-Dimensional Nanofabrication by Block Copolymer Self-Assembly. *Adv. Mater.* **26,** 4386–4396 (2014).

7. Hashizume, M., Murata, Y., Iijima, K. & Shibata, T. Drug loading and release behaviors of freestanding polysaccharide composite films. *Polym. J.* **48,** 545–550 (2016).

8. Rahman, A. *et al.* Non-native three-dimensional block copolymer morphologies. *Nat. Commun.* **7,** 13988 (2016).

9. Mishra, R. K., Datt, M. & Banthia, A. K. Synthesis and characterization of pectin/PVP hydrogel membranes for drug delivery system. *AAPS PharmSciTech* **9,** 395–403 (2008).

10. Jae Hyun Kim, †, Jyongsik Jang, *,† and & Wang-Cheol Zin*, ‡. Thickness Dependence of the Glass Transition Temperature in Thin Polymer Films. (2001). doi:10.1021/LA001125K

11. Fedorchenko, A. I., Wang, A.-B. & Cheng, H. H. Thickness dependence of nanofilm elastic modulus. *Appl. Phys. Lett.* **94,** 152111 (2009).

12. Michell, R. M., Blaszczyk-Lezak, I., Mijangos, C. & Müller, A. J. Confinement effects on polymer crystallization: From droplets to alumina nanopores. (2013). doi:10.1016/j.polymer.2013.05.029

13. Laroche, G., Fitremann, J. & Gherardi, N. FTIR-ATR spectroscopy in thin film studies: The importance of sampling depth and deposition substrate. *Appl. Surf. Sci.* **273,** 632–637 (2013).

14. Wang, Y. *et al.* Crystallization in the Thin and Ultrathin Films of Poly(ethylene-vinyl acetate) and Linear Low-Density Polyethylene. (2003). doi:10.1021/ma030456b

15. Ohta, K. Experimental Proof of the Relation Between Thickness of the Probed Surface Layer and Absorbance in FT-IR/ATR Spectroscopy.

16. Ramin, M. A. *et al.* PM-IRRAS Investigation of Self-Assembled Monolayers Grafted onto SiO_2 /Au Substrates. *Langmuir* **27,** 6076–6084 (2011).

17. Kim, J., Cho, J., Seidler, P. M., Kurland, N. E. & Yadavalli, V. K. Investigations of Chemical Modifications of Amino-Terminated Organic Films on Silicon Substrates and Controlled Protein Immobilization. *Langmuir* **26,** 2599–2608 (2010).

18. Shiyong Song, †,‡, Ruiqing Chu, §, Jinfang Zhou, †, Shengrong Yang, *,† and & Junyan Zhang*, †. Formation and Tribology Study of Amide-Containing Stratified Self-Assembled Monolayers: Influences of the Underlayer Structure. (2008). doi:10.1021/JP7100144

19. Bialkowski, S. *Photothermal spectroscopy methods for chemical analysis*. (Wiley, 1996).

20. Barnes, J. R. *et al.* A femtojoule calorimeter using micromechanical sensors. *Rev. Sci. Instrum.*

65, 3793 (1994).

21. Barnes, J. R., Stephenson, R. J., Welland, M. E., Gerber, C. & Gimzewski, J. K. Photothermal spectroscopy with femtojoule sensitivity using a micromechanical device. *Nature* **372,** 79–81 (1994).

22. Nunn, S. & Nishikida, K. Advanced ATR Correction Algorithm.

23. Bosco, F. G. *et al.* High throughput label-free platform for statistical bio-molecular sensing. *Lab Chip* **11,** 2411–6 (2011).

24. Ndieyira, J. W. *et al.* Surface-stress sensors for rapid and ultrasensitive detection of active free drugs in human serum. *Nat. Nanotechnol.* **9,** 225–232 (2014).

25. Patil, S. B. *et al.* Decoupling competing surface binding kinetics and reconfiguration of receptor footprint for ultrasensitive stress assays. *Nat. Nanotechnol.* **10,** 899–907 (2015).

26. Alsteens, D. *et al.* Nanomechanical mapping of first binding steps of a virus to animal cells. *Nat. Nanotechnol.* **12,** 177–183 (2016).

27. Bose, S. *et al.* Micromechanical string resonators: Analytical tool for thermal characterization of polymers. *ACS Macro Lett.* **3,** 55–58 (2014).

28. Khan, M. F. *et al.* Heat capacity measurements of sub-nanoliter volumes of liquids using bimaterial microchannel cantilevers. *Cit. Appl. Phys. Lett. Sci. Instrum* **108,** 211906–4191 (2016).

29. Larsen, T., Schmid, S., Villanueva, L. G. & Boisen, A. Photothermal Analysis of Individual Nanoparticulate Samples Using Micromechanical Resonators. *ACS Nano* **7,** 6188–6193 (2013).

30. Yamada, S., Schmid, S., Larsen, T., Hansen, O. & Boisen, A. Photothermal infrared spectroscopy of airborne samples with mechanical string resonators. *Anal. Chem.* **85,** 10531–10535 (2013).

31. Andersen, Alina Joukainen; Yamada, Shoko; Ek, Pramod Kumar; Andresen, Thomas Lars; Boisen, A. & Schmid, S. Nanomechanical IR spectroscopy for fast analysis of liquid-dispersed engineered nanomaterials. *Sens. Actuators B* **233,** 667–673 (2016).

32. Ghoraishi, M. S., Hawk, J. E., Phani, A., Khan, M. F. & Thundat, T. Clustering mechanism of ethanol- water mixtures investigated with photothermal microfluidic cantilever deflection spectroscopy. *Nat. Publ. Gr.* (2016). doi:10.1038/srep23966

33. Wig, A., Arakawa, E. T., Passian, A., Ferrell, T. L. & Thundat, T. Photothermal spectroscopy of Bacillus anthracis and Bacillus cereus with microcantilevers. *Sensors Actuators B Chem.* **114,** 206–211 (2006).

34. Biswas, T. S. *et al.* Femtogram-scale photothermal spectroscopy of explosive molecules on nanostrings. *Anal. Chem.* **86,** 11368–72 (2014).

35. Kurek, M. *et al.* Nanomechanical Infrared Spectroscopy with Vibrating Filters for Pharmaceutical Analysis. *Angew. Chemie Int. Ed.* **56,** 3901–3905 (2017).

36. Marizza, P. *et al.* Synthesis and characterization of UV photocrosslinkable hydrogels with poly(N-vinyl-2-pyrrolidone): Determination of the network mesh size distribution. *Int. J. Polym. Mater. Polym. Biomater.* **65,** 516–525 (2016).

37. Plungpongpan, K. *et al.* Preparation of PVP/MHEC Blended Hydrogels via Gamma Irradiation and their Calcium ion Uptaking and Releasing Ability. *Energy Procedia* **34,** 775–781 (2013).

38. Yamada, S., Schmid, S., Larsen, T., Hansen, O. & Boisen, A. Photothermal Infrared Spectroscopy of Airborne Samples with Mechanical String Resonators. *Anal. Chem.* **85,** 10531–10535 (2013).

39. Larsen, T., Schmid, S., Villanueva, L. G. & Boisen, A. Photothermal analysis of individual nanoparticulate samples using micromechanical resonators. *ACS Nano* **7,** 6188–93 (2013).

40. Zhu, X., Lu, P., Chen, W. & Dong, J. Studies of UV crosslinked poly(N-vinylpyrrolidone) hydrogels by FTIR, Raman and solid-state NMR spectroscopies. *Polymer (Guildf).* **51,** 3054–3063 (2010).

41. Miriyala, N., Khan, M. F. & Thundat, T. Thermomechanical behavior of a bimaterial microchannel cantilever subjected to periodic IR radiation. *Sensors Actuators B Chem.* **235,** 273–279 (2016).

42. Cleland, A. N. & Roukes, M. L. Noise processes in nanomechanical resonators. doi:10.1063/1.1499745

43. Schmid, S., Wu, K., Larsen, P. E., Rindzevicius, T. & Boisen, A. Low-Power Photothermal Probing of Single Plasmonic Nanostructures with Nanomechanical String Resonators. *Nano Lett.* **14,** 2318–2321 (2014).

44. Liu, Q. & Xiao, S. Effects of spectral resolution and signal-to- noise ratio of hyperspectral sensors on retrieving atmospheric parameters. (2013). doi:10.1364/OL.39.000060

45. Fan, J. & Trenary, M. Symmetry and the Surface Infrared Selection Rule for the Determination of the Structure of Molecules on Metal Surfaces. *Langmuir* **10,** 3649–3657 (1994).

46. Dupont, G., Caquineau, H., Despax, B., Berjoan, R. & Dollet, A. Structural properties of N-rich a-Si - N:H films with a low electron-trapping rate. *J. Phys. D. Appl. Phys.* **30,** 1064–1076 (1997).

SUPPLEMENTARY INFORMATION

MEMBRANE FABRICATION. Silicon-Rich silicon Nitride membrane(Figure 1) were fabricated by standard lithography techniques. A double side polished wafer was RC cleaned and a 100nm thick layer of low-stress Silicon Nitride(250MPa) was deposited by LPCVD. A sacrificial layer of silcon nitride is deposited through PECVD. The Inductively Coupled Plasma (ICP) etching performed on the backside after lithography to remove the LPCVD SiN layer but keeping intact the one on the front side protected by the PECVD SiN. KOH. The release of the membrane structure is done through KOH etching (4.5h) which defines the clamping of the membranes and then the PECVD SiN is removed through HF etch. The membrane has side length are 1000µm.

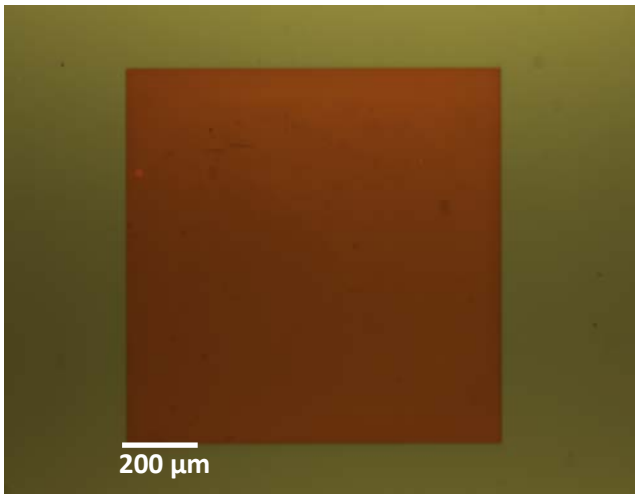

Figure s6 Silicon-Rich Silicon Nitride Membrane 1000µm side length. The initial stress was measured to be 250MPa

SAMPLE PREPARATION The membranes were functionalized using a spin coating. The spun solution consisted of the mixture(5% and 1 % wt) of PVP k-90 Mw 360000 in H_2O_2: H_2O(30%). The thickness layer was measured with ellipsometry(Filmtek). Spinning curves are reported in Figure s2 and the thickness of the polymer layer on the body chip of a membrane chip Figure s3

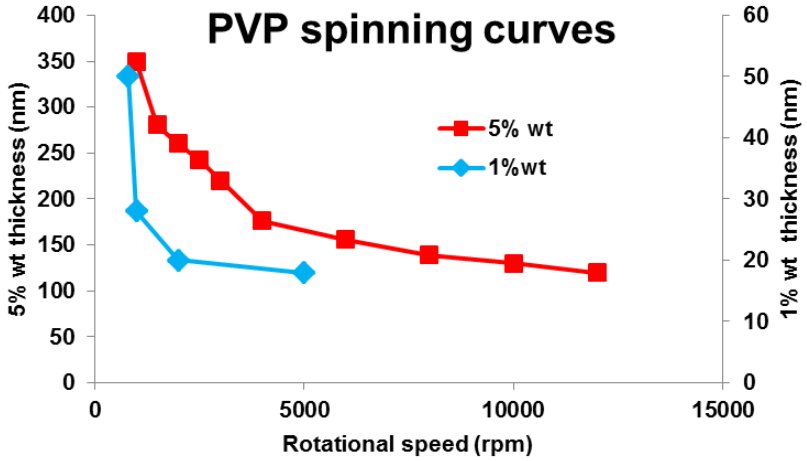

Figure s7 Spinning curves of PVP measured through ellipsometry.

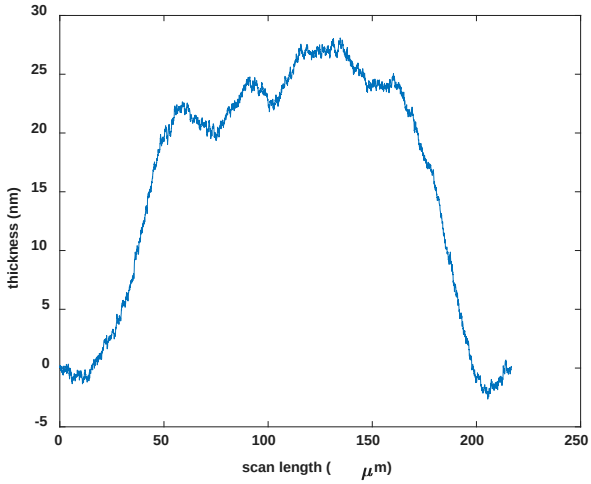

Figure s8 Profile for a PVP coated Silicon substrate spun at 5000 rpm.

TIME CONSTANT

The value of the thermal time constant was evaluated as described elsewhere[1] for different polymer coatings both in high vacuum and in low vacuum. The higher the thickness, the higher the time constant. High vacuum measurement yields to a higher value of time constant Figure s4

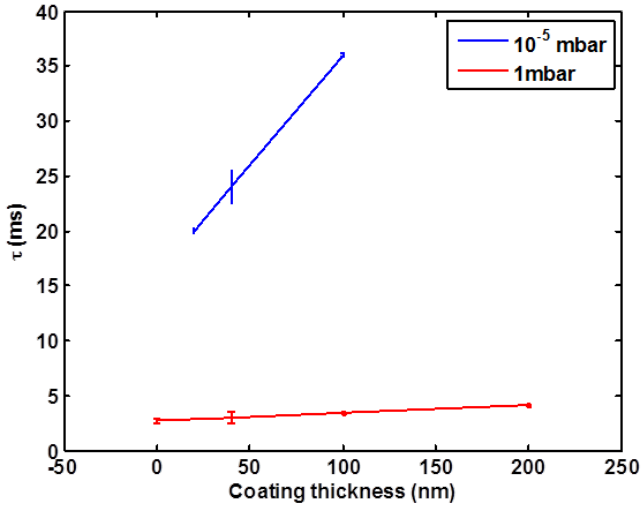

Figure s9 Thermal time constant for PVP coated membranes at low vacuum and high vacuum.

CHARACTERIZATION OF THE QCLLASER SOURCE The QCL power spectra is shown in figure s5

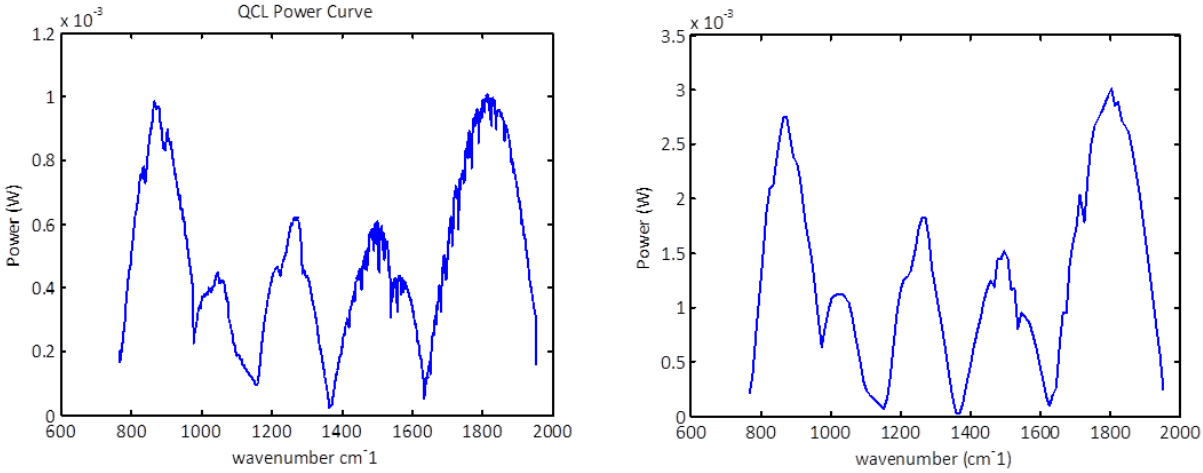

Figure s10 QCL laser power curve at 1% DC and 4% DC. It can be noted that the power does not scale linearly. This is due, according to the manufacturer specification to an overheating of the device which influences the linearity of the output. The power spectra at 4% DC are recorded with a coarser quantization (10cm^{-1}).

ALLAN DEVIATION MEASUREMENT

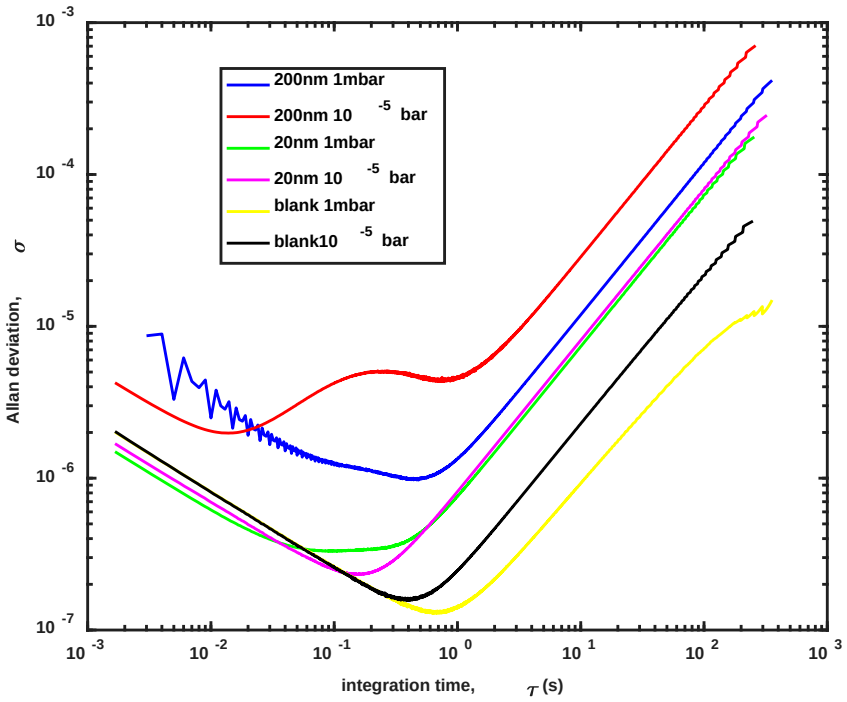

Figure s11. at 1680cm^{-1} correspondingly to the carbonyl stretching bond; d Allan deviation measurement for blank coated and uncoated membranes at 1mabr and 10^{-5} mbar

One of the factors that determine the limit of detection (LOD) for the NAM-IR spectroscopy is the resonant frequency measurement precision, which can be estimated through the Allan deviation (AD). We measured the Allan deviation for uncoated membrane at rest, and for 20 and 100nm PVP coated membrane when subjected to the IR light. We performed the measurement both in high vacuum (HV) and in low vacuum (LV). Surprisingly the Allan deviation ($\sigma_{(1s)}$) is higher for HV and this is probably due to the higher sensitivity of the of the membrane sensor to the fluctuations of the IR source. Finally, we also noticed an increase in the noise for increasing amount of material deposited. As we show in figure 3a, this might be due to an increase of the responsivity to the photothermal heating for coated membrane. The AD values need to be discussed from a spectroscopy perspective. The optimal integration time is bounded by thermal time constant τ_M(values of the thermal time constant are reported in the main manuscript). For a blank membrane τ_M is around 2.5ms at 1 mbar and around 20ms at 10^{-5}mbar. Therefore, to properly define the LOD we must consider the AD for an integration time $\tau_i < \tau_M$. In the light of this, we notice negligible differences between coated and uncoated membranes. Instead, considering 100nm coated membranes at the optimal

integration time ($\tau_M = 5ms \text{ and } 40ms$ for 1mbar and 10^{-5} mbar respectively) the AD values are in the order of 3ppm and 5ppm. In the main manuscript the LOD was evaluated for a 20nm PVP coated membrane and it has shown to be 2.5nW in terms of absorbed power.

NAM-IR SIGNAL POST PROCESSING

The NAM-IR spectra are caused by the release of the initial stress of the membrane resulting in a negative resonance frequency shift. For the sake of clarity, the spectra are finally mirrored on the horizontal axis.

1) **Averaging** (figure s7a-b)The QCL laser source (Block-Engineering) used in this work has a laser linewidth of 2cm^{-1}. The QCL sweeps stepwise the investigated wavelength range with a step size of 0.5cm^{-1}. According to the sweeping speed, the dwell time is automatically regulated. The dwell time has to be higher than 3τ allowing the membrane to reach the steady value upon IR absorption. The PLL bandiwth was set at 500Hz for all the recorded spectra, ensuring an integration time of 1.5ms or lower the sampling frequency was set at 3600sample/sec.For high vaucm measuremnt the QCL dwell time was reduced to match the thermal time constant of the device and the integration time of the PLL was set to 10ms.

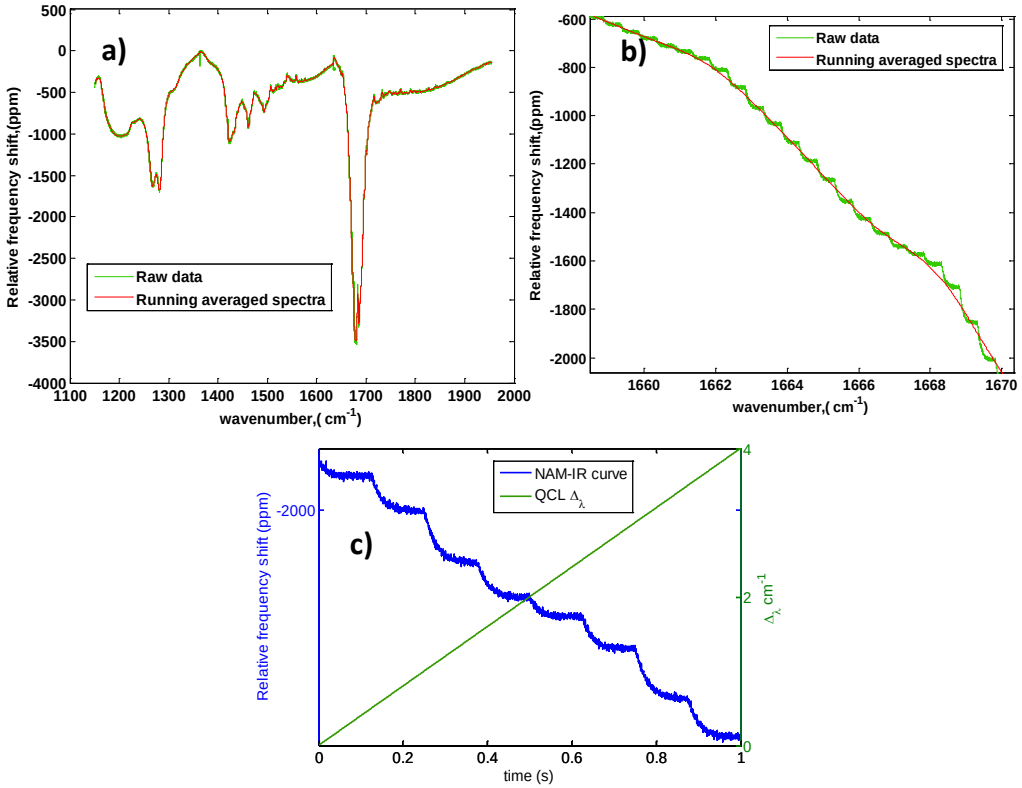

Figure S12 a-b)Raw NAM-IR spectra and averaged NAM-IR spectra; c) Subsequent IR absorption during spectroscopy. The spectral range of 4cm^{-1} is swept within 1 second in 8 steps. Although a formal definition resolution is not available the membrane sensor can clearly recognise the step width of 0.5cm^{-1} during spectroscopy.

The raw data are averaged with a moving average filter. The averaging window was chosen to match the laser linewidth of the QCL.

2) Removal of Silicon Nitride Background

The non-linearity of the laser source is reflected in the NAM-IR spectra. Despite the high transparency in the mid-infrared region, the fingerprint of the laser can be seen in the raw spectra (figure s8). The multiple local minima are clearly visible in the different spectra acquired reflected resonance frequency[2–4] value.

Although the region from 1150cm^{-1} to 1953 cm^{-1} the photothermal absorption is negligible, the fingerprint of their source is reflected in the spectra. The NAM-IR spectra of a blank membrane are subtracted from the spectra of the investigated material. The background of SiN is more evident In spectra in the nanometers measurement where the relative frequency shift due to the sample is in the same order of magnitude of the relative frequency shift of the background than for thicker coating. The subtraction of the background becomes necessary when the thickness of the investigated material is in the 10s of nm range. Due to the increase

in the relative frequency shift of coated sensor (figure 3a), before subtraction, the background is scaled according to the ratio of the SiN peak at 861cm^{-1}.

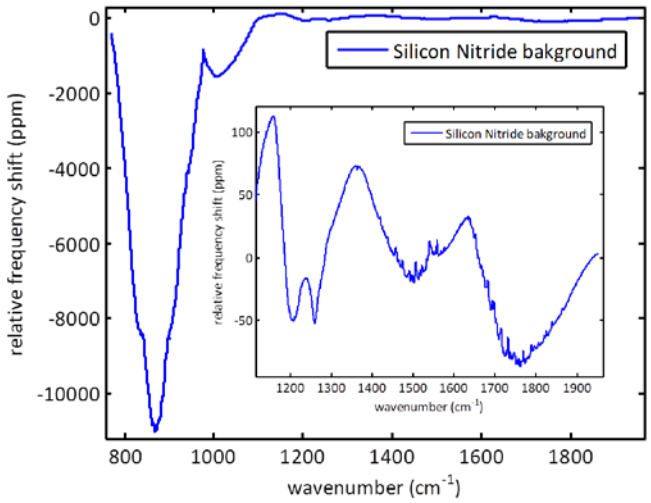

Figure S13 NAM-IR spectra of Silicon Nitride recorded at 4%DC at 1mbar. Analogous spectra are recorded in a high vacuum.

3) **Baseline Correction**. The same baseline correction is performed in ATR spectra and NAM-IR spectra figure s9.

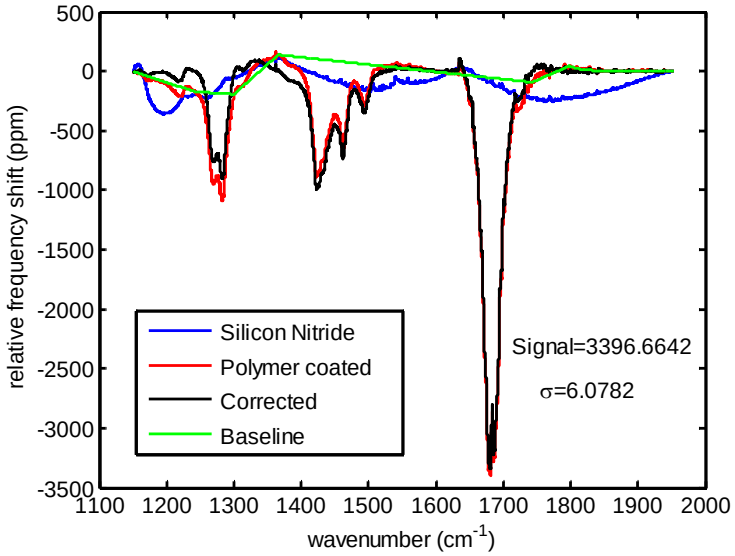

Figure s14 Averaged spectra are subtracted from the silicon nitride background. Afterwards, a baseline correction is performed. Here spectra of 40nm PVP coated device recorded at 10^{-5} mbar is showed.

Signal and noise calculation The signal to noise ratio of the spectra was evaluated considering as noise the standard deviation of the portion of the spectra ranging from 1800 to 1953cm^{-1} where there is no absorption of the investigated material(Figure s9 and figure s10). The same approach was used for the definition of the SNR for ATR and NAM-IR. As a signal, it was used the amplitude of the peak led from the carbonyl bond located around 1680cm^{-1}. All the calculation were performed on the data after the baseline correction. The raw data the Matlab-script for used for post-processing the date upon reasonable request

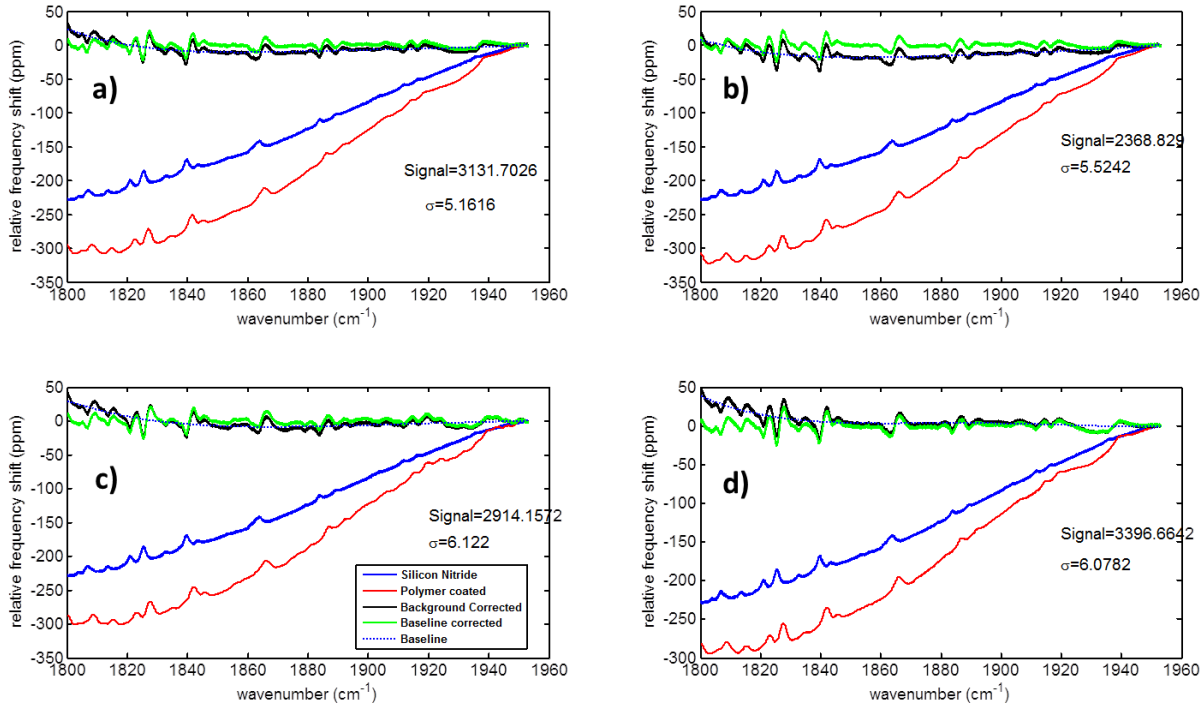

Figure s15 Noise calculation on Baseline corrected spectra. Most of the noise is due to the fluctuation of the signal due to the fluctuation of the QCL. The text in the figure indicates the noise, considered as the standard deviation of the signal between 1800 and 1953 cm-1. Here the noise on a 40nm coated membrane at 10^{-5}mbar.

Here we have reported as proof of concept the portion of the NAM-IR spectra calculated on a 40nm PVP coated membrane measured at 10^{-5} mbar.

ATR SPECTRA POST PROCESSING ATR-FTIR spectra are acquired with (Perkin-Elmer Spectrum-100) equipped with a broadband IR source of 5mW. The spectra are acquired with two different spectral resolutions; 4cm^{-1} and 2cm^{-1}. Higher values of the resolution did not provide reliable data due to the very low SNR. It is known that SNR increases for coarser resolution and for longer acquisition time[5]. The amplitude was corrected for compensating the difference in the penetration depth, the function of the incident wavelength. The sample background of the Silicon substrate is removed (figure s11), and finally, the spectra are further corrected by interpolating a baseline. The signal to noise ratio is then evaluated using the same criteria defined for NAM-IR spectra.

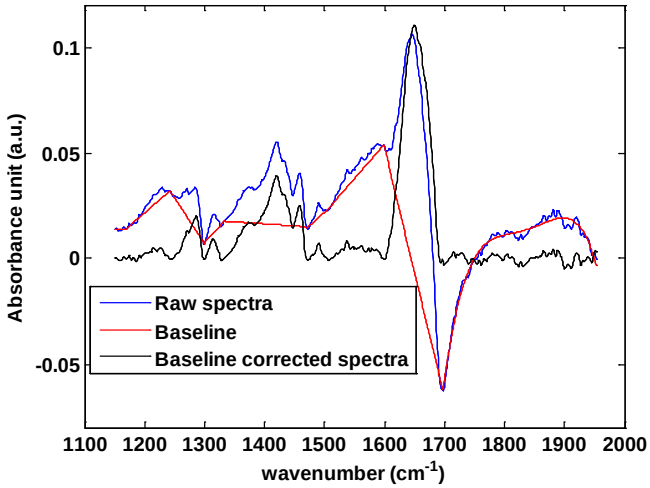

Figure s16 ATR signal of 200nm PVP thin film. The spectral resolution of 4cm^{-1}.The baseline is obtained such that the three main bands of the PVP can be easily identified. The signal to noise ratio is the evaluated considering the baseline corrected spectra.

EVALUATION OF THE ABSORBED POWER

The absorbed power from the membrane resonator results only in a fraction of the incident power. The absorbed power can be calculated by the model[6]:

$$P_{abs} = \frac{8\pi}{\alpha}\frac{\bar{k}\bar{h}\overline{\sigma_0}}{E}\frac{\Delta_f}{f}\left(\frac{2-v}{1-v} - 0.642\right)^{-1}$$

Considering a membrane resonator coated with 20 nm of PVP characterised by a time with an integration time of 7ms the Ad values is 2 pmm hence the absorption power LOD is 5nW.

These values once plugged in the equation above reported describing the absorption power, considering these parameters for the SiN[6] and PVP[7]. The values were averaged correspondingly to the thickness of the two layers. These values are reported in Table s1

Material	k	a	sigma	E
	Wm^{-1}	ppm	Mpa	Gpa
PVP	0.27	70	~	2
SIN	2.5	2.3	250	250

Table s 1Values for evaluating the absorbed power.

The thermal and mechanical parameters of the are averaged correspondingly to the sample and membrane thickness. The absorption power spectra for a 20nm membrane at 10^{-5}mbar is shown in (figure s12). The shades represent 5 times the standard deviation of spectra recorded on 4 different membrane coated chips.

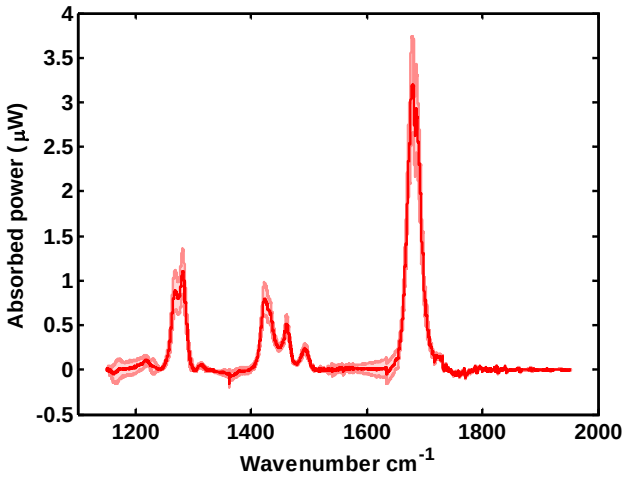

Figure s17 The absorbed power for 20nm thick PVP coating evaluated from (1). The absorbed power spectra is then used as input for the calculation of the temperature shift driven by the heat absorption

FINITE ELEMENT MODELLING

The temperature shift due to the light absorption is evaluated through a finite element model. We simulated the thermal transport throughout the entire device: bodychip and membrane resonator. The heat transport was assumed to be purely conductive throughout the device. A multi-layered structure was simulated to predict the heat transport in the presence of the PVP coating. The thermal properties of the PVP can be found elsewhere[8].

At the boundary, the temperature was set at 293.15K, and the heat source was placed in the centre of the membrane. The temperature reached for each absorbed power were calculated by solving the heat transport equation and the corresponding wavelength dependent

temperature field is evaluated (figure s13). The highest temperature reached matches with the absorption at 1680cm^{-1} of the carbonyl bond, and it is around 294K well below the glass transition temperature of the PVP which is around 453K [9].

Using the same approach we were able to define the noise equivalent temperature of 3mK, considering the standard deviation of the absorbed power spectra in the region where no absorption occurs.

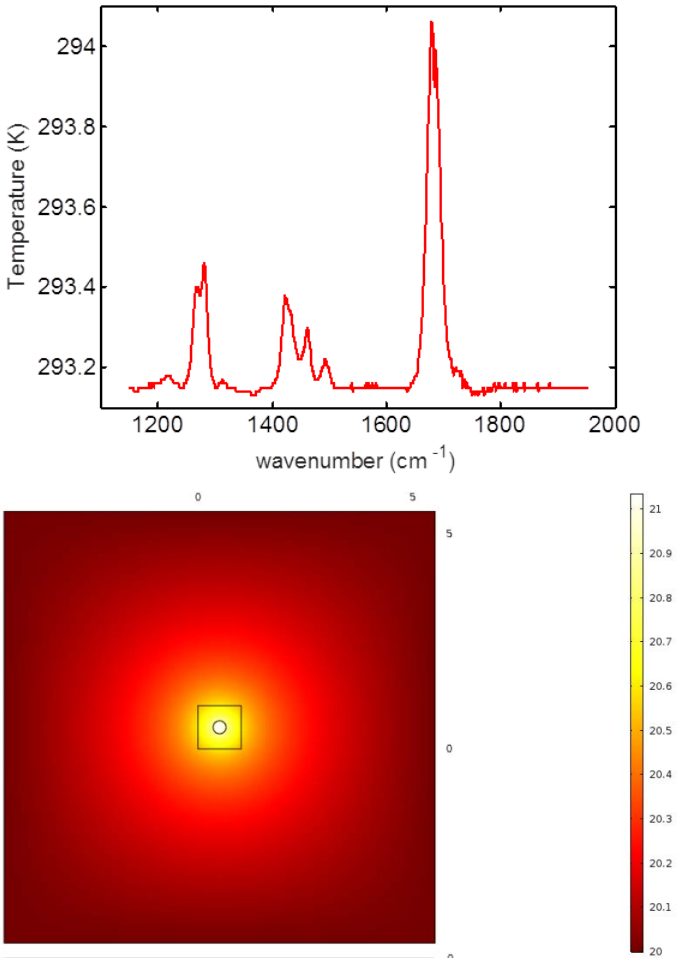

Figure s18 Temperature shift spectra and temperature field for a 20 nm PVP coated membrane, correspondingly to the power spectra. The membrane is located in the centre of the bodychip of 1cm side length.

SNR

The signal to noise ratio of PVP spectra recorded in a high vacuum were used to perform a linear fit and extrapolate a limit of detection Figure s14.

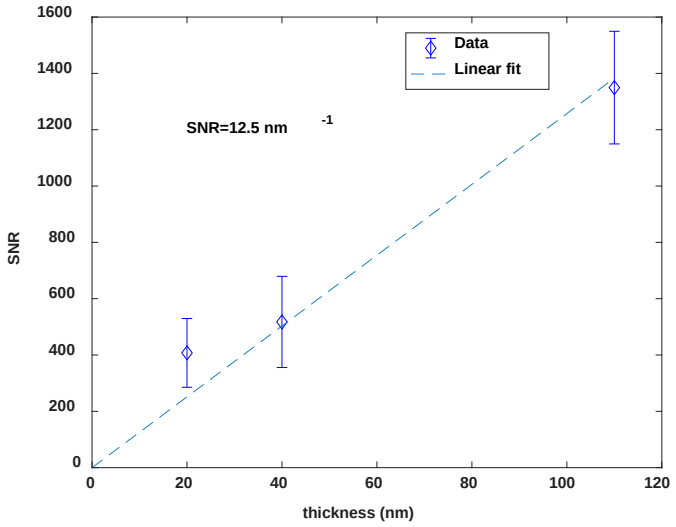

Figure s19 linear fit extrapolation of the SNR in high vacuum n=3

From the linear fit equation of the SNR, we can extrapolate the limit of detection.

The thickness that would give rise to a SNR of 2 for an incident power of 900 µW is

$$Thickness\ detection\ limit = \frac{2}{12.5} = 0.16nm = 160pm$$

160pm of material corresponds over the sampling area given by the laser spot size of 100µm in diameter.

PVP density is 1.3 pg um^{-3},

The sampling volume is 1.25 μm^3

The sampling mass is 1.66pg of PVP corresponding to roughly 4 attomol. Considering the PVP Mw is 360kDa

REFERENCE

[1] N. Miriyala, M.F. Khan, T. Thundat, Thermomechanical behavior of a bimaterial microchannel cantilever subjected to periodic IR radiation, Sensors Actuators B Chem. 235 (2016) 273–279. doi:10.1016/j.snb.2016.05.043.

[2] S. Bose, S. Schmid, T. Larsen, S.S. Keller, P. Sommer-Larsen, A. Boisen, K. Almdal, Micromechanical string resonators: Analytical tool for thermal characterization of polymers, ACS Macro Lett. 3 (2014) 55–58.

doi:10.1021/mz400470n.

[3] S. Bose, S. Schmid, T. Larsen, S. Sylvest Keller, A. Boisen, K. Almdal, Micromechanical fast quasi-static detection of α and β relaxations with nanograms of polymer, J. Polym. Sci. Part B Polym. Phys. 53 (2015) 1035–1039. doi:10.1002/polb.23745.

[4] S. Asad, M. Bukhari, M.F. Khan, A. Goswami, R. Mcgee, T. Thundat, Thermomechanical analysis of picograms of polymers using a suspended microchannel cantilever, (n.d.). doi:10.1039/c6ra25455a.

[5] Q. Liu, S. Xiao, Effects of spectral resolution and signal-to- noise ratio of hyperspectral sensors on retrieving atmospheric parameters, (2013). doi:10.1364/OL.39.000060.

[6] M. Kurek, M. Carnoy, P.E. Larsen, L.H. Nielsen, O. Hansen, T. Rades, S. Schmid, A. Boisen, Nanomechanical Infrared Spectroscopy with Vibrating Filters for Pharmaceutical Analysis, Angew. Chemie Int. Ed. 56 (2017) 3901–3905. doi:10.1002/anie.201700052.

[7] X. Xie, D. Li, T.-H. Tsai, J. Liu, P. V Braun, D.G. Cahill, Thermal Conductivity, Heat Capacity, and Elastic Constants of Water- Soluble Polymers and Polymer Blends, (n.d.). doi:10.1021/acs.macromol.5b02477.

[8] X. Xie, D. Li, T.-H. Tsai, J. Liu, P. V. Braun, D.G. Cahill, Thermal Conductivity, Heat Capacity, and Elastic Constants of Water-Soluble Polymers and Polymer Blends, Macromolecules. 49 (2016) 972–978. doi:10.1021/acs.macromol.5b02477.

[9] R. Chadha, V.K. Kapoor, A. Kumar, Analytical techniques used to characterize drug-polyvinylpyrrolidone systems in solid and liquid states – An overview, J. Sci. Ind. Res. 65 (2006) 459–469.

Paper 3

Nanomechanical photothermal analysis of crosslinking reaction in thin polymeric layers

Nanomechanical photothermal analysis of crosslinking reaction in thin polymeric layers

Andrea Casci Ceccacci, Alberto Cagliani, Luca Carnevali, Paolo Marizza, Danilo Demarchi, Silvan Schmid, Anja Boisen.

Abstract

The understanding of crosslinking reactions is of the higher interest especially for polymers and peptides of recent discovery and synthesis. Conventional spectroscopic infrared techniques used for featuring the chemical modifications are well established and widely used, although they need a milligrams quantity of samples and requiring time-consuming sampling technique. Newly discovered polymer are often available in small amounts. Hence techniques which enable to study the crosslinking chemistry on small quantities of material represents a valuable asset. Nanomechanical sensors can probe the light absorption of very thin polymeric layer, therefore enabling infrared analysis on sub-picogram amount of sample. In this work, we have developed nanomechanical membrane resonators which permit the characterization of the gelification reaction in submicron thick layer of poly(vinylpyrrolidone) starting from a 535 pg of polymer. This approach further allows to identify the various phenomena occurring upon exposure to the UV light, in particular the photo-oxidation. The presented method can be easily parallelized and scaled for high sensitive infrared fingerprinting.

HYDROGEL THIN FILM; THIN FILM SPECTROSCOPY; HIGH SENSITIVITY; SUB MICROMON GELIFICATION

Introduction

Understanding the mechanism of polymer crosslinking is of paramount importance due to its relevance in material engineering [1], for several biological applications [2] and represents a key reaction mechanism in polymer chemistry. In this work, we focus on the crosslinking of hydrogels,

which are hydrophilic three-dimensional networks, able to swell and retain a significant amount of water [3]. Thanks to these characteristics these materials resemble biological tissues, making them suitable for a broad range of applications, such as tissue engineering [4,5], biomedical technology such as ophthalmic systems [6,7], wound dressings [4,8,9], and drug delivery [10–12]. Furthermore, hydrogel coatings have shown to improve the performance of implantable glucose sensors [13] and optical sensors[14]. Drug delivery systems based on hydrogels can be used to provide distinct release kinetics of therapeutics by tuning the crosslinking density [10]. The tuning of the gelification process is also fundamental when hydrogels are used as a synthetic matrix for living tissue. The crosslinking density is directly connected to the viscoelastic behaviour of hydrogels which has a strong effect on the mechanical driving force determining the fate of stem living cell [5]. Hence, regardless of the final aim of a hydrogel based device, the ability to define and control hydrogel characteristics is crucial.

Poly(vinylpyrrolidone) (PVP) has been extensively studied for biomedical and pharmaceutical applications [10,15,16], and it has been shown to form chemical hydrogels by exposure to UV light or electron beam [10,17–19]. The addition of hydrogen peroxide enhances the reaction and increases the gel fraction[19]. However, in the presence of oxygen, UV exposure also causes photo-oxidation, which deconstructs the polymer network, converting polymer strand into macroradicals [17,20–22]. Recently, top-down approaches for creating very thin hydrogels layers have attracted attention, since the formation of hydrogel thin films was typically limited to layer by layer or, hybrid methods [23,24].In this case, the formation of such hydrogels relies on the mutual interaction between the layers. The production of hydrogels by direct exposure to light simplify the gel production significantly.

However probing the chemical modification taking place in the film throughout the gelification process is often challenging[17,25], and it requires tedious and cumbersome approaches [17,26] or combining multiple characterization techniques such as quartz crystal microbalance(QCM) and Surface Plasmon Resonance(SPR)[25]. Infrared spectroscopic analysis provides information in terms of chemical bonds

forming during the crosslinking process. Therefore, Fourier transform infrared spectroscopy(FTIR) and its implementation like attenuated total reflectance (ATR) are widely used to assess the formation of chemical bonds for gel structures [10,17,27]. Nevertheless, such techniques need a minimum amount of material in the mg range to perform the analysis, and the ATR-FTIR spectra are affected by artefacts when the film thickness is smaller than the sampling depth. These artefacts are due mainly on the reflection phenomena taking place at the sample substrate interface [28–30]. These phenomena add complexity to the spectra, and they have to be considered during the interpretation of the results. With this work, we present the application of nanomechanical infrared method (NAM-IR) to PVP hydrogel crosslinking analysis. Such spectroscopic method is capable of extracting the same IR spectra as the ATR-FTIR, but does not suffer from artefacts for very thin films and can work with only a few picograms of a polymer. NAM-IR spectroscopy is based on nano-resonating structures capable of transducing the minute temperature changes happening in the polymer upon IR photon absorption. The heat generation is translated into a change of the mechanical resonance frequency, thanks to a release of stress in the mechanical structure [31–33]. It has been shown how string based NAM-IR spectroscopy can recognise spectral features even for few femtograms of material [33], thanks to their ability to resolve minute temperature variation [34]. However, the mechanical fragility of nanostring significantly limits the possibilities of sample preparation (i.e., typically only for particle based sensing), making such structures not suitable for analysis of large arrays of assays [31,35].

By using membrane resonators, the robustness of the sensor, sample handling, and the overall experimental procedure can be improved. Membrane-like structures better comply with agile sample preparation methods such as drop casting or spin coating and facilitate precise analysis of the thin films [36]. The gelification is followed directly on a membrane prepared using drop casting and subsequently irradiated to initiate the crosslinking process. The NAM-IR spectra show the typical IR spectral fingerprint of PVP hydrogel after 20 minutes of UV exposure.

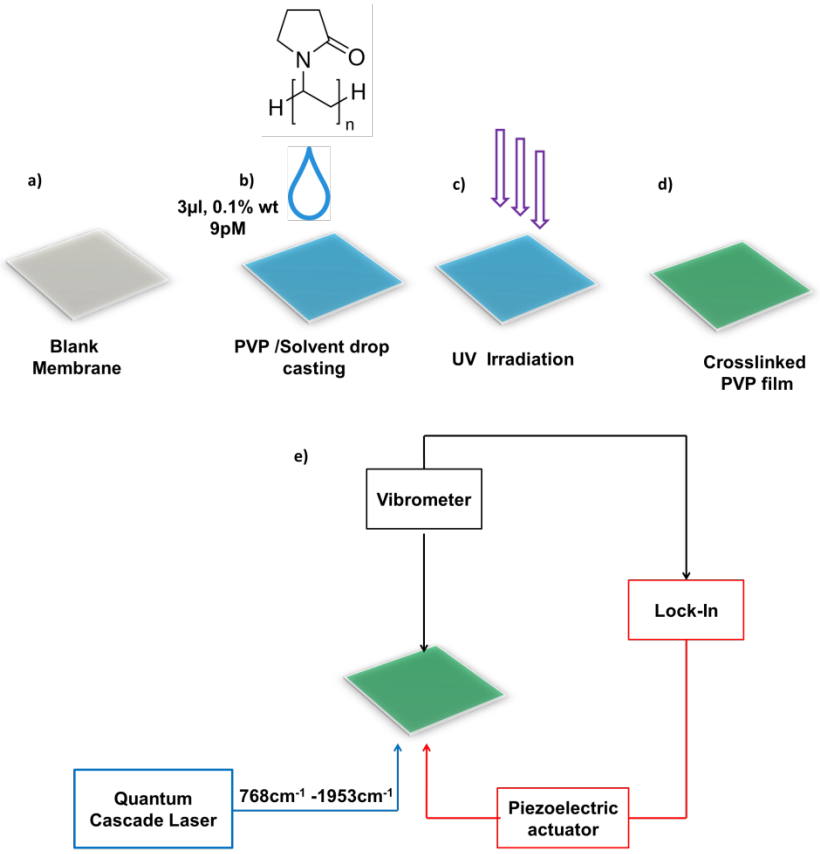

Figure 1 Experimental procedure: a) blank membrane, b) the membrane is coated using drop casting or spin coating c) and then is exposed to the UV light. d) The crosslinked film is let dry on a hot plate at 323 K and once dried, e) the NAM-IR spectra is acquired through the lock-in scheme detection as previously described[31,32,37]**.**

Experimental

Square silicon-rich silicon nitride membranes (size: 1×1 mm^2, thickness:100 nm) were fabricated by bulk micromachining. The silicon nitride was deposited by low-pressure chemical vapour deposition on a 4'' silicon wafers (LPCVD) and patterned through UV lithography and dry etching. Membrane resonators were then obtained through the removal of the bulk silicon through a KOH etching from the backside of the wafer.

The polymer solution was prepared by dissolving poly(vinylpyrrolidone) K90 powder (Mw=360 kDa, Sigma-Aldrich) with concentrations 1% and 5% wt. in aqueous solutions of hydrogen peroxide (H_2O_2, 30% Sigma-Aldrich). Hydrogen peroxide was added to achieve a faster and more efficient crosslinking process [17,19].

The experimental procedure is illustrated in Figure 1. A blank membrane (Figure 1a) is coated using two different approaches: i) spin coating aimed to obtain a fine control of the film thickness needed during the calibration phase, and then by drop casting a 3µl of polymer solution (Figure 1b) for the gelification experiments.The thickness of the spin-coated films was measured by ellipsometry. Prior to the exposure, the polymer film is wet by pipetting the same (H_2O_2 30% v/v) solution. The coated sensor chip was then exposed to UV in a chamber providing UV-B (313 nm) and UV-C radiation (256 nm) (Figure 1b-d).

For photothermal measurements, the sensor chip was mounted in a custom made vacuum chamber providing electrical connection, a glass window for optical readout, and a KBr window for IR irradiation (Figure 1e). Membranes were actuated with an external piezoelectric element and the readout with a laser-Doppler vibrometer (MSA-500, Polytech GmbH) equipped with a 632.8 nm Helium-Neon readout laser. The mechanical resonance frequency was monitored using a phase-locked loop (HF2LI-PLL, Zurich Instruments). The steps showed in Figure 1b-e are iterated to obtain and characterise a fully crosslinked film.

Results and discussion

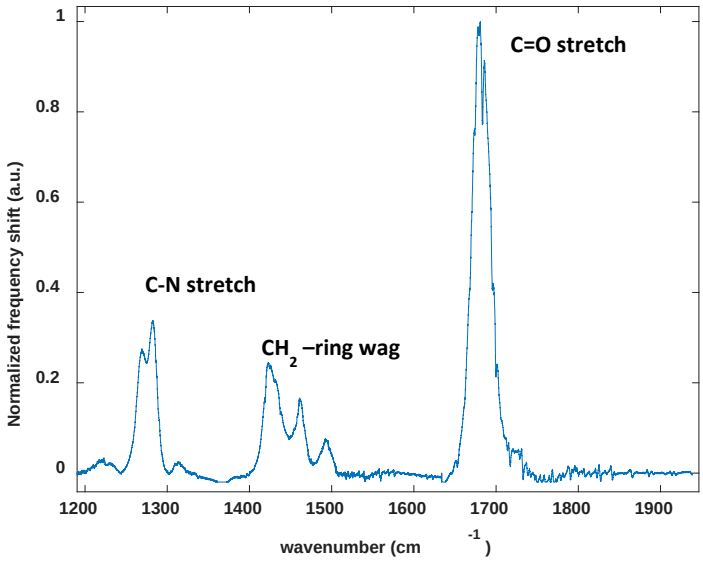

Figure 2 NAM IR spectra of PVP recorded on a 100nm coated membrane resonator. NAM-IR spectra are recorded as a negative frequency shift. Here, the spectra are mirrored along the horizontal axis achieving absorbance-like infrared spectra.

The IR spectra of PVP (see figure 2) consist of 3 main bands. The band at 1680cm^{-1} corresponds to the carbonyl bond of the pyrrolidone ring; at a lower frequency, there are two bands related to a triple peak due to the C-N stretching and CH_2-ring wagging [17,20].

To quantify the sensing performance of the photothermally induced heating by the membrane resonators, the responsivity *R* from a PVP coated membrane in two different IR spectral regions was studied (Figure 2 b-c).The responsivity curves were obtained by measuring the resonance frequency upon periodic IR irradiation, analogously on what previously shown by Miriyala et al. [38]. The procedure to obtain the responsivity curves is showed in the supplementary information.The wavelengths corresponding to the carbonyl bond stretching at 1680 cm^{-1} and to the Carbon-Nitrogen (C-N) stretch at 1290 cm^{-1} were used to test the membrane responsivity. Each point in the figure 3a-b

is the average of at least 150 points recorded on a single membrane chip. The magnitude of the photothermal response strongly depends on how efficiently the heat is transported towards the heat sinks, i.e. the body chip or the residual air in the chamber. Therefore, the responsivities were studied under two different pressure conditions: high vacuum (HV, 10^{-5} mbar) and low vacuum (LV, 1 mbar). The two pressure regimes determine different behaviours in the thermal transport; in HV conditions the heat is mainly lost by conduction throughout the body chip, instead, in LV part of the generated heat during light absorption is also dissipated by convection through the surrounding air.

These two different regimes give rise to two responsivity values, at HV, R=47 ppm μW^{-1} and at LV is R=3.8 ppm μW^{-1} on a membrane with a 200 nm PVP.

Interestingly, the responsivity curves obtained for the two different IR bands showed a linear trend relatively to the incident power, as happened for string resonators and bimaterial cantilevers[33,38] This indicates that the photothermally induced expansion of the polymer film maintains a linear behaviour throughout the incident power range tested. Such linearity clearly supports the assumption that the polymer does not reach the glass transition even at the highest incident power since the thermomechanical parameters would change drastically, and an abrupt change would be reflected in the resonance frequency [39–42]. Therefore, this linear behaviour confirms the capability of the system of obtaining IR spectra without inducing phase changes in the polymer morphology. Finally, it is interesting to notice that the responsitivity increases for polymer coated membranes compared to blank SiN (see supporting information SI).

The responsivity was further evaluated for different PVP coating thicknesses for an irradiating power of 400 µW at 10^{-5} mbar and 900 µW at 1 mbar considering the absorption peak at 1680 (Figure 3c). The same curves (figure 3c) were used as a calibration curve to estimate the thickness of the deposited layer of PVP when the drop-casting technique was used. It can be noticed that the responsivity increases for a higher amount of material deposited, due to a higher power absorption

(Figure3d) and consequently a higher heat generation. The absorbed power [43] is reported in Figure 3d. It linearly increases with the thickness of the deposited layer analogously to what has been previously showed for string based photothermal sensor [33,38]. The model used to calculate the absorbed power can be found in [43]

For resonator sensors, the frequency noise affecting the complete measurement chain is quantified by the Allan Deviation $\sigma_{(\tau)}$ therefore, the noise measurements are reported in the supplementary information. In particular, the noise measured for a membrane with 200 nm of PVP coated membrane is $\sigma_{(1s)} = 4ppm$, corresponding to a lowest detectable absorbed power at 1680 cm^{-1} of 3 nW, according to the model in [43] (see supplementary information).

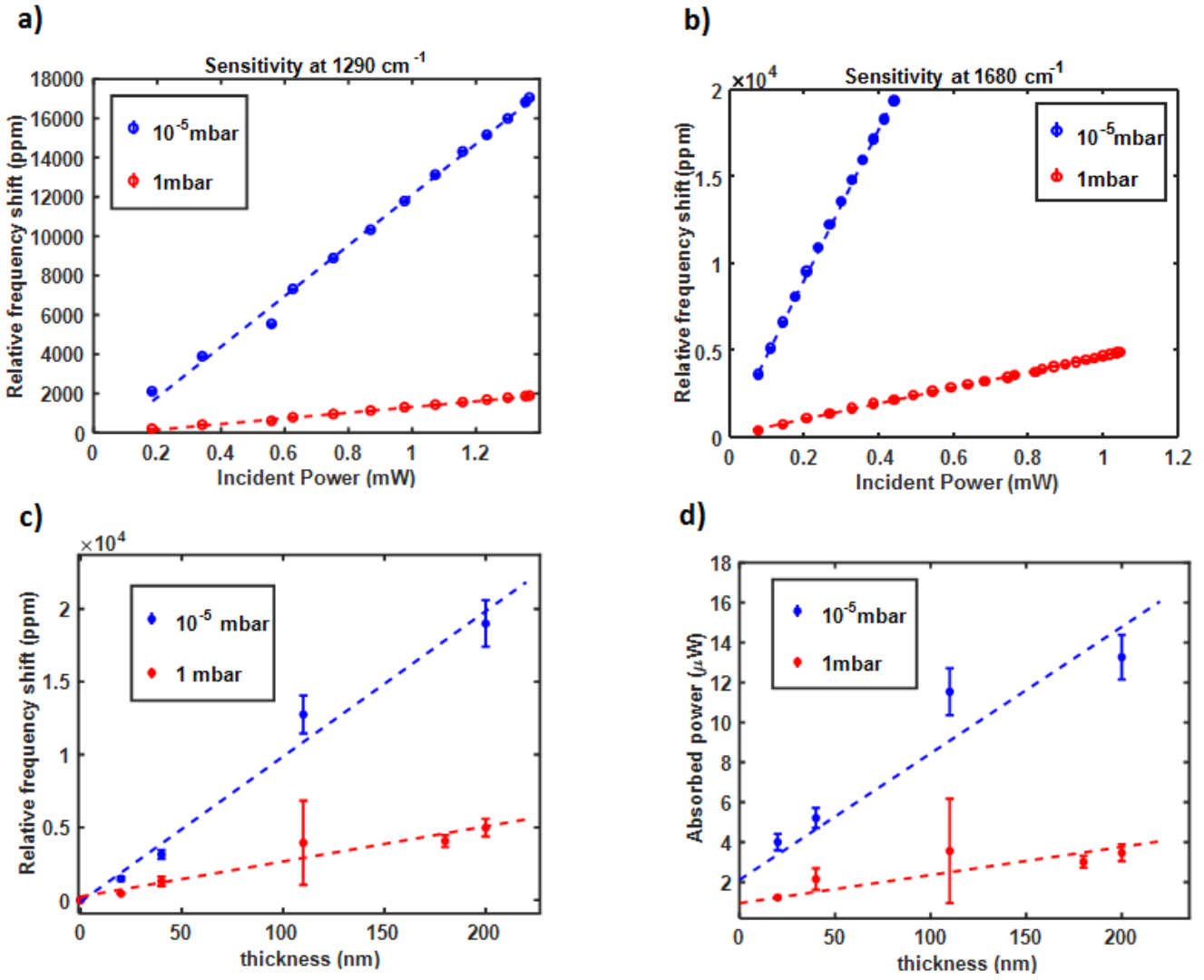

Figure 3.Responsivity and power absorption curves as a function of the polymer thickness. a) Responsivity measured on the absorption peak of the C-N bond at 10^{-5} mbar and 1 mbar;b) responsivity at the absorption peak of the carbonyl group at 1680cm^{-1}, for a 200 nm thick polymer coating at 10^{-5} mbar and 1 mbar error bars represents the standard deviation of multiple recordings on the same chip; c) amplitude of the relative frequency shift of the carbonyl peak for different PVP coating thickness at 10^{-5} mbar and 1 mbar obtained with an incident power of 400 µW and 900 µW, recorded on 3 different coated membrane ;d) absorbed power at 1 mbar and 10^{-5} mbar. PVP was deposited through spin coating and the thickness measured by ellipsometry. The spinning curves are showed in the supplementary material.

Photothermal spectra of UV crosslinked PVP

The UV crosslinking mechanism of PVP was elucidated by Zhu and co-workers [17]. They studied the gelification at different irradiation times on macroscopic hydrogel specimens. In this work, the samples were individually purified from the unreacted solution for 24 hours in deionized water and then dried in vacuum for further 24 hours. After this long sample preparation, the specimens were analysed. Such conventional approach is extremely time-consuming and is not suitable for fast analysis of a large array of polymer samples. In our work instead, we present a quicker and simpler method for realising submicron thin films of PVP hydrogel. Moreover, the NAM-IR system we used is also significantly faster and able to record the spectra with higher signal to noise ratio. In fact, NAM-IR allows recording spectra with a single acquisition with a signal to noise ratios of 200 in LV on 100 nm polymer thick layer, whereas our commercial ATR-FTIR equipment for the same polymer thickness yielded an SNR five times smaller [36]. The high SNR for NAM-IR recorded on a single acquisition allowed us to acquire each spectrum 43 times faster compared to ATR-FTIR apparatus as it would need multiple acquisitions to reach the same SNR.

The estimated thickness ranged from 80 to 300 nm (see supplementary information). To the best of our knowledge, this study is the first showing a gel formation on a submicron thick layer of PVP by direct UV illumination.

The IR spectrum of PVP can be analysed focusing on the three main bands from 1150 cm^{-1} to 2000cm^{-1}.The bands at 1300 cm^{-1} and 1450 cm^{-1} undergo significant changes during the crosslinking process and the gelification within the studied time frame of 90 min.

Variations in the spectroscopic pattern can be seen after 10 minutes of UV exposure (see Figure 3). The carbonyl group is involved in the formation of the intermolecular bonds with other polymer chains, which can be observed with shifts towards the lower frequency of the corresponding peak [17]. For

exposure times longer than 20 minutes a substantial change can be noticed in the carbonyl band at 1680 cm^{-1}. In the gel spectra, the peak shows a significant splitting, resulted in a broadening towards a lower frequency. Noteworthy, the dip is appearing in the middle of the band at 1684 cm^{-1} also present in unexposed PVP, and it is due to local power minima of the laser source (see supplementary information).

The hydrogel formation is further confirmed by assessing bands at 1400 cm^{-1} 1415 cm^{-1} and 1420cm^{-1}, respectively related to the bond wagging of C4-H and CH_2, and C-N bond stretching at 1257 cm^{-1} [17]. At the same time, the conversion of the pyrrolidone ring into succinimide ring is characterised by a strong band in the proximity of 1700 cm^{-1} related to the two carbonyl groups [17,20] which are a strong sign of the PVP gelification process [17].

The peak at 1280cm^{-1} became wider and shifted towards a higher frequency, and a new peak appears at 1215 cm^{-1} also attributed to the C-N stretching of the succinimide ring. The gel structure is further characterised by N-C-O-C bands which can be identified in spectra at 1170 cm^{-1}-1180 cm^{-1}.

Overexposure to UV light in the presence of H_2O and H_2O_2 and O_2 triggers the degradation of the polymer backbone known as photo-oxidation [22]. This phenomenon brings to the demolition of the polymer chains accompanied by the formation of degradation products [17,26,44].

With respect to PVP, UV overexposure leads to the formation of imide groups [17,26], undergoing hydrolysis and producing amide-II groups. These latter were probed by a band occurring at 1540-1550 cm^{-1} related to the N-H bending mode. Furthermore, at 1735 cm^{-1}, we noticed a shoulder of the main carbonyl peak due to the formation of carboxyl terminated non-cyclic imides [21,26,44] (Figure-3). After 90 min of exposure, the IR spectra differs sensibly from any of the previous gelificated structures [17] and the non-treated polymer. Nevertheless, the bands around 1400 cm^{-1} and 1170 cm^{-1} still show characteristic peaks related to PVP gel structure.

Although the IR spectral patterns describing the PVP gel structure are visible also for 90 min exposure time, an intensity increase of the band that is associated to photo-oxidation products was observed. As a figure of merit for describing the degree of photooxidation (see Figure 4), we evaluated the area of the band 1540-1560 cm^{-1}, normalised by the value in the same band for non-exposed PVP. This value is seen to increase as a function of the exposure time. The extent of the area doubles just for 10 minutes of exposure and becomes 16 times higher for the higher given dose at 90 min. This result further supports the hypothesis that the photo-oxidation is the prevailing phenomena when the exposure is prolonged[17,20].

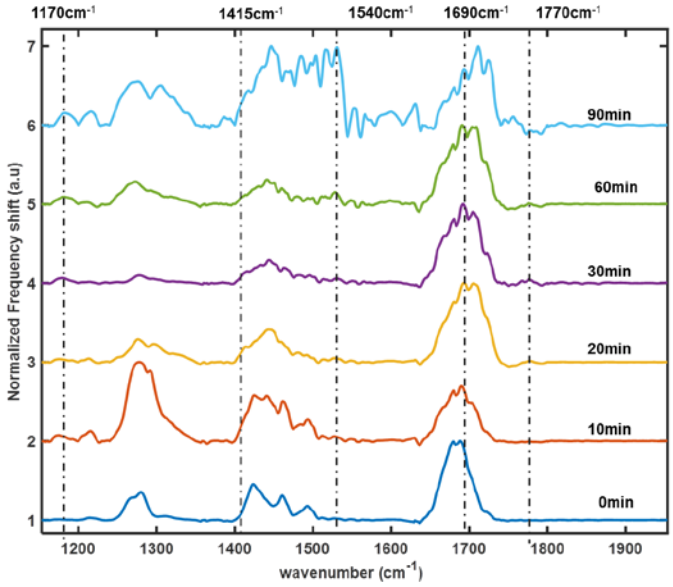

Figure 4 PVP hydrogel spectra for different exposure times. Each spectrum is the average of three acquisitions on the same membrane coated chip recorded on different location. The change in the IR spectral pattern was found being attributed to the formation of hydrogel structure.

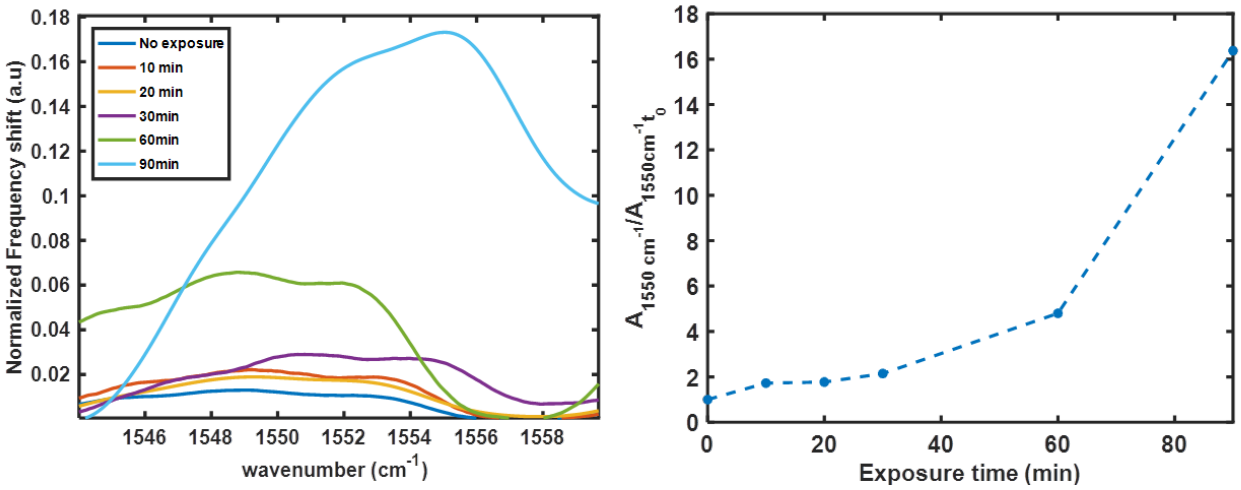

Figure 5 Effects of prolonged exposure time on the IR spectra of PVP. a) Area ascribed to the amide-II group a product of the photooxidation; b) Trend in the value of the area of the amide-II for different exposure times.

Conclusions

We have shown that the employment of prestressed membrane resonator as a photothermal sensor for characterising the gelification of thin PVP film can be a powerful analytical tool to study crosslinking of thin polymer films. The use of NAM-IR spectroscopy for monitoring the crosslinking of thin polymer film brought several advantages. The ratio SNR vs. acquisition time increased 5 times compared to conventional ATR-FTIR spectroscopy[28]. Moreover, the robustness of the membrane geometry better suits drop casting and spin coating of thin polymer layers, simplifying the sample preparation considerably.

In particular, the thickness of the dry hydrogel films and the typical IR spectral features allowed to assess the formation of gelified structures. The membrane resonators showed a responsivity up to 200 ppm nm^{-1} mW^{-1} and able to resolve up to 3 nW as absorbed power, which is in the same order of magnitude of string based photothermal spectrophotometer. The high sensitivity even at moderate vacuum conditions shown by membrane resonators allowed performing a highly defined *in situ*

infrared analysis of the gelification product and as well as characterise the photooxidation of the polymer which is important for long exposure times. A deeper understanding of the process might be obtained by investigating the transition from purely elastic film to a viscoelastic behaviour occurring during the crosslinking reaction. This might be possible by monitoring the evolution of the damping mechanism of the film on the resonating behaviour of the membrane. Finally, we envision that by tailoring the sensor features as well as the experimental setup this method can be integrated on high throughput sensing devices capable of assessing several other the physical and chemical properties.

[1] P. Ghosh, S. Katare, P. Patkar, J.M. Caruthers, V. Venkatasubramanian, K.A. Walker, SULFUR VULCANIZATION OF NATURAL RUBBER FOR BENZOTHIAZOLE ACCELERATED FORMULATIONS: FROM REACTION MECHANISMS TO A RATIONAL KINETIC MODEL, (n.d.). http://cepac.cheme.cmu.edu/pasi2008/slides/venkat/library/reading/RCT-ReviewPublishedPaper.pdf (accessed March 12, 2017).

[2] R. Kluger, A. Alagic, Chemical cross-linking and protein–protein interactions—a review with illustrative protocols, Bioorg. Chem. 32 (2004) 451–472. doi:10.1016/j.bioorg.2004.08.002.

[3] NILIMANKA DAS, PREPARATION METHODS AND PROPERTIES OF HYDROGEL: A REVIEW, Int. J. Pharm. Pharm. Sci. 5 (2013) 112–117.

[4] K.R. Kirker, Y. Luo, J.H. Nielson, J. Shelby, G.D. Prestwich, Glycosaminoglycan hydrogel films as bio-interactive dressings for wound healing, Biomaterials. 23 (2002) 3661–3671. doi:10.1016/S0142-9612(02)00100-X.

[5] O. Chaudhuri, L. Gu, D. Klumpers, M. Darnell, S.A. Bencherif, J.C. Weaver, N. Huebsch, H. Lee, E. Lippens, G.N. Duda, D.J. Mooney, Hydrogels with tunable stress relaxation regulate stem cell fate and activity, Nat. Mater. 15 (2015) 326–334. doi:10.1038/nmat4489.

[6] L. Xinming, C. Yingde, A.W. Lloyd, S. V Mikhalovsky, S.R. Sandeman, C.A. Howel, L. Liewen, Polymeric hydrogels for novel contact lens - based ophthalmic drug delivery systems : A review, (n.d.). doi:10.1016/j.clae.2007.09.002.

[7] L. Xinming, C. Yingde, A.W. Lloyd, S. V. Mikhalovsky, S.R. Sandeman, C.A. Howel, L. Liewen, Polymeric hydrogels for novel contact lens-based ophthalmic drug delivery systems: A review, Contact Lens Anterior Eye. 31 (2008) 57–64. doi:10.1016/j.clae.2007.09.002.

[8] M. Ishihara, K. Nakanishi, K. Ono, M. Sato, M. Kikuchi, Y. Saito, H. Yura, T. Matsui, H. Hattori, M. Uenoyama, A. Kurita, Photocrosslinkable chitosan as a dressing for wound occlusion and accelerator in healing process, Biomaterials. 23 (2002) 833–840. doi:10.1016/S0142-9612(01)00189-2.

[9] Z. Ajji, I. Othman, J.M. Rosiak, Production of hydrogel wound dressings using gamma radiation, Nucl. Instruments Methods Phys. Res. Sect. B Beam Interact. with Mater. Atoms. 229 (2005) 375–380. doi:10.1016/j.nimb.2004.12.135.

[10] P. Marizza, M. Abrami, S.S. Keller, P. Posocco, E. Laurini, K. Goswami, A.L. Skov, A. Boisen, D. Larobina, G. Grassi, M. Grassi, Synthesis and characterization of UV photocrosslinkable hydrogels with poly(N-vinyl-2-pyrrolidone): Determination of the network mesh size distribution, Int. J. Polym. Mater. Polym. Biomater. 65 (2016) 516–525. doi:10.1080/00914037.2015.1129964.

[11] N. Bhattarai, J. Gunn, M. Zhang, Chitosan-based hydrogels for controlled, localized drug delivery, Adv. Drug Deliv. Rev. 62 (2010) 83–99. doi:10.1016/j.addr.2009.07.019.

[12] C. Le Bourlais, L. Acar, H. Zia, P.A. Sado, T. Needham, R. Leverge, Ophthalmic drug delivery systems—Recent advances, Prog. Retin. Eye Res. 17 (1998) 33–58. doi:10.1016/S1350-9462(97)00002-5.

[13] B. Yu, C. Wang, Y.M. Ju, L. West, J. Harmon, Y. Moussy, F. Moussy, Use of hydrogel coating to improve the performance of implanted glucose sensors, Biosens. Bioelectron. 23 (2008) 1278–1284. doi:10.1016/j.bios.2007.11.010.

[14] A. Mateescu, Y. Wang, J. Dostalek, U. Jonas, Thin hydrogel films for optical biosensor applications, Membranes (Basel). 2 (2012) 49–69. doi:10.3390/membranes2010040.

[15] R.K. Mishra, M. Datt, A.K. Banthia, Synthesis and characterization of pectin/PVP hydrogel membranes for drug delivery system., AAPS PharmSciTech. 9 (2008) 395–403. doi:10.1208/s12249-008-9048-6.

[16] L. Perioli, V. Ambrogi, F. Angelici, M. Ricci, S. Giovagnoli, M. Capuccella, C. Rossi, Development of mucoadhesive patches for buccal administration of ibuprofen, J. Control. Release. 99 (2004) 73–82. doi:10.1016/j.jconrel.2004.06.005.

[17] X. Zhu, P. Lu, W. Chen, J. Dong, Studies of UV crosslinked poly(N-vinylpyrrolidone) hydrogels by FTIR, Raman and solid-state NMR spectroscopies, Polymer (Guildf). 51 (2010) 3054–3063. doi:10.1016/j.polymer.2010.05.006.

[18] K. Plungpongpan, K. Koyanukkul, A. Kaewvilai, N. Nootsuwan, P. Kewsuwan, A. Laobuthee, Preparation of PVP/MHEC Blended Hydrogels via Gamma Irradiation and their Calcium ion Uptaking and Releasing Ability, Energy Procedia. 34 (2013) 775–781. doi:10.1016/j.egypro.2013.06.813.

[19] L.C. Lopérgolo, A.B. Lugão, L.H. Catalani, Direct UV photocrosslinking of poly(N-vinyl-2-pyrrolidone) (PVP) to produce hydrogels, (n.d.). doi:10.1016/S0032-3861(03)00686-4.

[20] F. Hassouna, S. Therias, G. Mailhot, J.-L. Gardette, Photooxidation of poly(N-vinylpyrrolidone) (PVP) in the solid state and in aqueous solution, Polym. Degrad. Stab. 94 (2009) 2257–2266. doi:10.1016/j.polymdegradstab.2009.08.007.

[21] F. Hassouna, S. Morlat-Thérias, G. Mailhot, J.L. Gardette, Influence of water on the photodegradation of poly(ethylene oxide), (2007). doi:10.1016/j.polymdegradstab.2007.07.016.

[22] E. Yousif, A. Hasan, Photostabilization of poly(vinyl chloride) – Still on the run, J. Taibah Univ. Sci. 9 (2015) 421–448. doi:10.1016/j.jtusci.2014.09.007.

[23] B. Chollet, M. Li, E. Martwong, B. Bresson, C. Fretigny, P. Tabeling, Y. Tran, Multiscale Surface-Attached Hydrogel Thin Films with Tailored Architecture, ACS Appl. Mater. Interfaces. 8 (2016) 11729–11738. doi:10.1021/acsami.6b00446.

[24] E. Lee, H.-E. Jang, Y.Y. Kang, J. Kim, J.-H. Ahn, H. Mok, Submicron-sized hydrogels incorporating cyclic dinucleotides for selective delivery and elevated cytokine release in macrophages, Acta Biomater. 29

(2016) 271–281. doi:10.1016/j.actbio.2015.10.025.

[25] F.H. and, B. Kasemo, T. Nylander, Camilla Fant, and Kristin Sott, H. Elwing, Variations in Coupled Water, Viscoelastic Properties, and Film Thickness of a Mefp-1 Protein Film during Adsorption and Cross-Linking: A Quartz Crystal Microbalance with Dissipation Monitoring, Ellipsometry, and Surface Plasmon Resonance Study, (2001). doi:10.1021/AC0106501.

[26] Fatima Hassouna, Sandrine Therias, * G.M. b, Jean-Luc Gardette b, Photooxidation of poly(N-vinylpyrrolidone) (PVP) in the solid state and in aqueous solution, Polym. Degrad. Stab. (2009) 2257–2266.

[27] N.A. Mohamed, M.M. Fahmy, Synthesis and antimicrobial activity of some novel cross-linked chitosan hydrogels., Int. J. Mol. Sci. 13 (2012) 11194–209. doi:10.3390/ijms130911194.

[28] G. Laroche, J. Fitremann, N. Gherardi, FTIR-ATR spectroscopy in thin film studies: The importance of sampling depth and deposition substrate, Appl. Surf. Sci. 273 (2013) 632–637. doi:10.1016/j.apsusc.2013.02.095.

[29] G. Dupont, H. Caquineau, B. Despax, R. Berjoan, A. Dollet, Structural properties of N-rich a-Si - N:H films with a low electron-trapping rate, J. Phys. D. Appl. Phys. 30 (1997) 1064–1076. doi:10.1088/0022-3727/30/7/002.

[30] FTIR Measurement Data Storage and Control ---2 Thin Film Sample Measurement Methods and Precautions ---5 Question ---8, (n.d.). http://www.ssi.shimadzu.com/products/literature/ftir/ftir_talkletter_vol_7.pdf (accessed April 4, 2017).

[31] A. Andersen, Alina Joukainen; Yamada, Shoko; Ek, Pramod Kumar; Andresen, Thomas Lars; Boisen, S. Schmid, Nanomechanical IR spectroscopy for fast analysis of liquid-dispersed engineered nanomaterials, Sens. Actuators B. 233 (2016) 667–673.

[32] T. Larsen, S. Schmid, L.G. Villanueva, A. Boisen, Photothermal analysis of individual nanoparticulate samples using micromechanical resonators., ACS Nano. 7 (2013) 6188–93. doi:10.1021/nn402057f.

[33] T.S. Biswas, N. Miriyala, C. Doolin, X. Liu, T. Thundat, J.P. Davis, Femtogram-scale photothermal spectroscopy of explosive molecules on nanostrings., Anal. Chem. 86 (2014) 11368–72. doi:10.1021/ac503318e.

[34] A.O.N. T. Larsen,a S. Schmid, L. Grönberg, Ultrasensitive string-based temperature sensors, Appl. Phys. Lett. 98 (2011).

[35] S. Yamada, S. Schmid, T. Larsen, O. Hansen, A. Boisen, Photothermal infrared spectroscopy of airborne samples with mechanical string resonators, Anal. Chem. 85 (2013) 10531–10535. doi:10.1021/ac402585e.

[36] A.C.C.A.C.M.S.S.A. Boisen., Thin film Analysis by Nanomechanical infrared spectroscopy, Unpublished. (2017).

[37] S. Yamada, S. Schmid, T. Larsen, O. Hansen, A. Boisen, Photothermal Infrared Spectroscopy of Airborne Samples with Mechanical String Resonators, Anal. Chem. 85 (2013) 10531–10535. doi:10.1021/ac402585e.

[38] N. Miriyala, M.F. Khan, T. Thundat, Thermomechanical behavior of a bimaterial microchannel cantilever subjected to periodic IR radiation, Sensors Actuators B Chem. 235 (2016) 273–279. doi:10.1016/j.snb.2016.05.043.

[39] S. Bose, S. Schmid, T. Larsen, S.S. Keller, P. Sommer-Larsen, A. Boisen, K. Almdal, Micromechanical

string resonators: Analytical tool for thermal characterization of polymers, ACS Macro Lett. 3 (2014) 55–58. doi:10.1021/mz400470n.

[40] S. Bose, S. Schmid, T. Larsen, S. Sylvest Keller, A. Boisen, K. Almdal, Micromechanical fast quasi-static detection of α and β relaxations with nanograms of polymer, J. Polym. Sci. Part B Polym. Phys. 53 (2015) 1035–1039. doi:10.1002/polb.23745.

[41] S. Asad, M. Bukhari, M.F. Khan, A. Goswami, R. Mcgee, T. Thundat, Thermomechanical analysis of picograms of polymers using a suspended microchannel cantilever, (n.d.). doi:10.1039/c6ra25455a.

[42] N. Jung, H. Seo, D. Lee, C.Y. Ryu, S. Jeon, Nanomechanical Thermal Analysis of the Glass Transition of Polystyrene Using Silicon Cantilevers, Macromolecules. 41 (2008) 6873–6875. doi:10.1021/ma801539m.

[43] M. Kurek, M. Carnoy, P.E. Larsen, L.H. Nielsen, O. Hansen, T. Rades, S. Schmid, A. Boisen, Nanomechanical Infrared Spectroscopy with Vibrating Filters for Pharmaceutical Analysis, Angew. Chemie Int. Ed. 56 (2017) 3901–3905. doi:10.1002/anie.201700052.

[44] A. Roger, D. Sallet, J. Lemaire, Photochemistry of aliphatic polyamides. 4. Mechanisms of photooxidation of polyamides 6, 11, and 12 at long wavelengths, Macromolecules. 19 (1986) 579–584. doi:10.1021/ma00157a015.

SUPPLEMENTARY INFORMATION

1. PVP CONCENTRATION ON A 3µl drop.

Density of H_2O:H_2O_2 solvent 1.1mg/ml;

Molecular Weight of PVP k90= 360000 g/mol;

The PVP solution is concentrated at 0.1%wt. the polymer solution drop is 3µl having a mass of 3.3mg.

0.1% of 3.3 mg= corresponds to 3.3 µg which is an estimation of the mass of PVP in the drop which is cast on the total area of the membrane resonator chip plus the body-chip 1cm wide.

Considering the PVP molecular weight the amount of polymer in the whole drop corresponds to

$$\frac{Mass\ of\ PVP}{Mw} = \frac{3.3\ 10^{-6} g}{3\ 10^{5} g/_{mol}} = 9.1 pM \quad (1)$$

1.1 Mass quantification

The amount of polymer present in the drop is 3.3 µg, which result cast onto an approximately circular area of 8mm of diameter, yielding a surface density 65fg/µm^2.

The signal is provided by photothermal induced heat in generated within the laser spot which has a diameter of 100µm, or equal to an area of 7583µm^2.

Sensing mass = 7583µm^2 * 65fg/µm^2 =497pg (2)

Mass on the sensor = 65fg/um^2 *10^6 µm^2 =65ng (3)

2. PVP SPINNING CURVES

The membrane resonators were coated with this spinning parameters reported in figure s1. The spin-coated membranes were then used to obtain the calibration curve reported in the main manuscript in Figure 2c-d.

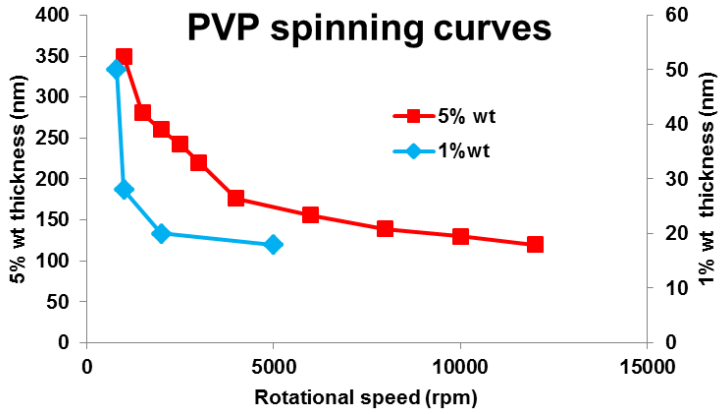

Figure s6 Spinning curves of PVP.

3. POWER SPECTRA OF THE IR LASER SOURCE

The quantum cascade laser used in this work has a non-constant power throughout the spectral range covered. The parameter that can be used to tune the power output of the laser is the duty cycle. The power spectra were recorded by a thermal sensor at the duty cycle of 1% and 4%. Which corresponds to the one used during the experiments.

a) **b)**

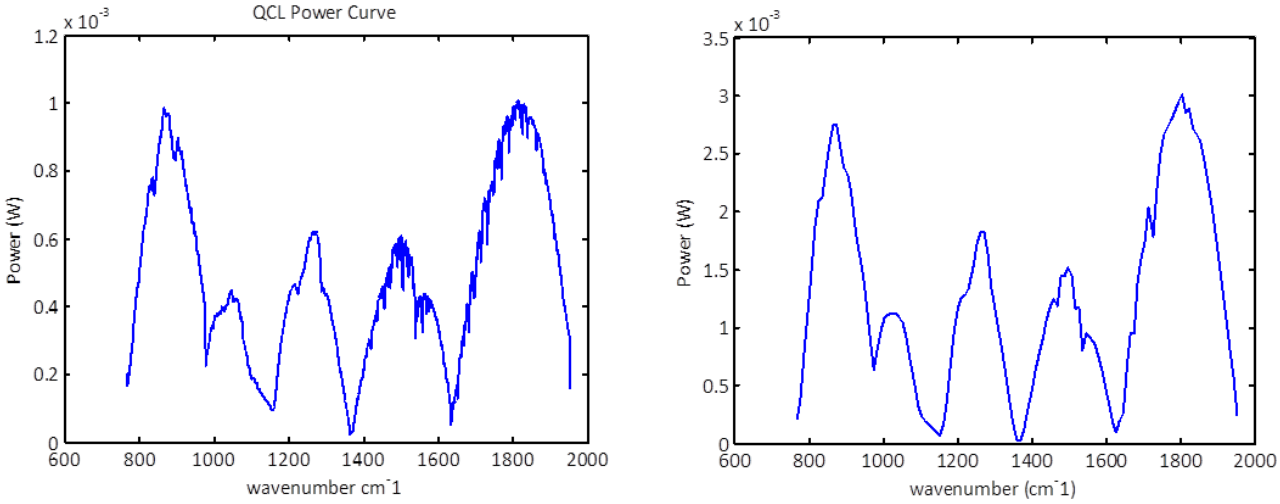

Figure s7 Power spectra for 1% DC a) and 4% DC b).

The two power spectra were recorded at two different spectral step size. For 1% DC the step size was of 1cm^{-1}, instead, for 4% DC the step size was of 10cm^{-1}. In the region between 1400 cm^{-1} and 1800 cm^{-1}, we notice several dip in the power curves which are reflected in the NAM-IR spectra.

4. EFFECT OF THE LOCAL MINIMA

The multiple local minima of the QCL laser source are reflected in the NAM-IR spectra(Figure s3) . To illustrate this effect we record the NAM-IR spectra on a PVP coated membrane and on a gold coated membrane which reflects almost all the incident IR radiation reported on a

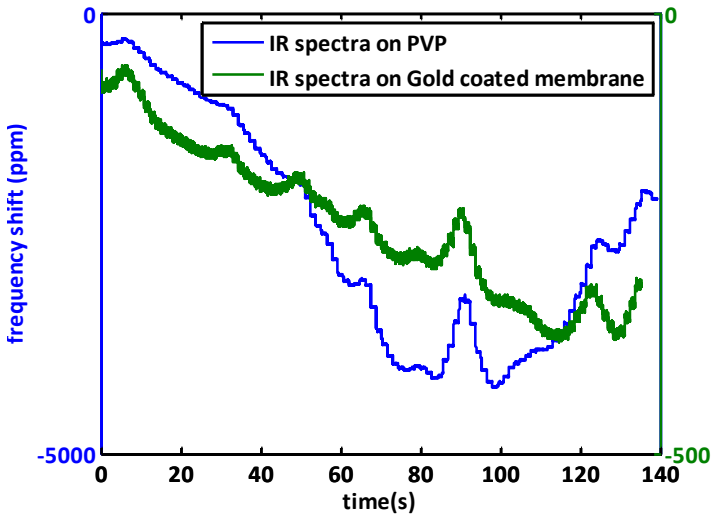

Figure s8 NAM-IR spectra recorded on a gold coated membrane and on a PVP coated membrane.

5. ENHANCEMENT OF RESPONSIVITY FOR POLYMER COATED MEMBRANES

The responsivity was also measured at 861cm^{-1} where the polymer has a very limited absorption. The responsivity increases for polymer coated membranes compared to blank SiN (figure s4). This sensing feature can be explained considering that the photothermally induced frequency shift is proportional to the ratio α/k where α is the thermal expansion coefficient and k is the thermal conductivity of the resonating structure. For a polymer coated membrane this ratio increases due to the higher thermal expansion coefficient of the polymer and the lower effective thermal conductivity of the bilayer structure. Finally, the responsivity value has to be normalised by the specific absorption coefficient.

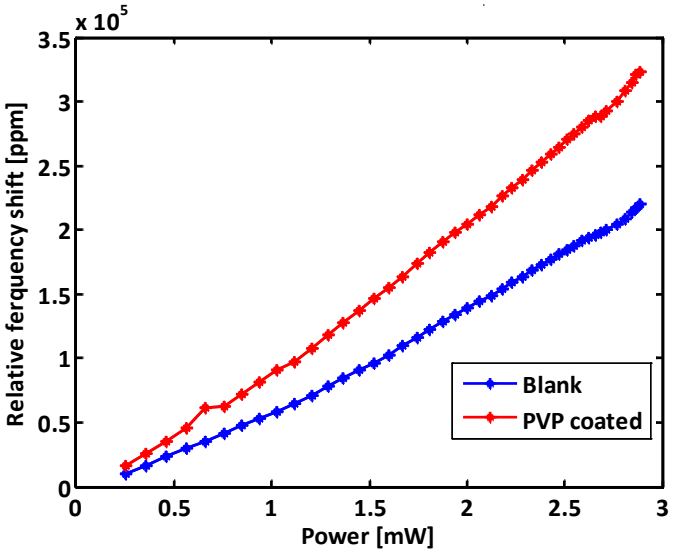

Figure s9 Relative frequency shift for a blank and polymer coated membrane measured ad 861cm^{-1} where PVP has a limited absorption. Here the responsivity is tested on a 200nm PVP coated membrane in High Vacuum 10^{-5} mbar.

6. EVALUATION OF PHOTOTHERMAL RESPONSIVITY

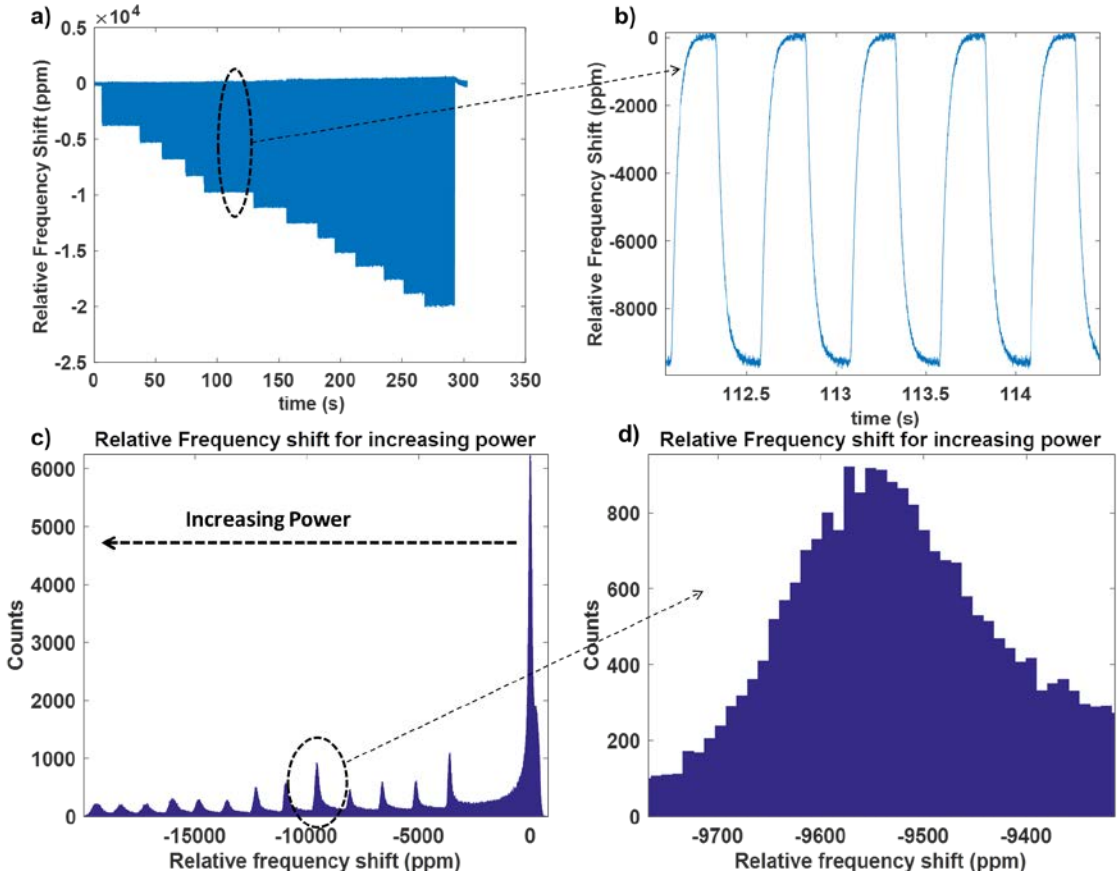

Figure s10 Methods for evaluating the photothermal responsivity of NAM-IR membrane. a) Relative frequency shift curve for increasing incident power. The light is mechanically chopped at 2Hz, giving rise to an b) ON-OFF pattern. c) Histogram of the signal reported in subfigure a, every single incident power value give rise to the distribution of resonance frequency from which the mean and standard deviation are drawn.

The resonance frequency was mechanically chopped at an arbitrary frequency, and the resonance frequency shift was recorded using the same lock-in scheme used for recording the NAM-IR spectra in the case represented in figure s5 the chopping frequency was 2 Hz.

The resonance frequency shift was recorded for increasing incident power. The on-off like pattern of the signal was statistically analysed. By studying the histogram of the relative frequency shift separate distributions can be identified (figure s5 c-d). From the analysis of these single distributions the mean value and the standard deviation were extracted and they represent a single point in the responsivity curves showed in figure 3ab of the main manuscript

7. EVALUATION OF THE PVP thickness through the calibration curve

The thickness of the deposited PVP by drop casting is evaluated by the calibration curve showed in the main manuscript (figure 3c).

The responsivity measured at 1680cm^{-1} was of 24 ppm/nm in low vacuum for a given incident power of 900µW.

Here we show the amplitudes of the carbonyl peak obtained PVP drop cast membrane resonator and by using the responsivity curves the thickness is estimated.

Table s 1 Values of estimated thickness for drop casted membranes

Chip ID	Relative frequency shift at 1680cm^{-1}	Estimated Thickness
M_125	8000 ppm	313 nm
M_142	4000 ppm	165 nm
M_133	6000 ppm	248 nm
M_136	2000ppm	82 nm
M_140	4000 ppm	165nm

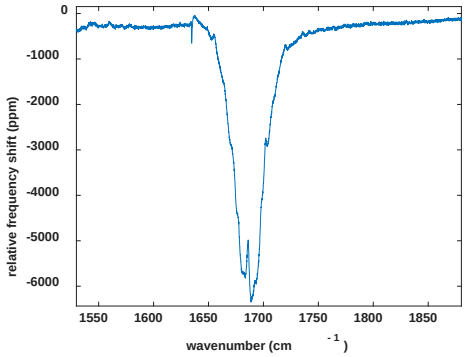

Figure s11 Membrane n 133 0-90 min

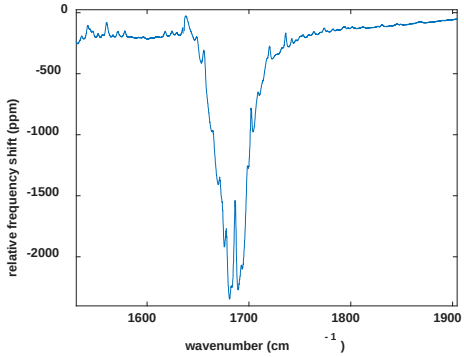

Figure s12 Membrane n 136 0-20 min

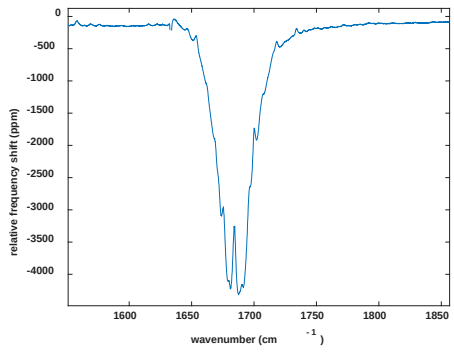

Figure s13 Membrane 140 0-20 min

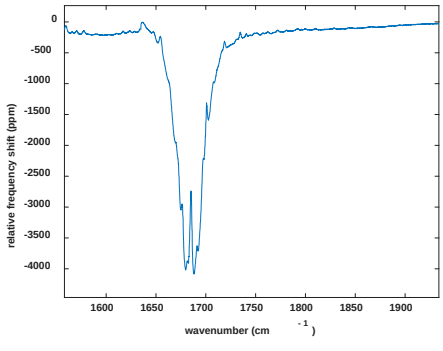

Figure s14 Membrane 140 0-60 min

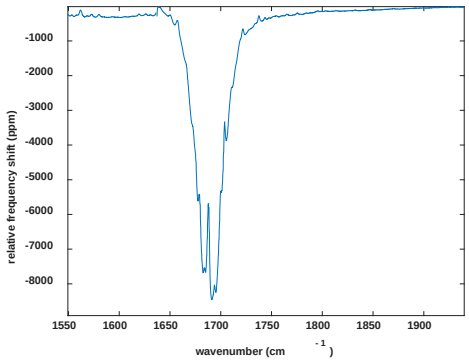

Figure s15 Membrane 125 0-60 min

4. ALLAN DEVIATION

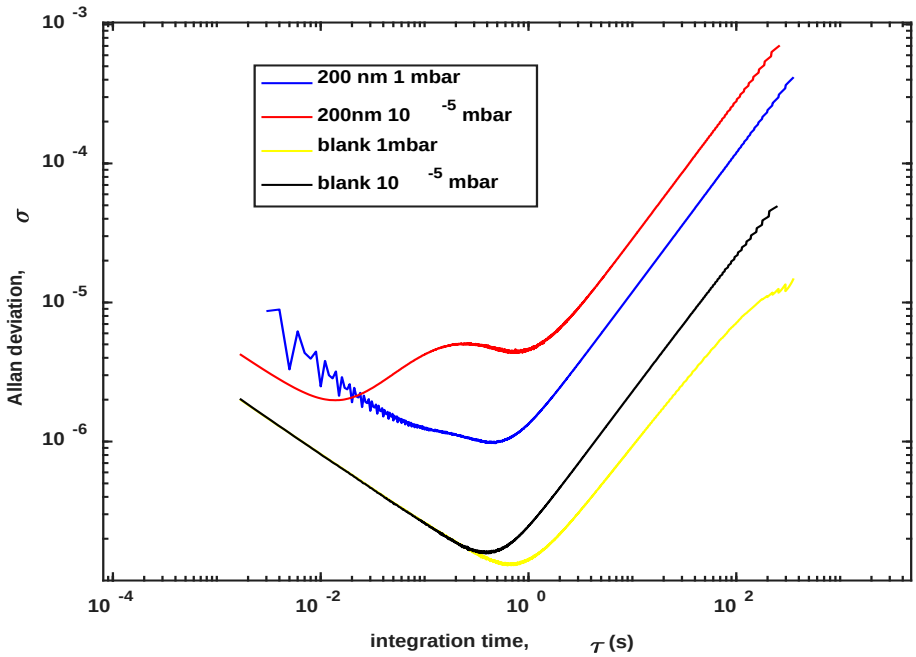

Figure s16 Allan Deviation Measurement.

Allan Deviation measurements of PVP-coated and blank membrane resonators in high vacuum and in low vacuum and reported in Figure s11. The polymer coating worsens the stability of the sensor. For high vacuum measurement, the noise is increased, this is probably due to the higher sensitivity of the membranes to the laser fluctuation.

Appendix A

Standard Operating Procedure

In the perspective to provide a user manual for operating with the systems this last section shows a step by step description of all the procedure needed to operate with the system.

1. Switch on the Power supply.
    a. Check that the PC recognises the 2 Blu-ray devices.
2. Open the last version of the *Bridge Measurement Control Software.*
    a. Wait initialization of the BR and the motor unit
    b. Once the Led light in the bottom left corner is Green, the system is ready to operate
3. Manual Initialization of the Motor.
    a. Bring the PUH to the leftmost corner and then to the righter most corner, being sure that the all the 8191 step of the motor were done in either direction, right to left(0 to 8191) and left to right(8191 to 0).
    b. Align the stage-motor y direction.
        i. Hold the stage and make sure that the PUH is in the centre of the microfluidic cartridge.
        ii. Bring the motor position counter around position 4000. In this way the motor will have half of the run to reach the bottom/upper part of the microfluidic cartridge.
        iii. Align the stage in the centre of the microbridge chip we want to measure.
        iv. Place a beam finder on the top of the cartridge in order to see the shadow of the Blu-Ray light.
        v. Start moving the stage with single step size in order to see the Blu-Ray light passing through the holes in the chip device.
        vi. The number of steps needed to cover 1000μm are around 250.
        vii. Once the light is starting to be visible regulate the number of steps according to the bridge width.
        viii. Save the y position.
4. Manually focus on one bridge, preferably the central one.
    a. Adjust the PUH-bridges distance by acting on the z-direction screw.
    b. Focus in the central part of the S-curve.
    c. Save the VCM position

5. Repeat the step 4b-iii-vii for measuring different bridges array.
    a. Focus on one bridge of the i^{th}, by only adjusting the VCM position
    b. Focus in the central part of the S-curve
    c. Save the VCM position once focused.
6. Repeat step 5 for the different bridge that we want to measure.
7. Repeat step n 3a.
8. Set Delay and threshold 10ms and 100 are reference value)
9. Set the number of Measurement
10. Press the ONE-button

Appendix B

Analytical Model for calculating the photothermal induced frequency shift

Developed by Professor Ole Hansen

Analytical Model for calculating the time constant of photothermally heated membrane

Developed by Professor Ole Hansen

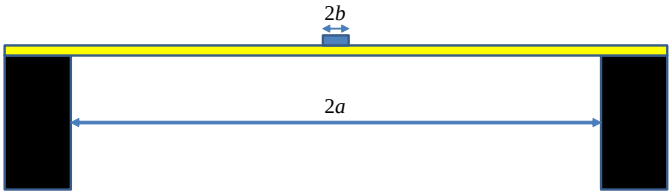

Equation of motion for a stressed membrane:

$$\begin{aligned} \varrho h\ddot{w} - \sigma_0 h \nabla_\perp^2 w &= p \\ \varrho h\ddot{w} - \sigma_0 h \frac{1}{r}\frac{\partial}{\partial r}\left(r\frac{\partial w}{\partial r}\right) &= p, \text{ (rotational symmetry)} \end{aligned}$$

Boundary conditions $w(a) = 0$ and $w(0)$ finite. Eigen-mode equation

$$\omega_n^2 \frac{\varrho}{\sigma_0} w + \frac{1}{r}\frac{\partial}{\partial r}\left(r\frac{\partial w}{\partial r}\right) = \omega_n^2 \frac{\varrho}{\sigma_0} w + \frac{1}{r}\frac{\partial w}{\partial r} + \frac{\partial^2 w}{\partial r^2} = 0$$

with the solution $w(r) = \mathrm{J}_0\left(r\sqrt{\omega_n^2 \frac{\varrho}{\sigma_0}}\right) = \mathrm{J}_0\left(k_n r\right)$ with the BC we have $w(a) = \mathrm{J}_0\left(k_n a\right) = \mathrm{J}_0\left(a\sqrt{\omega_n^2 \frac{\varrho}{\sigma_0}}\right) = 0$.

The first root of the bessel function is 2.4048, i.e., $a\sqrt{\omega_0^2 \frac{\varrho}{\sigma_0}} = ak_0 = 2.4048$ and the first angular resonant frequency is then

$$\omega_0 = \frac{2.4048}{a}\sqrt{\frac{\sigma_0}{\varrho}}$$

and

$$f_0 = \frac{2.4048}{2\pi a}\sqrt{\frac{\sigma_0}{\varrho}}.$$

Heat transfer: Fourier's law

$$\mathbf{J}_q = -\kappa \nabla T$$

where κ is the thermal conductivity. The heat continuity equation is

$$\begin{aligned} C_V \frac{\partial T}{\partial t} &= -\nabla \cdot \mathbf{J}_q + q \Rightarrow \\ C_V \frac{\partial T}{\partial t} &= \kappa \nabla^2 T + q \end{aligned}$$

where q is the heat dissipated per volume and C_V the heat capacity per unit volume at constant volume. In steady state

$$\kappa \nabla^2 T + q = 0 \Rightarrow \nabla^2 T = -q/\kappa$$

by integration across the thickness of the membrane, and assuming zero temperature gradient in the z-direction, we have

$$\nabla^2 T = -\frac{Q}{\kappa h} = \frac{1}{r}\frac{\partial}{\partial r}\left(r\frac{\partial T}{\partial r}\right)$$

where Q is the heat dissipated per unit surface area. Assume now that the dissipation is confined to $r < b$ an the temperature at $r = a$ is fixed, then the temperature varies logarithmically for $r > b$, i.e.,

$$\begin{aligned}
\Delta T(r) &= A \ln \frac{r}{a} \\
\frac{\partial T}{\partial r} &= \frac{A}{r} \\
\frac{A}{b} &= -\frac{P}{\kappa h}\frac{1}{2\pi b} \Rightarrow A = -\frac{P}{2\pi\kappa h}
\end{aligned}$$

$$\Delta T(r) = A \ln \frac{r}{a} = -\frac{P}{2\pi\kappa h} \ln \frac{r}{a}, \text{ for } a > r > b$$

where $P = Q\pi b^2$. Inside the heated disc the temperature becomes

$$\Delta T = \frac{1}{4}\frac{Q}{\kappa h}\left(b^2 - r^2\right) - \frac{Q\pi b^2}{2\pi\kappa h} \ln \frac{b}{a} = \frac{1}{4}\frac{P}{\pi\kappa h}\frac{\left(b^2 - r^2\right)}{b^2} - \frac{P}{2\pi\kappa h} \ln \frac{b}{a}$$

Stress-strain and displacement relations (assuming $\sigma_z = 0$ due to the free surface, $v = 0$ due to rotational symmetry)

$$\begin{aligned}
\epsilon_r &= \frac{1}{E}\left(\sigma_r - \nu\sigma_\theta\right) + \alpha\Delta T = \frac{\partial u}{\partial r} \\
\epsilon_\theta &= \frac{1}{E}\left(\sigma_\theta - \nu\sigma_r\right) + \alpha\Delta T = \frac{u}{r} + \frac{\partial v}{r\partial\theta} = \frac{u}{r} \\
\epsilon_z &= \frac{1}{E}\left(-\nu\sigma_\theta - \nu\sigma_r\right) + \alpha\Delta T = \frac{\partial w}{\partial z} \\
\gamma_{r\theta} &= \frac{\partial u}{r\partial\theta} + \frac{\partial v}{\partial r} - \frac{v}{r} = 0
\end{aligned}$$

i.e.,

$$\begin{aligned}
u &= r\left(\frac{1}{E}\left(\sigma_\theta - \nu\sigma_r\right) + \alpha\Delta T\right) \\
u &= \int\left(\frac{1}{E}\left(\sigma_r - \nu\sigma_\theta\right) + \alpha\Delta T\right)\mathrm{d}r
\end{aligned}$$

Equation of equilibrium

$$\frac{\partial\sigma_r}{\partial r} + \frac{\sigma_r - \sigma_\theta}{r} = 0$$

Timoshenko

$$\begin{aligned}
\sigma_r &= -\alpha E \frac{1}{r^2}\int_0^r Trdr + \frac{E}{1-\nu^2}\left(C_1(1+\nu) - \frac{C_2}{r^2}(1-\nu)\right) \\
\sigma_\theta &= \alpha E \frac{1}{r^2}\int_0^r Trdr - \alpha ET + \frac{E}{1-\nu^2}\left(C_1(1+\nu) + \frac{C_2}{r^2}(1-\nu)\right) \\
u &= (1+\nu)\alpha\frac{1}{r}\int_0^r Trdr + C_1 r + \frac{C_2}{r}
\end{aligned}$$

$u(0) = 0 \Rightarrow C_2 = 0$, and $u(a) = 0 \Rightarrow 0 = (1+\nu)\alpha\frac{1}{a}\int_0^a Trdr + C_1 a \Rightarrow$

$$C_1 = -(1+\nu)\alpha\frac{1}{a^2}\int_0^a Trdr$$

$$\begin{aligned}
\sigma_r &= -\alpha E \frac{1}{r^2}\int_0^r Trdr - \frac{(1+\nu)^2\alpha E}{1-\nu^2}\frac{1}{a^2}\int_0^a Trdr \\
\sigma_r &= -\alpha E \frac{1}{r^2}\int_0^r Trdr - \frac{(1+\nu)\alpha E}{1-\nu}\frac{1}{a^2}\int_0^a Trdr
\end{aligned}$$

$$\begin{aligned}
\sigma_\theta &= \alpha E \frac{1}{r^2}\int_0^r Trdr - \alpha ET - \frac{(1+\nu)^2\alpha E}{1-\nu^2}\frac{1}{a^2}\int_0^a Trdr \\
&= \alpha E \frac{1}{r^2}\int_0^r Trdr - \alpha ET - \frac{(1+\nu)\alpha E}{1-\nu}\frac{1}{a^2}\int_0^a Trdr
\end{aligned}$$

0.1 Stress profile

Outside the heated area we have $\Delta T(r) = A\ln\frac{r}{a} = -\frac{P}{2\pi\kappa h}\ln\frac{r}{a}$, $A = -\frac{P}{2\pi\kappa h}$ and then

$$\begin{aligned}
\sigma_r &= -\alpha E \frac{1}{r^2}\int_0^r Trdr - \frac{(1+\nu)\alpha E}{1-\nu}\frac{1}{a^2}\int_0^a Trdr \\
&= -\alpha E \frac{A}{r^2}\int_0^r r\ln\left(\frac{r}{a}\right)dr - \frac{(1+\nu)\alpha E}{1-\nu}\frac{A}{a^2}\int_0^a r\ln\left(\frac{r}{a}\right)dr
\end{aligned}$$

since $\int r\ln\left(\frac{r}{a}\right)dr = \frac{1}{2}r^2\left(\ln\frac{r}{a} - \frac{1}{2}\right)$ we have $\int_0^r r\ln\left(\frac{r}{a}\right)dr = \frac{1}{2}r^2\left(\ln\frac{r}{a} - \frac{1}{2}\right)$ and $\int_0^a r\ln\left(\frac{r}{a}\right)dr = -\frac{1}{4}a^2$, thus

$$\begin{aligned}
\sigma_r &= -\alpha E\frac{A}{r^2}\frac{1}{2}r^2\left(\ln\frac{r}{a} - \frac{1}{2}\right) - \frac{(1+\nu)\alpha E}{1-\nu}\frac{A}{a^2}\left(-\frac{1}{4}a^2\right) = \\
&= -\alpha EA\frac{1}{2}\left(\ln\frac{r}{a} - \frac{1}{2}\right) + \frac{(1+\nu)\alpha E}{1-\nu}\frac{A}{4} = \\
\sigma_r &= \frac{1}{2}A\alpha E\left(\frac{1}{1-\nu} - \ln\frac{r}{a}\right) = -\frac{P}{2\pi\kappa h}\frac{\alpha E}{2}\left(\frac{1}{1-\nu} - \ln\frac{r}{a}\right) \\
\sigma_r &= -\frac{\alpha EP}{4\pi\kappa h}\left(\frac{1}{1-\nu} - \ln\frac{r}{a}\right) = \frac{\alpha EP}{4\pi\kappa h}\left(\ln\frac{r}{a} - \frac{1}{1-\nu}\right)
\end{aligned}$$

0.2 Equation of motion

When the stress is dependent on radial position the equation of motion must be modified

$$\begin{aligned}
\varrho h\ddot{w} - \frac{1}{r}\frac{\partial}{\partial r}\left(\sigma h r \frac{\partial w}{\partial r}\right) &= p \\
\varrho\ddot{w} - \frac{1}{r}\frac{\partial}{\partial r}\left(\sigma r \frac{\partial w}{\partial r}\right) &= \frac{p}{h} \\
\varrho\ddot{w} - \sigma\left[w''_{rr} + \frac{1}{r}w'_r\right] - \sigma'_r w'_r &= \frac{p}{h}
\end{aligned}$$

where $\sigma = \sigma_0 + \sigma_r(r)$

This equation can probably not be solved with the logarithmic dependent stress. But with Rayleighs quotiont we may get some progress anyway. Assuming harmonic solutions to the homogeneous equation we get

$$\omega^2\varrho w + \sigma\left[w''_{rr} + \frac{1}{r}w'_r\right] + \sigma'_r w'_r = 0$$

and then

$$\begin{aligned}
\omega^2 &= -\frac{\int\left(\sigma\left[w''_{rr} + \frac{1}{r}w'_r\right] + \sigma'_r w'_r\right) w r dr}{\int(\varrho w)\, w r dr} = -\frac{\int_0^a\left(\sigma\left[y''_{rr} + \frac{1}{r}y'_r\right] + \sigma'_r y'_r\right) y r dr}{\int_0^a(\varrho y)\, y r dr} \\
&\simeq -\frac{\int_0^a\left(\sigma_0\left[y''_{rr} + \frac{1}{r}y'_r\right]\right) y r dr + \int_0^a\left(\sigma_r\left[y''_{rr} + \frac{1}{r}y'_r\right] + \sigma'_r y'_r\right) y r dr}{\int_0^a(\varrho y)\, y r dr} \\
&= \omega_0^2\left[1 + \frac{\int_0^a\left(\sigma_r\left[y''_{rr} + \frac{1}{r}y'_r\right] + \sigma'_r y'_r\right) y r dr}{\int_0^a\left(\sigma_0\left[y''_{rr} + \frac{1}{r}y'_r\right]\right) y r dr}\right]
\end{aligned}$$

where $y(r) = \mathrm{J}_0(k_0 r)$ is the eigenmode for $\sigma = \sigma_0$. Here $y''_{rr} + \frac{1}{r}y'_r = -k_0^2\,\mathrm{BesselJ}_0(rk_0) = -k_0^2 y$

Thus

$$\begin{aligned}
\omega^2 &= \omega_0^2\left[1 + \frac{\int_0^a\left(\sigma_r\left[y''_{rr} + \frac{1}{r}y'_r\right] + \sigma'_r y'_r\right) y r dr}{\int_0^a\left(\sigma_0\left[y''_{rr} + \frac{1}{r}y'_r\right]\right) y r dr}\right] = \omega_0^2\left[1 + \frac{\int_0^a\left(-k_0^2 y\sigma_r + \sigma'_r y'_r\right) y r dr}{\int_0^a\left(-k_0^2 y\sigma_0\right) y r dr}\right] \\
&= \omega_0^2\left[1 + \frac{\int_0^a\left(-k_0^2 y^2\sigma_r + \sigma'_r y'_r y\right) r dr}{\int_0^a\left(-k_0^2 y^2\sigma_0\right) r dr}\right] = \omega_0^2\left[1 + \frac{\int_0^a\left(\sigma_r y^2 - \frac{\sigma'_r}{k_0^2}y'_r y\right) r dr}{\sigma_0\int_0^a y^2 r dr}\right]
\end{aligned}$$

The integrals

$\int_0^a y^2 r dr = \int_0^a \mathrm{J}_0^2(k_0 r)\, r dr = \left[\frac{1}{2}r^2\left(\mathrm{J}_0^2(rk_0) + \mathrm{J}_1^2(rk_0)\right)\right]_0^a = \frac{1}{2}a^2\mathrm{J}_1^2(ak_0)$

$\int_0^a \left(\ln\left(\frac{r}{a}\right)\right) y^2 r dr = \int_0^a \left(\ln\left(\frac{r}{a}\right)\right)\mathrm{J}_0^2(k_0 r)\, r dr = \left[\frac{r^2}{4}\left[\left(2\ln\frac{r}{a} - 1\right)\mathrm{J}_0^2(k_0 r) + 2\left(\ln\frac{r}{a} - 1\right)\mathrm{J}_1^2(k_0 r) + \mathrm{J}_0(k_0 r)\,\mathrm{J}_2($

$\int_0^a \left(\ln\left(\frac{r}{a}\right)\right) y^2 r dr = \frac{a^2}{4}\left[-2\mathrm{J}_1^2(k_0 a)\right] = -\frac{a^2}{2}\mathrm{J}_1^2(k_0 a)$

$\int_0^a \frac{1}{r} y_r' y r dr = -k_0 \int_0^a \mathrm{J}_1(k_0 r)\,\mathrm{J}_0(k_0 r)\,dr = \left[\frac{1}{2}\mathrm{J}_0^2(k_0 r)\right]_0^a = -\frac{1}{2}$
Since we have

$$\begin{aligned}
\sigma_r &= -\frac{\alpha E P}{4\pi\kappa h}\left(\frac{1}{1-\nu} - \ln\frac{r}{a}\right) = \frac{\alpha E P}{4\pi\kappa h}\left(\ln\frac{r}{a} - \frac{1}{1-\nu}\right) = B\left(\ln\frac{r}{a} - \frac{1}{1-\nu}\right) \\
\sigma_r' &= \frac{B}{r}
\end{aligned}$$

we get

$$\begin{aligned}
\omega^2 &= \omega_0^2\left[1 + \frac{\int_0^a \left(\sigma_r y^2 - \frac{\sigma_r'}{k_0^2} y_r' y\right) r dr}{\sigma_0 \int_0^a y^2 r dr}\right] = \omega_0^2\left[1 + \frac{-\frac{a^2}{2}\mathrm{J}_1^2(k_0 a)\,B - \frac{1}{1-\nu}B\frac{1}{2}a^2\mathrm{J}_1^2(ak_0) - \frac{B}{k_0^2}\left(-\frac{1}{2}\right)}{\sigma_0 \frac{1}{2}a^2\mathrm{J}_1^2(ak_0)}\right] \\
&= \omega_0^2\left[1 + \frac{B}{\sigma_0}\left(-1 - \frac{1}{1-\nu} + \frac{1}{k_0^2 a^2 \mathrm{J}_1^2(ak_0)}\right)\right] = \omega_0^2\left[1 + \frac{B}{\sigma_0}\left(-\frac{2-\nu}{1-\nu} + \frac{1}{k_0^2 a^2 \mathrm{J}_1^2(ak_0)}\right)\right] = \\
&= \omega_0^2\left[1 + \frac{B}{\sigma_0}\left(-\frac{2-\nu}{1-\nu} + \frac{1}{1.5587}\right)\right] = \omega_0^2\left[1 + \frac{\alpha E P}{4\pi\kappa h}\frac{1}{\sigma_0}\left(-\frac{2-\nu}{1-\nu} + \frac{1}{1.5587}\right)\right] \\
\omega^2 &= \omega_0^2\left[1 - \frac{\alpha E P}{4\pi\kappa h}\frac{1}{\sigma_0}\left(\frac{2-\nu}{1-\nu} - \frac{1}{1.5587}\right)\right] = \omega_0^2\left[1 - \frac{\alpha E P}{4\pi\kappa h}\frac{1}{\sigma_0}\left(\frac{1.3584 - 0.35844\nu}{1-\nu}\right)\right]
\end{aligned}$$

where $ak_0 = 2.4048$
The final result is that

$$\begin{aligned}
\frac{\omega^2}{\omega_0^2} &= 1 - \frac{\alpha E P}{4\pi\kappa h}\frac{1}{\sigma_0}\left(\frac{1.3584 - 0.35844\nu}{1-\nu}\right) \\
\frac{\omega}{\omega_0} &= \sqrt{1 - \frac{\alpha E P}{4\pi\kappa h}\frac{1}{\sigma_0}\left(\frac{1.3584 - 0.35844\nu}{1-\nu}\right)} \\
&\simeq 1 - \frac{\alpha E P}{8\pi\kappa h}\frac{1}{\sigma_0}\left(\frac{1.3584 - 0.35844\nu}{1-\nu}\right)
\end{aligned}$$

or

$$\frac{\Delta f}{f_0} \simeq -\frac{\alpha E P}{8\pi\kappa h}\frac{1}{\sigma_0}\left(\frac{1.3584 - 0.35844\nu}{1-\nu}\right)$$

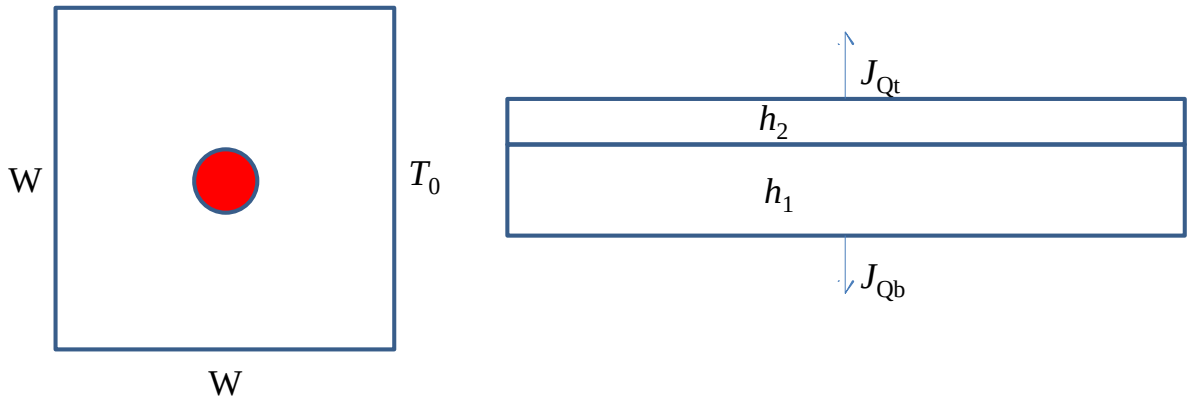

Here we consider a square membrane (side length W) consisting of several planar layers with thicknesses h_i, thermal conductivity κ_i and heat capacity per volume c_i, where $i \in [1, 2 \ldots N]$. The perimeter of the membrane is kept at temperature $T = T_0$ and the membrane is heated by absorbing photons from a collimated light beam with a gaussian intensity profile, the absorbed power is P. The membrane may lose heat to the ambient gas at pressure p; the magnitude of the heat flux densities are $J_{Q\text{top}}$ and $J_{Q\text{bott}}$ at the top and bottom of the membrane, respectively.

The heat continuity equation is

$$c_i \frac{\partial T}{\partial t} = -\nabla \cdot \mathbf{J}_{Qi} + q(r,t) = \nabla \cdot (\kappa_i \nabla T) + q(r,t) \simeq \kappa_i \nabla_\perp^2 T + \frac{\partial}{\partial z}\left(\kappa_i \frac{\partial T}{\partial z}\right) + q(r,t)$$

where $q(r,t)$ is the heat dissipation rate per unit volume and $\mathbf{J}_{Qi} = -\kappa_i \nabla T$ is the heat current density, while $\nabla_\perp^2$ is the two-dimensional Laplacian. Since the membrane is very thin compared to the width, we may take the temperature as approximately constant in the z-direction; then an integral across the total thickness of the membrane results in

$$\left(\sum_i h_i c_i\right) \frac{\partial T}{\partial t} = \left(\sum_i h_i \kappa_i\right) \nabla_\perp^2 T - J_{Q\text{top}} - J_{Q\text{bott}} + Q(x,y,t)$$

where $Q(x,y,t)$ is the dissipated power area density.

In a fairly large range of ambient pressures $J_{Q\text{top}}$ and $J_{Q\text{bott}}$ may be expected to vary linearily with pressure and membrane temperature, since the impinging molecular flux density is $\frac{1}{4}nv$ and each molecule is expected to remove the energy $\frac{f}{2}k_B(T - T_0)$ where f is the number of degrees of freedom for the molecules (say $f = 6$), $n = p/\left(k_B T_0\right)$ is the molecular density and v the mean molecular speed. It follows that

$$J_{Q\text{top}} = J_{Q\text{bott}} = \frac{1}{4} n v \frac{f}{2} k_B (T - T_0) = \frac{pvf}{8T_0}\left(T - T_0\right) = \frac{1}{2} H \left(T - T_0\right).$$

And then the final PDE governing the temperature becomes

$$\left(\sum_i h_i c_i\right)\frac{\partial T}{\partial t} = \left(\sum_i h_i \kappa_i\right)\nabla_\perp^2 T - H\left(T - T_0\right) + Q(x,y,t)$$

where we for convenience may take $T_0 = 0$ such that the temperatures in the equation are the deviatory temperature, thus

$$\begin{aligned} C\frac{\partial T}{\partial t} &= K\nabla_\perp^2 T - HT + Q(x,y,t);\; C = \left(\sum_i h_i c_i\right) \text{ and } K = \left(\sum_i h_i \kappa_i\right) \\ \frac{1}{D}\frac{\partial T}{\partial t} &= \nabla_\perp^2 T - \frac{H}{K}T + \frac{Q(x,y,t)}{K};\; \text{with } D = \frac{\sum_i h_i \kappa_i}{\sum_i h_i c_i} \end{aligned}$$

At first we are only interessted in solutions that are symmetrical in x and y and we may assume product solutions of the form $\varphi_n = A_n \cos(k_n x)\cos(k_n y)\exp\left(-\frac{t}{\tau_n}\right)$ with $\cos(k_n W/2) = 0 \Rightarrow k_n = \frac{\pi(2n+1)}{W}$. For the homogeneous part of the PDE we then get

$$\begin{aligned} -\frac{1}{D\tau_n} &= -2k_n^2 - \frac{H}{K} \Rightarrow \frac{1}{\tau_n} = D\left(2k_n^2 + \frac{H}{K}\right) \\ \tau_n &= \frac{1}{D\left(2k_n^2 + \frac{H}{K}\right)} \end{aligned}$$

In particular for the first mode ($n = 0$) which decays slower than the higher modes

$$\begin{aligned} \frac{1}{\tau_0} &= D\left(2k_0^2 + \frac{H}{K}\right) = D\left(\frac{2\pi^2}{W^2} + \frac{H}{K}\right) \\ &= \frac{2\pi^2}{W^2}\frac{\sum_i h_i \kappa_i}{\sum_i h_i c_i} + \frac{H}{\sum_i h_i c_i} \end{aligned}$$

A numerical evaluation using:
$\kappa_1 = 20\,\mathrm{W\,m^{-1}\,K^{-1}}$
$c_1 = \varrho C_p = 3100\,\mathrm{kg\,m^{-3}} \times 700\,\mathrm{J\,kg^{-1}\,K^{-1}}$
$W = 1\,\mathrm{mm}$
$h_1 = 100\,\mathrm{nm}$
results in $\tau_0 = \left(\frac{2\pi^2}{(1\,\mathrm{mm})^2}\frac{20\,\mathrm{W\,m^{-1}\,K^{-1}}}{3100\,\mathrm{kg\,m^{-3}}\times 700\,\mathrm{J\,kg^{-1}\,K^{-1}}}\right)^{-1} = 5.5\,\mathrm{ms}$ which seems to be in reasonable agreement with low pressure experiments.
$H = \frac{pvf}{4T_0}$
$v = \sqrt{\frac{\pi k_B T}{8m}} = \sqrt{\frac{\pi\times 1.3806568\times 10^{-23}\,\mathrm{J\,K^{-1}}\times 300\,\mathrm{K}}{8\times(28\times 0.8+32\times 0.2)\times 1.6605402\times 10^{-27}\,\mathrm{kg}}} = 184.42\,\frac{\mathrm{m}}{\mathrm{s}}$
$H_{1\mathrm{mbar}} = \frac{1\,\mathrm{mbar}\times 184.42\,\frac{\mathrm{m}}{\mathrm{s}}\times 6}{4\times 300\,\mathrm{K}} = 92.21\,\frac{\mathrm{W}}{\mathrm{m^2\,K}}$
$H_{\mathrm{low}} = \frac{10^{-5}\,\mathrm{mbar}\times 184.42\,\frac{\mathrm{m}}{\mathrm{s}}\times 6}{4\times 300\,\mathrm{K}} = 9.221\times 10^{-4}\,\frac{\mathrm{W}}{\mathrm{m^2\,K}}$

$\frac{H_{1\mathrm{mbar}}}{h_1 c_1} = \frac{92.21 \frac{\mathrm{W}}{\mathrm{m}^2\,\mathrm{K}}}{100\,\mathrm{nm} \times 3100\,\mathrm{kg\,m^{-3}} \times 700\,\mathrm{J\,kg^{-1}\,K^{-1}}} = \frac{424.93}{\mathrm{s}}$

$\tau_{01\mathrm{mbar}} = \frac{1}{\frac{2\pi^2}{(1\,\mathrm{mm})^2}\frac{20\,\mathrm{W\,m^{-1}\,K^{-1}}}{3100\,\mathrm{kg\,m^{-3}} \times 700\,\mathrm{J\,kg^{-1}\,K^{-1}}} + \frac{424.93}{\mathrm{s}}} = 1.6\,\mathrm{ms}$

$\frac{H_{\mathrm{low}}}{h_1 c_1} = \frac{9.221 \times 10^{-4} \frac{\mathrm{W}}{\mathrm{m}^2\,\mathrm{K}}}{100\,\mathrm{nm} \times 3100\,\mathrm{kg\,m^{-3}} \times 700\,\mathrm{J\,kg^{-1}\,K^{-1}}} = \frac{4.249\,3 \times 10^{-3}}{\mathrm{s}}$

$\tau_{0\mathrm{low}} = \frac{1}{\frac{2\pi^2}{(1\,\mathrm{mm})^2}\frac{20\,\mathrm{W\,m^{-1}\,K^{-1}}}{3100\,\mathrm{kg\,m^{-3}} \times 700\,\mathrm{J\,kg^{-1}\,K^{-1}}} + \frac{4.249\,3 \times 10^{-3}}{\mathrm{s}}} = 5.5\,\mathrm{ms}$

Revised materials properties:

Silicon Nitride: in ref (Review of Scientific Instruments 66, 1115 (1995); doi: 10.1063/1.1145989) we find

$\kappa_1 = 12\,\mathrm{W\,m^{-1}\,K^{-1}}$

$D = (1.3 - 1.7) \times 10^{-6}\,\mathrm{m^2/\,s}$

$\tau_0 = \left(\frac{2\pi^2}{(1\,\mathrm{mm})^2}\frac{12\,\mathrm{W\,m^{-1}\,K^{-1}}}{3100\,\mathrm{kg\,m^{-3}} \times 700\,\mathrm{J\,kg^{-1}\,K^{-1}}}\right)^{-1} = 9.161\,1 \times 10^{-3}\,\mathrm{s}$

$\tau_0 = \left(\frac{2\pi^2}{(1\,\mathrm{mm})^2} D\right)^{-1} = \left(\frac{2\pi^2}{(1\,\mathrm{mm})^2}(1.3) \times 10^{-6}\,\mathrm{m^2/\,s}\right)^{-1} = 3.897\,0 \times 10^{-2}\,\mathrm{s}$

$\left(\frac{2\pi^2}{(1\,\mathrm{mm})^2}(1.7) \times 10^{-6}\,\mathrm{m^2/\,s}\right)^{-1} = 0.029\,8\,\mathrm{s}$

1 Circular membrane

Now, we consider a circular membrane of radius a and thickness h. The rim of the membrane is assumed to be at fixed temperature T_0. The heat continuity equation is

$$c\frac{\partial\Theta}{\partial t} = -\nabla\cdot\mathbf{J}_\Theta + q(r,t)$$

where $\Theta = T - T_0$ is the temperature deviation, $\mathbf{J}_\Theta$ the heat flux density, and c is the heat capacity per unit volume. An integral over the volume of the membrane yields

$$c\frac{\partial\int\Theta d\mathcal{V}}{\partial t} = \pi a^2 hc\frac{\partial\left\langle\Theta\right\rangle}{\partial t} = -\int\mathbf{n}\cdot\mathbf{J}_\Theta d\mathcal{A} + \int q(r,t)d\mathcal{V} = \kappa h 2\pi a\frac{\partial\Theta(a,t)}{\partial r} + P(a,t)$$

Here Gauss's divergence theorem was used and $\langle\Theta\rangle$ is the mean of the temperature deviation.

In case of a Gaussian power distribution $q(r,t) = q_0\exp(-r^2/(2\sigma^2))\times\mathrm{H}(t)$ (note $q(r,t)$ is the power dissipated per unit volume and $\mathrm{H}(t)$ is Heavisides step function) we have

$$\begin{aligned} P(r,t) &= 2\pi hq_0\mathrm{H}(t)\int_0^r u\exp(-\frac{u^2}{2\sigma^2})\,\mathrm{d}u = \pi hq_0\mathrm{H}(t)2\sigma^2\int_0^{\frac{r^2}{2\sigma^2}}\exp(-z)\,\mathrm{d}z \\ &= \pi hq_0 2\sigma^2\left(1-\exp(-\frac{r^2}{2\sigma^2})\right)\times\mathrm{H}(t) \end{aligned}$$

while

$$P(a,t) = \pi hq_0 2\sigma^2\left(1-\exp(-\frac{a^2}{2\sigma^2})\right)\times\mathrm{H}(t) = P_0\left[1-\exp(-\frac{a^2}{2\sigma^2})\right]\times\mathrm{H}(t)$$

where $P_0 = \pi hq_0 2\sigma^2$ is the full power in the beam and $P(a,t)$ the power that is received by the membrane.

In steady state we have

$$\begin{aligned} 0 &= \kappa h 2\pi r\frac{\partial\Theta(r,\infty)}{\partial r} + P(r,\infty) \\ \frac{\mathrm{d}\Theta_s(r)}{\mathrm{d}r} &= -\frac{P_s(r)}{\kappa h 2\pi r} = -\frac{P_0\left(1-\exp(-\frac{r^2}{2\sigma^2})\right)}{\kappa h 2\pi r} \end{aligned}$$

By integration we get

$$\begin{aligned} \Theta_s(r) &= -\int\frac{P_s(r)}{\kappa h 2\pi r}\,\mathrm{d}r = -\int\frac{P_s(r)}{\kappa h 4\pi r^2}\,\mathrm{d}r^2 = \\ &= -\frac{P_0}{4\pi\kappa h}\int\frac{\left(1-\exp(-\frac{r^2}{2\sigma^2})\right)}{r^2}\,\mathrm{d}r^2 = \\ \Theta_s(r) &= \frac{P_0}{4\pi\kappa h}\left(\ln\frac{a^2}{r^2} - \mathrm{Ei}(\frac{r^2}{2\sigma^2}) + \mathrm{Ei}(\frac{a^2}{2\sigma^2})\right) \end{aligned}$$

where the exponential integral is $\mathrm{Ei}(z) = \int_z^\infty \frac{1}{t} e^{-t} dt$, note, in some literature $\mathrm{E}_1(z)$ is used to signify this integral.

The average temperature becomes

$$\begin{aligned}\langle \Theta_s \rangle &= \frac{1}{\pi a^2} \int_0^a 2\pi r \Theta_s \, \mathrm{d}r = \frac{1}{a^2} \int_0^{a^2} \Theta_s \, \mathrm{d}r^2 = \frac{1}{a^2} \frac{P_0}{4\pi\kappa h} \int_0^{a^2} \left(\ln \frac{a^2}{r^2} - \mathrm{Ei}(\frac{r^2}{2\sigma^2}) + \mathrm{Ei}(\frac{a^2}{2\sigma^2}) \right) \mathrm{d}r^2 \\ &= \frac{P_0}{4\pi\kappa h} \frac{1}{a^2} \left[a^2 + 2\sigma^2 \exp\left(-\frac{a^2}{2\sigma^2} \right) - 2\sigma^2 \right] = \frac{P_0}{4\pi\kappa h} \left[1 + \frac{2\sigma^2}{a^2} \exp\left(-\frac{a^2}{2\sigma^2} \right) - \frac{2\sigma^2}{a^2} \right]\end{aligned}$$

As a result, the thermal energy Q in the membrane is

$$Q = \pi a^2 hc \langle \Theta_s \rangle = \tau P_s(a) = \tau P_0 \left[1 - \exp(-\frac{a^2}{2\sigma^2}) \right]$$

and we may as indicated define a time constant τ by $Q \equiv \tau P_s(a)$, which results in

$$\begin{aligned}\tau &= \frac{\pi a^2 hc \langle \Theta_s \rangle}{P_0 \left[1 - \exp(-\frac{a^2}{2\sigma^2}) \right]} = \frac{a^2 c}{4\kappa} \frac{1 + \frac{2\sigma^2}{a^2} \exp\left(-\frac{a^2}{2\sigma^2} \right) - \frac{2\sigma^2}{a^2}}{1 - \exp(-\frac{a^2}{2\sigma^2})} \\ &= \tau_0 \frac{1 + \frac{2\sigma^2}{a^2} \exp\left(-\frac{a^2}{2\sigma^2} \right) - \frac{2\sigma^2}{a^2}}{1 - \exp(-\frac{a^2}{2\sigma^2})}\end{aligned}$$

This time constant is seen to be dependent on the size of the beam as illustrated in the plot below. Note, $\tau_0 = \frac{a^2 c}{4\kappa} = \frac{a^2}{4D}$ is essentially the time constant expected for a delta-function power distribution.

Just for plotting $\frac{1 + \frac{2x^2}{1^2} \exp\left(-\frac{1^2}{2x^2} \right) - \frac{2x^2}{1^2}}{1 - \exp(-\frac{1^2}{2x^2})}$

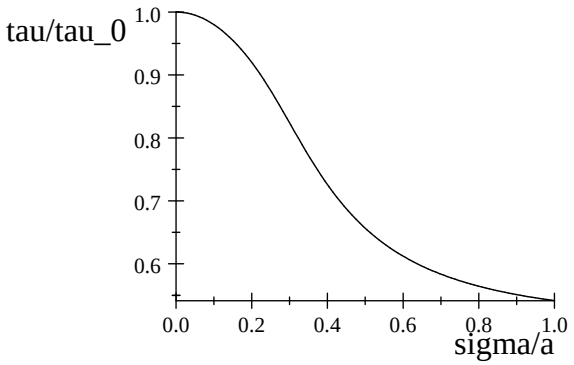

Figure 1: τ/τ_0 as a function of σ/a.

$U(r, a, \sigma) = \ln \frac{a^2}{r^2} - \mathrm{Ei}(\frac{r^2}{2\sigma^2}) + \mathrm{Ei}(\frac{a^2}{2\sigma^2})$

$U(r, 1, 0.1)$

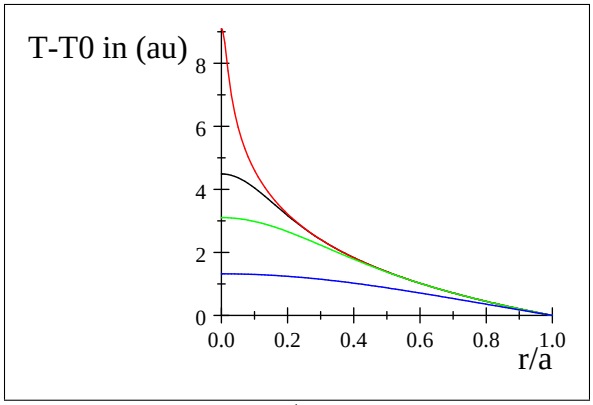

Temperature profile for $\sigma/a = 0.01$, 0.1, 0.2, and 0.5.

$rU(r, 1, 0.1)$

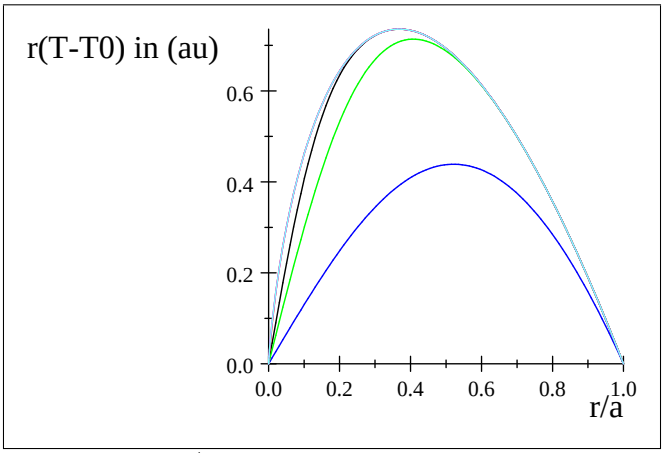

$r(T - T_0)$ profile for for $\sigma/a = 0.01$, 0.1, 0.2, and 0.5. In addition the profile for a delta function beam.

2 Bessel modes

Separation of the variables in the circular geometry leads to the rotational symmetric modes

$$\varphi_n(r, t) = \mathrm{J}_0(k_n r) \exp(-\frac{t}{\tau_n})$$

for which any real transient or static temperature profile may be built. The boundary condition $T(a, t) = 0$ requires that $k_n a$ are zeroes of the Bessel function, i.e. $\mathrm{J}_0(k_n a) = 0$. The first root is thus $k_n a = 2.4048$. The continuity equation requires $\tau_n = \frac{a^2}{D(k_n a)^2}$ and thus the time constant for the slower mode

is

$$\tau_1 = \frac{a^2}{D(k_1 a)^2} = \frac{a^2}{2.4048^2 D} \simeq 0.17292 \frac{a^2}{D}.$$

3 Laplace solution

For the case of a delta function power distribution it is possible to find the Laplace transformed temperature profile. Starting from the heat continuity equation expressed in terms of the temperature deviation Θ

$$\frac{\partial \Theta}{\partial t} = D\nabla^2 \Theta + \frac{q(r,t)}{C}$$

Laplace transform leads to

$$\begin{aligned} s\mathbf{\Theta} &= D\nabla^2 \mathbf{\Theta} + \frac{\mathbf{q}(r,s)}{C} = D\frac{1}{r}\frac{\partial}{\partial r}\left(r\frac{\partial \mathbf{\Theta}}{\partial r}\right) + \frac{\mathbf{q}(r,s)}{C}, \text{ or} \\ \frac{s}{D}\mathbf{\Theta} &= k^2 \mathbf{\Theta} = \nabla^2 \mathbf{\Theta} + \frac{\mathbf{q}(r,s)}{\kappa} \end{aligned}$$

Let us assume that $q(r,t) = \frac{P}{h}\delta(\mathbf{r})H(t)$ and thus the Laplace transform is $\mathbf{q}(r,s) = \frac{P}{sh}\delta(\mathbf{r})$.

The differential equation has solutions $\mathbf{\Theta} = A\,\mathrm{BesselK}_0(kr) + B\,\mathrm{BesselI}_0(kr)$, and from

$$\begin{aligned} \lim_{r\to 0} 2\pi r \frac{\partial \mathbf{\Theta}}{\partial r} &= -2\pi A = -\frac{P}{sh\kappa} \Rightarrow A = \frac{P}{2\pi sh\kappa} \\ \mathbf{\Theta}(a,s) &= 0 = A\,\mathrm{BesselK}_0(ka) + B\,\mathrm{BesselI}_0(ka) \Rightarrow B = -A\frac{\mathrm{BesselK}_0(ka)}{\mathrm{BesselI}_0(ka)} \end{aligned}$$

we find

$$\begin{aligned} \mathbf{\Theta} &= \frac{P}{2\pi sh\kappa}\left[\mathrm{BesselK}_0(kr) - \frac{\mathrm{BesselK}_0(ka)}{\mathrm{BesselI}_0(ka)}\mathrm{BesselI}_0(kr)\right] = \\ &= \frac{P}{2\pi sh\kappa}\left[\mathrm{BesselK}_0\left(\sqrt{\frac{s}{D}}r\right) - \frac{\mathrm{BesselK}_0\left(\sqrt{\frac{s}{D}}a\right)}{\mathrm{BesselI}_0\left(\sqrt{\frac{s}{D}}a\right)}\mathrm{BesselI}_0\left(\sqrt{\frac{s}{D}}r\right)\right] \end{aligned}$$

since $k = \sqrt{\frac{s}{D}}$.

By integration we find the average temperature $\langle\mathbf{\Theta}\rangle$

$$\begin{aligned} \langle\mathbf{\Theta}\rangle &= \frac{2\pi}{\pi a^2}\int r\mathbf{\Theta}\,\mathrm{d}r = \frac{2\pi}{\pi a^2}\frac{P}{2\pi sh\kappa}\int_0^a r\left[\mathrm{BesselK}_0(kr) - \frac{\mathrm{BesselK}_0(ka)}{\mathrm{BesselI}_0(ka)}\mathrm{BesselI}_0(kr)\right]\mathrm{d}r \\ &= \frac{1}{\pi}\frac{P}{sh\kappa}\frac{1}{k^2a^2}\left[1 - ka\,\mathrm{BesselK}_1(ka) - \frac{\mathrm{BesselK}_0(ka)}{\mathrm{BesselI}_0(ka)}ka\,\mathrm{BesselI}_1(ka)\right] \end{aligned}$$

A Taylor expansion leads to

$$\begin{aligned}\langle\boldsymbol{\Theta}\rangle &\simeq \frac{1}{\pi}\frac{P}{4h\kappa}\frac{1}{s}\frac{1}{1+\frac{3}{4\times4}(ka)^2+\frac{5}{576\times4}(ka)^4}\simeq\\ &\simeq \frac{1}{\pi}\frac{P}{4h\kappa}\frac{1}{s}\frac{1}{1+\frac{3}{4\times4}(ka)^2}=\frac{P}{4\pi h\kappa}\frac{1}{s}\frac{1}{1+\frac{3}{4\times4}\frac{sa^2}{D}}\end{aligned}$$

and thus a characteristic time constant of $\tau=\frac{3}{16}\frac{a^2}{D}$.

3.1 Uniform heat distribution

If we now assume $q(r,t)=\frac{P}{\pi a^2 h}\times\mathrm{H}(t)$ i.e. a uniform power distribution, we have $\mathbf{q}(r,s)=\frac{P}{\pi a^2 hs}$, then a particular solution is $k^2\boldsymbol{\Theta}_p=\frac{P}{\pi a^2 h\kappa s}\Rightarrow\boldsymbol{\Theta}_p=\frac{PD}{\pi a^2 h\kappa s^2}=\frac{P}{\pi a^2 h\kappa s}\frac{1}{k^2}$.

The homogeneous differential equation has solutions $\boldsymbol{\Theta}=A\,\mathrm{BesselK}_0(kr)+B\,\mathrm{BesselI}_0(kr)$ in this case $A=0$ and from the boundary conditions $\boldsymbol{\Theta}(a,s)=B\,\mathrm{BesselI}_0(ka)+\frac{P}{\pi a^2 h\kappa s}\frac{1}{k^2}=0$ we get $B=-\frac{P}{\pi a^2 h\kappa s}\frac{1}{k^2\,\mathrm{BesselI}_0(ka)}$ and thus

$$\boldsymbol{\Theta}(r,s)=\frac{P}{\pi a^2 h\kappa s}\left(\frac{1}{k^2}-\frac{\mathrm{BesselI}_0(kr)}{k^2\,\mathrm{BesselI}_0(ka)}\right)$$

The average temperature becomes

$$\begin{aligned}\langle\boldsymbol{\Theta}(s)\rangle &= \frac{2}{a^2}\int_0^a r\boldsymbol{\Theta}(r,s)dr=\frac{P}{\pi a^2 h\kappa s}\times\frac{2}{a^2}\int_0^a r\left(\frac{1}{k^2}-\frac{\mathrm{BesselI}_0(kr)}{k^2\,\mathrm{BesselI}_0(ka)}\right)dr\\ &= \frac{P}{\pi a^2 h\kappa s}\times\frac{2}{a^2}\left[\frac{a^2}{2k^2}-\frac{a\,\mathrm{BesselI}_1(ka)}{k^3\,\mathrm{BesselI}_0(ka)}\right]=\frac{P}{\pi a^2 h\kappa s}\times\left[\frac{1}{k^2}-\frac{2\,\mathrm{BesselI}_1(ka)}{ak^3\,\mathrm{BesselI}_0(ka)}\right]\\ &= \frac{P}{\pi h\kappa s}\times\left(\frac{1}{k^2a^2}-\frac{2\,\mathrm{BesselI}_1(ka)}{a^3k^3\,\mathrm{BesselI}_0(ka)}\right)\end{aligned}$$

A Taylor expansion leads to

$$\langle\boldsymbol{\Theta}(s)\rangle\simeq\frac{P}{\pi h\kappa s}\frac{1}{8}\frac{1}{1+\frac{1}{6}(ka)^2}=\frac{P}{\pi h\kappa s}\frac{1}{8}\frac{1}{1+\frac{1}{6}\frac{a^2}{D}s}\Rightarrow\tau=\frac{1}{6}\frac{a^2}{D},$$

but a better fit to $\langle\boldsymbol{\Theta}(s)\rangle$ over a wide range of Laplace frequencies is

$$\langle\boldsymbol{\Theta}(s)\rangle\simeq\frac{P}{\pi h\kappa s}\frac{1}{8}\frac{1}{1+\frac{1}{6.45}\frac{a^2}{D}s}\Rightarrow\tau=\frac{1}{6.45}\frac{a^2}{D}$$

which is obtained by integration.

Geometry	**Method**	τ	τ	**Notes**
Circular	Fundamental mode	$\frac{a^2}{2.4048^2 D}$	$0.173\frac{a^2}{D}$	
Circular	Average temperature Q/P	$\frac{a^2}{4D}$	$0.25\frac{a^2}{D}$	Beam width dependency
Circular	Laplace, delta function	$\frac{3}{16}\frac{a^2}{D}$	$0.188\frac{a^2}{D}$	
Circular	Laplace, uniform	$\frac{1}{6.45}\frac{a^2}{D}$	$0.155\frac{a^2}{D}$	
Square	Fundamental mode	$\frac{W^2}{2\pi^2 D}=\frac{2(W/2)^2}{\pi^2 D}$	$0.203\frac{(W/2)^2}{D}$	

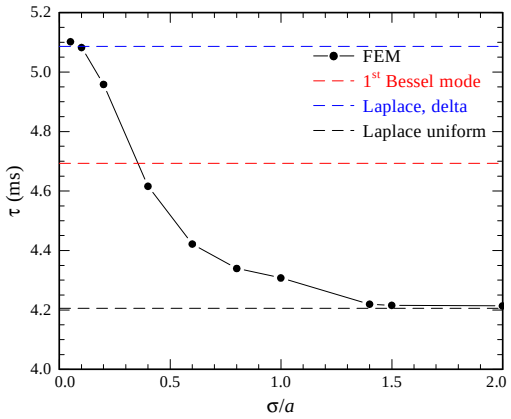

Figure 2: Time constants from FEM analysis and analytical models.

$\kappa_1 = 20\,\mathrm{W\,m^{-1}\,K^{-1}}$
$c_1 = \varrho C_p = 3100\,\mathrm{kg\,m^{-3}} \times 700\,\mathrm{J\,kg^{-1}\,K^{-1}}$
$D = \frac{\kappa_1}{c_1} = \frac{20\,\mathrm{W\,m^{-1}\,K^{-1}}}{3100\,\mathrm{kg\,m^{-3}} \times 700\,\mathrm{J\,kg^{-1}\,K^{-1}}} = 9.216\,6 \times 10^{-6}\,\frac{\mathrm{m}^2}{\mathrm{s}}$
$a = 0.5\,\mathrm{mm}$
$0.173\frac{a^2}{D} = 0.173 \times \frac{(0.5\,\mathrm{mm})^2}{9.216\,6 \times 10^{-6}\,\frac{\mathrm{m}^2}{\mathrm{s}}} = 4.692\,6 \times 10^{-3}\,\mathrm{s}$
$0.25\frac{a^2}{D} = 0.25 \times \frac{(0.5\,\mathrm{mm})^2}{9.216\,6 \times 10^{-6}\,\frac{\mathrm{m}^2}{\mathrm{s}}} = 6.781\,2 \times 10^{-3}\,\mathrm{s}$
$\frac{3}{16}\frac{a^2}{D} = \frac{3}{16} \times \frac{(0.5\,\mathrm{mm})^2}{9.216\,6 \times 10^{-6}\,\frac{\mathrm{m}^2}{\mathrm{s}}} = 5.085\,9 \times 10^{-3}\,\mathrm{s}$
$\frac{1+\frac{2\times(0.1)^2}{0.5^2}\exp\left(-\frac{0.5^2}{2\times0.1^2}\right)-\frac{2\times0.1^2}{0.5^2}}{1-\exp(-\frac{0.5^2}{2\times0.1^2})} \times 6.781\,2 \times 10^{-3}\,\mathrm{s} = 0.92 \times 6.781\,2 \times 10^{-3}\,\mathrm{s} = 6.238\,7 \times 10^{-3}\,\mathrm{s}$

$1\,\mathrm{W\,cm^{-2}} \times 2 \times \pi \times (100\,\mu\mathrm{m})^2 = 6.283\,2 \times 10^{-4}\,\frac{\mathrm{m}^2}{\mathrm{s}^3}\,\mathrm{kg}$
$\mathrm{W} = \frac{\mathrm{m}^2}{\mathrm{s}^3}\,\mathrm{kg}$

$\frac{P_0}{4\pi\kappa h} = \frac{6.0\times10^{-4}\,\mathrm{W}}{4\pi\times20\,\mathrm{W\,m^{-1}\,K^{-1}}\times0.1\,\mu\mathrm{m}} = 23.873\,\mathrm{tmpK} = 25.0\,\mathrm{tmpK}$
$\frac{P_0}{4\pi\kappa h}\left[1 + \frac{2\sigma^2}{a^2}\exp\left(-\frac{a^2}{2\sigma^2}\right) - \frac{2\sigma^2}{a^2}\right] =$
$1 + \frac{2\times0.1^2}{0.5^2}\exp\left(-\frac{0.5^2}{2\times0.1^2}\right) - \frac{2\times0.1^2}{0.5^2} = 0.92$
$23.873 \times 0.92 = 21.963 + 293.15 = 315.11$
$1 + \frac{2\times0.2^2}{0.5^2}\exp\left(-\frac{0.5^2}{2\times0.2^2}\right) - \frac{2\times0.2^2}{0.5^2} = 0.694\,06$
$0.694\,06 \times 25.0 = 17.352 + 293 = 310.35$

$1 + \frac{2\times0.05^2}{0.5^2}\exp\left(-\frac{0.5^2}{2\times0.05^2}\right) - \frac{2\times0.05^2}{0.5^2} = 0.98$
$293.15 + 23.873 \times 0.98 = 316.55$
$\frac{P_0}{4\pi\kappa h}\left(\ln\frac{a^2}{r^2} - \mathrm{Ei}(\frac{r^2}{2\sigma^2}) + \mathrm{Ei}(\frac{a^2}{2\sigma^2})\right) = \frac{1}{4\pi h\kappa}P_0\left(\mathrm{gamma} + \mathrm{Ei}\left(\frac{1}{2}\frac{a^2}{\sigma^2}\right) + \ln\frac{1}{2}\frac{r^2}{\sigma^2} + \ln\frac{a^2}{r^2}\right) - \frac{1}{8\pi h}\frac{r^2}{\kappa\sigma^2}P_0 + \frac{1}{64\pi h}\frac{r^4}{\kappa\sigma^4}P_0 - \frac{1}{576\pi h}\frac{r^6}{\kappa\sigma^6}P_0 + \frac{1}{6144\pi h}\frac{r^8}{\kappa\sigma^8}P_0 - \frac{1}{76\,800\pi h}\frac{r^{10}}{\kappa\sigma^{10}}P_0 + \frac{1}{1105\,920\pi h}\frac{r^{12}}{\kappa\sigma^{12}}P_0 - \frac{1}{18\,063\,360\pi h}\frac{r^{14}}{\kappa\sigma^{14}}P_0 + \frac{1}{330\,301\,440\pi h}\frac{r^{16}}{\kappa\sigma^{16}}P_0 - \frac{1}{6688\,604\,160\pi h}\frac{r^{18}}{\kappa\sigma^{18}}P_0 + O\left(r^{20}\right)$
$\frac{1}{4\pi h\kappa}P_0$
$\left(\mathrm{gamma} + \mathrm{Ei}\left(\frac{1}{2}\frac{0.5^2}{0.05^2}\right) + \ln\frac{1}{2}\frac{0.5^2}{0.05^2}\right)$
$\ln\frac{1}{2}\frac{0.5^2}{0.05^2} = 3.912$
$\mathrm{Ei}\left(\frac{1}{2}\frac{0.5^2}{0.05^2}\right) = 3.783\,3 \times 10^{-24}$
$\ln\frac{1}{2}\frac{0.5^2}{0.05^2} + \mathrm{gamma} = 4.489\,2 \times 23.873 = 107.17 + 293.15 = 400.32$

$\int r\ln\frac{a^2}{r^2}dr = \frac{1}{2}a^2\left(\ln\frac{a^2}{a^2} + 1\right) = \frac{1}{2}a^2$
$0.76\,\mathrm{m^{-1}} \times 2\pi \times 0.5\,\mathrm{mm} = 2.387\,6 \times 10^{-3}$
$0.19\,\mathrm{m^{-1}} \times 2\pi \times 0.5\,\mathrm{mm} = 5.969 \times 10^{-4}$

$\frac{P_0}{4\pi\kappa h}\left[1 + \frac{2\sigma^2}{a^2}\exp\left(-\frac{a^2}{2\sigma^2}\right) - \frac{2\sigma^2}{a^2}\right]$
$\frac{P_0}{4\pi\kappa h} = 23.873$

$\frac{1+\frac{2x^2}{1^2}\exp\left(-\frac{1^2}{2x^2}\right)-\frac{2x^2}{1^2}}{1-\exp(-\frac{1^2}{2x^2})}$

6.781 2

$\frac{s}{D}\mathbf{\Theta} = k^2\mathbf{\Theta} = \nabla^2\mathbf{\Theta} + \frac{\mathbf{q}(r,s)}{\kappa} = \frac{1}{r}\frac{\partial}{\partial r}\left(r\frac{\partial \mathbf{\Theta}}{\partial r}\right) + \frac{\mathbf{q}(r,s)}{\kappa}$

The homogeneous differential equation has solutions $\mathbf{\Theta} = A\,\mathrm{BesselK}_0(kr) + B\,\mathrm{BesselI}_0(kr)$

If we now assume $q(r,t) = \frac{P}{\pi a^2 h} \times \mathrm{H}(t)$ i.e. a uniform power distribution, we have $\mathbf{q}(r,s) = \frac{P}{\pi a^2 h s}$, then a particular solution is $k^2\mathbf{\Theta}_p = \frac{P}{\pi a^2 h \kappa s} \Rightarrow \mathbf{\Theta}_p = \frac{PD}{\pi a^2 h \kappa s^2} = \frac{P}{\pi a^2 h \kappa s}\frac{1}{k^2}$ in this case $A = 0$ and from the boundary conditions $\mathbf{\Theta}(a,s) = B\,\mathrm{BesselI}_0(ka) + \frac{P}{\pi a^2 h\kappa s}\frac{1}{k^2} = 0$ we get $B = -\frac{P}{\pi a^2 h\kappa s}\frac{1}{k^2\,\mathrm{BesselI}_0(ka)}$ and thus

$$\mathbf{\Theta}(r,s) = \frac{P}{\pi a^2 h \kappa s}\left(\frac{1}{k^2} - \frac{\mathrm{BesselI}_0(kr)}{k^2\,\mathrm{BesselI}_0(ka)}\right)$$

$$\begin{aligned}
\langle\mathbf{\Theta}(s)\rangle &= \frac{2}{a^2}\int_0^a r\mathbf{\Theta}(r,s)dr = \frac{P}{\pi a^2 h\kappa s} \times \frac{2}{a^2}\int_0^a r\left(\frac{1}{k^2} - \frac{\mathrm{BesselI}_0(kr)}{k^2\,\mathrm{BesselI}_0(ka)}\right)dr \\
&= \frac{P}{\pi a^2 h\kappa s} \times \frac{2}{a^2}\left[\frac{a^2}{2k^2} - \frac{a\,\mathrm{BesselI}_1(ka)}{k^3\,\mathrm{BesselI}_0(ka)}\right] = \frac{P}{\pi a^2 h\kappa s} \times \left[\frac{1}{k^2} - \frac{2\,\mathrm{BesselI}_1(ka)}{ak^3\,\mathrm{BesselI}_0(ka)}\right] \\
&= \frac{P}{\pi h\kappa s} \times \left(\frac{1}{k^2a^2} - \frac{2\,\mathrm{BesselI}_1(ka)}{a^3k^3\,\mathrm{BesselI}_0(ka)}\right) \simeq \frac{P}{\pi h\kappa s}\frac{1}{8 + \frac{4}{3}(ka)^2} = \frac{P}{\pi h\kappa s}\frac{1}{8}\frac{1}{1+\frac{1}{6}(ka)^2} \\
&= \frac{P}{\pi h\kappa s}\frac{1}{8}\frac{1}{1+\frac{1}{6}\frac{a^2}{D}s} \Rightarrow \tau = \frac{1}{6}\frac{a^2}{D}
\end{aligned}$$

$\int r\,\mathrm{BesselI}_0(kr)\,dr = \frac{r\,\mathrm{BesselI}_1(kr)}{k}$

$\frac{1}{\frac{1}{x^2} - \frac{2\,\mathrm{BesselI}_1(x)}{x^3\,\mathrm{BesselI}_0(x)}} = 8 + \frac{4}{3}x^2 - \frac{1}{144}x^4 + O\left(x^6\right)$

$\frac{1}{6}\frac{a^2}{D} = 0.166\,67\frac{a^2}{D} = \frac{1}{6} \times \frac{(0.5\,\mathrm{mm})^2}{9.216\,6\times10^{-6}\,\frac{\mathrm{m}^2}{\mathrm{s}}} = 4.520\,8\times10^{-3}\,\mathrm{s}$

$\frac{P}{\pi h\kappa}\frac{1}{8} = \frac{P}{\pi h\kappa s}\frac{1}{8} = \frac{6.0\times10^{-4}\,\mathrm{W}}{8\pi\times20\,\mathrm{W\,m^{-1}\,K^{-1}}\times0.1\,\mu\mathrm{m}} = 11.937\,\mathrm{tmpK}$

$\frac{P_0}{4\pi\kappa h} = \frac{6.0\times10^{-4}\,\mathrm{W}}{4\pi\times20\,\mathrm{W\,m^{-1}\,K^{-1}}\times0.1\,\mu\mathrm{m}}$

$1 - \exp(-\frac{1^2}{2\times1^2}) = 0.393\,47 \times 11.937 = 4.696\,9$

$\frac{1}{k^2} - \frac{\mathrm{BesselI}_0(kr)}{k^2\,\mathrm{BesselI}_0(ka)} = \left(\frac{1}{4}a^2 - \frac{1}{4}r^2\right) - k^2\left(\frac{3}{64}a^4 - \frac{1}{16}a^2r^2 + \frac{1}{64}r^4\right) + O\left(k^4\right)$

$\left(\frac{1}{4}a^2 - \frac{1}{4}r^2\right)^2 = \frac{1}{16}a^4 - \frac{1}{8}a^2r^2 + \frac{1}{16}r^4$

$\frac{3}{64}a^4 - \frac{1}{16}a^2r^2 + \frac{1}{64}r^4 - \frac{1}{2}\left(\frac{1}{4}a^2 - \frac{1}{4}r^2\right)^2 = \frac{1}{64}a^4 - \frac{1}{64}r^4$

$\frac{1}{\frac{1}{k^2} - \frac{\mathrm{BesselI}_0(kr)}{k^2\,\mathrm{BesselI}_0(ka)}} = \frac{1}{\frac{1}{4}a^2 - \frac{1}{4}r^2} + \frac{k^2}{\left(\frac{1}{4}a^2 - \frac{1}{4}r^2\right)^2}\left(\frac{3}{64}a^4 - \frac{1}{16}a^2r^2 + \frac{1}{64}r^4\right) + O\left(k^4\right)$

$\frac{1}{\left(\frac{1}{4}a^2 - \frac{1}{4}r^2\right)^2}\left(\frac{3}{64}a^4 - \frac{1}{16}a^2r^2 + \frac{1}{64}r^4\right) = \frac{3a^2 - r^2}{4a^2 - 4r^2}$

$\frac{1}{\frac{1}{k^2} - \frac{\mathrm{BesselI}_0(kr)}{k^2\,\mathrm{BesselI}_0(ka)}} \simeq \frac{1}{\frac{1}{4}a^2 - \frac{1}{4}r^2} + k^2\frac{3a^2 - r^2}{4a^2 - 4r^2}$

$$\frac{1}{k^2}-\frac{\mathrm{BesselI}_0(kr)}{k^2\,\mathrm{BesselI}_0(ka)}\simeq\frac{\frac{1}{4}\left(a^2-r^2\right)}{1+\frac{1}{16}k^2(3a^2-r^2)}$$

$$\int r\frac{\frac{1}{4}\left(a^2-r^2\right)}{1+\frac{1}{16}k^2(3a^2-r^2)}dr=\frac{2}{k^4}\left(16\ln\left(-\frac{1}{k^2}\left(3a^2k^2-k^2r^2+16\right)\right)+k^2r^2+2a^2k^2\ln\left(-\frac{1}{k^2}\left(3a^2k^2-k^2r^2+16\right)\right)\right)$$

$$\left(\frac{2\,\mathrm{BesselI}_1(ka)}{a^3k^3\,\mathrm{BesselI}_0(ka)}\right)^{-1}=a^2k^2+\frac{1}{8}a^4k^4-\frac{1}{192}a^6k^6+O\left(k^8\right)$$

$$\left(\frac{1}{k^2a^2}-\frac{2\,\mathrm{BesselI}_1(ka)}{a^3k^3\,\mathrm{BesselI}_0(ka)}\right)^{-1}=8+\frac{4}{3}a^2k^2-\frac{1}{144}a^4k^4+O\left(k^6\right)$$

$$\frac{1}{10\,\mathrm{nm}\times1\,\mathrm{cm}^2/(\,\mathrm{V\,s})\times10^{17}\,\mathrm{cm}^{-3}\times1.60217733\times10^{-19}\,\mathrm{C}}=\frac{6.241\,5\times10^7}{\mathrm{A}^2}\,\frac{\mathrm{m}^2}{\mathrm{s}^3}\,\mathrm{kg}=\frac{62415.}{\mathrm{A}^2}\,\frac{\mathrm{m}^2}{\mathrm{s}^3}\,\mathrm{kg}$$

$$\frac{310\times\sqrt{2}}{2}=219.2$$
$$100/\sqrt{2}=70.711$$
$$90/\sqrt{2}=63.640$$

$$\mathrm{BesselK}_0\left(k\sqrt{(x-x_0)^2+y^2}\right)-\mathrm{BesselK}_0\left(k\sqrt{(-x+x_0+d)^2+y^2}\right)$$

$$q(k,x,y,d,x_0)=\mathrm{BesselK}_0\left(k\sqrt{(x-x_0)^2+y^2}\right)-\mathrm{BesselK}_0\left(k\sqrt{(-x+x_0+d)^2+y^2}\right)$$

$$\mathrm{BesselK}_0\left(k\sqrt{(x-x_0)^2+y^2}\right)-\mathrm{BesselK}_0\left(k\sqrt{(-x+x_0+d)^2+y^2}\right)=\left(\ln\tfrac{1}{2}k\sqrt{(d-x+x_0)^2+y^2}-\ln\tfrac{1}{2}k\right.$$

$$k^2\left(\left((x-x_0)^2+y^2\right)\left(\tfrac{1}{4}\,\mathrm{gamma}-\tfrac{1}{4}\right)-\left((d-x+x_0)^2+y^2\right)\left(\tfrac{1}{4}\,\mathrm{gamma}-\tfrac{1}{4}\right)+\left(\ln\tfrac{1}{2}k\sqrt{(x-x_0)^2+y^2}\right)\left(\tfrac{1}{4}\,(x-\right.\right.$$

$$k^4\left(\left((x-x_0)^2+y^2\right)^2\left(\tfrac{1}{64}\,\mathrm{gamma}-\tfrac{3}{128}\right)-\left((d-x+x_0)^2+y^2\right)^2\left(\tfrac{1}{64}\,\mathrm{gamma}-\tfrac{3}{128}\right)+\left(\ln\tfrac{1}{2}k\sqrt{(x-x_0)^2+y^2}\right.\right.$$

$$O\left(k^6\right)$$

$$\mathrm{BesselK}_0\left(k\sqrt{(x-x_0)^2+y^2}\right)+\alpha\,\mathrm{BesselI}_0\left(k\sqrt{(x-x_0)^2+y^2}\right)$$

$$x^2+y^2=a^2\Rightarrow y^2=a^2-x^2$$

$$\mathrm{BesselK}_0\left(k\sqrt{(x-x_0)^2+a^2-x^2}\right)+\alpha\,\mathrm{BesselI}_0\left(k\sqrt{(x-x_0)^2+a^2-x^2}\right)=$$

$$0$$

$$\alpha=-\frac{\mathrm{BesselK}_0\left(k\sqrt{(x-x_0)^2+a^2-x^2}\right)}{\mathrm{BesselI}_0\left(k\sqrt{(x-x_0)^2+a^2-x^2}\right)}$$

$$(x-x_0)^2+a^2-x^2=a^2+x_0^2-2xx_0$$

$$\frac{\mathrm{BesselK}_0\left(k\sqrt{a^2+x_0^2-2xx_0}\right)}{\mathrm{BesselI}_0\left(k\sqrt{a^2+x_0^2-2xx_0}\right)}=\frac{1}{\mathrm{BesselI}_0\left(k\sqrt{a^2+x_0^2}\right)}\,\mathrm{BesselK}_0\left(k\sqrt{a^2+x_0^2}\right)+x\left(k\frac{\frac{x_0}{\sqrt{a^2+x_0^2}}}{\mathrm{BesselI}_0\left(k\sqrt{a^2+x_0^2}\right)}\,\mathrm{BesselK}\right.$$

$$x^2\left(\frac{1}{\mathrm{BesselI}_0\left(k\sqrt{a^2+x_0^2}\right)}\left(\frac{1}{2}k^2x_0^2\frac{\mathrm{BesselK}_0\left(k\sqrt{a^2+x_0^2}\right)+\frac{1}{k\sqrt{a^2+x_0^2}}\,\mathrm{BesselK}_1\left(k\sqrt{a^2+x_0^2}\right)}{a^2+x_0^2}+\frac{1}{2}k\frac{x_0^2}{\left(a^2+x_0^2\right)^{\frac{3}{2}}}\,\mathrm{BesselK}_1\left(k\sqrt{a^2+\right.\right.\right.\right.$$

$$x^3 \left(\frac{1}{\operatorname{BesselI}_0\left(k\sqrt{a^2+x_0^2}\right)} \left(\frac{1}{2}k^2 x_0^3 \frac{\operatorname{BesselK}_0\left(k\sqrt{a^2+x_0^2}\right)+\frac{1}{k\sqrt{a^2+x_0^2}}\operatorname{BesselK}_1\left(k\sqrt{a^2+x_0^2}\right)}{\left(a^2+x_0^2\right)^2} + \frac{1}{6}k^2\frac{x_0^2}{a^2+x_0^2}\left(x_0 \frac{\operatorname{BesselK}_0\left(k\sqrt{a^2+x_0^2}\right.\right.\right.

$\left(\frac{3}{64}a^4 - \frac{1}{16}a^2r^2 + \frac{1}{64}r^4\right) - \frac{1}{2}\left(\frac{1}{4}a^2 - \frac{1}{4}r^2\right)^2 = \frac{1}{64}a^4 - \frac{1}{64}r^4 =$
$\frac{1}{64}a^4 - \frac{1}{64}r^4 = \frac{1}{64}(a^2 - r^2)(a^2 + r^2)$ is true

$\frac{\frac{1}{2}\frac{1}{4}\left(a^2-r^2\right)^2+\frac{1}{64}(a^2-r^2)(a^2+r^2)}{\frac{1}{4}(a^2-r^2)} = \frac{\frac{1}{2}\frac{1}{4}\left(a^2-r^2\right)+\frac{1}{64}(a^2+r^2)}{\frac{1}{4}} = \frac{9}{16}a^2 - \frac{7}{16}r^2 = \frac{1}{8}a^2 + \frac{7}{16}\left(a^2 - r^2\right)$

$\left(\frac{1}{k^2} - \frac{\mathrm{BesselI}_0(k0)}{k^2\,\mathrm{BesselI}_0(ka)}\right)^{-1} = \frac{4}{a^2} + \frac{3}{4}k^2 + \frac{5}{576}a^2k^4 + O\left(k^6\right)$

$\left(\frac{1}{k^2} - \frac{\mathrm{BesselI}_0(ka/2)}{k^2\,\mathrm{BesselI}_0(ka)}\right)^{-1} = \frac{16}{3a^2} + \frac{11}{12}k^2 - \frac{1}{2304}a^2k^4 + O\left(k^6\right)$

$\frac{11}{12}\frac{3}{16}$

$\left(\frac{1}{k^2} - \frac{\mathrm{BesselI}_0(kr)}{k^2\,\mathrm{BesselI}_0(ka)}\right)^{-1} = \frac{1}{\frac{1}{4}a^2-\frac{1}{4}r^2} + \frac{k^2}{\left(\frac{1}{4}a^2-\frac{1}{4}r^2\right)^2}\left(\frac{3}{64}a^4 - \frac{1}{16}a^2r^2 + \frac{1}{64}r^4\right) - k^4\frac{\frac{1}{\frac{1}{4}a^2-\frac{1}{4}r^2}\left(\frac{19}{2304}a^6-\frac{3}{256}a^4r^2+\frac{1}{256}a^2r^4-\frac{1}{2304}r^6\right)-\frac{1}{\left(\frac{1}{4}a^2-\frac{1}{4}r^2\right)^2}\left(\frac{3}{64}a^4-\frac{1}{16}a^2r^2+\frac{1}{64}r^4\right)^2}{\frac{1}{4}a^2-\frac{1}{4}r^2} + O\left(k^6\right)$

$\frac{1}{\left(\frac{1}{4}a^2-\frac{1}{4}r^2\right)}\left(\frac{3}{64}a^4 - \frac{1}{16}a^2r^2 + \frac{1}{64}r^4\right)$

$\frac{16}{3\left(\frac{1}{4}1^2-\frac{1}{4}r^2\right)}\left(\frac{3}{64}1^4 - \frac{1}{16}1^2r^2 + \frac{1}{64}r^4\right)$

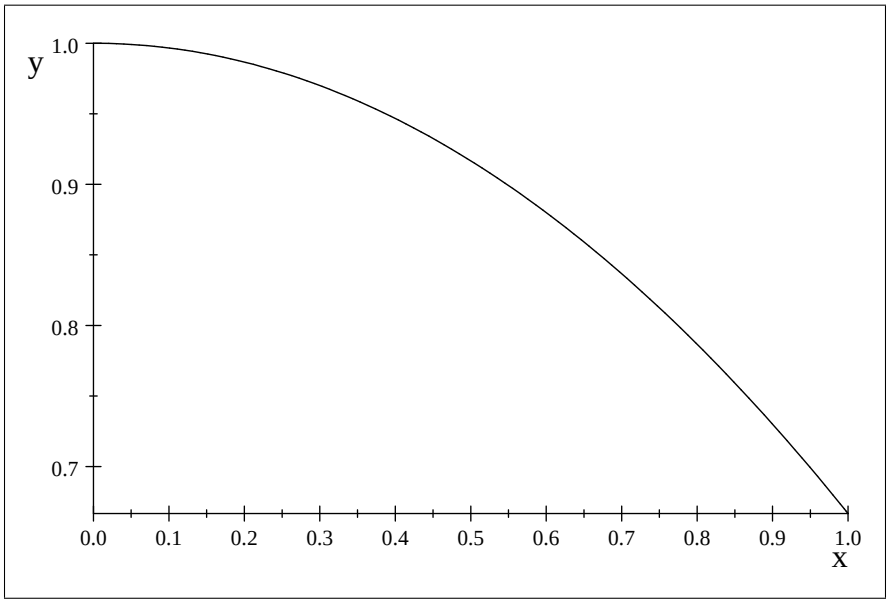

$\left(\frac{1}{k^2a^2} - \frac{2\,\mathrm{BesselI}_1(ka)}{a^3k^3\,\mathrm{BesselI}_0(ka)}\right)^{-1} = 8 + \frac{4}{3}a^2k^2 - \frac{1}{144}a^4k^4 + O\left(k^6\right)$

$\left(\frac{1}{k^2a^2} - \frac{2\,\mathrm{BesselI}_1(ka)}{a^3k^3\,\mathrm{BesselI}_0(ka)}\right) = \frac{1}{8} - \frac{1}{48}a^2k^2 + \frac{11}{3072}a^4k^4 + O\left(k^6\right)$

$ak\,\mathrm{BesselI}_0\left(ka\right) - 2\,\mathrm{BesselI}_1\left(ka\right) = \frac{1}{8}a^3k^3 + \frac{1}{96}a^5k^5 + \frac{1}{3072}a^7k^7 + O\left(k^9\right)$

$a^3k^3\,\mathrm{BesselI}_0\left(ka\right) = a^3k^3 + \frac{1}{4}a^5k^5 + \frac{1}{64}a^7k^7 + O\left(k^9\right)$

$\frac{\frac{1}{8}a^3k^3+\frac{1}{96}a^5k^5+\frac{1}{3072}a^7k^7}{a^3k^3+\frac{1}{4}a^5k^5+\frac{1}{64}a^7k^7} = \frac{a^4k^4+32a^2k^2+384}{48a^4k^4+768a^2k^2+3072}$

$\frac{768}{3072} = \frac{1}{4}$

$\frac{32}{384} = \frac{1}{12}$

$\frac{384}{3072} = \frac{1}{8}$

$\frac{48}{3072} = \frac{1}{64}$

$D(a,k) = \left(\frac{1}{k^2 a^2} - \frac{2\,\mathrm{BesselI}_1(ka)}{a^3 k^3\,\mathrm{BesselI}_0(ka)}\right)$

$D(1,\sqrt{s}) = \frac{1}{s} - \frac{2}{s^{\frac{3}{2}}\,\mathrm{BesselI}_0\left(\sqrt{s}\right)}\,\mathrm{BesselI}_1\left(\sqrt{s}\right)$

$\frac{1}{\frac{1}{s} - \frac{2}{s^{\frac{3}{2}}\,\mathrm{BesselI}_0\left(\sqrt{s}\right)}\,\mathrm{BesselI}_1\left(\sqrt{s}\right)} = 8 + \frac{4}{3}s - \frac{1}{144}s^2 + \frac{1}{4320}s^3 - \frac{7}{829\,440}s^4 + \frac{11}{34\,836\,480}s^5 + O\left(s^6\right)$

$\frac{1}{\frac{1}{s} - \frac{2}{s^{\frac{3}{2}}\,\mathrm{BesselI}_0\left(\sqrt{s}\right)}\,\mathrm{BesselI}_1\left(\sqrt{s}\right)} \times \frac{1}{8} = 1 + \frac{1}{6}s - \frac{1}{1152}s^2 + \frac{1}{34\,560}s^3 - \frac{7}{6635\,520}s^4 + \frac{11}{278\,691\,840}s^5 - \frac{797}{535\,088\,332\,800}s^6 + \frac{181}{3210\,529\,996\,800}s^7 + O\left(s^8\right)$

$(D(1,\sqrt{x}))^{-1}$

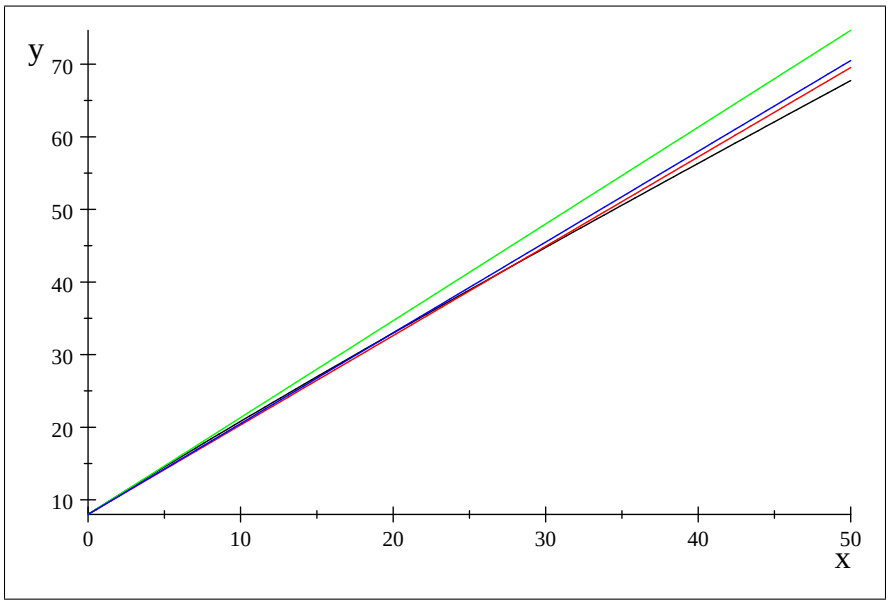

$L(s,\alpha) = \frac{1}{\frac{1}{s} - \frac{2}{s^{\frac{3}{2}}\,\mathrm{BesselI}_0\left(\sqrt{s}\right)}\,\mathrm{BesselI}_1\left(\sqrt{s}\right)} \times \frac{1}{8(1+s/\alpha)}$

$L(s,6.45)$

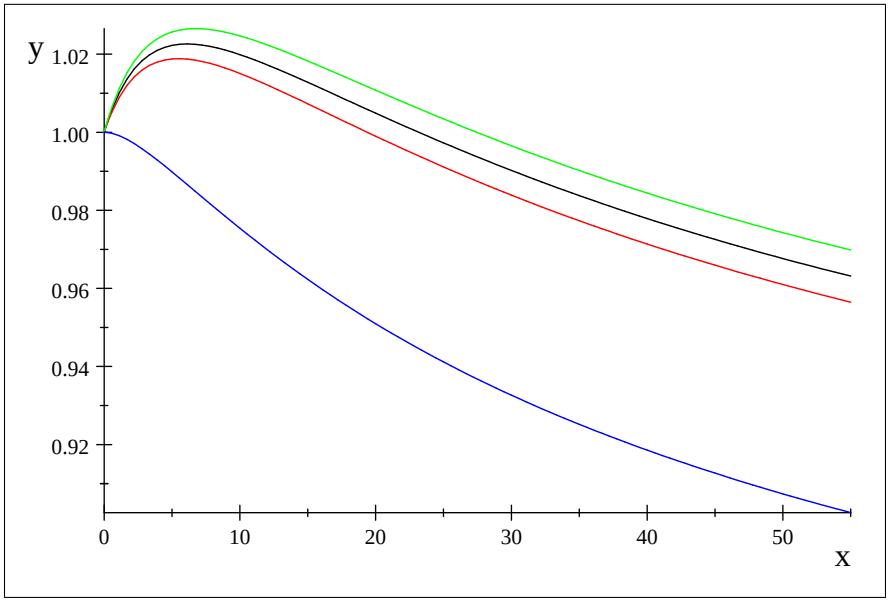

$\int_0^{6\times 10} \frac{1}{\frac{1}{s}-\frac{2}{s^{\frac{3}{2}}\ \mathrm{BesselI}_0(\sqrt{s})}\ \mathrm{BesselI}_1(\sqrt{s})} \times \frac{1}{8} ds = 332.91 = 100.37 = 43.815 = 8.$
945 5

$\int_0^{6\times 10}(1+\alpha s)ds = 1800\alpha + 60 = 450\alpha + 30 = 162\alpha + 18 = 18\alpha + 6$

$18\alpha + 6 = 8.9455$, Solution is: $(0.16364)^{-1} = 6.1110$

$162\alpha + 18 = 43.815$, Solution is: $(0.15935)^{-1} = 6.2755$

$450/\alpha + 30 = 100.37$, Solution is: 6.3948

$1800/\alpha + 60 = 332.91$, Solution is: 6.5956

$$P(K) = \frac{\int_0^{6\times K}\left(\frac{1}{\frac{1}{s}-\frac{2}{s^{\frac{3}{2}}\ \mathrm{BesselI}_0(\sqrt{s})}\ \mathrm{BesselI}_1(\sqrt{s})} \times \frac{1}{8} - 1\right) ds}{\int_0^{6\times K} s ds}$$

$(P(20))^{-1} = 6.8222 = 6.2007 = 6.3948 = 6.5956$

$(P(x))^{-1}$

…And There Was Light